Doctoral theses at NTNU, 2019:340

Trond Brandvik

Degradation of Refractory Lining in Carbon Anode Baking Furnaces

Doctoral thesis

Trond Brandvik

Doctoral theses at NTNU, 2019:340

NTNU

NTNU
Norwegian University of Science and Technology
Thesis for the Degree of
Philosophiae Doctor
Faculty of Natural Sciences
Department of Materials Science and
Engineering

ISBN 978-82-326-4276-2 (printed ver.)
ISBN 978-82-326-4277-9 (electronic ver.)
ISSN 1503-8181

NTNU
Norwegian University of
Science and Technology

NTNU
Norwegian University of
Science and Technology

Trond Brandvik

Degradation of Refractory Lining in Carbon Anode Baking Furnaces

Thesis for the Degree of Philosophiae Doctor

Trondheim, November 2019

Norwegian University of Science and Technology
Faculty of Natural Sciences
Department of Materials Science and Engineering

NTNU
Norwegian University of
Science and Technology

NTNU
Norwegian University of Science and Technology

Thesis for the Degree of Philosophiae Doctor

Faculty of Natural Sciences
Department of Materials Science and Engineering

ISBN 978-82-326-4276-2 (printed ver.)
ISBN 978-82-326-4277-9 (electronic ver.)
ISSN 1503-8181

Doctoral theses at NTNU, 2019:340

Printed by NTNU Grafisk senter

Preface

This thesis has been submitted to the Norwegian University of Science and Technology (NTNU) in partial fulfillment of the requirements for the Degree of Philosophiae Doctor. The work presented in this thesis has been performed at the Department of Materials Science and Engineering (IMA) from august 2015 to august 2019, including 3.5 months of research stay at Laval University in Quebec, Canada from January to April 2019. During my time as a PhD candidate, 17 months of various teaching activities have been carried out in addition to the scientific work. The industrial autopsies have been carried out at the anode baking furnaces at Hydro Årdalstangen and Alcoa Mosjøen. The measurements of pit gas atmosphere have been carried out at the anode baking furnace at Alcoa Mosjøen. The work has been supervised by Professor Tor Grande (IMA) as main supervisor, and Senior Research Scientist Arne Petter Ratvik (SINTEF Industry) and Associate Professor/Research Scientist Zhaohui Wang (IMA and SINTEF Industry) as co-supervisors. Professor Louis Gosselin and Research Professional Hicham Chaouki supervised me during my stay at Laval University. The project has been a part of the CaRMa project (Reactivity of Carbon and Refractory Materials used in Metals production Technology, project number 236665). The CaRMa project has been funded by the Norwegian Research Council, SINTEF, NTNU and the industry partners Hydro Aluminium, Alcoa Norway, Elkem Carbon and Skamol A/S. The research stay at Laval University has been funded by INTPART Norwegian-Canadian Partnership in Research and Education on Primary Production of Aluminium (CaNAl), project number 274984. The XRF analysis has been carried out by Torill Sørløkk at the Department of Geoscience and Petroleum (NTNU). The computed tomography has been carried out in collaboration with Raymond Luneng (NTNU).

A list of all publications included in the thesis with a summary of the contributions provided in each work is found below. The publications are included in their entirety in Appendix D.

The work presented in this thesis is based on the following publications and conference proceedings:

1. **T. Brandvik**, A. P. Ratvik and T. Grande. Thermodynamic Assessment of the Chemical Durability of Refractory Lining in Anode Baking Furnaces, *Travaux 45, Proceedings of the 34th International ICSOBA Conference*, 2016.
   Contributions: TB performed the calculations with input from TG; TB and TG analyzed and interpreted the results, and wrote the paper with input from APR.

2. **T. Brandvik**, Z. Wang, A. P. Ratvik and T. Grande. Investigations of Spent Refractory Lining in Anode Baking Furnaces, *Light Metals*, pages 1281-1288, 2017.
   Contributions: TB performed all autopsy sampling and characterization experiments with input from TG, except the coke sample which was characterized by ZW; TB and TG analysed and interpreted the results, and wrote the paper with input from ZW and APR.

3. **T. Brandvik**, A. P. Ratvik and T. Grande. Effects of Water Cooling of Green Anodes on Anode Furnace Operation *Travaux 47, Proceedings of the 36th International ICSOBA Conference*, pages 555-562, 2018.
   Contributions: TB performed the calculations with input from TG; TB and TG analyzed and interpreted the results, and wrote the paper with input from APR.

4. **T. Brandvik**, Z. Wang, A. P. Ratvik and T. Grande. Autopsy of Refractory Lining in Anode Kilns With Open and Closed Design, *J. App. Ceram. Tech.*, 16(2):602-613, 2019.
   Contributions: TB performed all autopsy sampling and characterization experiments with input from TG, except the coke sample which was characterized by ZW; TB and TG analysed and interpreted the results, and wrote the paper with input from ZW and APR.

5. **T. Brandvik**, H. Gaertner, A. P. Ratvik, T. Grande and T. A. Aarhaug. *In situ* Monitoring of Pit Gas Composition During Baking of Anodes for Aluminium Electrolysis, *Metall. Mater. Trans. B.*, 50(2):950-957, 2019
   Contributions: TB, HG, APR, TG and TAA designed and built the experi-

mental equipment; TB and HG performed the experiments at the furnace; TAA analyzed the IR spectra; TB, TG, TAA and APR interpreted the results and wrote the paper.

I have also contributed to the following conference proceedings not included in the dissertation:

1. T. A. Aarhaug, **T. Brandvik**, O. S. Kjos, H. Gaertner and A. P. Ratvik. A Study of Anode Baking Gas Composition, *Light Metals*, pages 1379-1385, 2018.
   Contributions: TB, TAA, HG and APR designed and built the experimental equipment; TB and HG performed the experiments at the furnace; TAA analyzed the IR spectra; TB, TAA, OSK, and APR interpreted the results; TAA, TB, OSK and APR wrote the paper.
2. T. A. Aarhaug, **T. Brandvik**, H. Gaertner, A. P. Ratvik and O. S. Kjos. Assessment of Anode Baking Furnace Gas Composition, *Proceedings of the* 12^{th} *Australasian Aluminium Smelting Technology Conference*, 2018.
   Contributions: TB, HG, APR, and TAA designed and built the experimental equipment; TB and HG performed the experiments at the furnace; TAA analyzed the IR spectra; TB, TAA, OSK and APR interpreted the results; TB, TAA, OSK and APR wrote the paper.

Trond Brandvik
August 2019
Trondheim

Acknowledgments

The submission of this thesis and the subsequent defence mark the end of my PhD period and is the final effort during my nine years at NTNU. For the last five years, during both my MSc and PhD projects, I have been under the supervision of Tor, and I am very grateful for the collaboration we have had during these years. You have been a wonderful supervisor, and I have really enjoyed our conversations and your guidance. I would also like to thank my co-supervisor Arne Petter for all our good discussions, especially in the more industrial aspect of my project. Your input have been an invaluable source of industrial experience, which have been deeply appreciated. I am also very grateful for the help and feedback I have gotten from my second co-supervisor, Zhaohui, especially during the FEM modeling project. Your input on FEM and COMSOL has been very helpful, both during the modeling and writing of the manuscript. During the spring semester of 2019 I visited the REGAL community at Université Laval in Quebec City, by the invitation of Professor Houshang Alamdari. I would like to thank Houshang for the warm welcome in Quebec, and for making it possible for me to visit Université Laval during my PhD work. I would also like to thank Louis Gosselin and Hicham Chaouki at Université Laval for guiding me through the world of finite element modeling. I really appreciate the the effort you made during my stay at Laval, making the FEM modeling a nice addition to my PhD work.

A considerable part of my PhD period has been related to various teaching activities, where the lectures in Inorganic chemistry during the spring of 2018 have been the definitive highlight. I am deeply grateful to Mari-Ann Einarsrud who trusted in me and gave me the opportunity and responsibility to lecture this course. I also had the opportunity to co-supervise Lene Jensberg Hansen during her specialization project in the fall of 2018. I learned a lot from our collaboration on the gas monitoring project, thank you for that. Thanks to the people in K1 for all our good (and long) lunches, our various discussions about anything and everything, and the opportunities to take a brake from the scientific work from time to time. Thanks to the FACET group, the department, and all the people who contribute to the excellent social and working environment we have at IMA. I have really appreciated our department parties, Thursday lunches, IS-CREAM seminars etc. The CaRMa project has involved a lot of people at NTNU, SINTEF and in the industry, who have contributed to various aspects of my PhD work. First of all I want to thank Raymond, Samuel and Gøril for doing their PhD work together with me on the CaRMa project. Being a small group of PhD students working on similar projects and facing similar challenges has been very motivating. I have always had someone close to ask whenever I was having questions, thank you for that! I want to thank the people in SINTEF and in the industry who have been available for questions and discussions whenever I have needed it. As a new PhD student starting to work with the aluminium industry, having someone to discuss various challenges with, has been invaluable. Thor Anders Aarhaug and Heiko Gaertner in SINTEF deserve a special thank you for the effort you put into the gas monitoring project in Mosjøen. We would not have come this far with this project without your help. I have been at various industry locations during this work, taking samples or carrying out measurements. I am very grateful for all the support and help I have gotten from the people working at the anode plants at Alcoa Mosjøen and Hydro Årdalstangen. Thank you for all welcoming me to the plants and for helping out during my visits by sharing your knowledge and experience related to anode baking.

To all my friends in Trondheim, both in and outside of NTNU, these last nine years would not have been the same without you! I would like to thank my family for the support and encouragement over the years and for the help and feedback during the writing of this thesis. I am especially grateful to my grandma, Dagrun, for always showing interest in my work and being proud of my accomplishments. Last, to Maria, for being here by my side.

Abstract

Carbon anodes constitutes an important part of the production of primary aluminium. Petroleum coke, coal tar pitch and recycled anodes are mixed and formed into green anodes before heat treatment in the anode baking furnace. The desired anode properties are obtained during baking, and proper operation of the baking furnace is important for the quality of the metal product and the efficiency of the reduction process. The major part of the anode baking furnace consists of aluminosilicate refractories which are exposed to harsh operational conditions, both chemically and thermally, during baking. The degradation and wear of the refractory lining are of great importance to the furnace operation, due to maintenance of flue walls becoming necessary after years in operation. The aim of this PhD work was to increase the understanding of the degradation processes in the refractory lining, focusing on autopsies of spent refractory lining and the chemical environment surrounding the flue wall. Based on the experimental investigations, the aim was to describe the dominating factors of the refractory degradation.

Spent refractory linings from two anode baking furnaces, with open and closed furnace design, were investigated in this work. The samples were collected during maintenance of flue walls, and characterized by X-ray diffraction, scanning electron microscopy and measurements of density and open porosity. Changes in density and open porosity, microstructure and phase composition were described and linked to operational conditions and wear mechanisms. Significant variations in density and open porosity were observed, especially in the open furnace, depending on both sampling height and the distance from the anode. The highest density was measured closest to the anode side and in the bottom of the furnace. Reaction layers depleted of silica were found in the middle and bottom sections of the open furnace, while regions with deposited silica were observed in the top section. These observations demonstrate a transport of silica from the bottom and middle section of the furnace, towards the top

section. Similar qualitative observations were found at all sampling heights in the close furnace. These differences are discussed in relation to the furnace designs. High operational temperature in combination with reducing atmosphere were suggested to be important for the volatility of silica and hence the transport inside the furnace. In the closed furnace, particles with a high content of impurity elements (e.g. Fe, Ni, Zn, Mg) were also observed.

To better understand the processes going on in the anode pit during baking, an experimental setup to monitor pit gas atmosphere was constructed. Pit gas was extracted from the pit during baking and analyzed with an FTIR instrument and a gas chromatograph. The thermal decomposition of pitch occurring during heating was found to produce large quantities of CH_4 and H_2. At maximum temperature, CO is the dominating carbon specie, while it shifts towards CO_2 during cooling, in good accordance with the thermodynamic equilibrium calculations. Water was tapped from the the condensation vessel during the first 24 h of the baking cycle, demonstrating a significant water content in the green anodes. Thermodynamic calculations show that the presence of water in combination with recycled anodes give rise to the formation of HF, which in turn could react with the lining forming SiF_4 in the end. Significant concentrations of HF was measured at the maximum temperature, demonstrating an alternative mechanism for the observed depletion and deposition of silica in the refractory lining.

A finite element method (FEM) model was used to investigate creep as a potential densification mechanism for the refractory lining. A 2D model of a refractory brick separating the anode side from the flue side was designed in COMSOL Multiphysics and used to model the behavior of the lining during anode baking. Gravity was proposed to be the driving force for the densification taking place during the baking cycle and particularly at high temperatures. The gradient in the stress level was considered by estimating the stress level at the three sampling heights used in the autopsies. Data for creep in similar materials was used in the model. The modeling demonstrated that the calculated variation in stress level at the sampling positions are large enough to yield a variation in open porosity as observed in the spent lining. Creep by viscous flow is therefore proposed to be a probable mechanism for densification in the the refractory lining.

Both the chemical and physical nature of the refractory lining were observed to change after years in operation in the baking furnace. The contribution to the overall degradation leading to the need for relining of the furnace, is however not equal for all degradation phenomena. The transport of silica and the deposition of particles with high content of impurity elements are affecting a sub-millimeter region of the lining, while the density and open porosity are varying across the full width of the refractory lining. The latter is thus causing a much greater thermomechanical instability in the flue wall, resulting in a significant contribution to the overall degradation of the flue wall.

Sammendrag

Karbonanoder utgjør en stor og viktig del av veridkjeden til produksjon av primæraluminium. Petroleumskoks og resirkulerte anoder knuses og blandes med kulltjærebek før anodemassen formes til ønsket anodeform. Anodene varmebehandles så i anodebrennovner. Optimale anodeegenskaper oppnås gjennom varmebehandlingen, og driften av slike brennovner er derfor viktige for å sørge for at anodene har den kvaliteten som trengs videre i produksjonsprosessen av aluminium. Hovedandelen av materialer i en anodebrennovn består av ildfaste foringer som utsettes for krevende forhold under drift. Nedbrytning av disse ildfaste foringene fører til at materialene periodevis må skiftes ut, noe som både er tidkrevende og kostbart. Hovedmålet med dette doktorgradsprosjektet har derfor vært å øke kunnskapen om prosessene som fører til nedbrytning av materialene i brennovnen, ved å fokusere på undersøkelser av autopsiprøver og det kjemiske miljøet rundt foringene. Basert på slike eksperimentelle undersøkelser har målet vært å beskrive de dominerende faktorene som påvirker nedbrytningen.

Prøver av ildfaste foringer fra to anodebrennover med åpen og lukket design ble undersøkt i dette arbeidet. Prøvene har blitt samlet inn i forbindelse med vedlikeholdsarbeid i ovnene, og ble karakterisert ved hjelp av røntgendiffraksjon, elektronmikroskopi, og målinger av tettet og åpen porøsitet. Endringer i tettet og åpen porøsitet, mikrostruktur og fasesammensetning ble beskrevet og sett i sammenheng med operasjonelle forhold i ovnene samt nedbrytningsmekanismer. Store variasjoner i tetthet og åpen porøsitet ble observert, hvor variasjonene var avhenging både av plasseringen til prøven i ovnen samt avstanden fra anodesiden. Den største økningen i tetthet ble observert nær anodesiden for prøvene som ble samlet inn fra bunnen av ovnen. Reaksjonlag utarmet av silisiumoksid ble funnet i den midtre og nedre seksjonen i den åpne ovnen, mens området med deponert silisiumoksid ble funnet i den øvre seksjonen. Disse observasjonene viser at det har vært en transport av silisiumoksid fra nedre del av

ovnen oppover mot øvre del. Tilsvarende, kvalitative observasjoner ble funnet i den lukkede ovnen, men i alle seksjoner. Disse variasjonene mellom ovnene ble diskutert i relasjon til ovnenes design. Høy temperatur og reduserende atmosfære ble vurdert til å være viktig for flyktigheten og dermed transporten av silisiumoksid. I den lukkede ovnen ble det også observert partikler med høy innhold av andre elementer enn hva som er i foringene i utgangspunktet (for eksempel Fe, Ni, Zn, Mg).

Et oppsett for måling og analysering av gassen i anodekammeret ble designet og bygget for å bedre forstå de ulike prosessene som foregår i anodebrennovnen under drift. Gass ble sugd ut av ovnen under drift og analysert med et FTIR instrument og en gaskromatograf. Store mengder CH_4 og H_2 ble målt under oppvarming og kommer fra den termiske dekomponeringen av kulltjærebek. Ved maksimum temperatur ble CO målt til å være den dominerende karbonforbindelsen. Dette skifter til CO_2 når temperaturen går ned, noe som stemmer bra med termodynamiske likevektsberegninger. I løpet av de første 24 timene ble betydelige mengder vann tappet fra kondensasjonsenheten, noe som viser at vann kommer inn i brennovnen sammen med anodene før varmebehandling. En termodynamisk analyse viser at tilstedeværelsen av vann i kombinasjon med resirkulerte anode gir opphav til dannelse av HF som i neste omgang kan reagere med foringen og danne SiF_4. Betydelige mengder HF ble målt rundt 1000 °C og dermed bekrefter at vann har reagert med rester av elektrolytten fra de resirkulerte anodene. Denne observasjonen gir opphav til en alternativ mekanism som forklarer transporten av silisiumoksid i anodebrennovnen.

En FEM (Finite Element Method) modell ble brukt for å undersøke signing som en mulig fortettningsmekanisme. En 2D modell av en ildfast foring ble laget i COMSOL Multiphysics og brukt til å modellere oppførselen til materialet under varmebehandling. Den drivende kraften for fortetning ble foreslått å være vekten av veggen selv i kombinasjon med høy temperatur og lang driftstid. Den faktiske vekten som hver prøve har blitt utsatt for under drift ble beregnet ut fra hvor prøvene ble hentet i veggen. Denne vekten ble brukt i modelleringen sammen med øvrige parametere som ble funnet i literaturen. Modelleringen demonstrerte at en gradvis økning i vekt gir en gradvis økning i fortetning av materialet. Siging ble derfor foreslått som en sannsynelig mekansime for fortetningen som er observert i disse materialene.

Den ildfaste foringen ble observert å endre seg både fysisk og kjemisk i løpet av tiden i drift i anodebrennovnen. Bidraget til den overordnende nedbrytningen er likevel ikke like stor fra alle de observerte endringene. Transporten av silisiumoksid og deponering av partikler med høyt metallinnhold påvirker områder av foringen på et mikrometer-nivå. Endringene i tetthet og åpen porøsitet ble observert over hele bredden av foringen, og forårsaker derfor en mye større reduksjon i termomekanisk stabilitet.

Contents

Chapter 1

Introduction

1.1 Background and motivation

The production of primary aluminium has grown steadily over the last decades, and was in 2018 exceeding 64 million metric tonnes worldwide [1]. Aluminium is the second most used metal in the world and the contribution to the global economy is becoming significant as aluminium is increasingly being used for various applications. The main features of aluminium metal is its high corrosion resistance due to a thin oxide layer, high strength to weight ratio, good recyclability and malleability. Firstly, the high corrosion resistance is highly wanted as the world's steel constructions require a high degree of maintenance. A study from 2016 estimates the worldwide costs of corrosion to 3.4 % of the global GDP [2], demonstrating the need for alternative materials to steel. Secondly, aluminium has in general a higher strength to weight ratio, compared to steel. Replacing steel with aluminium would thus reduce the weight of an object without reducing its overall strength. Aluminium is however more expensive than steel, which has a large impact on whether steel or aluminium is the preferred metal in specific applications. Traditionally, aluminium has been widely used in the aerospace industry, where low weight is crucial and material cost a second priority. A modern aircraft today consists of approximately 80 % aluminium [3]. Recent EU regulations aimed to reduce the CO_2 emissions from the transport sector, have motivated the automotive industry to find ways to reduce energy consumption [4]. Partial replacement of steel with aluminium has thus been an effective way to reduce the overall weight, without compromising performance and safety of the vehicle [3, 5, 6].

The primary aluminium production is very energy intensive, globally consuming more than 867 TWh per year [1], approximately 6.5 times the annual energy consumption of Norway [7]. The electric power related to producing one kilogram of aluminium has been on a steady decline the last century, having a great impact on the carbon foot print of aluminium production. The awareness of carbon footprint is increasing and a reduction in the overall energy consumption in aluminium production is important.

The main principle of aluminium electrolysis used in the current technology was developed simultaneously and independently by Charles Martin Hall and Paul Héroult in 1886 [8]. The Hall-Héroult process, named after the two inventors, is based on electrochemical reduction of alumina (Al_2O_3). Figure 1.1 shows the schematics of a modern electrolysis cell [8]. Alumina is dissolved in a molten salt electrolyte consisting of mainly cryolite (Na_3AlF_6) heated to 960 °C. During electrolysis, alumina is reduced to liquid aluminium, while the carbon oxidizes to CO_2, in accordance with Equation 1.1.

$$2\,Al_2O_3(diss) + 3\,C(s) = 4\,Al(liq) + 3\,CO_2(g) \tag{1.1}$$

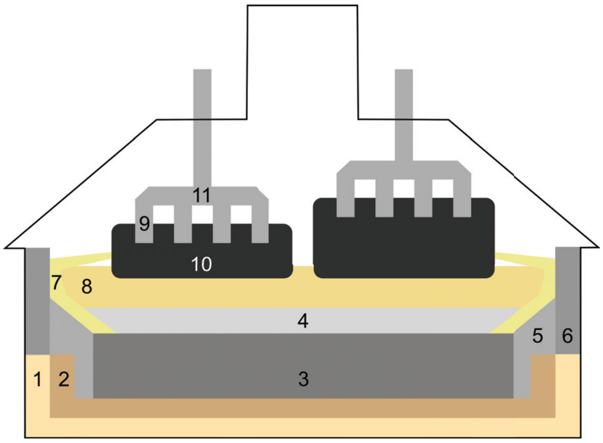

Figure 1.1: Sketch of aluminium electrolysis cell. The parts of the cell are named in accordance with the following numbering. 1) insulation lining, 2) refractory lining, 3) carbon cathode block, 4) aluminium pad, 5) ramming paste, 6) sidelining, 7) frozen sideledge, 8) molten cryolite, 9) anode stud, 10) carbon anode, 11) anode yoke/stem.

Carbon anodes constitute an important part of the electrochemical production of primary aluminium [9]. The industrial carbon anodes have two different designs; the Søderberg anode and the prebaked anode [10–12]. Modern prebaked anode technology has proven superior to the Søderberg technology, resulting in prebaked carbon anodes being the technology of choice in modern smelters [10–13]. The anode recipe is based on petroleum coke and coal tar pitch for both anode technologies. The main difference is the lower pitch content in the prebaked anodes, in addition to the use of anode butts from recycled anodes [12, 13]. In terms of production, the differences are more distinct, with the Søderberg anodes continuously being self-baked during the electrolysis, while the prebaked anodes are formed and heat treated in separate baking furnaces prior to the electrolysis process [10, 12, 13].

The anode baking process also adds to the energy consumption related to aluminium production [14]. Comparisons of the two anode technologies point to the lower current efficiency, higher cell voltage, higher energy consumption and higher emissions of the Søderberg technology [15, 16]. The Søderberg anode technology has therefore been gradually phased out by choosing prebaked anodes when building new smelters [15, 16]. Some older smelters with Søderberg technology have also been retrofitted with prebake technology [17]. In the prebaked anode cell design, the number of anodes per cell may vary from 16 to 40 [10]. The anodes are consumed during electrolysis, and are usually replaced when they are 25 % of their original size. Normal lifetime for a prebaked anode is 22 to 30 days, resulting in one to two anodes per cell being replaced every day on average [10, 11].

During anode baking, the refractory lining in the anode baking furnaces suffers from thermal cycling and a harsh chemical environment in the pit. This results in deformation and cracking of the flue walls and the surrounding lining. The need for refractory maintenance is substantial over time, leading to a considerable consumption of materials and manpower due to replacement of flue walls. The wear of refractories is thus constituting a challenge for the operation of anode baking furnaces, and detailed insight in degradation mechanisms and the driving forces for the wear is of great interest. The main focus in this thesis was to investigate and understand the mechanism of degradation of refractory lining.

This PhD work has been a part of the CaRMa project (Reactivity of Carbon and Refractory Materials used in Metals Production Technology). The overall goal in the CaRMa project was to obtain new knowledge for enhancing material performance in the aluminium electrolysis industry, focusing on carbon, insulating and refractory materials. A general increase in the lifetime of electrolysis cells and flue walls in anode baking furnaces, and a corresponding reduction in consumption and waste generation per produced unit were defined as the main goals. Increasing the lifetime of the refractory lining in the anode baking furnace is one way to contribute to the achievement of the project goals. The current PhD work was aiming to enhance the understanding of the degradation of refractory lining, and in turn contribute to an extended lifetime of the lining in anode baking furnaces.

1.2 Aim of the work

Studies of refractory degradation within the aluminium industry has to a large extend been focusing on the cathode lining in the electrolysis cell. The degradation processes of refractory flue walls in the anode baking furnace have, on the other hand, not been subject to an equally extensive focus. In order to enhance the understanding of the refractory deterioration in the baking furnaces, investigations on industrial samples are needed. The overall aim of this PhD work was therefore to investigate degradation of refractory lining in anode baking furnaces, focusing on observed wear patterns from refractory walls in anode baking furnaces. Based on the investigations of samples from autopsies, the aim was to describe the major factors influencing the degradation. The PhD work was divided into three parts, each with a different approach to the degradation process.

The first part was focusing on industrial autopsies and investigations of samples from refractory flue walls after long time in operation. This work is presented and discussed in Chapter 4. The industrial autopsy has proved to be a valuable tool for investigating cathodes after cell shut-down, and a similar approach was therefore used on the spent lining in the anode baking furnace [18]. Thermodynamic assessments of lining material in contact with corrosive species were constituting the theoretical basis on which the industrial investigations were discussed. Based on the autopsies, it became clear that the pit gas atmosphere was influencing the stability of the lining.

The aim for the second part was thus to investigate the pit gas composition during anode baking, and relate the findings to the observed degradation patterns from the autopsies. *In situ* monitoring of pit gas composition was however not reported prior to this project, and the experimental methodology was partly established during this work. Fourier Transformed Infrared (FTIR) spectroscopy has earlier proved useful when determining off-gas from an electrolysis cell, and was therefore used to monitor the pit gas from the anode baking furnace [19–21]. Chapter 5 presents the results and discussions of the second part.

Last, a finite element method (FEM) model of the refractory lining in the flue wall was constructed based on the results from the autopsy samples, as presented in Chapter 6. Implementation of experimental data in a FEM model proved useful in describing some of the factors causing the observed behavior of the flue walls. The flue wall behavior during baking was modeled and discussed in relation to the observed degradation phenomenon.

Chapter 2

Literature review

2.1 Production of carbon anodes

2.1.1 The carbon anode

The production of prebaked carbon anodes is carried out in anode baking furnaces separated from the pot rooms and electrolysis cells, and can thus be regarded as an independent part of the primary aluminium value chain. The typical anode recipe consists of petroleum coke (60 wt% to 70 wt%), anode butts (15 wt% to 30 wt%) and coal tar pitch (14 wt% to 17 wt%) [22, 23]. The petroleum coke and anode butts are comprising the anode matrix, while the coal tar pitch works as a binder, holding the anode together. The chemical composition of a carbon anode is usually > 97 wt% carbon, with the main impurity element being sulfur in addition to a range of other minor impurities [24]. The petroleum coke, the coal tar pitch and the anode butts contribute to various impurities in the baked anodes [24]. The petroleum coke is a by-product from oil refining, and the feedstock quality is therefore an important parameter in the production of carbon anodes, especially with respect to the content of aromatics, asphaltenes, sulfur and other metal constituents [22, 25]. The typical range of impurities in petroleum coke is presented in Table 2.1. From the perspective of an oil refinery, the value of the petroleum coke is constituting only 2 % of the total value of products refined from the crude oil [24]. Hence, there are very few incentives for the refineries to maintain the production of high quality petroleum coke. However, as long as the quality of the crude oil is high, the quality of the petroleum coke will be correspondingly high [24]. In recent years, the refineries have been processing more heavy, sour crude oils, and thereby increasing the level of impurities in the petroleum coke [12, 26, 27]. The coal tar pitch serving as the binder is a by-product from the production of metallurgical coke [24]. Coal tar pitch is evaporated from the coal during calcination, and is thus consisting of a wide range of polycyclic aromatic hydrocarbons (PAHs) and heterocyclic hydrocarbons (organic molecules containing rings and inorganic elements as nitrogen, sulfur or oxygen) [24]. It is therefore difficult to exactly determine the chemical composition of the coal tar pitch [24]. The elemental composition is however measured and typical values of impurity content are presented in Table 2.1. In addition to the petroleum coke and the coal tar pitch, the anode butts are also a source of impurities in the green anodes. During electrolysis, the anodes are exposed to the cryolite bath, and may transfer contaminations from the bath to the green anode if not properly cleaned after being removed from the cell. The typical levels of impurities in the anode butts are presented in Table 2.1. Here, it is mostly sodium and fluorine from the bath, and iron from the anode studs. When examining the average level of impurities in the baked anode in Table 2.2, it is apparent that the petroleum coke is governing the overall impurity levels, in addition to contributions to sodium, fluorine and iron from the anode butts.

Table 2.1: Typical range of important impurities in anode raw materials [24].

Element	Unit	Petroleum coke	Coal tar pitch	Anode butts
Sulfur	[wt%]	0.5 - 3.5	0.4 - 0.6	
Sodium	[ppm]	30 - 120	50 - 250	500
Chlorine	[ppm]		50 - 150	
Vanadium	[ppm]	30 - 350		
Nickel	[ppm]	50 - 220		
Silicon	[ppm]	50 - 250		
Iron	[ppm]	50 - 400	50 - 200	700
Aluminium	[ppm]	50 - 250		200
Zink	[ppm]		100 - 500	
Lead	[ppm]		100 - 300	
Calcium	[ppm]	20 - 100	20 - 100	
Fluorine	[ppm]			700
Magnesium	[ppm]	10 - 30		

Table 2.2: Typical range of important impurities in baked carbon anodes [24].

Element	Unit	Worldwide ranges	Targets for good anodes
Sulfur	[wt%]	0.5 - 3.0	≤ 2.2
Sodium	[ppm]	100 - 1000	≤ 200
Vanadium	[ppm]	20 - 350	≤ 220
Nickel	[ppm]	40 - 250	≤ 130
Silicon	[ppm]	50 - 300	≤ 150
Iron	[ppm]	100 - 800	≤ 350
Calcium	[ppm]	50 - 500	≤ 300
Fluorine	[ppm]	150 - 1500	≤ 300
Magnesium	[ppm]	5 - 50	
Phorphorus	[ppm]	1 - 30	≤ 4

During the production of green carbon anodes, the petroleum coke, coal tar pitch and recycled anode butts are crushed and mixed to form an anode paste [24, 28, 29]. To obtain optimum properties of the anode paste and later the baked anode, the dry aggregates (crushed petroleum coke and butts) must be properly wetted by the pitch [24]. The ratio of dry aggregates to pitch is therefore important for the anode properties [24]. The typical softening point of an anode grade pitch is 110 °C to 120 °C and the mixing and forming processes are often carried out at temperatures 50 °C above the pitch' softening point [24, 28–39]. When the raw materials are mixed and homogenized, the anode paste is fed to a mold and formed by a hydraulic press or a vibrocompactor [24, 39]. After forming, the pitch is still warm enough for the green anodes to deform if measures are not taken, and the anodes are therefore cooled prior to storage in order to maintain their dimensions and shape [39, 40]. Depending on the mixing temperature, the anodes are cooled either by air, water spraying or submersion into a water basin [40, 41]. The heat treatment is the final and most expensive step in the production process, and is carried out in anode baking furnaces at elevated temperatures for extended periods of time. The carbon anodes used in aluminium electrolysis are subjected to several requirements for optimal operation in the electrolysis process. Key properties are high chemical purity, high electrical conductivity, high mechanical strength and high homo-

Table 2.3: Impurities found in the petroleum coke and how they affect the performance of the baked anode and the electrolysis process [24].

Element	Area of impact				
	Metal purity	Anode consumption	Current efficiency	Pollution	Electrolyte properties
Sulfur		•		•	
Sodium		•			•
Vanadium	•	•	•		
Nickel	•	•			
Silicon	•				
Iron	•				
Calcium		•			•
Magnesium		•			•
Phosphorus			•		

geneity combined with low reactivity towards CO_2 and O_2 [13, 22]. The effect of potential impurities on these properties is shown in Table 2.3. In order to obtain the wanted baked anode quality, it is important to have control on the quality and composition of the anode precursors, in addition to the baking process [13, 22].

2.1.2 The anode baking process

The anode baking furnace technology is mostly based on two configurations, the open and closed top furnace. The overall working principle is the same for both configurations, but with some variations in operational design. After the green anodes are formed and cooled, the green anodes are stacked within the baking furnace pits and heat treated to obtain the wanted structural and electrochemical properties needed for the electrolysis process. The temperature during the baking process usually ranges from ambient up to ~1200 °C over the course of a baking cycle lasting 14-17 days. During heating, the structural integrity is reduced as the temperature reaches the softening point of the pitch [42], and to prevent anodes deformation during the first part of the baking process, the anodes are placed in a confined space (the pit), with limited room for movement. In order to avoid oxidation of carbon during baking, packing coke is used to fill the space between the anodes and the flue walls and to cover the top of the anodes. The packing coke usually consists of the same petroleum coke as used in the anode production [42]. Due to its sacrificial role towards the anodes, the packing coke is to some extend consumed during the baking process, usually 6 to 10 kg per ton baked anode [42]. During the heat treatment of the anodes various processes occurs at various temperature intervals. From 200 °C to 600 °C, the temperature has exceeded the softening point of the binder, and the anodes becomes structural unstable [42]. In the same temperature region, from 250 °C to 550 °C, the pitch begins to crack resulting in a release of volatile hydrocarbons and H_2 in the furnace [42]. As the temperature increases further, the pitch is calcined in the temperature range of 600 °C to 900 °C, and the final transition from green to baked anode occurs at 1050 °C to 1150 °C [42]. The dwelling time in each of the temperature intervals determines the quality of the final baked anode. It is therefore important to have control of the heat balance in the furnace, in order to keep the temperature gradients in the anodes as intended throughout the baking [42].

2.2 The anode baking furnace

2.2.1 General baking principle

The industrial anode baking furnace is in general designed in two ways, with the open top and closed top furnace design, where both designs are similar with respect to the overall baking principle. Both furnaces are designed with sections connected in series, where each section is divided into several pits. Typical pit dimensions are 5 m x 5 m x 1 m, making room for three layers of anodes with five to seven anodes in each layer [43, 44]. The series of sections are built in two rows where the end of the first row is connected to the start of the second row by a crossover. In this way, the sections are forming a ring where the baking equipment is moving around during production. The temperature in the furnace is controlled by the injection of burning fuel which is heating the flue gas. The pits are separated from each other by hollow refractory flue walls, controlling where the hot flue gas is flowing. Heaters, typically fueled by natural gas, liquid propane gas or oil, are used to adjust the flue gas temperature during the baking cycle. An important part of the baking furnace operation are the fire trains. A fire train typically covers eight or more sections, where the three in front are assigned to pre-heating, the three in the middle to baking at maximum temperature, and the rest to cooling. The heaters are mounted at the three sections assigned to baking at maximum temperature. During operation, the fire train moves one section every 22-28 hours, causing a given section to be pre-heated for three periods, baked at maximum temperature for three periods before cooling occurs. In an anode baking furnace, there are usually two or three fire trains in operation simultaneously. Between each fire train, there are several sections not covered by the operational equipment. In these unoccupied sections, baked anodes are unloaded, green anodes are loaded into the pits and lining maintenance carried out if necessary. The main difference between the open and closed top furnace design is the use of section covers in the closed design. The section covers are affecting the flow pattern of the flue gas in the furnaces, and hence the operational environment in the furnace during baking.

2.2.2 The open top furnace design

In the open top baking furnace design, there are no section covers [45]. This means that the anodes and the pits are not physically sealed off from the surrounding environment during anode baking. An image of an open top baking furnace is shown in Figure 2.1.

Here, two rows of sections are shown with fire trains containing burners, an exhaust manifold in front of the burners and cooling ramps behind. The exhaust manifold creates a reduced pressure in front of the burners, causing the hot flue gas to flow forward and thus pre-heat the upcoming sections [42, 45]. The reduced pressure, and hence the draft from the exhaust manifold, is controlled by the temperature measurement ramp. If the temperature is below the predefined temperature profile, the draft is increased and the forward flow of hot flue gas from the baking zone is increased. If the temperature is too high, the flow is reduced. Behind the cooling ramps, there is room for loading and unloading of anodes.

Since there are no section covers, the importance of the packing coke covering

Figure 2.1: The open top anode baking furnace. Reprinted with permission from Riedhammer [46].

the anodes is crucial. To avoid potential air burn of the anodes during baking, the packing coke is covering the anodes at all times, where some of the packing coke is consumed during baking. In addition, cracks in the lining, may cause the packing coke to pour out into the fire channel of the flue wall. In case, it is necessary to refill some of the pits with packing coke during the baking process. The flue walls in the open top baking furnace is built of two uni-layered walls of refractory materials in parallel with the flow direction. Between the two walls, there are some additional bricks forming channels for the flue gas in addition to stiffen the flue wall itself. The flow pattern is illustrated in Figure 2.2a.

The flue walls in one section are connected to the flue walls in the next section, constituting independent channels for the flue gas. The flue gas is therefore never in direct contact with the anodes or the surrounding atmosphere. Hence, in the open top baking furnace, the flue walls are closed and the flue gas separated from the rest of the furnace. The exhaust manifold creates the reduced pressure inside the flue walls, causing a pressure difference between the anode side and the flue side of the flue wall. On the anode side, the decomposition of pitch during heating results in the formation of volatile hydrocarbons. Due

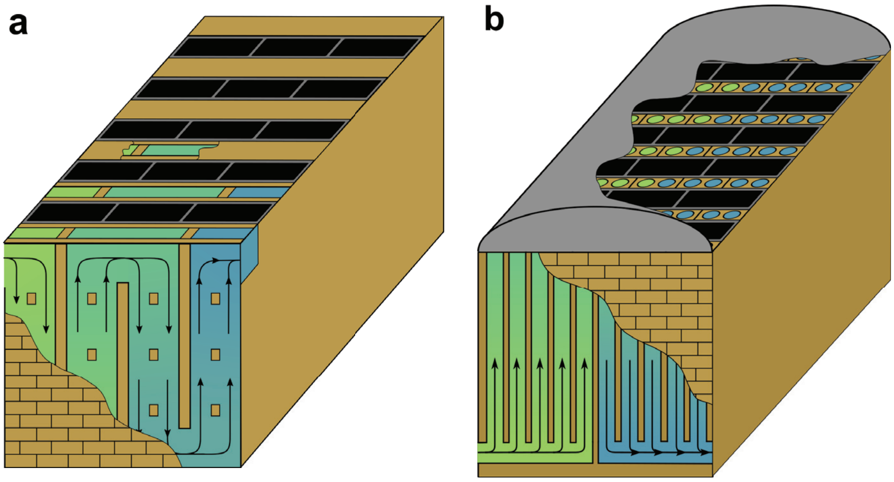

Figure 2.2: Sketch of an a) open and b) closed anode baking furnace section. The flow pattern of the flue gas is indicated by the arrows. Reprinted from Brandvik *et al.* [47] with permission from Springer.

to the pressure gradient across the flue wall, the hydrocarbons are transported into the flue channels where they are combusted. The decomposition products from the pitch is therefore contributing to the overall energy input to the baking process.

2.2.3 The closed top furnace design

An image of a closed top baking furnace is shown in Figure 2.3. Here, the distinction between the open top and closed top furnace is more pronounced. All sections under pre-heating, baking or active cooling are covered by section covers, allowing for a different flow pattern of the flue gas compared to the open furnace [45]. As for the open top furnace, there is a reduced pressure in front causing a flow of flue gas from the baking section towards the pre-heating sections. In the closed top baking furnace, the flue walls are not sealed of from the anode surroundings. The flue channels are releasing the flue gas under the section cover, before the reduced pressure in the next section transports the flue gas forward. There are various ways of constructing the flue channels, where one configuration is presented in Figure 2.2b. The flue gas flows upwards in the

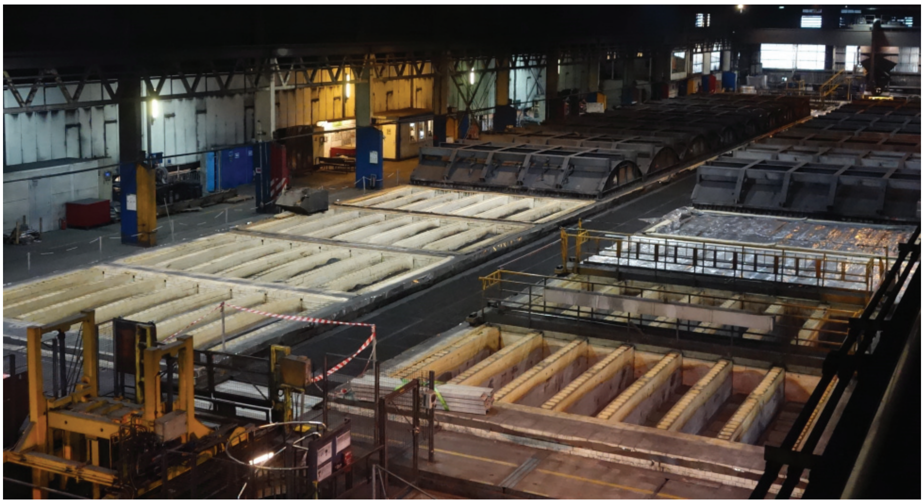

Figure 2.3: The closed top anode baking furnace at Hydro Årdalstangen. Printed with permission from Norsk Hydro.

first part of the wall (green in the figure), and is released underneath the section cover, before being transported downwards (blue in the figure) by the reduced pressure in the next section. In the closed furnace, the decomposition products from the pitch also contributes to the overall energy input to the baking process, but not to the same extent as in the open furnace.

2.3 Refractory lining materials

2.3.1 Main material qualities

A wide range of refractory materials is used in various high temperature applications, where oxides, nitrides and carbides with high melting temperatures constitute the basis of these materials. Al_2O_3, SiO_2, MgO, CaO, ZrO_2, Cr_2O_3 are the base oxides which a large range of commercial materials are based on, with additions of SiC, B_4C, Si_3N_4 and BN used in special applications [48, 49]. An important class of refractory materials used in furnaces and other high temperature applications are the chamotte materials, also known as fireclays. Fireclays and other aluminosilicate materials are relatively cheap compared to more special refractories, and are therefore widely used [50]. The chamotte classification originates from the composition of clay found in the soil, which is an important source of raw material for refractories. The aluminosilicate fireclays consist of a variety of minerals where kaolinite ($Al_2O_3 \cdot 2\,SiO_2 \cdot 2\,H_2O$) and montmorillonite ($Al_2O_3 \cdot 4\,SiO_2 \cdot 2\,H_2O$) are two common examples. Pure samples of kaolinite will after calcination consist of 45 wt% alumina and 55 wt% silica, constituting the upper limit for alumina content of the chamotte materials. Pure, calcined samples of montmorillonite will similarly consist of 30 wt% alumina and 70 wt% silica. The refractoriness tend to increase with increasing alumina content, and hence define one of the most important properties of a refractory material. Fireclay products are therefore classified according to their alumina content, where «fireclay products» have 30 wt% to 45 wt% alumina, and «low alumina fireclay products» have 10 wt% to 30 wt% alumina and $<$ 85 wt% silica. The clays found in nature are however rarely pure aluminosilicates, and impurities are often observed in the raw materials. The result is often fireclay products containing some degree of impurities, such as K, Na, Ca or Mg [48]. In applications where higher refractoriness is necessary, materials with increased alumina content are used. High-alumina refractory materials have an alumina content larger than 45 wt%, and are based on other raw materials than the fireclay brick. In order to increase the alumina content, raw materials as bauxite, sillimanite ($Al_2O_3 \cdot SiO_2$), andalusite ($Al_2O_3 \cdot SiO_2$), mullite ($3Al_2O_3 \cdot 2\,SiO_2$) or pure alumina are used in the production. Sillimanite and andalusite have the same chemical composition, but different crystal structures. Upon calcination at 1550 °C, both minerals decomposes to mullite and silica, with a theoretical expansion of 7-8 % and 3-5 %, respectively [48]. The low expansion during decomposition makes uncalcined andalusite an important raw material for high-alumina refractories [48]. The binary phase diagram of silica and alumina is shown in Figure 2.4. Here, the two-phase regions of silica and mullite, and corundum and mullite are shown, in addition to the compositional regions of various raw materials. In the aluminium industry, refractories with alumina content varying from 15 wt% to $\sim$60 wt% have been used [9, 50–55]. The need for high refractoriness is usually more pronounced in the anode baking furnace, compared to the electrolysis cell, leading to different compositions usually used in the two applications.

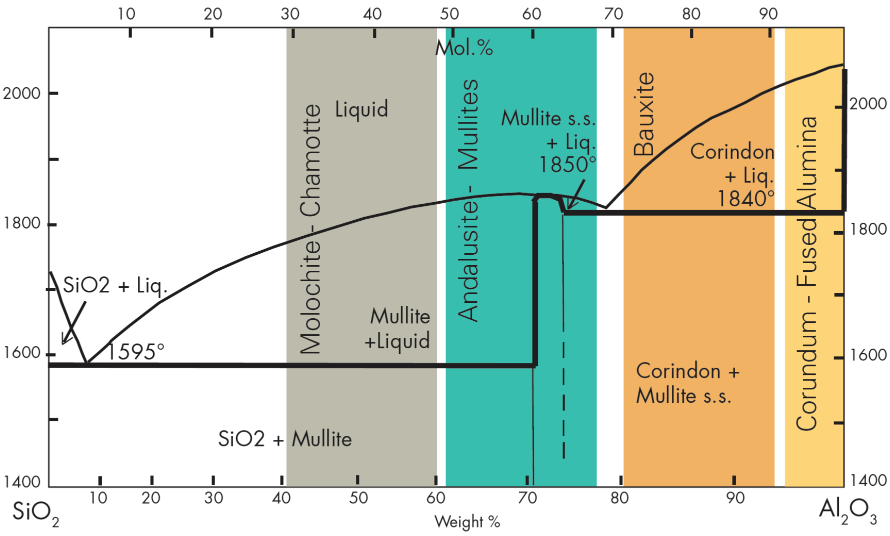

Figure 2.4: Binary phase diagram of the alumina and silica system. The diagram shows the compositional regions for various raw materials. Reprinted from Frulli with permission from Göller Verlag GmbH [56].

The production process of the chamotte materials is fairly similar regardless of the final composition. Raw materials (i.e. clays, sillimanite, andalusite, bauxite, silica, alumina etc.) are mixed in wanted ratios, formed into bricks (or some other shape) and heat treated at 1300 °C to 1500 °C [48, 50]. During the heat treatment process, the desired mineralogical composition of the final materials is obtained. For aluminosilicate materials with an alumina content below $\sim$70 wt%, the equilibrium phases at temperatures below 1600 °C are mullite ($3\,Al_2O_3 \cdot 2\,SiO_2$) and cristobalite ($SiO_2$) or tridymite ($SiO_2$), as shown in Figure 2.4. Alumina present from the precursors will react and from mullite during calcination.

2.3.2 Structure, mineralogy and properties

Refractory materials are widely used in high temperature applications, mainly because of the ability to withstand high temperatures without deforming, the high chemical stability in operational conditions and high compressional strength.

In the aluminium industry, the operational temperature in the electrolysis cell is 960 °C, and the hottest regions in the anode baking furnace may reach 1300 °C. Refractory materials are therefore an important part of the lining in the electrolysis cell, in addition to comprising almost all materials in the anode baking furnace. Some common aluminosilicate refractory materials and their properties are presented in Tables 2.4 and 2.5.

Table 2.4: The chemical composition (in weight percent) of a selection of aluminosilicate refractory materials. Typical properties of these materials are presented in Table 2.5 [57].

Material	Chemical composition [wt%]				Material type
	Al_2O_3	SiO_2	Fe_2O_3	Na_2O	
1	20 - 30	64 - 75	1.6 - 3.0		Low alumina firebrick
2	40 - 45	50 - 55	1-2		Firebrick
3	50 - 55	43 - 47	< 2	< 1.7	Mullitized raw materials
4	72	26	< 1	< 0.6	Sintered mullite bricks
5	90 - 95	4 - 9	< 0.6	< 0.5	Sintered corrundum bricks

Independently of the chemical composition, the microstructure is one of the defining properties of a refractory material. In order to maintain the structural integrity at elevated temperatures, a certain distribution of grain sizes is necessary. A typical refractory material have a microstructure consisting of two major parts; a matrix of fines and pitch serving as a bonding phase, and a range of

Table 2.5: Typical properties of some aluminosilicate refractory materials (cold crushing strength (CCS) and refractoriness under load (RUL)). The chemical composition of these materials are presented in Table 2.4 [57].

Material	Density [$g\,cm^{-3}$]	Open por. [%]	CCS [MPa]	RUL [°C]	Therm. cond. [$W\,m^{-1}\,K^{-1}$]
1	2.05- 2.17	1 - 18	35 - 90	1260	1.4
2	2.20 - 2.30	15 - 18	40 - 70	1380-1450	1.4
3	2.3 - 2.4	13 - 19	60 - 100	> 1400	1.7 - 1.9
4	2.55	16	100	1650	
5	3.0 - 3.2	13 - 17	100 -180	> 1700	2.5 - 3.3

coarser particles that could be several millimeter in size [58–60]. In addition, a varying degree of porosity is present. The microstructure of a refractory material is shown in Figure 2.5. The largest particles are in contact with each other, while the voids between these particles are filled with the binder. The mineralogy of the two parts may be very different, due to the increased reactivity for smaller grains. During production, the refractories are fired and the fines and binder in the bonding phase sinter together if the temperature is sufficiently high. The coarser grains are less likely to react with the bonding phase, and are mostly undergoing chemical reactions inside the grains. As the final refractory brick is ready for implementation in a furnace, the mineralogy of the bonding phase and the coarser grains could be significantly different. When assessing a potential new refractory material for an industrial application, the average composition of the brick does not necessarily give the actual composition of the various parts of the material. The refractoriness is defined by the highest temperature the material can withstand before undergoing deformation at a certain load and time frame. If the coarser particles start to soften at 1850 °C, but

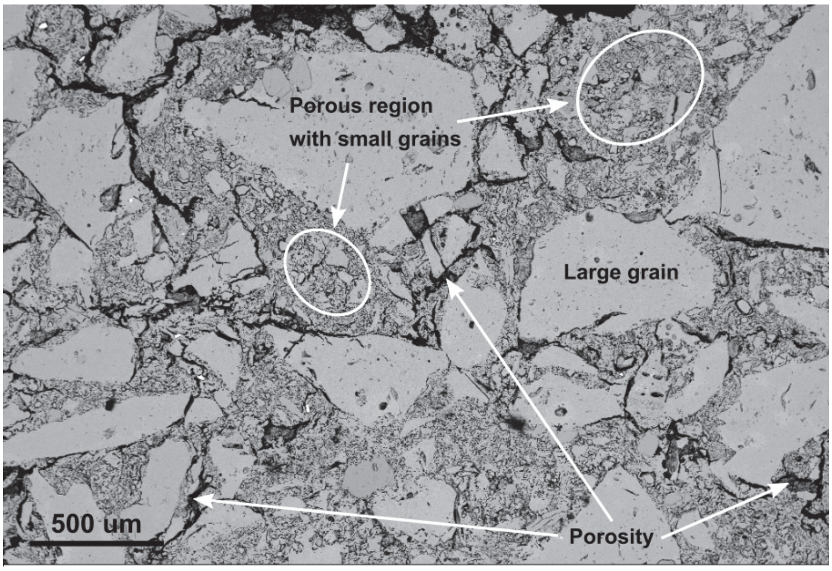

Figure 2.5: SEM image showing the microstructure of a refractory material. The typical large grains, regions with small grains and the porosity are indicated.

the bonding phase starts already at 1500 °C, the overall refractoriness will be governed by the bonding phase. When the bonding phase start to soften, the coarser grains will begin to slip and overall material will deform. It is therefore important to address the mineralogy of both the grains and the bonding phase when investigating a refractory material for a potential application.

In addition to coarse grains and a bonding phase, there is a varying degree of porosity in refractory materials. In the refractory materials used in the electrolysis cell and the anode baking furnaces, approximately 90 % of the porosity exists as open porosity [58]. Porosity in general have an important effect on the structural properties of ceramic materials, e.g. elastic modulus (Young's modulus), creep and strength. In addition, the gas permeability of a refractory is largely governed by the open porosity. The elastic modulus of a material is determined by the strength of the bonds between the atoms in the given material, and the stronger bonding between the atoms, the higher the elastic modulus [61]. When porosity is introduced into a material, the elastic modulus is always reduced [62, 63], resulting in a reduced threshold for material deformation during load. This relationship was summarized for alumina by Spriggs [62] and Knudsen [63] showing an approximately linear decrease in elastic modulus at room temperature for increasing porosity. This correlation is shown in Figure 2.6. The porosity is therefore an important parameter when addressing the strength of refractory materials.

Refractory materials are normally used in operational conditions of elevated temperatures, and creep is an important factor to consider when assessing the mechanical stability of such materials. Creep is defined as *a time-dependent permanent deformation of a solid material subjected to an elevated temperature at a stress level lower than the yield strength of the material* [71]. Normally, plastic deformation is taken into account when the temperature is approaching the softening point of a material. At lower temperatures, no significant deformation would be expected, as long as the material is not exposed to a load. In situations where a combination of temperature and load is applied to the material, and especially over an extended period of time, plastic deformation by creep becomes significant. Creep is normally divided into three stages, where the primary and tertiary stages describe the non-linear deformation occurring in the beginning

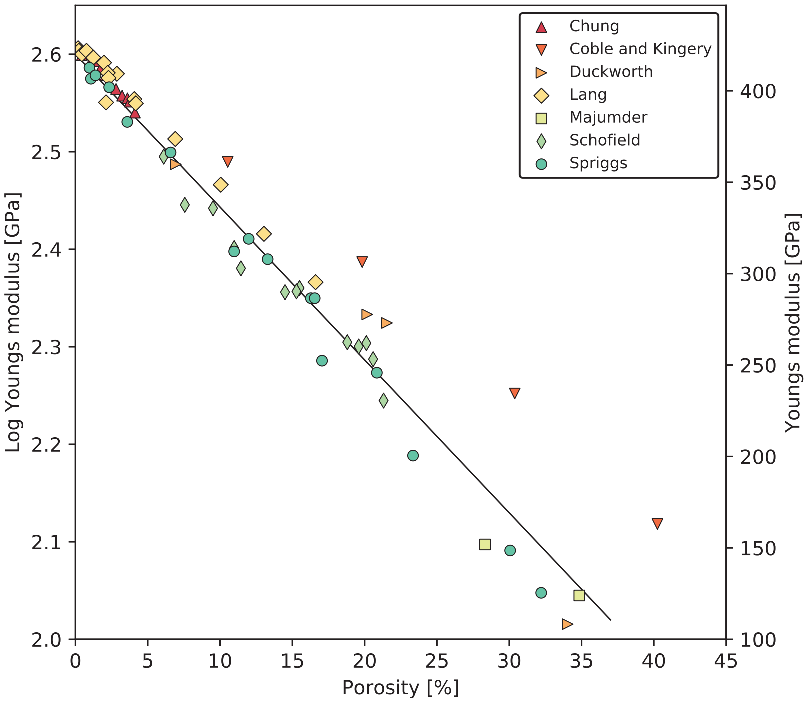

Figure 2.6: Young's modulus of alumina measured at room temperature for varying degree of porosity. The figure is redrawn from Knudsen [63]. The literature data is originating form various sources with a spread in synthesis and testing methods [64–70]. The line demonstrates the linear relationship between the Young's modulus and porosity.

of the deformation and towards the point of failure [72]. The secondary creep stage describe the constant rate of deformation (also known as the *steady-state creep*) and is useful when assessing the lifetime of materials. The steady-state creep can be expressed by the equation

$$\frac{\mathrm{d}\epsilon}{\mathrm{d}t} = \frac{C\sigma^n}{d^b} \exp\left(\frac{-Q}{RT}\right) \tag{2.1}$$

where the ϵ is the creep strain, σ the applied stress, Q the activation energy for creep, T the absolute temperature, d the grain size, and C, b and n are constants specific for the material in question. The rate-controlling creep mechanism can be identified by value of the n parameter, where dislocation mechanisms ($1 \leq n \leq 4.5$), grain boundary sliding ($2 \leq n \leq 3$) and diffusion creep and vacancy flow ($n = 1$) are known categories of mechanism with the ranges of stress exponent values indicated. For coarse grained polycrystalline ceramics, the deformation observed at high temperature and stress level is usually yielding an n value ≥ 3, making it relatively easy to identify the mechanism controlling the creep rate [73]. At moderate stress levels, the number of potential rate-controlling mechanism increases, and the determination of which mechanism is dominating becomes more difficult.

Studies on creep behavior of firebricks, mullite and alumina at various temperatures and loads have been carried out during the last part of the 20th century, and a summary of creep rates is presented in Figure 2.7 [74–83]. Here, series of creep rates measured at various temperatures are presented for increasing stress level. Details on the materials presented in Figures 2.7 and 2.8 are shown in Table 2.6. The variation in creep rates for the firebricks, even though with a fairly similar alumina content, is caused by the significant difference in impurity content. The impurities measured in these materials are mostly alkali elements, causing the formation of phases with lower thermal stability compared to a pure aluminoslicates, which in turn increases the creep rate of the material. The significant spread in creep rates is not only due to the impurity levels, but also the variation in experimental temperature, and the samples' overall chemical composition and microstructure. The temperature is very important for the creep process, as can be seen from the Arrhenius relationship between the creep rate and the temperature. Most creep experiments are carried out at high loads in order to speed up the deformation process and hence reduce the duration of the experiments. In industrial linings, the load on the refractory materials are more moderate, and the data from Figure 2.7 is extrapolated to a load of 0.1 MPa and presented for varying temperature in Figure 2.8. The creep rates presented in Figure 2.8 are thus more representative for the conditions in industrial linings. The data given in Figures 2.7 and 2.8 are corresponding with the expression for secondary creep, Equation 2.1. The effect of porosity on the creep rate is also substantial [72]. The measured creep rate of polycrystalline alumina is found to increase significantly with the increase of porosity in the material [72].

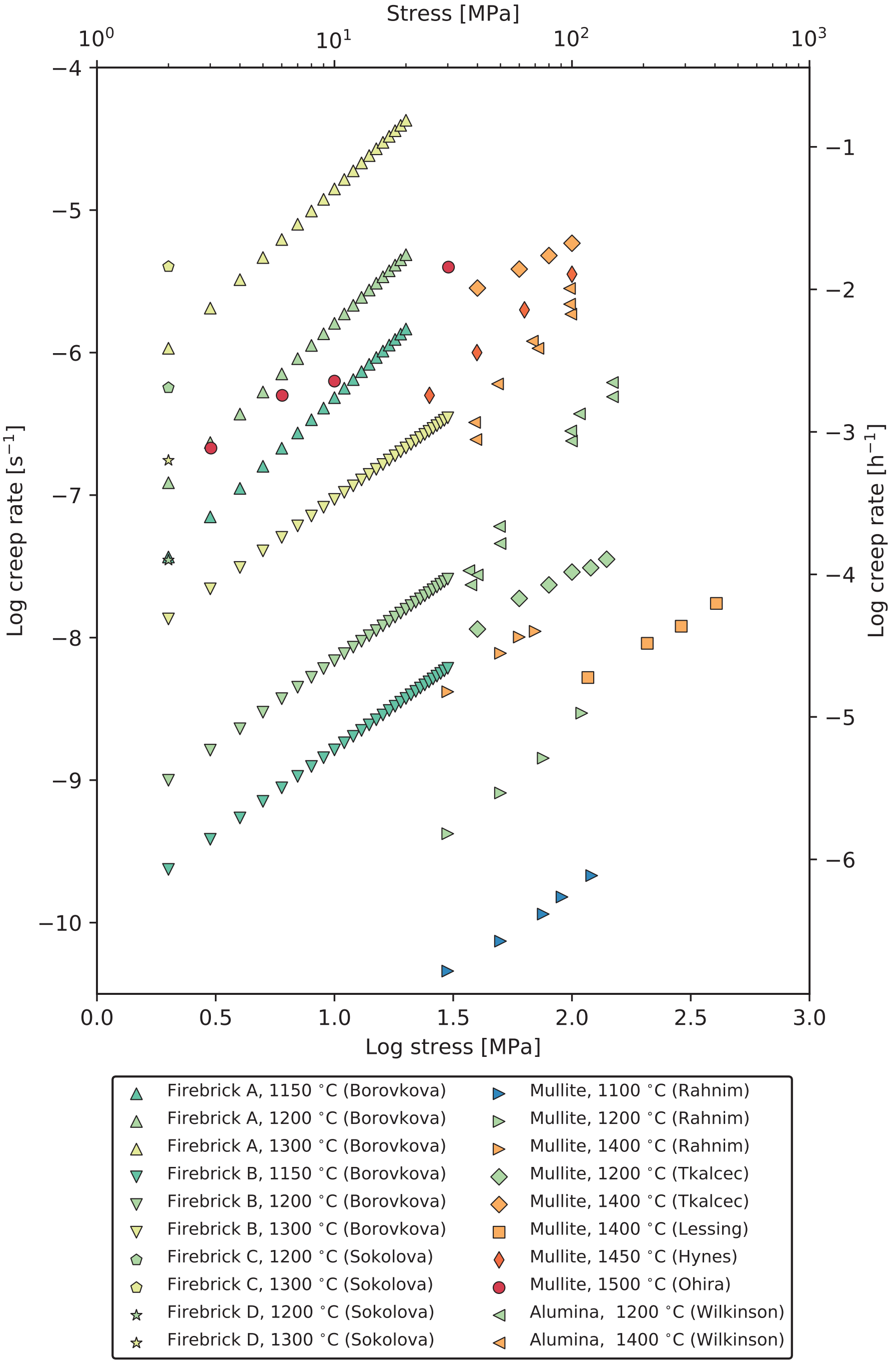

Figure 2.7: Summary of creep rates for alumina, mullite and firebrick samples measured for varying stress levels at various temperatures [74–81].

Table 2.6: Details on the materials presented in Figures 2.7 and 2.8. The impurities reported in the firebricks are mostly alkali elements.

Material	Source	Al_2O_3 [wt%]	Comment
Firebrick A	Borovkova [74]	40	Impurity level of 7 wt%. Open porosity = 14.8 %
Firebrick B	Borovkova [74]	42	Impurity level of 3 wt%. Open porosity = 13.0 %
Firebrick C	Sokolova [75]	43	Impurity level of 4.5 wt%. Open porosity = 8.8 %
Firebrick D	Sokolova [75]	40	Impurity level of 5.5 wt%. Open porosity = 15.0 %
Mullite	Rahnim [78]	71.8	Average grain size < 7μm. Density = 95.5 %
Mullite	Tkalcec [81]	71.8	Average grain size 0.2-8 μm. Density = 99.2 - 99.5 %
Mullite	Lessing [76]	71.8	NA
Mullite	Hynes [77]	73.0	Average grain size 0.74 μm. Density = 99 %
Mullite	Ohira [79]	71.8	Average grain size 1.2 μm. Density = 99 %
Alumina	Lin [80]	100	Average grain size 1.5 μm Density = 99.8 %

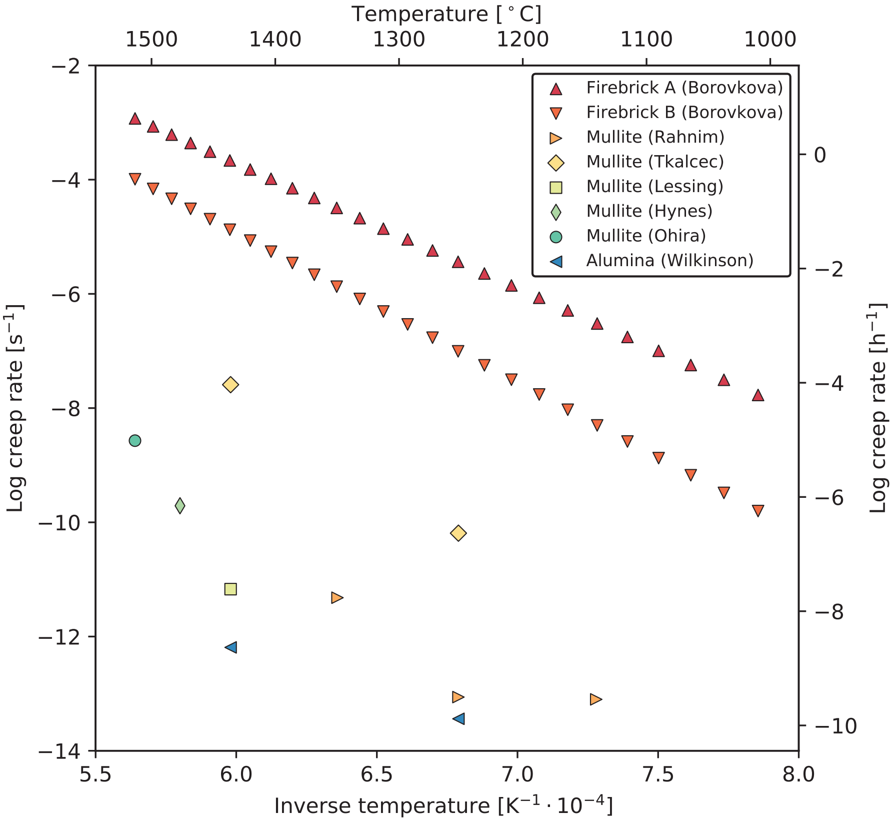

Figure 2.8: Summary of creep rates for alumina, mullite and firebrick samples at a stress level of 0.1 MPa. The values are based on the data in Figure 2.7 and extrapolated to a stress level of 0.1 MPa [74–81].

2.4 Refractories in the aluminium industry

2.4.1 Operational conditions and key material properties

In the aluminium industry, as in many other high temperature industries, refractory materials are used in many production processes [54]. The electrolysis cell, the anode baking furnace, the cast house etc. are all facilities where the refractory material's chemical and thermal stability are of great importance to the operation. The operational conditions do however vary from one application to another, resulting in different requirements of the refractory materials. In the anode baking furnace, both the lining surrounding the furnace and the interior flue wall and side walls are largely made of refractory materials. The baking temperature is cycling between ambient temperature and ~1200 °C in approximately two weeks, imposing thermomechanical stress caused by the recurring thermal expansion and contraction. The temperature in the baking furnaces is also higher at its maximum, compared to the cathode cell, requiring a higher degree of refractoriness in the lining. In the electrolysis cell, the refractory lining is found below the carbon cathode block, having an operational temperature of 800 °C to 850 °C [51, 84]. The temperature is stable throughout the lifetime of the cell, and the thermomechanical stress is thus not of great importance to the material's performance. The main challenge is the fluoride melt and elemental sodium moving down through the cathode and infiltrating the refractory layer during operation [51, 84–86]. In order to maintain its structural and thermal integrity, it is important for the refractory layer to have a high resistance towards both the cryolite melt and the elemental sodium.

A lot of work has been carried out on the cryolite resistance of the refractory lining in the electrolysis cell. In order measure the degree of reaction between various firebricks and a fluoride melt, the so-called cup test is used [51, 55, 87]. A hole is drilled in a refractory sample and filled with a mixture of cryolite and sodium fluoride, before heat treatment at 950 °C for 24 hours. The sample is then cut diagonally and the cross section investigated to determine the reacted sample volume [51, 55, 87]. To get a quantitative measure of how extensive the reaction has been, the reaction area at the cross section is measured and linked to the silica content of the sample. Several investigations of cryolite resistance of refractories with varying alumina to silica ratio have been carried out during the last decades [51, 55, 87]. The results are summarized in Figure 2.9, where the reacted area from the cup test is plotted as a function of silica content. Here, the degree of cryolite impact on the refractory is strongly decreasing when increasing the silica content. In the cup test, the melt in the sample hole often separates into two phases, with a viscous silicate melt in the bottom and a fluoride melt at the top [87]. The silicate phase works as a protective barrier between the reactive fluoride melt and the refractory, reducing the corrosive reactions in the bottom of the hole. Both the viscosity and the thickness of the protective silicate layer is found to increase with the silica content of the sample [87]. When these refractory materials are exposed to sodium fluorides, two sodium aluminosilicate phases are expected: nepheline ($NaAlSiO_4$) and albite ($NaAlSi_3O_8$). The reduction in reacted area is explained by an increasing tendency for albite formation, as the silica content in the refractory increases.

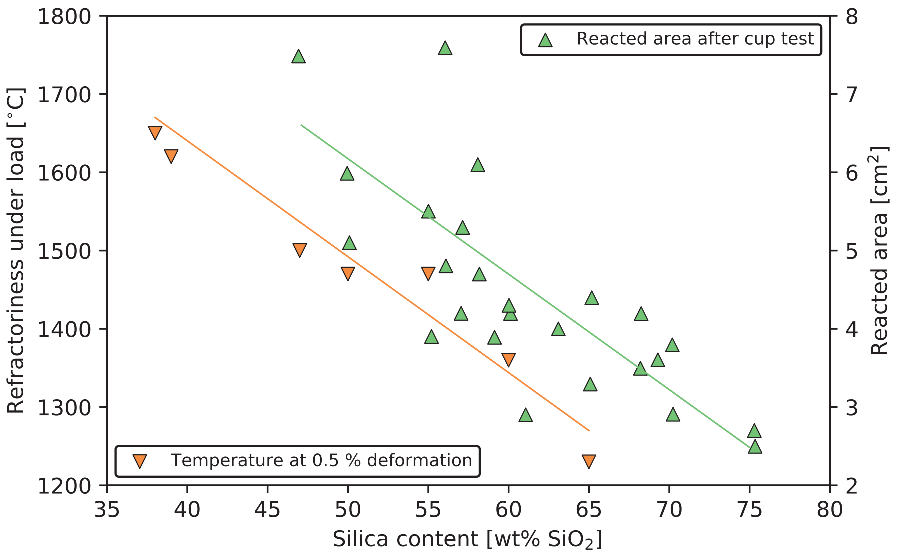

Figure 2.9: Performance of aluminosilicate refractory materials represented by refractoriness under load and cryolite resistance as a function of silica content [55, 88]. The cryolite resistance is expressed as reacted area after the cup test, as explained in Schøning *et al.* [55]. The refractorniess is expressed as the refractoriness under load ($T_{0.5}$).

Albite is an excellent glass former, and the amount of albite in the melt is found to affect the thickness of the silicate melt [55].

Another important property of refractory materials in these applications is the refractoriness, which can be expressed by the temperature for refractoriness under load ($T_{0.5}$). This temperature is a measure of how much it is possible to heat a sample, while being under a certain load, before it reaches a given level of deformation. The refractoriness under load has been investigated for similar samples as those tested in the cup test, and both properties are presented in Figure 2.9. For increasing silica content, it is evident that the refractoriness is decreasing while the cryolite resistance is increasing. High alumina content (i.e. low silica content) is beneficial for the refractoriness due to the increase in liquidus temperature and the higher melting temperature for alumina compared to silica. The silica to alumina ratio of the refractory lining is hence governing a trade-off between two important properties for the aluminium industry. The chemical composition of the refractory can thus be used as a variable when refractoriness and cryolite resistance is to be weighed against each other. Investigations of spent lining show that the typical silica content is ranging from 40 wt% to 50 wt% silica for the lining in the anode baking furnaces [9, 52, 89, 90]. Whereas in the cathode cell, the silica content is usually in the range of 60 wt% to 70 wt% silica [51]. This corresponds to the need for higher refractoriness in the anode baking furnace, while the cathode lining is more dependent on resistance towards cryolite attack.

2.4.2 Degradation of cathode lining

Degradation of the refractory lining in the cathode cell has been extensively investigated over the last decades [51, 55, 84–87, 91–103]. During cell operation, Na and bath components are transported downwards through the cathode block and into the refractory lining, causing significant mineralogical transformations, cathode heaving and ultimately cathode failure. The infiltration of bath components down in the cell is present from the beginning, and is especially severe during the first period after cell start-up [104]. As the diffusion length and the viscosity of the reaction products increases, the penetration rate is reduced, but some degree of penetration is maintained throughout the cell's life time [104].

Investigations of the reacted refractory materials below the cathode block show the presence of solid NaF, Na_3AlF_6, β-alumina, nepheline ($NaAlSiO_4$) and albite ($NaAlSi_3O_8$) in various amounts. The following reactions are suggested to occur in the lining material during cell operation:

$$6\,\mathrm{NaF}\ (l) + 3\,\mathrm{SiO_2}\ (s) + 2\,\mathrm{Al_2O_3}\ (s) = 3\,\mathrm{NaAlSiO_4}\ (s) + \mathrm{Na_3AlF_6}\ (s) \tag{2.2}$$

$$4\,\mathrm{Na}\ (g) + 5\,\mathrm{SiO_2}\ (s) + 2\,\mathrm{Al_2O_3}\ (s) = 4\,\mathrm{NaAlSiO_4}\ (s) + \mathrm{Si}\ (s) \tag{2.3}$$

Albite was also observed in the reacted refractory material, and Equation 2.3 can be generalized to cover both sodium aluminosilicate phases:

$$\mathrm{Na}\ (g) + \mathrm{SiO_2}\ (s)\ (\text{in refractory lining}) = \text{Sodium aluminosilicate} + \mathrm{Si}\ (s) \tag{2.4}$$

A recent study by Tschöpe *et al.* observed a reaction front in the refractory layer below the cathode block [86]. Detailed analysis of the reaction front showed that sodium was located farther down into the lining compared to the fluoride bath, demonstrating that gaseous sodium is diffusing in front of the percolating fluorides through the refractory lining [86]. Sodium is thus the first to react with the refractory lining, as suggested in Equations 2.2 to 2.4. The reducing conditions in the sodium front is supported by the observation of elemental silicon in the spent lining [86].

2.4.3 Degradation of flue walls in anode baking furnaces

In the anode baking furnace, the refractory flue walls are exposed to challenging conditions of thermal, mechanical and chemical nature during furnace operation. Over the course of years, the flue walls are observed to change both macro- and microscopically, gradually causing a reduction in the flue walls' overall performance. The need for maintenance is thus increasing over time to the point where the walls are replaced in order to maintain sufficient furnace operation.

Investigations of spent refractory lining from anode baking furnaces have been carried out over the last decades in order to address the mechanisms for flue wall degradation [9, 52, 53, 105–109]. In these studies, various degradation mechanism are discussed and related to the operational conditions in the furnace. Most of the studies report on elevated levels of sodium found in the regions closest to the anode pit [9, 52, 53, 105–109]. The use of recycled anode butts in green anode production is suggested to be the main source of sodium containing fluorides in the anode baking furnace. This is due to the exposure towards the fluoride bath which the anodes are experiencing during electrolysis. Elemental analysis of cleaned anode butts have shown a typical sodium content of 500 ppm and fluorine content of 700 ppm [24]. Insufficient cleaning will, however, increase the level of bath components in the green anode significantly. As the temperature increases during the baking process, sodium fluorides or metallic sodium are suggested to evaporate from the anodes and react with the lining material [9, 53, 89, 105, 108]. Various reactions are suggested for the formation of sodium oxide, as shown in Equations 2.5 and 2.6.

$$2\,\mathrm{Na}\,(g) + \mathrm{CO}\,(g) = \mathrm{Na_2O}\ (liq) + \mathrm{C}\,(s) \tag{2.5}$$

$$4\,\mathrm{NaF}\,(g) + \mathrm{SiO_2}(s) = 2\,\mathrm{Na_2O}\ (liq) + \mathrm{SiF_4}(g) \tag{2.6}$$

Sodium oxide is then reacting with the surrounding refractory lining to form sodium aluminosilicates. These are some of the same mechanisms as described for the degradation of the cathode cell, where gaseous sodium reacts with the lining. The result is a refractory material containing sodium aluminosilicate phases with lower melting points compared to the sodium-free refractories present in the wall before sodium exposure. The thermomechanical behavior at elevated temperatures is thus not the same as for the pristine flue wall, opening for a reduction in structural stability of the flue wall during furnace operation.

In addition to the activity of sodium containing fluorides in the pit gas, other gaseous compounds have also been addressed as potential sources of refractory destabilization, with a special focus on the reducing atmosphere in the pit [9, 53, 105]. Close to the anode side, in the same regions with elevated sodium and fluorine levels, the flue wall is observed to have regions with reduced levels of silica content [9, 52, 53, 105]. Butter and Bongers [105] suggested mechanisms where either AlF_3 or NaF react with silica to form SiF_4 and thereby removing silica from the lining, shown in Equations 2.6 and 2.7.

$$4\,AlF_3(g) + 3\,SiO_2(s) = 3\,SiF_4(g) + 2\,Al_2O_3(s) \tag{2.7}$$

Brunk [53] described a reaction path where the high temperature in combination with a reducing atmosphere favors the formation of volatile SiO as shown in Equation 2.8.

$$SiO_2(s) + CO(g) = SiO(g) + CO_2(g) \tag{2.8}$$

Common for all mechanism described in Equations 2.5 to 2.8 is the transport of pit gas components into the flue wall through the open porosity [9]. This enables reactions with the lining, not only on the surface, but also in the interior of the material.

Last, the flue walls are subjected to various physical strains during their lifetime in the furnace [53, 110]. For every baking cycle, the temperature cycles between ambient and approximately 1200 °C, causing a large degree of thermal expansion and contraction of the lining material. The furnace is designed and built to handle the thermal cycling, but this ability is however declining as the years in operation go by. The expansion joints are gradually filled with packing coke reducing their ability to absorb the thermal cycling, and the build-up of thermal stresses is subsequently increasing with every year in operation. The periodical movement of green anodes, packing coke and baked anodes, are also having an impact on the lifetime of the flue walls. The filling sequence of packing coke is especially important when it comes to avoiding flue wall bending. As the packing coke is filled in one pit while the adjacent pit still is empty, a horizontal force is acting on the flue wall, potentially inducing a small bending of the wall [111]. A combination of increasing stress in the flue walls and a horizontal force from the packing sequence will, if care is not taken during the filling operation, cause the flue to bend making it difficult to fit the anodes in the pit. A possible way to minimize the effect of the flue wall bending is to vary the filling direction during operation.

Chapter 3

Methods

3.1 Autopsy of anode baking furnaces

3.1.1 The furnaces

Samples of spent refractory lining were collected from two anode baking furnaces, with open top and closed top furnace design. The furnaces are referred to as the *open furnace* and *closed furnace* in the following chapters. The flue walls were estimated to have been in operation in the open and closed furnace for 160 and 73[1] cycles, respectively. Technical information on the pristine materials are presented in Table 3.1 as given in the data sheets from the manufacturers.

Table 3.1: Technical data for the pristine materials as provided by the manufacturers. The materials used in the open and closed furnace, respectively, are Gouda Dense Refractory Bricks Type AK 46S (Gouda, Holland), and HR 50 (PD Refractories, Germany).

	Open furnace	Closed furnace
Al_2O_3	49.5 wt%	$\geq$ 50 wt%
SiO_2	44.5 wt%	$\leq$ 48 wt%
Fe_2O_3	0.9 wt%	$\leq$ 1.1 wt%
TiO_2	$\leq$ 1.4 wt%	N/A
CaO + MgO	N/A	$\leq$ 1.5 wt%
$Na_2O + K_2O$	0.4 wt%	$\leq$ 0.6 wt%
Apparent density	2.4 $\mathrm{g\,cm^{-3}}$	$\geq$ 2.35 $\mathrm{g\,cm^{-3}}$
Open porosity	$<$ 15 %	$\leq$ 17 %
Refractoriness under load	1540 °C ($T_{0.5}$)	$\geq$ 1510 °C (T_a)

---

[1] Corrected estimate of earlier published value [47].

3.1.2 Material sampling and preparation

The samples of spent refractory lining were collected during scheduled autopsies of the flue walls. Sampling was carried out in a similar manner in both furnaces, where three sampling heights were used to collect samples: top, middle and bottom, as shown in Figure 3.1. The samples from the top layer were collected approximately 1 m below the packing coke, and from the bottom layer approximately 1 m above the bottom of the furnace. The middle layer was located approximately in equal distance from the top and bottom layer. In the open furnace, samples were collected in three horizontal positions for each height, resulting in nine samples. In the closed furnace, two samples were collected from the Part A and two from the Part B for each height, giving a total of 12 samples. All characterization of the samples were related to their specific location in the furnace. Typical cross sections of the refractory material separating the flue gas from the anode pit are shown in Figure 3.2. There is a color gradient going from white/yellow on the flue side, towards black on the anode side, demonstrating the discoloring of the lining close to the anode pit atmosphere.

Both the position at the wall, i.e. the vertical position, and the distance from the anode side of the refractory were addressed in this work. In order to characterize the material as a function of distance from the anode, the samples were divided into smaller sections as shown in Figure 3.3. The cross sectional width

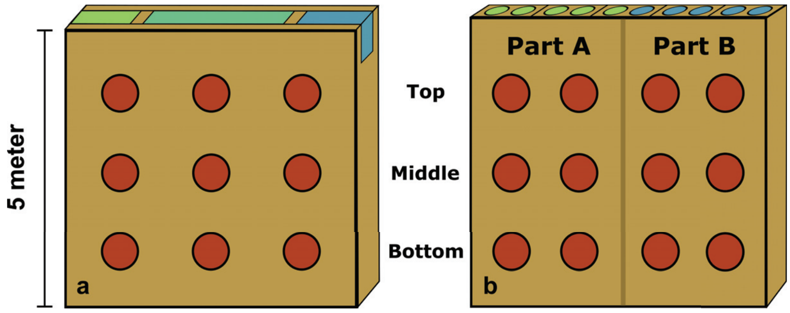

Figure 3.1: Sketches of flue walls from a) the open furnace and b) the closed furnace. The red circles show the positions from where the samples were taken. The vertical line in the middle of the closed furnace indicates the separation between Part A and Part B. The scale bar is an indication of the size of the furnace pits, but not an exact measure.

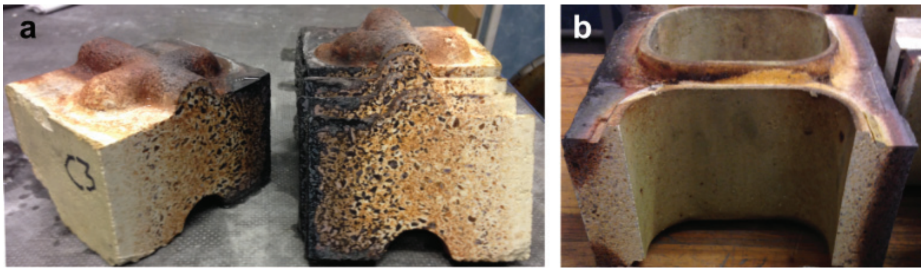

Figure 3.2: Images of the samples taken from a) the open furnace and b) the closed furnace. The pristine refractory material is white/yellow in color, similar as the material close to the flue side. Close to the anode side, the color changes and the spent lining becomes darker and ultimately black in the region closest to the anode side.

of the samples vary depending on the design of the furnace from which the samples originated. The samples from the open furnace had a width of 11 cm and were divided into eight sections, while the width of the samples from the closed furnace was 4 cm, and were divided into four or five sections. All sectioning of samples were carried out with a circular saw with diamond covered steel blade, using water as a cooling medium.

Phase and elemental composition were determined by X-ray diffraction (XRD) and X-ray fluorescence (XRF), respectively. For both analysis techniques, the samples were ground into powders by a Herzog HSM pulverizing mill in a WC

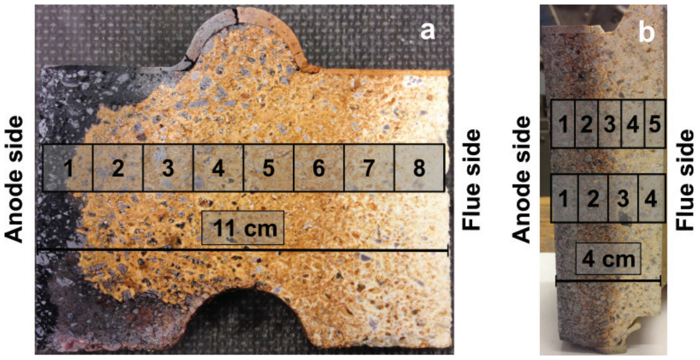

Figure 3.3: Images of samples from the a) the open furnace and b) the closed furnace showing the sectioning of the samples from the anode side to the flue side.

vessel before sieving, yielding a powder with grain size $< 63\,\mu$m. For the determination of density and open porosity, the cross section of the flue walls were sectioned as presented in Figure 3.3 and cut into samples of 2-3 cm^3. X-ray computed tomography analysis was carried out on core drilled samples with a diameter of 20 mm.

The determination of carbon content by mass loss during heat treatment was carried out on both powders as well as cubic-shaped samples. The cubic samples were sectioned in accordance with the description in Figure 3.3a. The powder samples were ground similarly as the samples for XRD and XRF analysis. Two series of powder samples were measured, each covering various parts of the brick's width. The first powder series covered the full width of the sample's cross section, similar as for the cubic samples. The second powder series covered 2 cm of the outermost part of the sample facing the anode side. This sample was sectioned in 5 mm width, yielding four samples. Carbon content was qualitatively characterized by X-ray diffraction. Two samples were cut from the bottom of the open furnace, being 3 mm and 5 mm in width. The width is measured from the anode facing surface for both samples.

Prior to microstructural investigations, the cross sections were embedded in epoxy and polished to $1\,\mu$m with SiC polishing paper and Struers DiaPro water based diamond suspension. To avoid problems with charging of the samples, all samples were coated with a layer of carbon before analysis. The samples were prepared in two ways. The majority of the samples were polished in the explained manner, and most results were thus from the investigated polished surfaces. In addition, some investigations were carried out on fracture surfaces.

3.2 Material characterization

3.2.1 X-ray diffraction and fluorescence

The X-ray diffraction measurements were performed with a Bruker D8 DaVinci diffractometer with a LynxEye SuperSpeed detector and CuK$_\alpha$ radiation. Additional instrumental details are found in Table 3.2. The analysis of X-ray diffractograms was carried out with the software Diffrac.EVA 5.0 from Bruker, using the PDF-4 (Powder Diffraction File) database [112]. Identification of phases were done using the following PDF cards: mullite (PDF 04-008-9526 [113]), α-cristobalite (PDF 04-007-2134 [114]), β-cristobalite (PDF 04-007-2468 [115], andalusite (PDF 04-009-4464 [116]) and tridymite (PDF 04-008-8461 [117]).

Table 3.2: Instrumental parameters used for the powder X-ray diffraction experiments.

Feature	Detail / Value
Instrument	Bruker D8 DaVinci diffractometer
Detector	LynxEye SuperSpeed
Geometry	Bragg-Brentano
Operation mode	θ-θ
Primary Soller slit	2.5°
Secondary Soller slit	2.5°
Data collection range (2θ)	15° to 75°
Divergence slit	Variable divergence slit. The illuminated length on the samples is constant and 6 mm.
Step size	0.013°/step
Radiation	CuK_α

The X-ray fluorescence analysis was carried out by a Bruker S8 Tiger 4 kW X-ray spectrometer. The sample powder were mixed with a flux material, melted and solidified into a glass sample. The XRF analysis were carried out on the glass samples, and the results calculated to the original sample.

3.2.2 Density and open porosity

Density and open porosity were determined by the Archimedes' method using water as immersion liquid in accordance with ISO5017 [118]. The samples were first dried at 120 °C for a minimum duration of 12 hours. Then the dry weight (m_{dry}) was measured before submersion into water at room temperature. After the submersion procedure, the weight of the sample was measured submersed in water (m_{sub}), and above water with submersion liquid filling the open porosity (m_{wet}).

The bulk density was then calculated from Equation 3.1.

$$\rho_{\text{bulk}} = \frac{m_{\text{dry}}}{m_{\text{wet}} - m_{\text{sub}}} \cdot \rho_{\text{water}} \tag{3.1}$$

where ρ_{bulk} is the bulk density of the sample and ρ_{water} is the density of water. The open porosity was calculated from Equation 3.2.

$$p_{\text{open}} = \frac{m_{\text{wet}} - m_{\text{dry}}}{m_{\text{wet}} - m_{\text{sub}}} \cdot 100\,\% \tag{3.2}$$

where p_{open} is the percentage of open porosity in the sample. All measurements were carried out with two parallels at each sampling position. After the initial characterization, the samples were heat treated in the laboratory at 1150 °C for 48 hours in air, before all measurements were repeated. The difference in density and open porosity before and after heat treatment was thus determined.

Two parallels were collected and the values averaged for each sampling point in both the open and closed furnace. No significant variation in density and open porosity was observed for the samples collected at each height. The average value for each height is therefore reported for the open furnace, and the average values at each height in Part A and in Part B are reported in the closed furnace.

3.2.3 Microstructure and phase distribution

The microstructural investigations were carried out with a Zeiss Supra 55 VP field emission scanning electron microscope (FESEM), and its associated energy dispersive X-ray spectrometer (EDS). The SEM imaging was carried out in either the backscatter electron mode or the secondary electron mode. Most images were obtained on polished samples were the atomic contrast from the backscatter electron imaging was utilized. The non-polished samples of the fracture surface were imaged with secondary electrons to capture the topography of the sample. The acceleration voltage was ranging from 10 kV to 15 kV, while the working distance was 10 mm for the SEM analysis and 15 mm for the EDS analysis.

3.2.4 Deposition of carbon

The deposition of carbon was determined by the mass loss after heat treatment for 48 hours at 1150 °C in air. Both the cubic samples and the powders samples were investigated after heat treatment. Two powder samples were also investigated by X-ray diffraction with the same settings as given in Table 3.2.

3.2.5 X-ray computed tomography (CT)

The CT analysis was carried out with a Nikon XT H225 ST instrument, with a molybdenum X-ray source. The imaging was performed at 185 kV and 60 μA, recording 3141 projections per revolution at a speed of 0.707 projections per second. The voxel size (combination of «volume» and «pixel») in each dimension was 11.2 μm, indicating the resolution of the analysis. Image post processing was carried out in the software ImageJ [119].

3.3 Pit gas analysis

3.3.1 Experimental setup

The initial setup for series 1

In situ measurements of pit gas atmosphere were carried out in three series in the open furnace. A flow chart showing the setup for all series is shown in Figure 3.4, and the final setup for the experiments is shown in Figure 3.5. The main idea was to construct an experimental setup for extraction of pit gas during anode baking, with a following analysis of the extracted gas. Kanthal APM [120] (a FeCrAl alloy) was chosen as the probe material due to its good mechanical and chemical stability at high temperature. The alloy contains mostly Fe, with additions of Cr (20.5 wt% to 23.5 wt%) and Al (5.8 wt%).

The probe was designed with two concentrically mounted Kanthal pipes (dimensions are given in Table 3.3) which both were mounted in a stainless steel (SS) connector in the top. The double pipe construction was chosen for enhanced mechanical support of the inner tube, while the shorter inner tube was for reducing the risk of pipe blockage by packing coke.

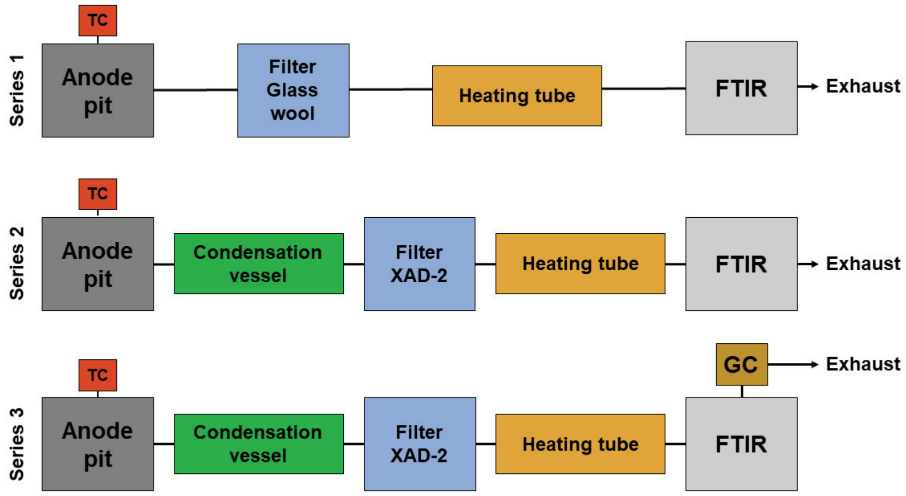

Figure 3.4: Flow chart illustrating the experimental setup for all series. The thermocouple (TC) is positioned close to the probe inlet in the anode pit. The gas chromatograph (GC) is connected after the FTIR, resulting in both instruments analyzing the same gas flow in series 3.

The probe was placed in the gap between the anodes and the flue walls, before filling of packing coke, as shown in Figure 3.5. The measurements were carried out on pits in the center of a furnace section, and thereby avoiding the potentially colder regions in the outermost pits. The probe tip was positioned approximately one meter above the pit floor and in the center of the pit, i.e. in the middle between the two adjacent head walls. A thermocouple was positioned in the packing coke together with the probe, monitoring the temperature throughout the baking cycle. From the SS connector in the top of the probe, the gas was transported through a SS pipe (OD = 6.35 mm, length = 5 m) to a filter

Table 3.3: Dimensions for the inner and outer pipes used in the Kanthal probe.

Pipe	Inner diameter [mm]	Outer diameter [mm]	Length [mm]
Inner pipe	20.9	36.7	4200
Outer pipe	34	40	4500

unit containing glass wool. The filter unit was connected to the Fourier transformed infrared spectroscopy (FTIR) by a heating tube (20 m, 180 °C), heating the gas to the operational temperature of the FTIR.

Improvements in the setup for series 2 and series 3

Based on the experience from series 1, several parts of the experimental setup were improved before series 2 and series 3. The final experimental setup used in series 2 and series 3 is shown in Figure 3.5. In order to deal with condensation of water and pitch components, a condensation vessel was constructed. The vessel comprised a stainless steel cylinder with a removable lid, and gas inlet and outlet through the lid. The filter material was changed from glass wool to

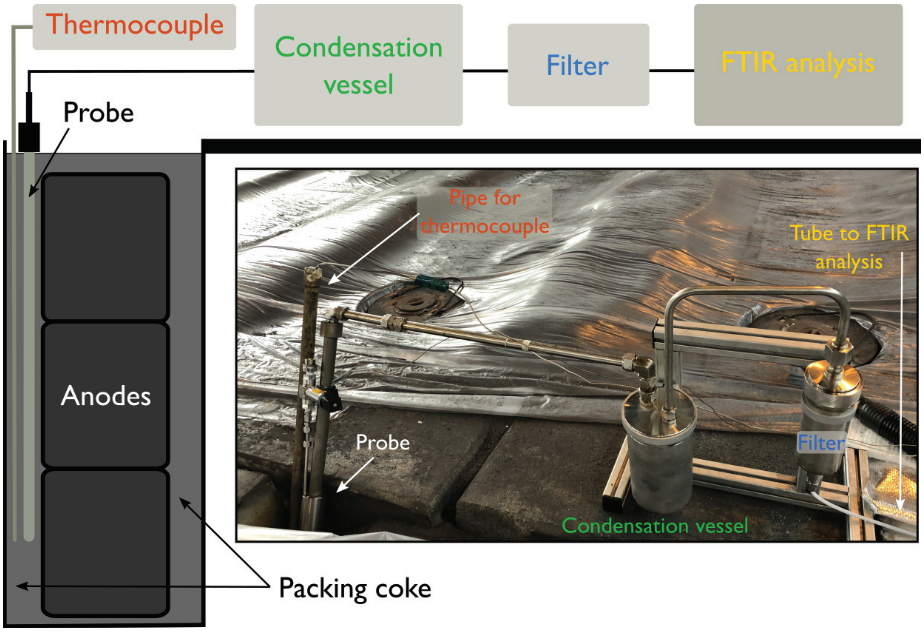

Figure 3.5: Sketch and image of the experimental setup used during series 2 and series 3. The gas is transported from the pit through the probe, condensation vessel and filter unit before it enters the heating tube and finally the FTIR instrument. The heating tube is not connected in the current image, but was used during the measurements. Reprinted from Brandvik *et al.* [121] with permission from Springer.

an absorption material (styrene-divinylbenzene (XAD2) from Sigma-Aldrich). To avoid blockage of the pipes between the probe, condensation vessel and filter unit, the pipe diameter was increased. Between the probe and condensation vessel, the outer diameter increased from 6.35 mm to 19.05 mm, and between the vessel and filter unit, from 6.35 mm to 12.7 mm. The heating tube (20 m, 180 °C) was connecting the filter unit to the FTIR instrument. A gas chromatograph was used during series 3 to expand the analysis to comprise H_2, O_2, N_2.

3.3.2 Analysis methodology

A Protea LTD ProtIR 204M analyzer was used to carry out the FTIR analysis. Data was recorded in the frequency range from 800 cm^{-1} to 5000 cm^{-1} with a resolution of 1 cm^{-1} and averaged every 1-5 minutes. The instrument performed the analysis at 180 °C. Manual interpretation of spectral data was performed by comparison with library FTIR data captured with the same model by the instrument producer. Quantification of pit gas concentration was performed by linear regression of peak height values. Extrapolation of library data was done when the experimental spectral data were outside the range of the library data. In some cases, the build-in calibration model of the instrument was applicable, and was used accordingly. These cases are indicated. If nothing is otherwise stated, the manual interpretation method is used.

An Agilent 490 Pro Micro GC with a Thermal Conductivity Detector was used to quantify H_2, O_2, N_2 and CO_2. Channel 1 was equipped with a 10 m Molsieve 5 Å column, operated at 90 °C using argon as carrier gas. Channel 2 was equipped with a 10 m PPQ column, running at 90 °C using helium as carrier gas. The pressure on both columns was set to 150 kPa with an injector temperature of 70 °C. The length of each CG cycle was 135 s. The GC was connected to the outlet of the FTIR in order to analyze the same gas flow with both instruments. The GC was used in shorter periods during the third series.

3.4 Thermodynamic calculations

The thermodynamic stability of phases in varying chemical environments was investigated with the thermochemical software FactSage (versions 7.0 and 7.1)

[122]. The *Equilibrium* and *Reaction* modules were used in combination with the *FactPS* database [123]. The software minimizes the Gibbs' free energy for a given system, and thereby determines the composition of phases yielding the lowest total energy. Various approaches have been utilized during this work. Initially, the full compositional range of aluminosilicates was investigated, calculating the response to increasing amounts of NaF and $NaAlF_4$ at 1300 °C. Secondly, fluoride volatility from pure cryolite and an industrial electrolyte were investigated, both in a dry atmosphere and in the presence of water. Lastly, the effect of fluorides on the stability of aluminosilicate materials was investigated.

3.5 Finite element modeling

3.5.1 Introduction to the Finite Element Method (FEM)

The use of differential equations has for many physical applications proved too complex to be solved by classical analytical methods [124]. During the last 75 year, the development of the finite element method (FEM) has provided a numerical way of solving such problems [125]. The first papers describing the discretization of continuous domains for solving elasticity or structural problems dates back to the 1940s, published by Hrennikoff [126] and Courant [127]. In 1973, the book *An Analysis of the Finite Element Method* by Strang and Fix [128] gave further contributions to the fundamental mathematics of the finite element method [125]. The development has since then led to the method being used for numerical modeling of many physical systems such as structural mechanics, heat transfer, electromagnetism and fluid dynamics [125, 129].

When describing physical processes with differential equations, the equations are assumed to hold for a given region of the domain in question [124]. The core feature of the finite element method is the assumption that a given approximation does not need to hold over the whole domain, but only across chosen sub-domains. The domain is divided into smaller sub-domains of finite size, i.e. *finite elements*, and the differential equation is solved for each element instead of the entire domain. By dividing a large domain into smaller sub-domains, it is possible to assume a linear approximation across each sub-domain, even though the variable varies highly non-linearly across the domain as a whole.

Since the 1960s, a variety of softwares have been developed for carrying out finite element computations on a broad range of problems, where ABAQUS and COMSOL are some of the more recent [129]. The accuracy of the FEM modeling is very dependent on the size of the elements used in the computation, where smaller elements increases the accuracy. As the elements become smaller, the mesh more detailed and the number of elements increases, the computational cost of the modeling increases considerably. The increase in computer speed over the last decades has therefore been an important factor for the utilization of FEM in both the industry and academia [129].

3.5.2 The model, geometry and boundary conditions

The main objective with this modeling was to determine the change in porosity due to high temperature creep. The experimental measurements of density and open porosity in the open furnace (Section 4.2.2) gave a good basis for comparison, and the modeling was therefore related to the experimental data from the open furnace. A 2D geometry simulating the cross section of the refractory brick was chosen as shown in Figure 3.6. Here, the gravimetric stress for all sections is shown, in addition to the different pre-exponential factors applied to region 1, 2 and 3. The size of each section is 7.5 cm by 12 cm. The modeling is carried out with the software COMSOL®5.4, using the modules for *Structural Mechanics* (including the module for *Non-linear Structural Materials*) [130]. The mesh sequence type was set to *Physics-controlled mesh*, and the mesh size was set to *Normal*.

Removal of porosity is based on the secondary creep mechanism, described by the following expression

$$\dot{\epsilon} = A\sigma^n \exp\left(\frac{-Q}{RT}\right) \tag{3.3}$$

where $\dot{\epsilon}$ is the creep rate, σ is the stress level and A, n and Q are material dependent constants. The stress, σ, acting on the wall is caused by the weight of the wall itself and only the gravimetric force is considered in the model. The thermal activation barrier for creep is given by Q.

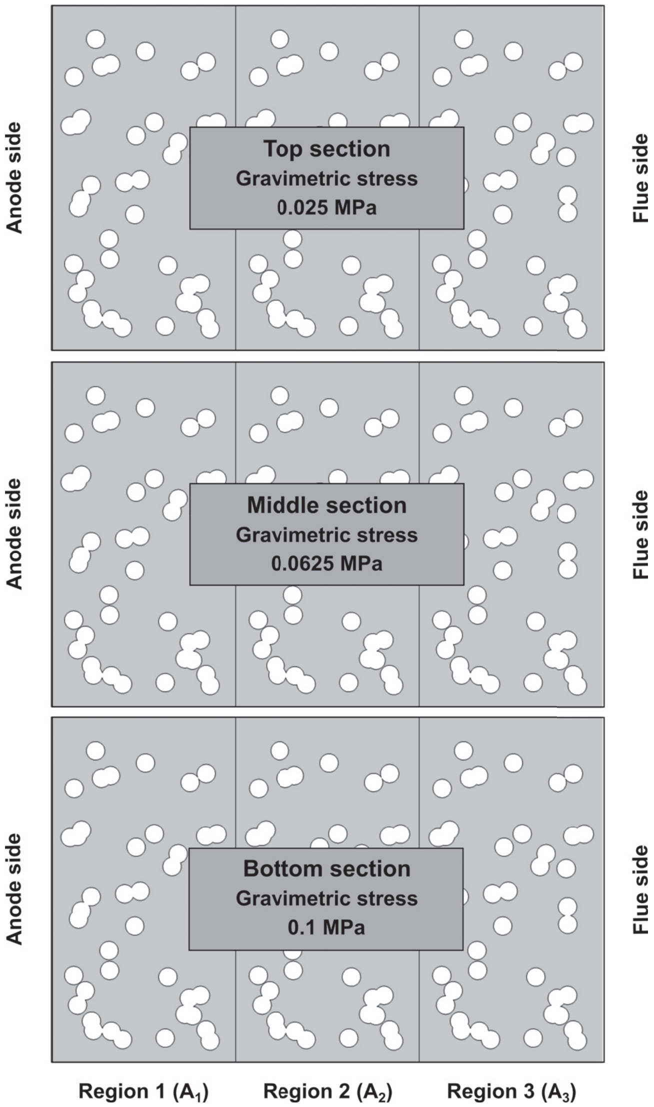

Figure 3.6: Illustration of the model geometry with pore radius 2 mm shown for all sections with the corresponding gravimetric stress. The model is divided into three regions, permitting various conditions to be implemented across the model through varying the pre-exponential factor (*A*).

Creep is a high temperature phenomenon and for the simulation of creep during anode baking, only the baking time above a certain temperature threshold is considered. The threshold was set to 1100 °C and the temperature fixed to that level during simulations. The temperature in the furnace could reach 1150 °C to 1200 °C for shorter periods, and fixing the temperature at 1100 °C is thus simplification of the actual temperature regime. Since the creep rate is dependent on the temperature, and the temperature is fixed, a simplification to the creep rate is also imposed during the modeling. The temperature is measured to be above this threshold approximately 30 h for each baking cycle. The open furnace had experienced 160 baking cycles, giving an approximate total of 4800 h above the temperature threshold. Each simulations was thus carried out at 1100 °C for a duration of 5000 h.

Reducing atmosphere is shown to have a destabilizing effect on certain perovskites, yttria doped ceria and coal ash slags, [131–135]. Based on these observations, it was suggested that the reducing atmosphere in the pit is reducing the thermomechanical stability of the lining by enhanced creep rate. The geometry was therefore sectioned into three regions (Region 1, 2 and 3) as shown in Figure 3.6, permitting various creep conditions to apply for each region in the model. The porosity was randomly introduced as spheres in the geometry. In order to address the effect of pore size, all simulations were carried out with the sphere radius set to 0.5 mm, 1 mm and 2 mm. The sphere radius was kept constant for each simulation, with the total porosity adding up to the open porosity of the pristine materials (17 %).

Boundary conditions

The modeling was carried out in two cases, with two sets of boundary conditions imposed on the geometry. In Case 1, all vertical boundaries were free to move vertically, but not horizontally. This was implemented by using Prescribed displacement ($u_x = 0$). In Case 2, the two internal vertical boundaries were free to move in all directions, while the two outermost vertical boundaries had the same boundary conditions as in Case 1 (Prescribed displacement: $u_x = 0$). The horizontal boundary on the bottom of the geometry were fixed for both cases. A boundary force was applied to the horizontal boundary in the top part of the geometry. This force simulated the load from the bricks in the wall above a given layer. Three values for the top boundary force were applied, corresponding to the level of gravimetric load at the three sampling heights. The top boundary force was set to 0.025 MPa, 0.0625 MPa and 0.1 MPa representing the top, middle and bottom sections, respectively.

3.5.3 Material properties

The material properties used in the FEM simulations are summarized in Table 3.4. Young's modulus (E), the thermal activation barrier for creep (Q), the pre-exponential factor (A) and the stress exponent (n) are based on literature data from similar refractory materials, and given in Table 3.4. The Arrhenius relationship between the creep rate and the thermal activation barrier makes creep especially sensitive to the value of Q.

Table 3.4: Input data used in the simulations, with literature data for comparison.

Property	Lit. value	Values used in simulations	Unit	Reference
E	2 - 15	10	GPa	[59, 136–138]
Q	450 - 500	485	$\mathrm{kJmol^{-1}}$	[74, 75]
n	1.2 - 1.6	1.2	[-]	[74]
A (Region 1)	10^{11} - 10^{12}	$3 \cdot 10^{11}$	[-]	[74]
A (Region 2)	10^{11} - 10^{12}	$8 \cdot 10^{10}$	[-]	[74]
A (Region 3)	10^{11} - 10^{12}	$3 \cdot 10^{10}$	[-]	[74]

The autopsy of the open furnace shows a significant variation in open porosity. A reduction in open porosity was observed close to the anode side, while becoming less pronounced closer to the flue side. The difference in oxygen partial pressure at the anode side compared to the flue side is suggested as a possible explanation for this observation. The model was divided into three sections, where each is assigned with a specific value for the pre-exponential factor. Region 1 is simulating the region close to the anode side with a significant creep, while Region 3 is close to the flue side with almost no creep. The value for

Region 2 is set to the midpoint between Region 1 and Region 3. The method for determination of the values for the pre-exponential factor is described below and the values for all regions are shown in Table 3.4.

3.5.4 Determination of the change in porosity

The constitutive law used in the modeling does not account for changes in density of the geometry. The variation in porosity is therefore caused by a redistribution of the geometry with a corresponding reduction in the internal pore area. COMSOL does not export the internal pore area directly, and the relative porosity post modeling was calculated indirectly. The geometry was deforming in an downward manner due to the creep of the top boundary load, as illustrated in Figure 3.7. The vacant area at the top after modeling was therefore used as a measure for the reduction in internal pore area. By exporting the average displacement of the top boundary from COMSOL, and multiplying it with the geometry width, the change in internal pore area was estimated.

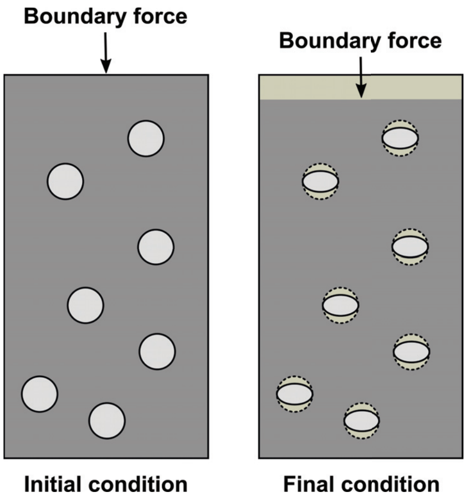

Figure 3.7: Illustration of the deformation occurring during modeling in Case 1. The boundary load on the upper horizontal boundary results in the geometry deforming in an downward manner. The internal pore area is reduced after modeling, corresponding to the vacant area at the top. In Case 2, the geometry is also allowed to deform in the horizontal direction at the two interior vertical boundaries.

3.5.5 Tuning the pre-exponential factor (A)

As the temperature, simulation duration, the stress exponent (n) and the creep activation barrier (Q) were set based in literature data, the only undetermined variable left was the pre-exponential factor (A). The pre-exponential factor in the creep equation (Equation 3.3) were tuned to fit the experimental data from region 1 for a stress level of 0.1 MPa. The modeling was then carried out for the two other stress levels (0.025 MPa and 0.0625 MPa), with all other parameters kept constant. This resulted in a distribution of densification levels for the increasing stress corresponding with the experimental data. In region 3, the same procedure was carried out, only with the experimental data from the flue side (region 3) used in the tuning. The observed deformation in region 3 is much less than in region 1, and the pre-exponential factor was found to be accordingly smaller. The variation in creep rate is assumed to be linked to the difference in chemical conditions at the anode side and the flue side, and represented in the modeling by variations in the A parameter. The A parameter for region 2 was thus chosen to be at the midpoint between the values determined for region 1 and region 3.

Chapter 4

Degradation of the refractory lining

4.1 Pristine composition and microstructure

The microstructure of the pristine material used in the open furnace is shown in Figure 4.1. The characteristic heterogeneity of refractory materials is clearly visible, with a broad grain size distribution and significant levels of open porosity. The same characteristics are found in the pristine material used in the closed baking furnaces, demonstrating that the two pristine materials are quite similar in nature prior to service.

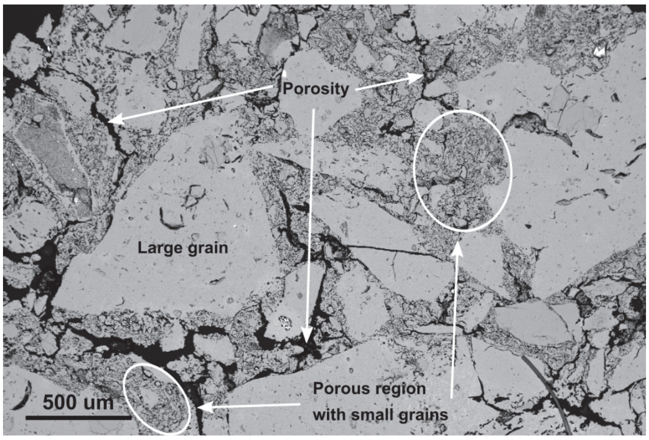

Figure 4.1: SEM image showing the microstructure of the pristine refractory material used in the open furnace. The typical large broad grain size distribution and a significant degree of open porosity are clearly visible.

The elemental composition of the materials measured by XRF is summarized in in Table 4.1. The content of alumina and silica and the level of impurity elements are fairly similar for the two refractory materials. The most pronounced difference is the higher alumina content in the refractory material used in the closed baking furnace. No Na_2O was detected in either material demonstrating a sodium content below the XRF's detection limit of 0.02 wt%. Impurity oxides are also detected in both materials, where Fe_2O_3 and TiO_2 are the most significant. The X-ray diffraction patterns of the two pristine materials are displayed in Figure 4.2. The figure show the whole 2θ range measured with the insert focusing on the main reflections at low angle. Identification of phases is possible from the reflections present in the insert of Figure 4.2, and the following figures are thus focusing on 2θ range at low angles. The two main phases identified by XRD are mullite and cristobalite, which is in good accordance with the overall

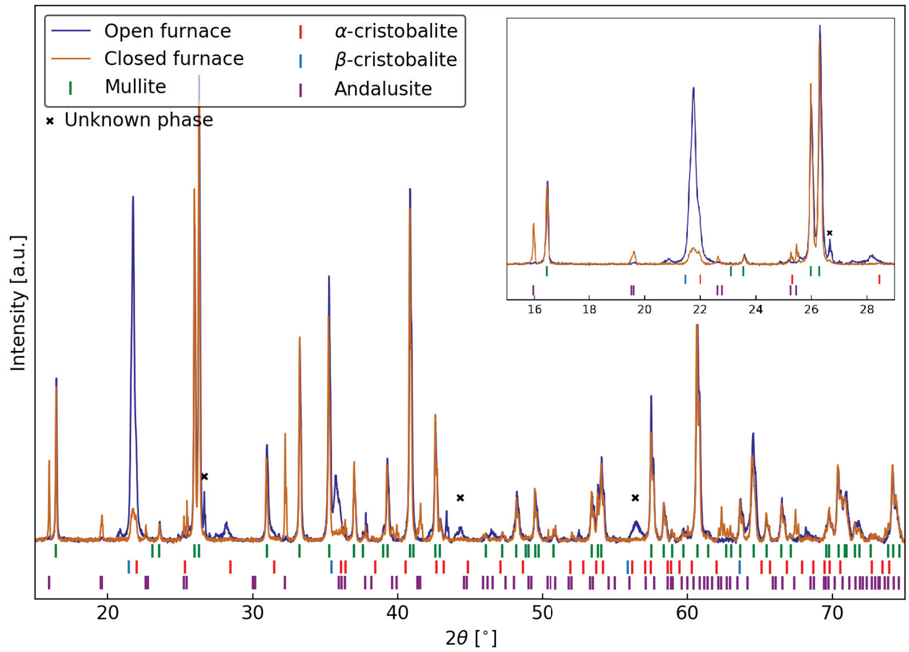

Figure 4.2: X-ray diffraction patterns of pristine materials from the open and closed baking furnace. Insert: diffraction patterns at low 2θ range.

Table 4.1: Elemental composition of pristine refractory materials used in open and closed anode baking furnaces. The data is measured by XRF and given in wt%.

Furnace	Al_2O_3	SiO_2	Fe_2O_3	TiO_2	CaO	K_2O	MgO
Open	50.8	46.3	1.1	1.6	0.2	0.2	0.1
Closed	55.0	42.7	1.0	0.8	0.0	0.4	0.2

chemical composition and the $SiO_2-Al_2O_3$ phase diagram [139]. In addition, the pristine material from the closed furnace contains a fraction of unreacted andalusite ($SiAl_2O_5$), originating from the raw materials. The Bragg reflection related to cristobalite is significantly higher for the material from the open furnace due to the lower silica content in the sample from the closed furnace and the fact that some silica is still bound as andalusite.

4.2 Investigations of spent refractory lining

4.2.1 Phase composition

Open top baking furnace

The X-ray diffraction patterns of samples from the bottom section in the open furnace are compared to the pristine material and presented in Figures 4.3 and 4.4. The main phases identified are mullite and cristobalite, as expected from the investigations of the pristine materials. No significant variation in the phase composition was identified by XRD irrespectively of the location of the sample in the wall. However, a variation in the Bragg reflection of cristobalite was observed as shown in Figure 4.4. The X-ray diffraction patterns shown in Figures 4.3 and 4.4 are representative for samples from the middle and top sections of the furnace. Diffraction patterns of samples from the middle and top sections are found in Appendix A. The variation in the Bragg reflection of cristobalite is highlighted in Figure 4.4, with indications of the regions where the reflection of α- and β-cristobalite are expected to be found. The phase transition between α- and β-cristobalite is reported to take place between 170 °C and 270 °C, where strain or defects in the material affect the transition temper-

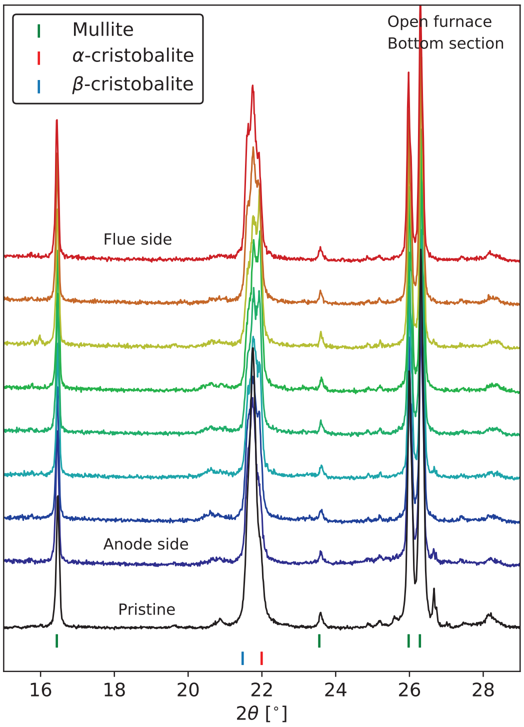

Figure 4.3: X-ray diffraction patterns of samples from the bottom section of the open furnace compared to the pristine material. The samples are collected at various distance from the anode (in accordance with the sectioning in Figure 3.3), here shown with an offset in intensity to highlight the variations in the cristobalite reflection at ~21.9°.

ature [140–143]. β-cristobalite, the high temperature polymorph, is in general expected to be found above the transition temperature. Figures 4.3 and 4.4 demonstrate however that both α-cristobalite and β-cristobalite are present in the materials at room temperature. Suppression of the transition from β- to α-cristobalite has been investigated, and is reported to be caused by the presence of impurity oxides [141–143]. The shift between α- and β-cristobalite is varying from one sample to another, but with no clear linear dependence with the distance from the anode.

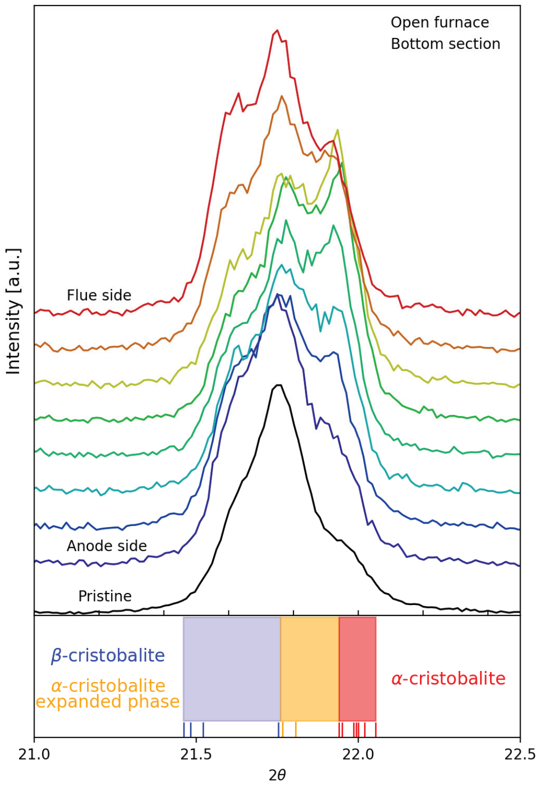

Figure 4.4: X-ray diffraction patterns of samples from the bottom section of the open furnace compared to the pristine material. The shift between α- and β- cristobalite as a function of distance from the anode is emphasized. The lower part of the figure is adapted from Damby *et al.* [140].

Closed top baking furnace

X-ray diffraction patterns of samples from the bottom section of Part A in the closed furnace are compared to the pristine material in Figures 4.5 and 4.6. The main phases identified are mullite and cristobalite, in addition to andalusite and traces of tridymite, as expected from the pristine phase composition shown in Figure 4.2. As for the open furnace, no significant variation in the phase composition was identified, and the data presented in Figures 4.5 and 4.6 are therefore representative for the entire furnace. Diffraction patterns from other parts of the wall are given in Appendix A. Small variations were however found

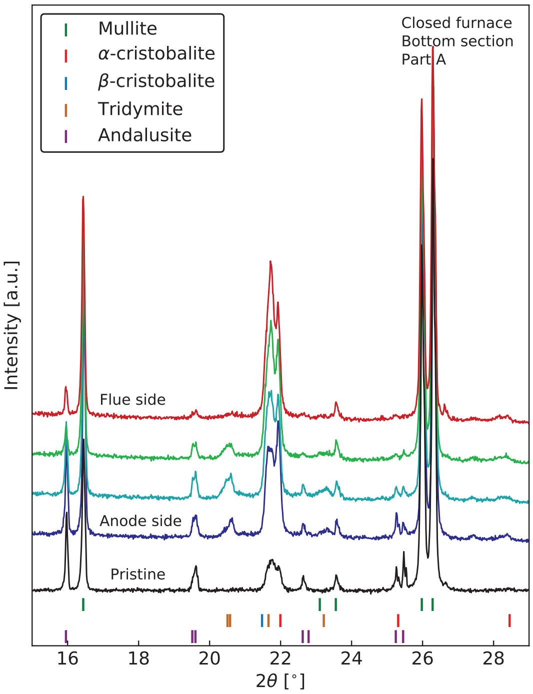

Figure 4.5: X-ray diffraction patterns of samples from the bottom section of Part A in the closed furnace compared to the pristine material. The samples are collected at various distance from the anode (in accordance with the sectioning in Figure 3.3), here shown with an offset in intensity to highlight the variations in the cristobalite reflection at ~21.9°.

for the Bragg reflections of andalusite and tridymite seen in Figure 4.5 and for cristobalite highlighted in Figure 4.6.

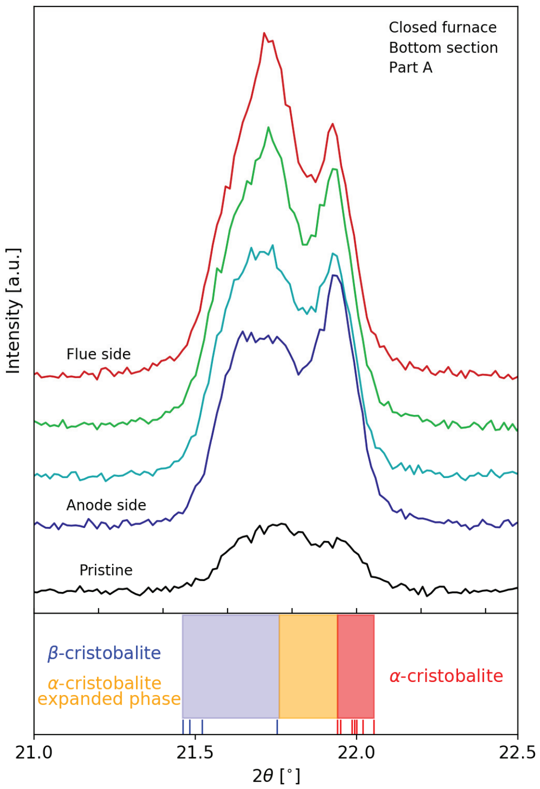

Figure 4.6: X-ray diffraction patterns of samples from the bottom section of Part A in the closed furnace compared to the pristine material. The shift between α- and β- cristobalite as a function of distance from the anode is emphasized. The lower part of the figure is adapted from Damby *et al.* [140].

The amount of andalusite is not constant, and is varying with the distance from the anode side. Closest to the anode side, the content of andalusite is largest, while decreasing going from the anode side towards the flue side. This is clearly visible in Figure 4.5, and similar trends are found in both Part A and Part B, and for all sampling heights in the furnace. Tridymite is also present in low amounts except for the sample closest to the flue side. The shift between α-cristobalite and β-cristobalite is presented in Figure 4.6, showing a transition from α- to β-cristobalite going from the anode side towards the flue side. X-ray diffraction analysis was also carried out for all sampling heights in Part B in the closed furnace, with no significant deviations for the analysis of Part A.

4.2.2 Density and open porosity

The density of samples from the open furnace is presented in Figure 4.7. The gray region in the lower part of the figure represent the variation in density measured for the pristine refractory material. Samples from all heights show a significant increase in density. The increase in density is however not uniform, but varying across the brick. The variations in density are observed to have two major characteristics. First, the density is higher close to the anode side, com-

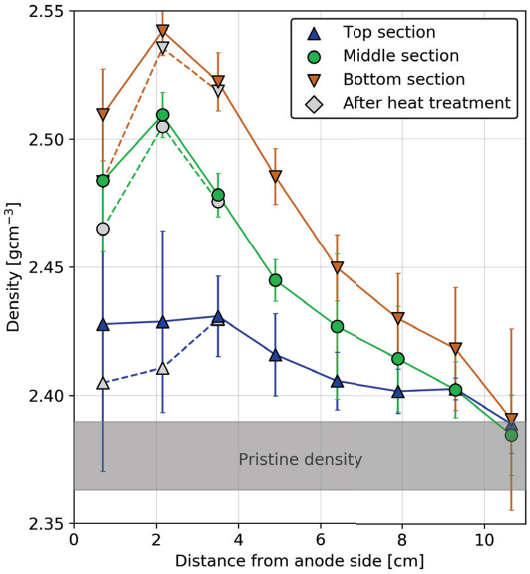

Figure 4.7: Density of samples from top, middle and bottom sections of the open furnace. The error bars give the value for the standard deviation of the measurements, and the gray region represent the variation in density measured on pristine materials. The gray symbols connected with the dotted lines show the density of samples after laboratory heat treatment.

pared to the flue side. The density is observed to converge towards the pristine density close to the flue side, while peaking for the samples approximately 2 cm from the anode side. Closest to the anode side, there is a drop in density for the middle and bottom section. Second, the increase in density is more pronounced for the bottom section of the furnace, compared to the middle and top sections. This is consistent for all measurements shown in Figure 4.7. After the measurements, all samples were heat treated in air at 1150 °C before the measurements of density and open porosity were repeated. The gray symbols in Figure 4.7 represent the data from the heat treated samples, where only the samples showing a significant deviation from the original measurements are included. The density after heat treatment is found to be lower than before the heat treatment, but still higher compared to the pristine material. The effect of the heat treatment is also found to be most pronounced in the top section compared to the middle and bottom section.

Figure 4.8 shows the open porosity for all samples from the open furnace. The open porosity has two major characteristics resembling the findings with respect to the density. In general, there is a significant reduction in open porosity for the spent lining. The reduction in open porosity is more pronounced close to the anode side, and is diminishing at the flue side. In addition, the reduction becomes more significant the further down in the furnace the samples are collected. This is consistent with the measured density, where samples with a significant reduction in open porosity demonstrate a correspondingly increase in density.

Density for samples from the closed furnace is presented in Figure 4.9. Compared to the pristine density (indicated by the gray region), an increase in the density is demonstrated for nearly all samples measured. The increase in density is slightly more pronounced for the samples from the middle and bottom section compared to the samples from the top section. A clear trend in density variations with sampling height is however not equally distinct as for the open furnace. There were no significant change in density after heat treatment, and the post heat treatment data are therefore not included in the figure. The open porosity for samples from the closed furnace is presented in Figure 4.10. The standard deviation shown for the measurements demonstrate large variations

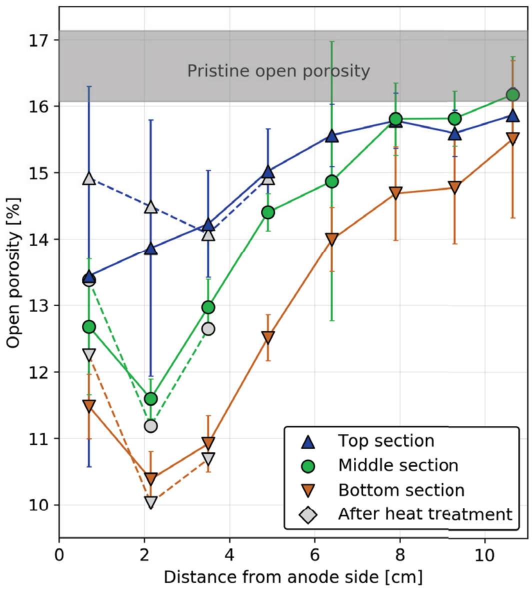

Figure 4.8: Open porosity of samples from the top, middle and bottom sections in the open furnace. The error bars give the value for the standard deviation of the measurements, and the gray region represent the variation in open porosity measured on pristine materials. The gray symbols connected with the dotted lines show the density of samples after laboratory heat treatment.

between the data sets, but the measurements from the spent samples coincides to some degree with the pristine open porosity.

Lining from the bottom section in the open furnace was investigated by computed tomography (CT), and presented in Figures 4.11 and 4.12. The traditional CT contrast is shown in Figure 4.11, where the refractory material is shown in gray and the pores in black. In Figure 4.12, the contrast is changed to show the refractory material in black and the pores in white, making it easier to see the variations in porosity. When comparing the anode side (the upper figures) to the flue side (the lower figures) it is clear the the level of porosity is significantly reduced at the anode side. Most of the reduction in porosity is observed in the binder phase, where the pores are significantly smaller.

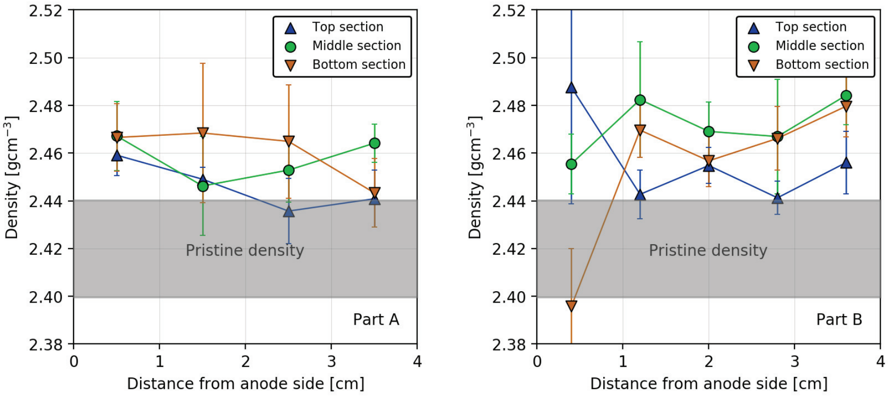

Figure 4.9: Density of the samples from the closed baking furnace. The error bars give the value for the standard deviation of the measurements. The gray region show variation in the density measured on pristine materials.

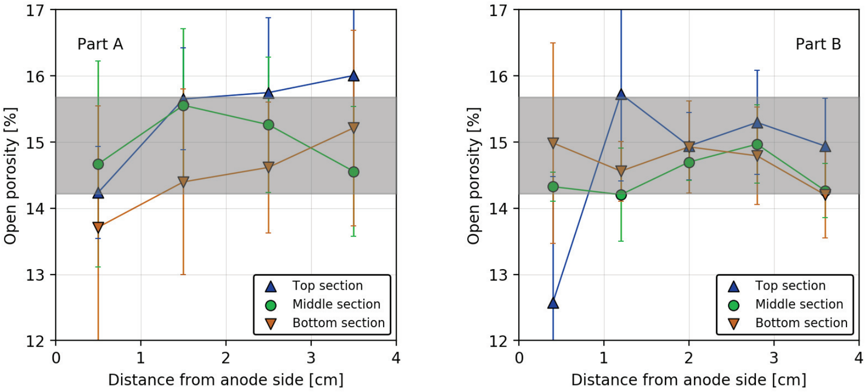

Figure 4.10: Open porosity of the samples from the closed baking furnace. The error bars give the value for the standard deviation of the measurements. The gray region show variation in the open porosity measured on pristine materials.

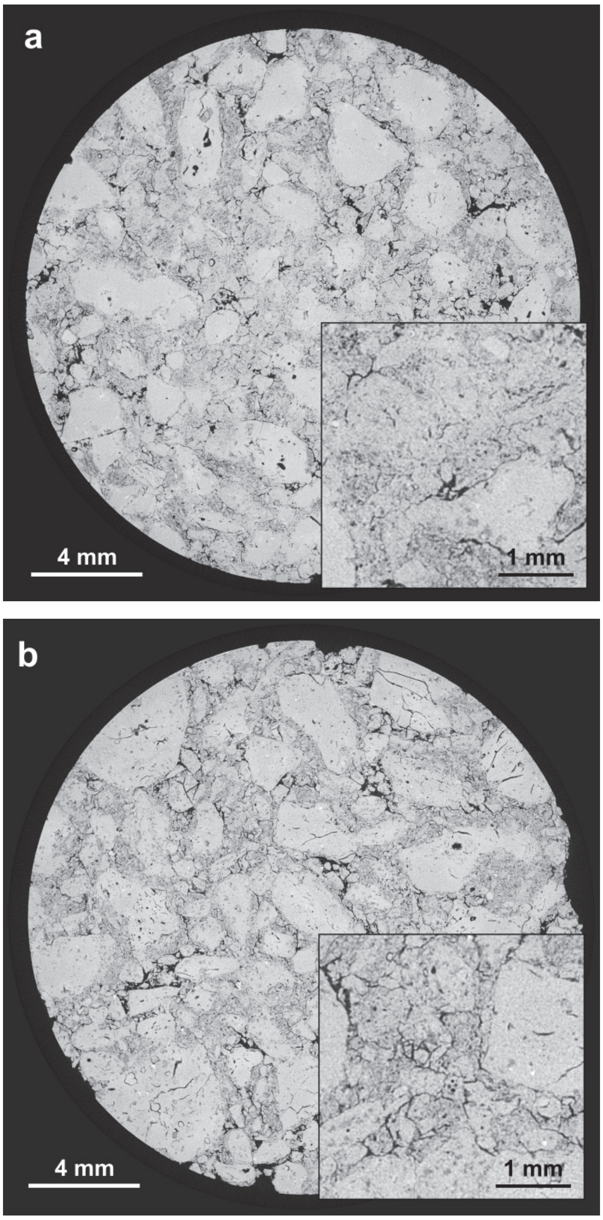

Figure 4.11: CT images from the bottom section of the open furnace at a) the anode side, and b) the flue side. The refractory material is shown in gray and the pores shown in black.

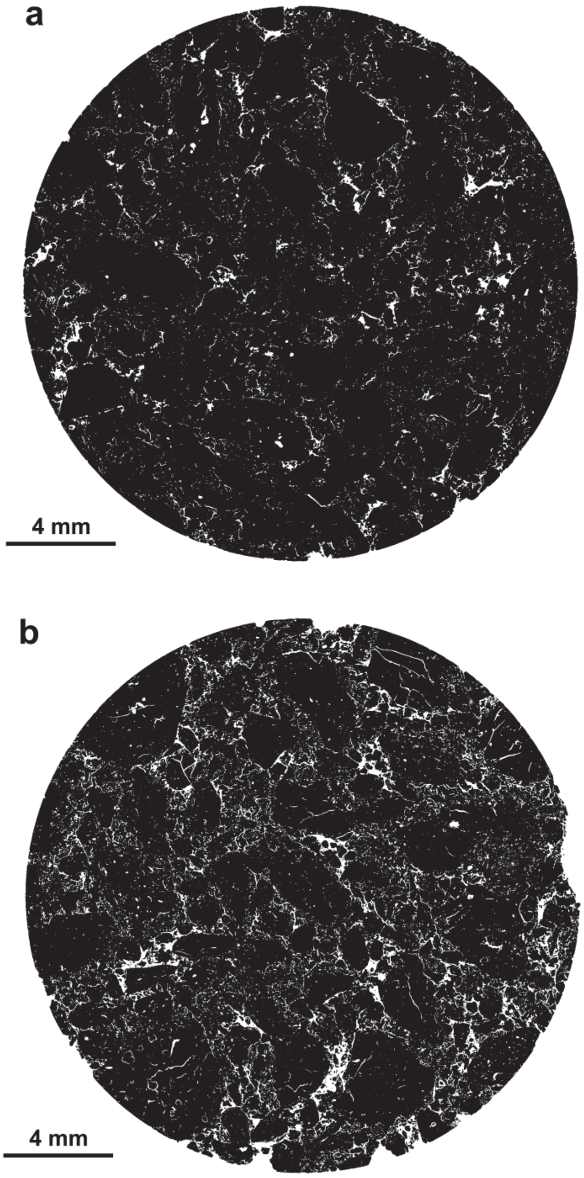

Figure 4.12: CT images from the bottom section of the open furnace at a) the anode side, and b) the flue side. The refractory material is shown in black and the pores are shown in white.

4.2.3 Deposition of carbon

Images of the samples from the bottom section of the open furnace before and after laboratory heat treatment in air (48 h at 1150 °C), are shown in Figure 4.13. The same cross sections are shown in the images presented in Figures 3.2 and 3.3, where the discoloring of the regions closest to the anode side is clearly visible.

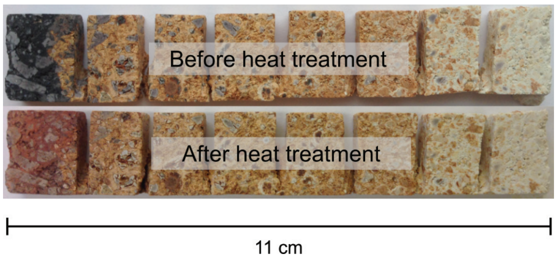

Figure 4.13: Image of sectioned samples from the bottom section in the open furnace, before (top) and after (bottom) heat treatment in air for 48 h at 1150 °C.

The blackening of the lining, present close to the anode side prior to the heat treatment, is gone post heat treatment. The refractory material has become red

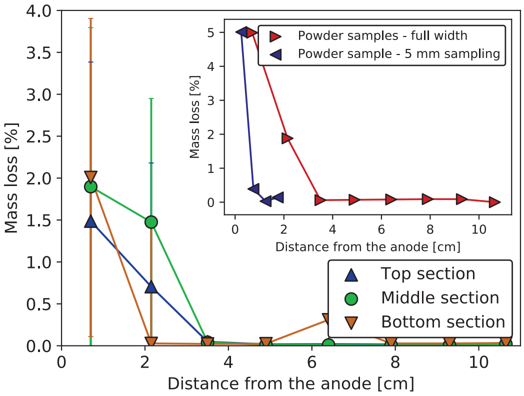

Figure 4.14: Mass loss of samples from the open furnace after heat treatment in air for 48 h at 1150 °C. The figure shows cubic shaped samples from all heights, averaged over six data sets with the corresponding standard deviation. The cubic shaped samples are similar to the samples shown in Figure 4.13. Insert: mass loss of powder samples.

in the same region. Iron is present in the lining, and the color of iron oxide is very dependent on the oxidation state of iron, where FeO is black and Fe_2O_3 is red. The variation in chemical conditions (reducing in the pit and oxidizing during heat treatment) can thus have an effect on the reduction potential of iron and hence explain some of the color changes shown in Figure 4.13. The weight loss of various samples from the open furnace is presented in Figure 4.14. The data plotted in the figure is the dry weight measured during the determination of density and open porosity, before and after heat treatment. The mass loss is considerable for the outermost sample, i.e. the sample closest to the anode side. For the samples 1-2 cm into the material, the mass loss is reduced, before diminishing almost completely further into the lining. Heat treatment in air causes the removal of blackening and a significant weight loss close to the anode side. In Figure 4.15, X-ray diffraction patterns of two refractory samples are compared to a coke sample. The relative carbon content is clearly higher in the 3 mm thick sample, while the content of cristobalite and mullite is almost the same. A reduction in thickness of the refractory sample increases the relative carbon content significantly, demonstrating that the deposited carbon originates from the anode pit environment.

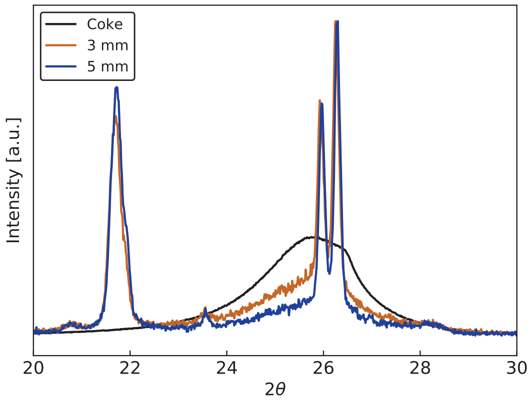

Figure 4.15: X-ray diffraction patterns of two refractory samples from the bottom section of the open furnace. The samples are 3 mm and 5 mm thick and compared to the X-ray diffraction pattern of a coke sample. The thinner refractory sample has a higher relative carbon content compared to the thicker sample.

4.2.4 Depletion and deposition of SiO_2

A sample from the bottom layer of the open furnaces is presented in Figure 4.16, showing a part of the lining facing the anode pit atmosphere. The figure shows the characteristic wear pattern with a needle-like microstructure. A larger part of the same sample is shown in Figure 4.17e. The wear pattern is mainly observed in grains facing the anode pit directly or in the vicinity of open porosity. The reaction layer vary in width, often depending on the distance from the anode pit. Close to the pit the layer is at its thickest, up to 300 μm in some regions. The thickness is reduced further into the brick's surface. A broader overview of the wear patterns in the middle and bottom section is found in Appendix B.

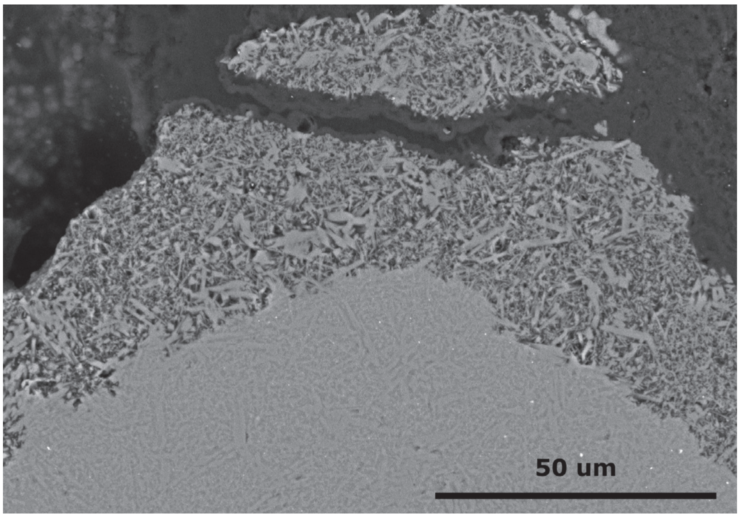

Figure 4.16: SEM image showing the microstructure of a sample from the bottom section of the open furnace, with the pit facing surface pointing upwards in the figure. The needle-like microstructure is typical for the wear pattern found in the baking furnace. Reprinted from Brandvik *et al.* [144] with permission from Springer.

The relative distribution of silicon, aluminium and oxygen close to the surface facing the anodes is shown in Figure 4.17. The intensity of the colors corresponds to the amount of an element in a given region. It it is clear that the content of silicon is significantly reduced in the reaction layer, compared to the interior region in the lower part of each image. Aluminium, on the other hand,

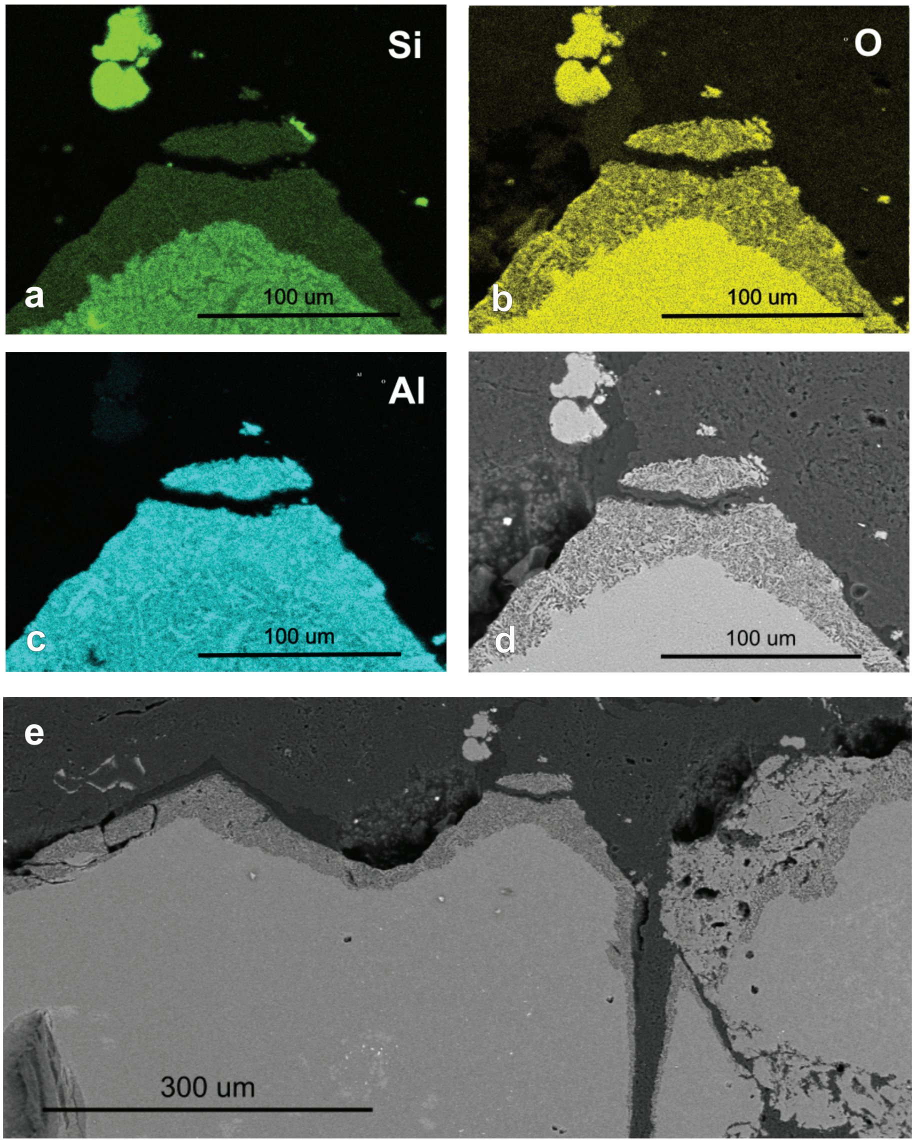

Figure 4.17: SEM image showing the microstructure of the sample from the bottom section of the open furnace. Subfigures a, b and c show the distribution of silicon, oxygen and aluminium in the sample. The intensity of the colors corresponds to the relative amount of an element in the sample. The subfigures d and e show the microstructure and the distribution of the reaction layer.

is uniformly distributed over the whole sample, with no clear variation in content across the boundary between the to regions. Hence, it is only silicon which is removed from the lining in the reaction layer, while the aluminium is not affected by the operational condition in the furnace. This wear patterns are mainly, but not exclusively, found in the middle and bottom sections of the open furnace. There are some observations of the same wear patterns in the top section of the furnace also, but not to the same extent as for the middle and bottom sections.

The elemental distribution in a sample from the top section in the open furnace is presented in Figure 4.18. The interior of the refractory material is shown in the bottom of each image, evident from the higher alumina content. This is the pit facing surface of the lining, which is covered by a cluster of particles with high silica content. In the middle section of the open furnace, both silica depletion and deposition is observed. The elemental distribution is shown for a sample from the middle section in Figure 4.19, where silicon and aluminium is shown with a yellow and purple color, respectively. Three regions are marked in Figure 4.19, and the measured chemical composition in these regions are presented in Table 4.2, demonstrating the deposition of silica rich phases. In other parts of the middle section, silica depletion is observed as shown in Figure B.4.

From Figure 4.18, it becomes clear that the characteristic wear pattern found in the middle and bottom section of the open furnace, are not the dominating pattern in the top section. The changes observed are mostly consisting of deposition of particles with a high silica content. The wear patterns and the depletion of silica, are however also observed in the top section, but not to the same extent as in the lower sections.

The microstructural changes observed in the open furnace are also found in the closed furnace. Both the chemical wear and deposition of silica are observed, but with some distinct differences. First, the chemically etched regions with the needle-like microstructure are not found as continuous layers as in the open furnace. Instead, the chemical wear is found as localized regions, usually close to the anode facing surface or open porosity. The wear is also found at all sampling heights, and not mainly in the middle and bottom sections as was the case in the open furnace.

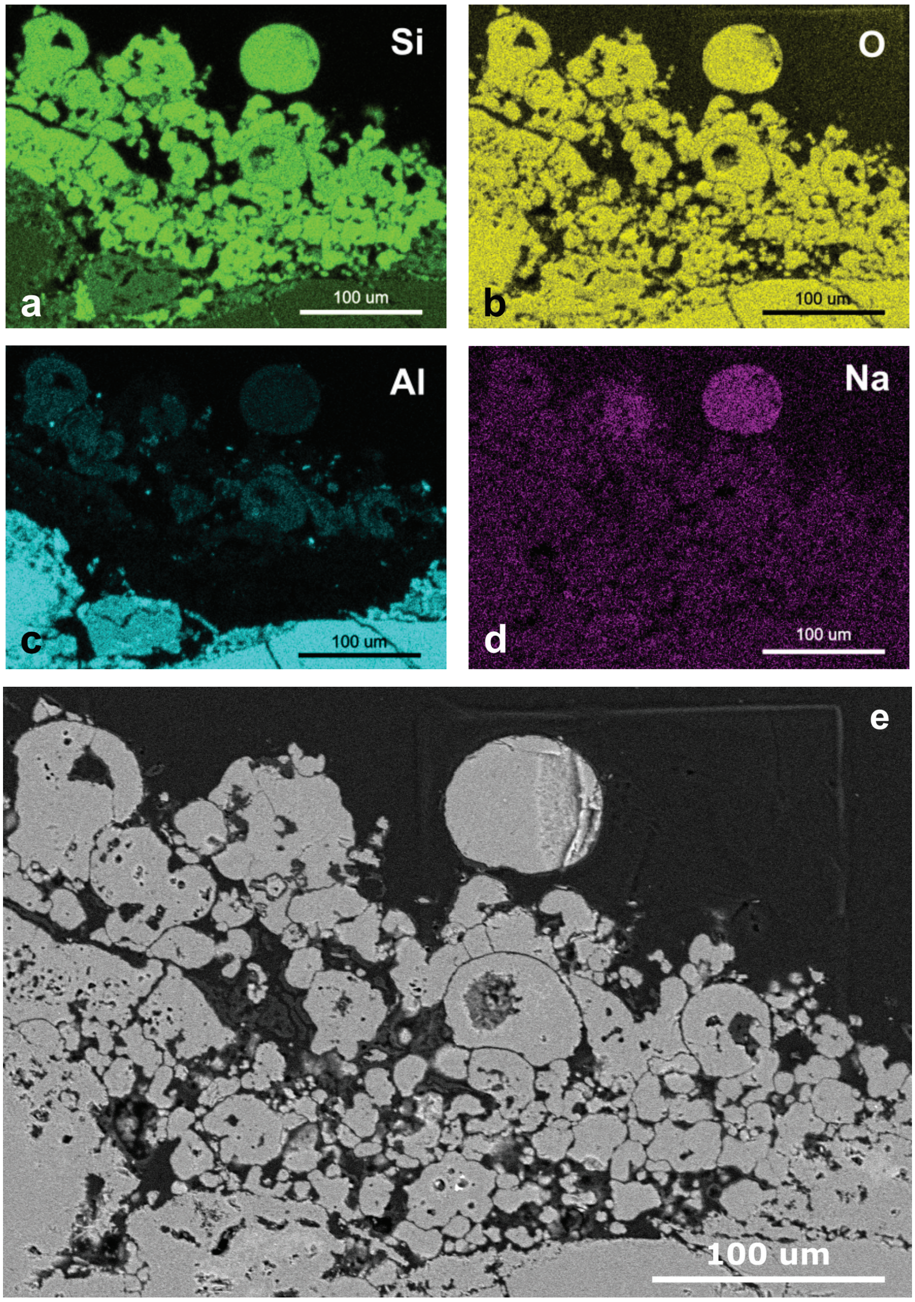

Figure 4.18: SEM image showing the microstructure of the sample from the top section of the open furnace. Subfigures a to d show the distribution of silicon, oxygen, aluminium and sodium in the sample. The intensity of the colors corresponds to the relative amount of an element in the sample. Subfigure e shows the microstructure.

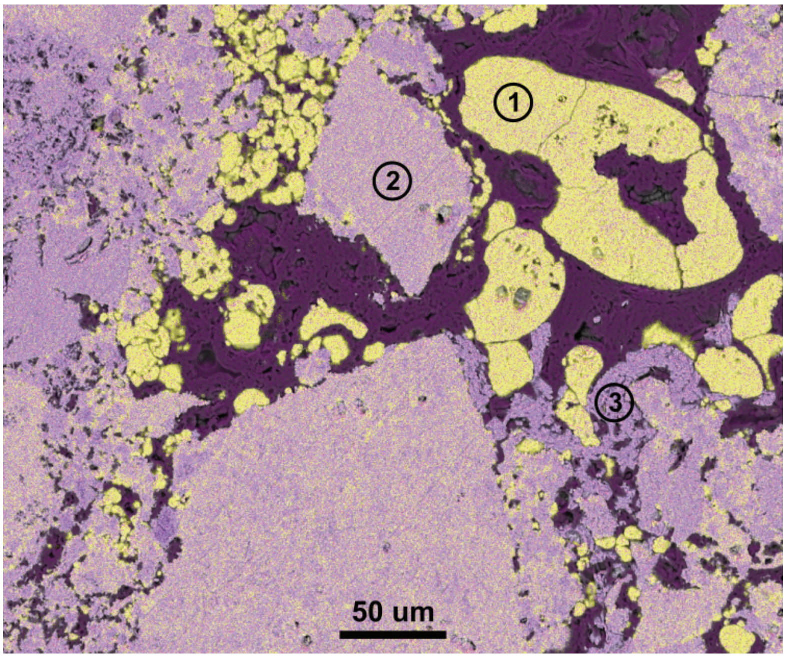

Figure 4.19: Elemental distribution in the sample from the anode facing region of the middle section in the open furnace. The yellow color indicates silicon and the purple color indicates aluminium. The chemical composition measured at region 1-3 is given in Table 4.2. Reprinted from Brandvik *et al.* [47] with permission from Wiley.

Table 4.2: Elemental distribution (mol%) in the regions marked in Figure 4.19.

Region	Al	Si	O	Na
1	6.1	30	63	0.5
2	22	17	61	-
3	33	8	59	-

The deposition of near-spherical particles with high silica content were also observed in the closed furnace. The systematic variations that were observed in the open furnace are not equally distinct in the closed furnace. Both the chemical wear and silicon deposition were observed all over the wall without any clear correlation with the vertical position in the wall. The wear patterns observed in the closed furnace are however less pronounced compared to the open furnace, possibly reflecting the different number of baking cycles experienced by the two walls.

4.2.5 Particle precipitates

A sample from the top section of Part A from the closed furnace is shown in Figure 4.20. The regions close to the anode side or in the vicinity of open porosity are covered with particles with a lighter contrast compared to the surrounding phase. The average chemical composition of the phase found in these particles is presented in Table 4.3, marked as region 4. The phase has a high content of aluminium, iron, nickel and oxygen, demonstrating a very different composition from the overall refractory lining.

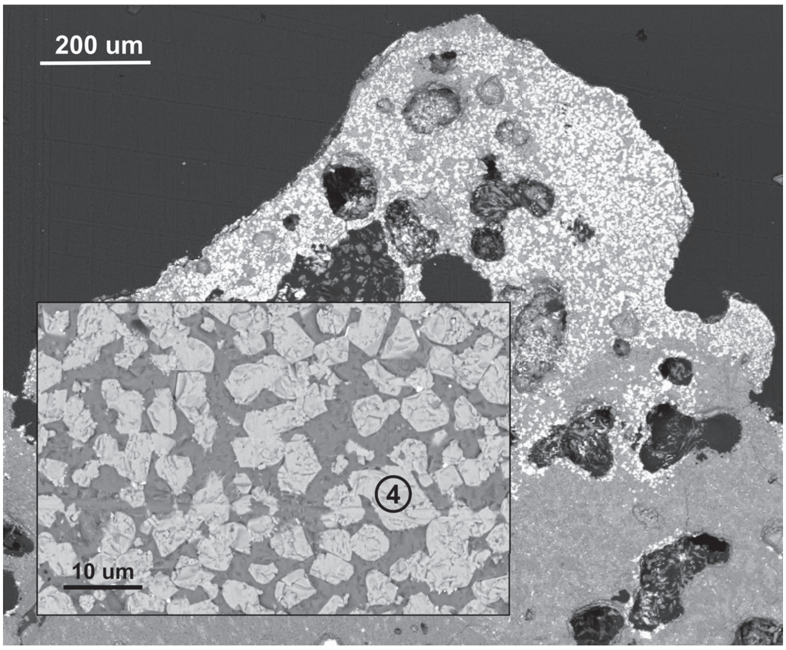

Figure 4.20: SEM image showing the microstructure of sample from the top section from the closed baking furnace, showing a phase with lighter contrast closed to the anode side or open porosity. The average chemical composition measured in region 4 is given in Table 4.3. Reprinted from Brandvik *et al.* [47] with permission from Wiley.

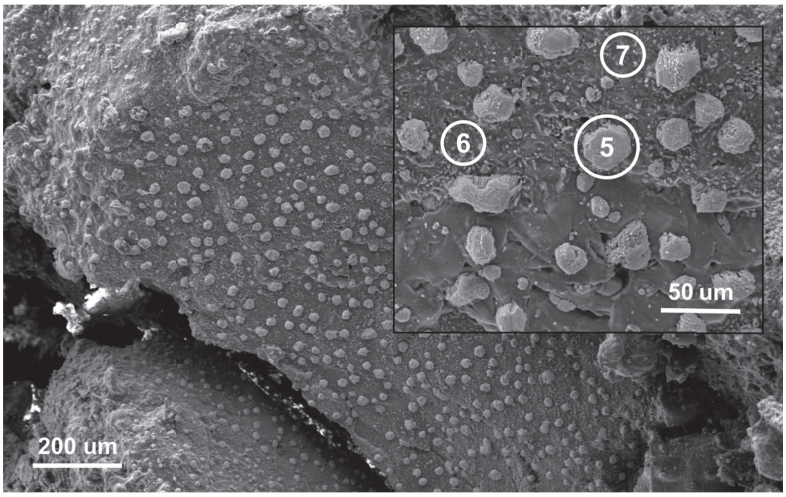

Figure 4.21: SEM image showing the fracture surface from the bottom section of the closed furnace. The average chemical composition measured at regions 5 to 7 is given in Table 4.3. Reprinted from Brandvik *et al.* [47] with permission from Wiley.

In the bottom section of the closed furnace, a fracture in the brick going from the flue side and into the brick was discovered during sampling. The following data are thus from the fracture surface and not from polished cross sectional surfaces as the previous data. Two characteristic features were observed on the fracture surface with electron microscopy, both presented in Figures 4.21 and 4.22. In Figure 4.21, a part of the surface is shown, being completely covered with particles. The chemical composition of the particles marked as region 5 and found in

Table 4.3: Elemental distribution (mol%) in the regions marked in Figures 4.20 to 4.22.

Region	Al	Si	O	Na	Mg	Fe	Ni	Zn
4	19	0.2	54	1.6	3.4	14	6.6	0
5	1.9	0.6	57	0.8	0.2	36	0.1	2.0
6	0.8	34	64	0.2	-	0.1	0.1	0.3
7	27	9.0	63	0.5	0.3	0.7	0.1	0.4
8	0.8	34	64	0.2	-	-	-	0.3
9	1.9	1.4	64	0.7	-	31	-	1.2

Table 4.3, demonstrating a high and stable content of iron and oxygen. Region 6 and 7 reflect the chemical composition of the background material, where one is mostly silicon and oxygen, and the other an aluminosilicate phase. A broader overview of the distribution of particles is found in Appendix B.

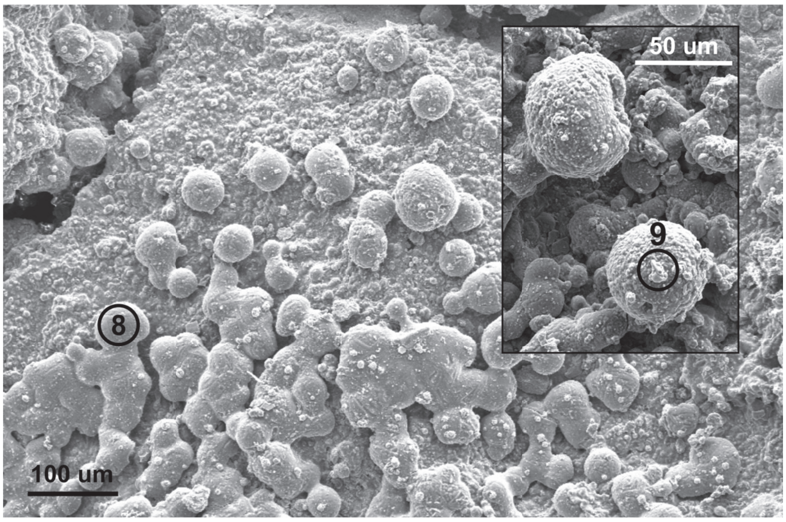

Figure 4.22: SEM image showing the fracture surface from the bottom section of the closed furnace. The average chemical composition measured at regions 8 and 9 is given in Table 4.3. Reprinted from Brandvik *et al.* [47] with permission from Wiley.

Another part of the same fracture surface is shown in Figure 4.22, with the corresponding chemical composition presented in Table 4.3. Here, particles of almost only silicon and oxygen were observed. The morphology of these particles were near-spherical, as observed for the silica particles found in the open furnace. On top of these silica particles, some smaller particles consisting mostly of iron and oxygen were observed. The iron particles seems to have grown on top of the silica particles. All these particles were observed in great amounts close to the anode side, while becoming less frequent and smaller in size when moving away from the anode side and into the interior of the cracked brick. The fracture was found in the brick prior to sampling startup, demonstrating that the fracture occurred during baking and that the surface have been exposed to the pit atmosphere present during baking. It is therefore reasonable to suggest that the anode pit atmosphere would have an impact on the formation of these particles.

4.2.6 Sodium content in spent refractory lining

The region of a bottom sample from the open furnace facing the anode side is presented in Figure 4.23. In this figure there is an atomic contrast between the outer region (lighter) and the inner region (darker). The average chemical composition in these two regions is presented in Table 4.4, demonstrating a higher content of alkali metals in the lighter phase closer to the anode side. The content of sodium in the spent lining is, however, in general not very high. Both from X-ray diffraction and microstructural investigations, no significant amounts of amorphous phases was detected in any of the refractory walls after

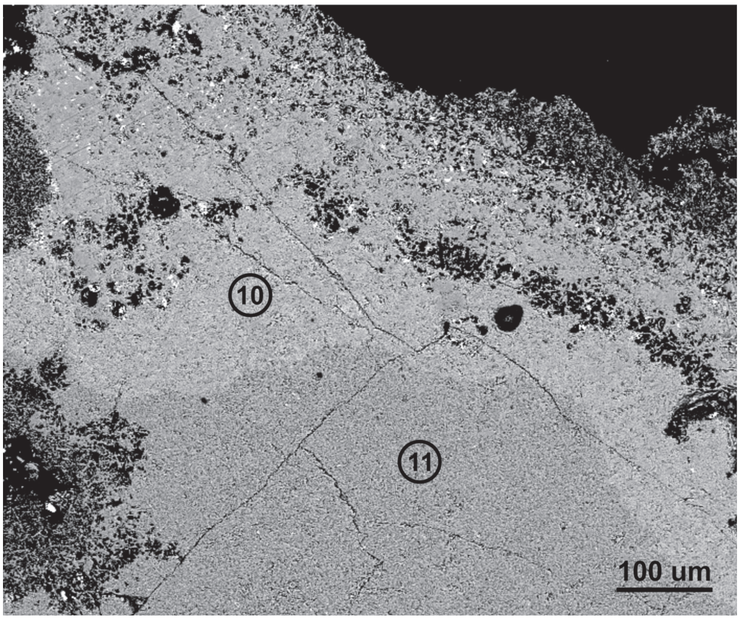

Figure 4.23: SEM image showing the anode facing region of a bottom sample from the open furnace. The atomic contrast show the difference between the outer region (lighter) and the inner region (darker). The average chemical composition measured at regions 10 and 11 is given in Table 4.4. Reprinted from Brandvik *et al.* [47] with permission from Wiley.

operation. Neither was any crystalline phases with sodium measured in significant amounts. These observations demonstrate that the formation of sodium aluminosilicates has not taken place to a large extent. The overall sodium content is however low in both regions, which corresponds well with a low content of amorphous phase. The elemental investigations did also not give evidence for significant concentration of fluorine ions in any of the autopsy samples. Previous investigations of materials from similar furnaces have often reported a glassy layer with a high sodium content in the anode facing parts of the walls [9, 53]. This is however not observed in any of the samples analyzed in this work.

Table 4.4: Elemental distribution (mol%) in the regions marked in Figure 4.23.

Region	Al	Si	O	Na	K	Ca	Mg	Ti
10	20	17	61	0.8	0.5	0.2	0.4	0.7
11	20	17	62	0.2	0.1	0.6	0.3	0.5

4.3 Discussion

4.3.1 Densification mechanism

The variation in density and open porosity observed in the spent lining, demonstrates significant changes in the refractory lining caused by years in operation. The increase in density is accompanied by a reduction in open porosity and dimensional changes of the bricks. This is illustrated by the deformation observed for the lining from the open furnace shown in Figure 4.24, where the brick is bent towards the anode side. Refractory materials are designed and manufactured to operate at high temperature conditions while at the same time maintaining dimensional stability by mitigation of high temperature sintering and densification. A prerequisite for densification of polycrystalline ceramics is a mechanism for material transport, in addition to a driving force for that mechanism to occur [145]. During manufacturing, the refractory materials are heat treated at 1300 °C to 1500 °C, removing a lot of those driving forces and hence reducing the tendency for further densification in service. Combined with the heterogeneous nature of the microstructure, this result in slow sintering kinetics and high structural stability, crucial for refractory materials. By this argument, it is not likely that high temperature alone could account for the observed variation in density in the spent refractory lining.

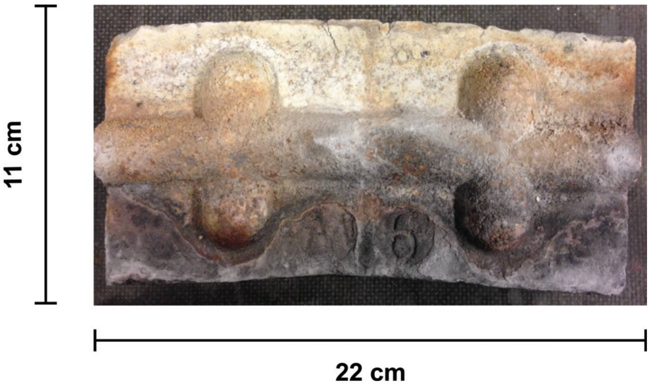

Figure 4.24: Image of a sample from the bottom section of the open furnace. The sample is bent towards the anode side (the lower, black side). The bending corresponds with the increase in density at the anode.

The variation in density and open porosity presented in Section 4.2.2 are highly non-uniform, and converging towards the pristine levels at the flue side. This demonstrates that the high service temperature is, indeed, not enough to change the density and open porosity of the material. The chemical conditions in the flue channel is comparable to the conditions during manufacturing of the lining, and is thus not affecting structural stability of the material. On the anode side, there is a definitive increase in density and reduction in open porosity. Based on the above mentioned arguments, the service temperature alone is not enough to induce such changes, opening the question to what could be the origin of the observed variations in density and open porosity on the anode side. Investigations of high temperature properties in mullite based refractories show that viscous flow by grain boundary sliding is a probable mechanism [82, 146–149]. Refractories with a high content of mullite is shown to contain a small amount of amorphous phase. The content is often too low for detection by X-ray diffraction experiments, and usually found evenly distributed along the grain boundaries in the material [82, 146–149]. When exposed to an external force at high temperature, the amorphous phase softens and gives in to the stress, causing the grains to slide relative to each other. This enables the grains in the material to reorient in a more compact manner. The CT data presented in Figures 4.11 and 4.12 show that the majority of the reduction in porosity is found in the binder matrix. This is the region with the smallest grains and pores, with a higher tendency for reorientation and densification compared to the larger grains.

There is a significant increase in density at the anode side compared to the almost unaffected material on the flue side. The refractory material separating the two sides, see Figure 3.3, is hence exposed to a significantly different chemical environment on the two sides. The question is how the chemical conditions on the anode side is affecting the lining. The two most probable mechanisms are either the diffusion of gaseous species (e.g. NaF or $NaAlF_4$) which react with the lining within the open porosity, or the direct effect of the pit atmosphere on the lining. First, the presence of glass modifiers (e.g. Na, K or Ca) would significantly increase the sintering kinetics of the aluminosilicate refractory material. Sodium is especially interesting, due to its introduction in the pit through the use of anode butts as green anode raw materials. In the literature, there is a general agreement that gaseous sodium containing fluorides are important factors in the degradation of refractory lining in anode baking furnaces [9, 89, 97, 105, 108, 150, 151]. The investigations in this work generally showed a low content of sodium, while no traces of fluorides were observed. However, elevated sodium levels were observed in regions close to the anode facing surface, as shown in Figure 4.23 and Table 4.4. If the sodium fluorides is part of a mechanism causing reduction in porosity in the lining, a clear correlation between sodium content and variation in porosity would be expected. This is not observed. The regions with elevated sodium content is mostly located to the outer parts of the refractory ($< 500\,\mu$m), closest to the anode pit or close to open porosity. The observed reduction in porosity in the open furnace is however ranging across most of the brick's cross section ($\sim$11 cm) as presented in Figure 4.8. The investigation of spent lining has not found any correlations between the sodium content and the reduction in porosity. Based on the present data, it is clearly demonstrated that the effect of sodium containing fluorides on the mechanism for reduction in porosity is negligible in the wall investigated here.

The second factor potentially affecting the lining is the pit atmosphere with particular importance of the variation from the anode side to the flue side. At the flue side, the combustion of fuel show that the atmosphere must be fairly oxidizing, i.e. having a relative high content of oxygen. The atmosphere in the anode pit, on the other hand, is shown to be more reducing, as discussed in Chapter 5. The chemical effect of the reducing pit atmosphere on the lining is thus of great interest. Investigations of perovskite stability in reducing media have shown that both non-stoichiometry (oxygen deficiency) and decomposition are occurring when the oxygen pressure becomes low enough [133, 134]. Coal ash slags are reported to show a reduction in viscosity for decreasing partial pressures of oxygen [131, 132], and it is also reported that creep in yttria doped ceria is increasing with decreasing oxygen partial pressure [135]. It is therefore suggested that reducing atmosphere is destabilizing the lining and increasing the densification rate at the anode side, resulting in the observed reduction in open porosity. The difference in color shown in Figure 4.13 is illustrating the effect of reducing and oxidizing atmosphere, and is proposed to give support for this hypothesis.

The non-uniformity of the density variations is not limited to the distance from the anode, but also affected by the vertical position. The increase in density is significantly more pronounced in the bottom section compared to the top section. The bricks in the flue wall are exposed to the gravimetric load of all the overlaying bricks, which is increasing from the top towards the bottom. The combination of high temperature and external stress would cause the refractory lining to creep by viscous flow, resulting in deformation of the brick after years in operation. Since the gravimetric loads are quite modest (0.025 MPa to 0.1 MPa) and the creep rate itself is very low, time becomes an important factor, which may result in a significant creep after years in operation. This results in a compaction process similar to hot pressing, only with lower loads and considerable longer duration. Further discussion of the creep mechanism is found in Chapter 6.

The measured densification of the spent lining is less pronounced after the laboratory heat treatment in air at 1150 °C for 48 h (Figures 4.7 and 4.8). During the heat treatment, deposited carbon in the open porosity would oxidize to CO or CO_2 and be removed from the open porosity of the refractory sample. Deposition of carbon in open porosity could thus partly explain the reduction in porosity measured in the spent lining. During the first part of the baking cycle, coal tar pitch in green anodes becomes thermally unstable and decomposes while forming volatile hydrocarbons [152–156]. Subsequently, the gaseous hydrocarbons are found to crack to form solid carbon [157–162]. The cracking would take place on the solid surfaces in the anode pit, including the open pores in the refractory flue wall. Carbon deposition would fill parts of the open porosity, and hence increase the apparent density of the material. After heat treatment in air, the density is reduced in the regions close to the anode side, due to burn out of deposited carbon. The X-ray diffraction experiments presented in Figure 4.15 show that the relative carbon content of the sample is increasing towards the anode side. Measurements of mass loss from samples after heat treatment in air, as presented in Figure 4.14, are showing the highest mass loss close to the anode side. As the distance from the anode increases, the mass loss declines quickly, and above 2 cm, the mass loss is negligible. These observations corresponds well with literature data on similar samples showing layers of carbon build-up at the refractory flue wall [163]. The combination of X-ray diffraction analysis and the mass loss measurements demonstrate that the carbon deposition is taking place in the open porosity of the lining, and thus being partly responsible for the measured increase in density close to the surface towards the pit.

4.3.2 Assessing the effects of sodium

The regions exposed to the anode pit atmosphere do demonstrate a degree of elevated sodium content, even though the overall level of sodium in the lining is low. The presence of sodium has previously been reported to be a considerable challenge for the refractory lining [9, 89, 97, 105, 108, 150, 151]. Addressing the effects and consequences of the use of butts in green anodes, is from a thermodynamic point of view therefore important.

The use of recycled anode butts as a raw material in anode production gives rise to a potential source of solid electrolyte in the baking furnace. Cryolite constitute the major component of the electrolyte, and pure cryolite can thus be used as a model system for understanding the effect of volatile fluorides in the anode baking furnace. The chemical stability of cryolite is temperature dependent, causing volatile fluorides to evaporate during baking. As the temperature increases, cryolite becomes increasingly destabilized causing it to decompose into NaF and $NaAlF_4$, according to Equation 4.1. In addition, there is a reaction between $NaAlF_4$ and NaF forming $NaAl_2F_5(g)$.

$$Na_3AlF_6(s) = 2\,NaF\,(l) + NaAlF_4(g) \tag{4.1}$$

The equilibrium activities[1] of $NaAlF_4$, $NaAl_2F_5$ and NaF for a system containing pure cryolite are presented in the lower part of Figure 4.25. The onset of fluoride volatility becomes visible at approximately 1050 °C, and the volatility quickly becomes significant as the temperature increases further. The corresponding vapor pressure above an industrial electrolyte is shown in the top part of Figure 4.25. The chemical composition of the industrial electrolyte is 80 wt% cryolite, 11.5 wt% AlF_3, 5 wt% CaF_2 and 3.5 wt% Al_2O_3. When comparing the upper and lower parts of Figure 4.25, it becomes clear that the onset temperature of fluoride volatility is shifted towards lower temperatures for the industrial electrolyte. The overall fluoride activity is also higher for the electrolyte. The important difference between cryolite and the electrolyte is in this context the significantly higher content of AlF_3. The addition of AlF_3 has made the electrolyte more acidic, reducing the liquidus temperature of the electrolyte. The acidity of the electrolyte has a direct effect on the volatility of the fluorides, which is increasing with increasing content of AlF_3. Electrolyte present in the green anodes will thus give rise to the formation of volatile sodium containing fluorides.

Refractory lining and $NaAlF_4$

The thermodynamic stability of the aluminosilicate refractory lining is very dependent on the level of NaF or $NaAlF_4$ in the pit atmosphere. Both fluorides would react with the lining, dramatically changing the phase composition of the flue wall. The following assessment focuses on the chemical reactions oc-

---

[1] The thermodynamic activity is defined as p/p_0, where the standard state is used as reference.

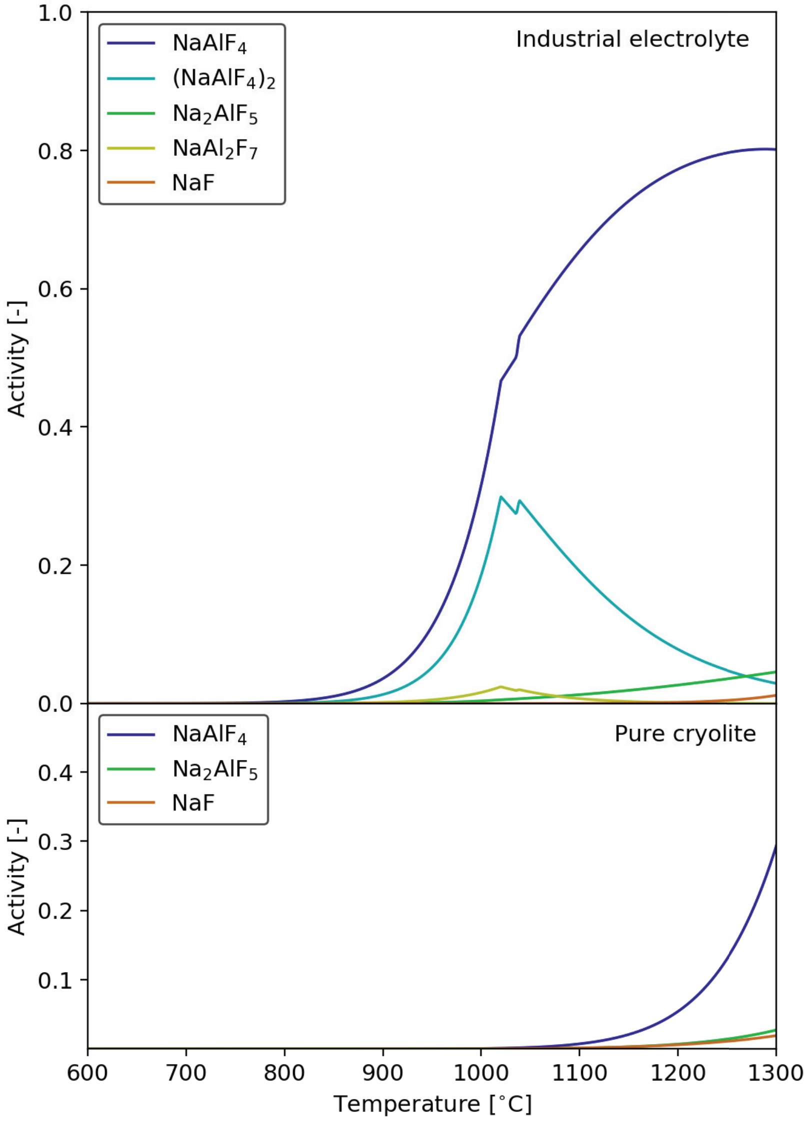

Figure 4.25: Comparison of fluoride volatility in pure cryolite and industrial electrolyte. The industrial electrolyte contains 80 wt% cryolite, 11.5 wt% AlF_3, 5 wt% CaF_2 and 3.5 wt% Al_2O_3. The volatility of fluorides is significantly shifted towards lower temperatures for the industrial electrolyte compared to pure cryolite, in addition to showing higher fluoride activity in general.

curring in the lining under the influence of volatile fluorides originating from the industrial electrolyte. In Figure 4.26, a degradation map of the Al_2O_3 to SiO_2 compositional range for various additions of $NaAlF_4$ at 1300 °C is presented. The diagram shows the thermodynamically stable condensed phases, making it is possible to follow the phase composition for an increasing amount of $NaAlF_4$. The composition along the x-axis (when no $NaAlF_4$ is present) is the 1300 °C isotherm in the binary phase diagram of SiO_2 and Al_2O_3, with mullite ($Al_6Si_2O_{13}$) shown at 40 mol% silica. Below 40 mol% silica, mullite and alumina are co-existent, while mullite and silica are co-existent above 40 mol%. By adding $NaAlF_4$ to the system, one of two sodium aluminosilicate phases is formed, depending on whether the initial composition is above or below 40 mol% silica. At low silica content, i.e. below 40 mol%, $NaAlF_4$ reacts with mullite and forms nepheline ($NaAlSiO_4$), whereas for higher silica contents, albite ($NaAlSi_3O_8$) is formed instead. For a composition above 40 mol%, the

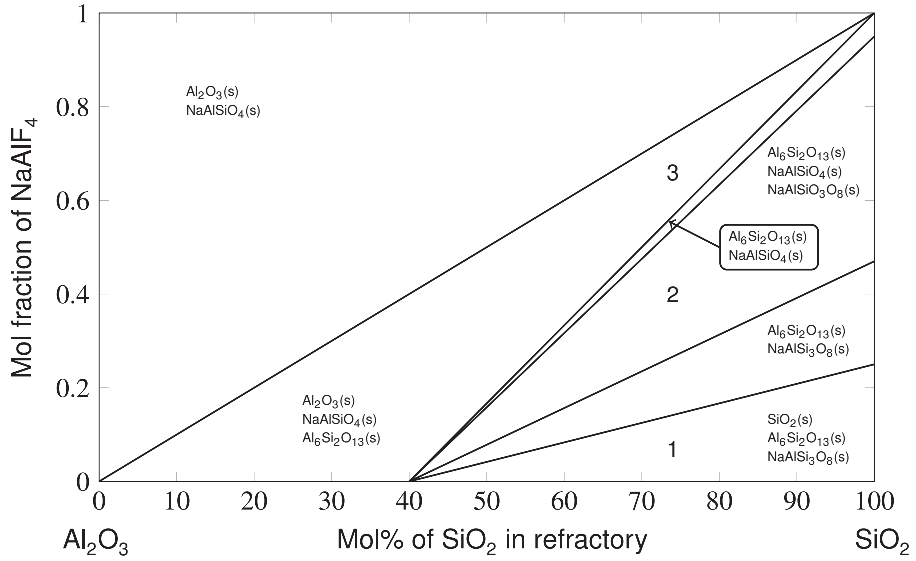

Figure 4.26: Degradation map of the Al_2O_3 to SiO_2 compositional range for an increasing degree of $NaAlF_4$ exposure at 1300 °C. Chemical reactions occurring in the regions indicated by the numbers 1 to 3 are presented in Table 4.5. Reprinted from Brandvik *et al.* [164] with permission from ICSOBA.

reactions occurring for an increasing degree of $NaAlF_4$ exposure, in the regions indicated as 1 to 3, are presented in Table 4.5. In region 1, SiO_2 reacts with $NaAlF_4$ to form albite and SiF_4(g), and will continue to do so until all SiO_2 is consumed. After all SiO_2 is consumed, the next phase to react with $NaAlF_4$ is albite, forming SiF_4(g) and nepheline. In the end, when only alumina, mullite and the reaction products nepheline and albite are left in the solid phase, mullite reacts as shown by region 3 in Table 4.5. Region 3 is also covering the composition with silica content below 40 mol%, and the reaction found for region 3 in Table 4.5 is thus relevant for both cases.

Table 4.5: Chemical reactions occurring during exposure to $NaAlF_4$ at 1300 °C in region 1 to 3, shown in Figure 4.26.

R	Chemical reaction
1	$4\,SiO_2(s) + NaAlF_4(g) = SiF_4(g) + NaAlSi_3O_8(s)$
2	$NaAlSi_3O_8(s) + NaAlF_4(g) = SiF_4(g) + 2\,NaAlSiO_4(s)$
3	$Al_6Si_2O_{13}(s) + NaAlF_4(g) = SiF_4(g) + 3\,Al_2O_3(s) + NaAlSiO_4(s)$

The order of reaction between $NaAlF_4$ and the other reactants, silica, albite and mullite, can thus be determined by Figure 4.26 and Table 4.5. Alumina is found to be co-existent with $NaAlF_4$ at 1300 °C and will therefore not react under these conditions.

Refractory lining and NaF

A degradation map is constructed for the Al_2O_3 to SiO_2 compositional range for various additions of NaF at 1300 °C, and presented in Figure 4.27. This diagram is more complex compared the diagram for $NaAlF_4$, especially for a high exposure of NaF. For moderate levels of NaF, the diagram shows similar behavior as shown for exposure of $NaAlF_4$. For low silica content, mullite and NaF reacts to form nepheline. The reaction path for compositions below 40 mol% silica is indicated with blue numbers in Figure 4.27 and is presented in Table 4.6.

At higher silica levels, exposure NaF causes the formation of albite over nepheline, as illustrated by the reaction path for a composition of 70 mol% silica, indicated by the red numbers in Figure 4.27 and Table 4.7. The main reactions occurring

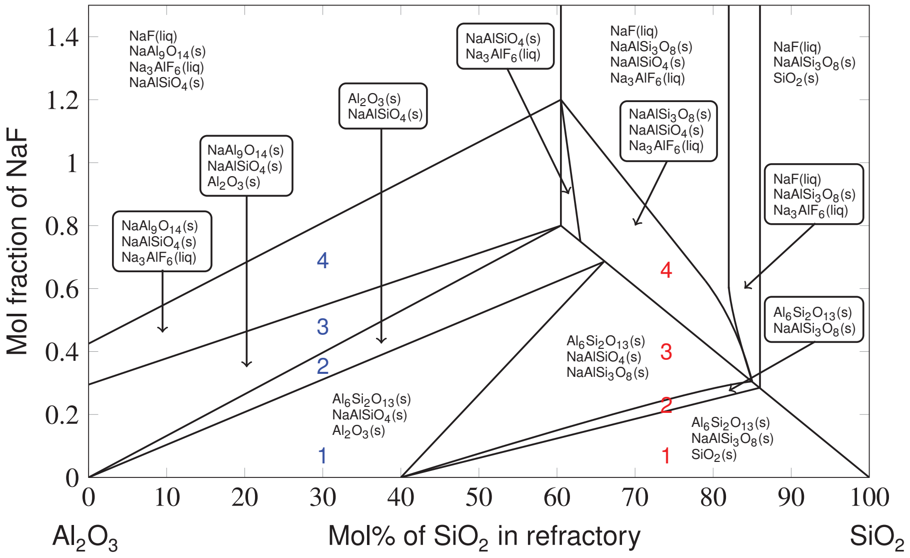

Figure 4.27: Degradation map of the Al_2O_3 to SiO_2 compositional range for a increasing degree of NaF exposure at 1300 °C. The reaction path for compositions below 40 mol% silica is indicated by blue numbers and is presented in Table 4.6. The reaction path for the composition of 70 mol% silica is indicated by red numbers and presented in Table 4.7. Reprinted from Brandvik *et al.* [164] with permission from ICSOBA.

for moderate exposure of NaF are thus similar to the reactions found for exposure of $NaAlF_4$, where nepheline and albite are the main reaction products for low and high silica content, respectively.

Relevance of the assessment to the current work

The assessment has given insight in possible reaction paths between the aluminosilicate refractory lining and sodium containing fluorides originating from the solid electrolyte. Common for all these reaction paths is the formation of sodium aluminosilicate compounds, i.e. nepheline and albite. If the pressures of NaF or $NaAlF_4$ becomes considerable in the pit, the formation of either nepheline or albite is inevitable, according to the thermodynamics. Both compounds are thermodynamically stable in the operational conditions of the baking furnace, and would, once formed, be present in the spent refractory lining after end

Table 4.6: Chemical reactions occurring for compositions below 40 mol% silica during exposure to NaF at 1300 °C as given by the blue numbers in Figure 4.27.

R	Chemical reaction
1	$3\,Al_6Si_2O_{13}(s) + 8\,NaF(g) = 5\,Al_2O_3(s) + 6\,NaAlSiO_4(s) + 2\,NaAlF_4(g)$
2	$4\,Al_2O_3(s) + 8\,NaF(g) + 3\,SiF_4(g) = 3\,NaAlSiO_4(s) + 5\,NaAlF_4(g)$
3	$14\,Al_2O_3(s) + 4\,NaF(g) = 3\,NaAl_9O_{14}(s) + NaAlF_4(g)$
4	$2\,NaF(g) + NaAlF_4(g) = Na_3AlF_6(liq)$

of service. Neither albite nor nepheline were detected by the X-ray diffraction analysis, and the general sodium content from the SEM and EDS analysis is low. These observation are in strong contrast to reported sodium levels from similar works in the literature [9, 89, 97, 105, 108, 150, 151]. Based on the results from the autopsies it can be concluded that the level of volatile sodium containing fluorides in the anode pit has been very low during the operation of the two anode baking furnaces investigated in this work.

Table 4.7: Chemical reactions occurring for the composition of 70 mol% silica during exposure to NaF at 1300 °C as given by the red numbers in Figure 4.27.

R	Chemical reaction
1	$2\,Al_6Si_2O_{13}(s) + 35\,SiO_2(s) + 12\,NaF(g) = 12\,NaAlSi_3O_8(s) + 3\,SiF_4(g)$
2	$8\,Al_6Si_2O_{13}(s) + 48\,NaF(g) + 23\,SiF_4(g) = 35\,NaAlF_4(g) + 13\,NaAlSi_3O_8(s)$
3	$4\,Al_6Si_2O_{13}(s) + 24\,NaF(g) + 5\,SiF_4(g) = 11\,NaAlF_4(g) + 13\,NaAlSiO_4(s)$ $NaAlSi_3O_8(s) + NaAlF_4(g) = 2\,NaAlSiO_4(s) + SiF_4(g)$
4	$2\,NaAlSiO_4(s) + SiF_4(g) = NaAlSi_3O_8(s) + NaAlF_4(g)$ $2\,NaF(g) + NaAlF_4(g) = Na_3AlF_6(liq)$

4.3.3 Transport of SiO_2

Studies in the literature are mainly supporting two reaction schemes for the main causes of variation in silicon oxide content in spent refractory lining. These are either a reaction with gaseous sodium containing fluorides, or a reaction caused by high temperature and reducing atmosphere [9, 53, 89, 105, 144, 150, 151, 164]. As discussed previously, the lack of amorphous phases and sodium aluminosilicates in the spent lining disregards any major role of the gaseous sodium containing fluorides in the current observations. The reducing atmosphere may on the other hand give an explanation for the observed behavior of SiO_2 in the furnaces. Various works propose that a low partial pressure of oxygen, combined with the presence of compounds like CO, CH_4 or H_2, at elevated temperatures may have a destabilizing effect on the refractory lining [9, 53, 105]. Silica based ceramics exposed to a chemically reducing environment at sufficiently high temperature, are shown to favor the formation of gaseous SiO [165–170]. In the present work, reaction layers depleted of silica were mainly observed in the middle and bottom of the open furnace. If silica is to be removed from the lining by the formation of SiO, the surrounding conditions must favor sufficiently high partial pressures of SiO over the aluminosilicate lining. The material system describing the local conditions at the anode facing part of the lining consists of solid carbon and silica, in addition to gaseous CO, CO_2, O_2 and SiO, where the partial pressures of the four compounds are all dependent on each other and the temperature. The material system can be described by the chemical equilibria shown in Equations 4.2 to 4.4.

$$2\,\mathrm{CO}\,(g) = \mathrm{C}\,(s) + \mathrm{CO_2}(g) \tag{4.2}$$

$$2\,\mathrm{CO_2}(g) = 2\,\mathrm{CO}\,(g) + \mathrm{O_2}(g) \tag{4.3}$$

$$2\,\mathrm{SiO_2}(s) = 2\,\mathrm{SiO}\,(g) + \mathrm{O_2}(g) \tag{4.4}$$

By applying Gibbs' phase rule, the number of degrees of freedom at isothermal conditions becomes 1 for the given material system. This means that by fixing one of the partial pressures, it is possible to calculate the equilibrium partial pressures of the remaining compounds. The relations between the partial pressures presented in Equations 4.2 to 4.4 are shown in Figure 4.28. The top part of Figure 4.28 shows the equilibrium pressures of CO and CO_2 when solid car-

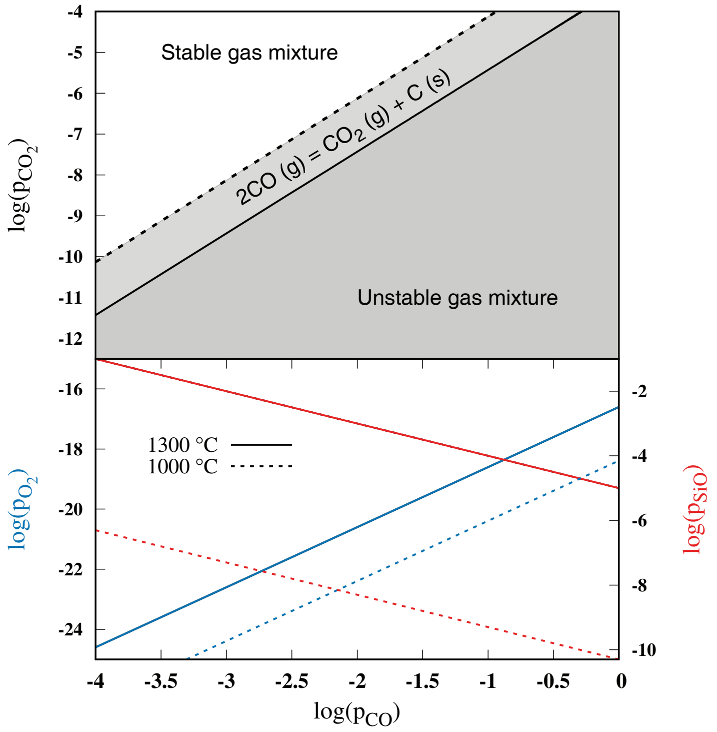

Figure 4.28: Partial pressures of CO_2, O_2 and SiO plotted for 1000 °C and 1300 °C as function of p_{CO}. Pressures for 1000 °C and 1300 °C are plotted with dotted and solid lines, respectively. The upper part of the figure shows the relation between CO and CO_2, governed by the Boudouard reaction in Equation 4.2. The lower part of the figure shows the pressures of O_2 and SiO. Reprinted from Brandvik *et al.* [47] with permission from Wiley.

bon is present. The dotted and solid lines correspond to pressures calculated for 1000 °C and 1300 °C, respectively. As long as the system is in equilibrium, the partial pressures of CO and CO_2 are dependent of each other and their equilibrium ratio is fixed as shown by the line in the top part of Figure 4.28. By changing the pressure of either gas specie and moving into the gray region, the system will no longer be in equilibrium and the gas mixture will become unstable and solid carbon is precipitated. The partial pressures of O_2 and SiO are calculated from Equations 4.3 and 4.4 and plotted in the lower part of Figure 4.28 as a function of CO partial pressure. The figure shows that as the partial pressure of oxygen is reduced, the partial pressure of SiO increases. At very low partial pressures of oxygen, the partial pressures of SiO at 1300 °C is sufficiently high to expect some volatility of SiO. Even at 1000 °C the volatility is significant at low partial pressures of oxygen, and with a maximum measured pit temperature between 1100 °C and 1200 °C, the temperature in the furnace should be sufficient for the formation of SiO and transport of SiO_2.

In the bottom of the open furnace, the oxygen level is expected to be low. The conditions in the bottom section would thus favor volatility of SiO, corresponding to the observed depletion of silica in this part of the furnace. The precipitation of near-spherical silica particles in the top section of the open furnace demonstrate a different chemical environment in this part of the furnace. The qualitative different observations in the top and bottom of the furnace suggest a transport of SiO from the bottom to the top of the furnace, where a re-oxidation of SiO into SiO_2 would occur. In the open furnace, the reduced pressure in the flue wall and the pit causes air to enter during baking. To avoid direct contact between oxygen in the air and the carbon anodes, the anodes are covered with a layer of packing coke. As the air is entering the furnace, oxygen is reacting with the packing coke before reaching the anodes, and thus avoiding anode air burn. The reaction between the coke and oxygen is probably not ensuring complete removal of oxygen, resulting in a potentially higher partial pressure of oxygen in the top section compared to the rest of the furnace. By having a higher partial pressure of oxygen in the top section, the corresponding equilibrium pressure of SiO would be reduced, as shown in Figure 4.28. Consequently, the re-oxidation of SiO into SiO_2 would occur, resulting in precipitation of solid SiO_2. The thermodynamic analysis of the material system described by Equations 4.2 to 4.4 demonstrate that it is possible to have volatilization of silica in the lower part of the furnace and a re-oxidation in the top part, as long as a significant difference in partial pressure of oxygen is present. The main trend in the open furnace, was the observation of silica depletion in the lower parts of the furnace and silica deposition in the top part. Both phenomena were however been observed in some regions, demonstrating that there are conditions locally that could favor both reactions. This has also been reported in similar investigations, where both silica depletion and re-oxidation are observed in the same region [163]. The volatilization of silica is very temperature dependent, and the local conditions would change drastically as the temperature changes during the baking cycle. The cyclically varying temperature is thus an important factor in the silica volatilization process, causing both silica depletion and re-oxidation to occur in the same region of the furnace.

Similar observations of silica depletion and re-oxidation were also reported for the closed furnace. The trend is however not as clear with respect to position in the furnace as for the open furnace. Both the depletion and the re-oxidation is found at all sampling heights in this furnace. This relates to the difference in furnace design between the open and closed furnace. In the closed furnace, the pit is covered with section covers, under which some of the burners are mounted. The surrounding atmosphere above anodes in the closed furnace is very different from the open furnace, both due to the combustion of fuel and due to the reduced inflow of air. The reduced pressure down in the pit in the closed furnace would also be less than in the open furnace. In total, the oxygen gradient expected to be present in the open furnace should not be found in the closed furnace. This corresponds well with the lack of systematic trend in the observations of silica depletion and re-oxidation, indicating that the local conditions favor both depletion and re-oxidation, and that a transport of silica occurs on a more localized scale.

4.3.4 Particle precipitates

The particles presented in Figure 4.20 have a distinctly different chemical composition compared to the aluminosilicate phases in the lining. A strong elemental contrast shown in the back scatter imaging demonstrate the presence of heavier elements in the particles with lighter contrast compared to the darker surrounding bulk lining. This is confirmed by the elemental analysis presented in Table 4.3. Here, the high content of iron and nickel is especially striking, and it is difficult to rationalize the high content of metal cations by the lining's nominal chemical composition. The pristine refractory materials contain approximately 1 wt% Fe_2O_3 while nickel was not detected by the XRF analysis, as shown in Table 4.1. It is therefore less likely that the metal cations in the spent lining originate from the metal impurities found in the pristine refractory material. Both the packing coke, the carbon anodes and the fuel could be sources of the metal cations observed in the spent lining. No further studies were however carried out to verify this suggestion. In addition to the polished surfaces, fracture surfaces from the closed furnace are shown in Figures 4.21 and 4.22. Particles with a high iron content are covering the fracture surfaces. The highest density of such particles is found close to the anode side, and the density is clearly reduced when going away from the pit, and into the crack towards the flue side. This observation supports the suggestion of the pit gas atmosphere having a role in the precipitation of these particles. Observation of similar particles with high iron content have been reported in the literature [108]. In this work, the iron containing particles were found in both the open and closed furnace, suggesting that the furnace design is of less importance for the formation process, even though the present work only found such particles in the closed furnace. Volatilization of iron by the formation of iron hydroxide could be a potential carrier mechanism [171, 172]. Detailed investigations are needed to further determine the origin and transport mechanism of the metal constituents. Such studies are however beyond the scope of this work, and has not been carried out.

4.3.5 Importance of furnace design and flow pattern

The observed depletion and deposition of silica were to a large extent found in a systematic manner with respect to the vertical position in the open furnace. In the bottom and middle sections of the furnace, uniform layers of chemical wear was observed, as shown in Figure 4.17. In the top section, silica was found as deposited particles on the side of the lining facing the anode pit, Figure 4.18. Similar observations were found in the closed furnace, though not as systematic as for the open furnace. First, there was no clear trend with respect to vertical position in the wall. In the closed furnace, both the depletion and deposition were observed at all sampling heights. Second, the depletion of silica was not found as uniform layers covering larger parts of the lining surface, but in more localized regions at the anode facing surface or in open porosity. A combination of high temperature and reducing atmosphere resulting in transport of silica is discussed in the previous sections. When it comes to the effect of pit gas atmosphere on the silica volatility, the flow pattern of the flue gas plays an important role. The differences in design of the open and closed furnaces are determining how the flue gas flows, as shown in Figure 2.2. In the open furnace, the flue gas is flowing inside the flue wall and is never in direct contact with the anode side of the lining. The section covers in the closed furnace enables the flue gas to be released underneath the cover before being transported further into the next flue wall. There are two main factors that drive the transport of flue gas inside the furnace during baking. The pressure difference across the flue wall ensures a transport of gas from the anode pit through the flue wall and into the flue channels. This is mainly occurring in the open furnace, and is an important way to transport pitch volatiles from the anode pit to the flue channel for combustion. In the closed furnace, there is a reduced pressure above the anodes and underneath the section cover, compared to the pressure down in the anode pit. This pressure difference would cause a larger degree of vertical transport compared to the open furnace design.

The difference in the main transport of pit gas out of the anode pit in the open and closed furnace, should have an impact on the observed degradation patterns. In the closed furnace, the lack of clear trends in depletion and deposition of silica with respect to the vertical sampling position, could be related to the upwards transport of pit gas, reducing any vertical variations in the pit atmosphere. Both the depletion and deposition of silica are found at all sampling heights, most likely due to local conditions favoring both phenomena. This is in contrast to the observations in the open furnace, where there is a clear trend in silica depletion and deposition with respect to vertical position. Here, the reduced pressure causes a horizontal transport of gas from the pit atmosphere through the flue wall. Any variations in pit atmosphere along the furnace height would thus be maintained to a larger extent, due to less gas movement in the vertical direction. The observed depletion and and deposition of silica does, however, suggest that there is some degree of transport of gaseous SiO from the bottom and middle section towards the top section. The amount of silica transported is difficult to estimate, due to the fact that deposition could have occurred in the flue walls or elsewhere in the furnace. It is however clear that over the course of approximately 160 baking cycles, the total silica wear is only a few hundred micro meter, suggesting the flow of SiO in each baking cycle to be quite moderate compared to the overall transport of pit gas through the flue wall. The depletion and deposition mechanism would also be highly dependent on the temperature cycling, making it even more difficult to describe.

The total degree of depletion and deposition of silica were much larger in the open furnace compared to the closed furnace. When considering the difference in number of baking cycles each of the samples have undergone, it is however not surprising. The flue wall from the closed furnace was taken out of service after 73 cycles, while the flue wall from the open furnace remained in service for 160 cycles. Both flue walls were however taken out of operation due to their reduced performance in terms of structural and mechanical integrity. With these observations in mind, it is natural to conclude that the silica depletion and deposition are not the governing mechanism for the overall reduction in thermomechanical stability of the flue walls. The variation in density and open porosity is most likely having a larger impact on the thermomechanical stability of the lining.

When comparing the densification of the lining from the open and closed furnace, Figures 4.7 and 4.9, there are some notable differences. First of all are the clear trends found in the open furnace, not present to the same degree in the closed furnace. The reasons for this observation could be many, with variations in flow patterns of the flue gas being one of them. The cross sectional width separating the anode pit from the flue channel is another important difference. The width of the bricks from the closed furnace is approximately one third of the bricks form the open furnace, as shown in Figure 3.2. When comparing the density variations in the first 4 cm of the open furnace to the full width of the closed furnace, the results are not too different. The position of the burners used to control flue gas temperature is also different, and thus affecting the pit gas atmosphere differently in the two furnaces. In the closed furnace, the burners are located both in the head wall and underneath the section covers. The flue gas would contain combustion residues and could mix with the pit atmosphere and hence affect the chemical environment surrounding the refractory lining in the pit. The open top furnace, on the other hand, is designed with the burners inside the flue walls, and the combustion residues will thus not be in contact with the pit atmosphere. Any chemical processes going on at the surface lining in the pit would thus not be affected by the burners. Last, the particle size distribution of the packing coke used in the two furnaces are not equal. In the closed furnace, the coke fines are removed from the packing coke in order to reduce the degree of coke sticking to the wall after baking. In the open furnace, on the other hand, the fines are included in the packing coke filling the voids between the coarser particles to a larger extend.

Chapter 5

In situ monitoring of pit gas composition

5.1 Development of pit composition during baking

5.1.1 First measurement campaign

The concentration of CO and CO_2 from series 1 is presented in Figure 5.1, where the gas composition is shown as a function of time. The probe temperature is also shown, demonstrating the correlation between the concentration of CO

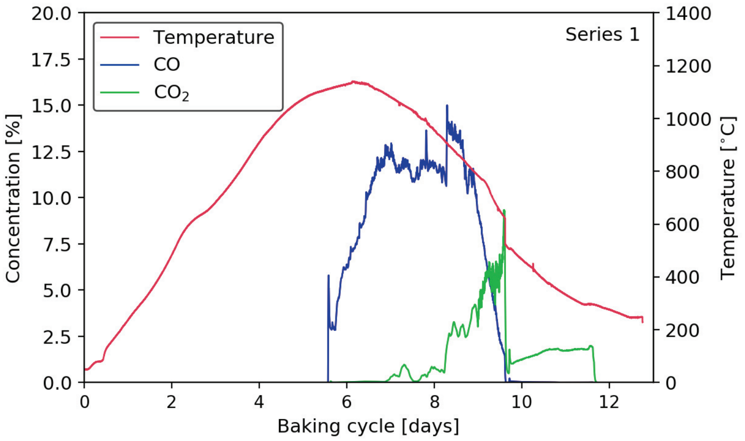

Figure 5.1: Concentration of CO and CO_2 from series 1, presented as a function of time. Reprinted from Brandvik *et al.* [121] with permission from Springer.

and CO_2 and the probe temperature. The duration of the measured cycle in Figure 5.1 is 13 days, with a maximum temperature measured to almost 1200 °C, both being typical characteristics for a baking cycle. The measurements were initiated ~5.5 days into the cycle. This was to avoid the pitch decomposition processes occurring during heating in the first part of the baking cycle. The period of measurement initiation was dominated by CO with a low concentration of CO_2. Upon cooling, the concentration of CO decreased, while the concentration of CO_2 increased. The measurements presented in Figure 5.1 were interrupted and reconnected after ~9.5 days, before being continued another two days, obtaining only a partial coverage of the baking cycle. Based on the experience from the first series, some modifications, outlined in Chapter 3, were carried out in the second and third measurement campaign.

5.1.2 Second and third measurement campaign

Shift in CO and CO_2 concentration

The concentration of CO and CO_2 for all three series is shown in Figure 5.2. The temperature profile is not varying much from series to series, and the same temperature profile is used for all three series. The observations made with series 1 are emphasized by the data from the second and third series. In the first part of the cycle, series 2 shows CO_2 as the dominating gas specie, having a maximum value of 12 % to 13 %. When looking at all three series, the CO concentration is clearly increasing as the temperature increases, and CO becomes the dominating specie at the maximum temperature. CO remains the dominating gas specie until the temperature drops below approximately 750 °C to 800 °C, and CO_2 again dominates at a maximum of 15 % to 16 %.

To complement the overall trends in CO and CO_2 concentration during the baking cycle, a more detailed analysis of the pit gas atmosphere is presented in Table 5.1. Here, the pit gas composition is given at three stages in the baking cycle, at 700 °C during heating, at the maximum baking temperature of 1150 °C, and at 700 °C during cooling. Gaseous compounds other than CO and CO_2 are also included to broaden the overview of the chemical composition of the pit gas atmosphere. The data presented in Table 5.1 enables a more detailed comparison of the pit gas concentration at 700 °C during heating and cooling. The

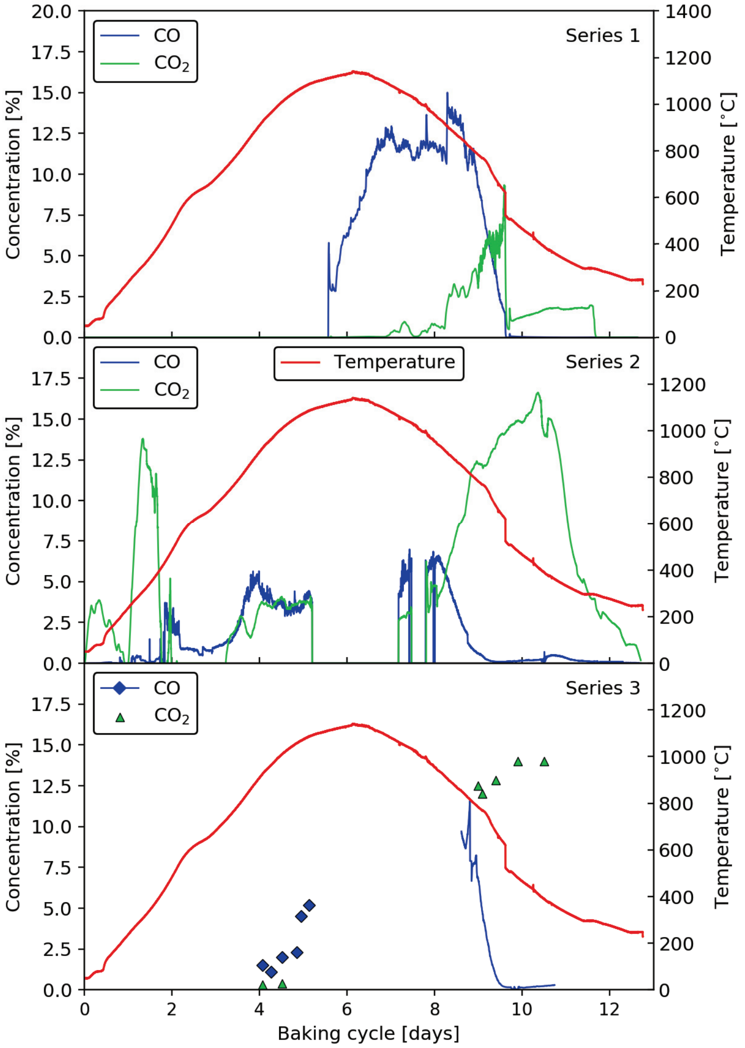

Figure 5.2: Concentration of CO and CO_2 for series 1-3, presented as a function time. The temperature profile recorded during series 2 is shown all three series.

Table 5.1: Pit gas composition at three stages in the baking cycle, at 700 °C during heating, at the maximum baking temperature of 1150 °C, and at 700 °C during cooling.

	700 °C (heating)		1150 °C (max. T)		700 °C (cooling)		
	S1	S2	S1	S3	S1	S2	S3
CO [%]	1.5	1.1	2.9	5.3	1.5	0.18	1.1
CO_2[%]	0.15	2	175 ppm	0.1	8	12.5	12.9
H_2O[%]	2.2	1	2	0.5	0.6	6.3	0.7
CH_4[%]	29	7	0.1	285 ppm	0	0	0
NH_3[%]	~1	~0.1	0	0	0	0	0
C_6H_6[%]	> 0.1	0	0	0	0	0	0
HF [ppm]	0	0	0	400 to 620	0	0	0

measured concentration of CO_2 is both higher and more stable towards the end of the baking cycle, compared to the beginning. In series 1 and 2, the concentration of CO_2 at 700 °C during heating is measured to 0.15 % and 2 %, respectively. At 700 °C during cooling, on the other hand, the measured concentration of CO_2 is in the range of 8 % to 12.9 %. The data for CO and CO_2 are to a large extent supporting the overall picture presented in Figure 5.2, where CO_2 is the dominating carbon specie at low temperature and CO at high temperature.

The uneven measurements during the first part of series 2 was due to difficulties with overlapping IR response from CO_2 and water. This is illustrated in Figure 5.3, where IR spectral data from series 1 at approximately 700 °C during heating is shown and compared to calibration data for CH_4, CO, CO_2 and H_2O. The measurements in series 2 were initiated at the beginning of the baking cycle, resulting in significant amounts of water and humidity in the pit gas. The primary peak of CO_2 is very strong and reaches the detector saturation limit at a concentration >1 %, and the secondary peak is thus used for quantitative analysis. Water is overlapping with the secondary peak of CO_2, making it difficult to get exact values for the CO_2 concentration.

CH_4, HF and other compounds

CH_4 was detected at 700 °C during heating, with a concentration of 29 % in series 1 and 7 % in series 2, as shown in Table 5.1. The concentration of CH_4 is

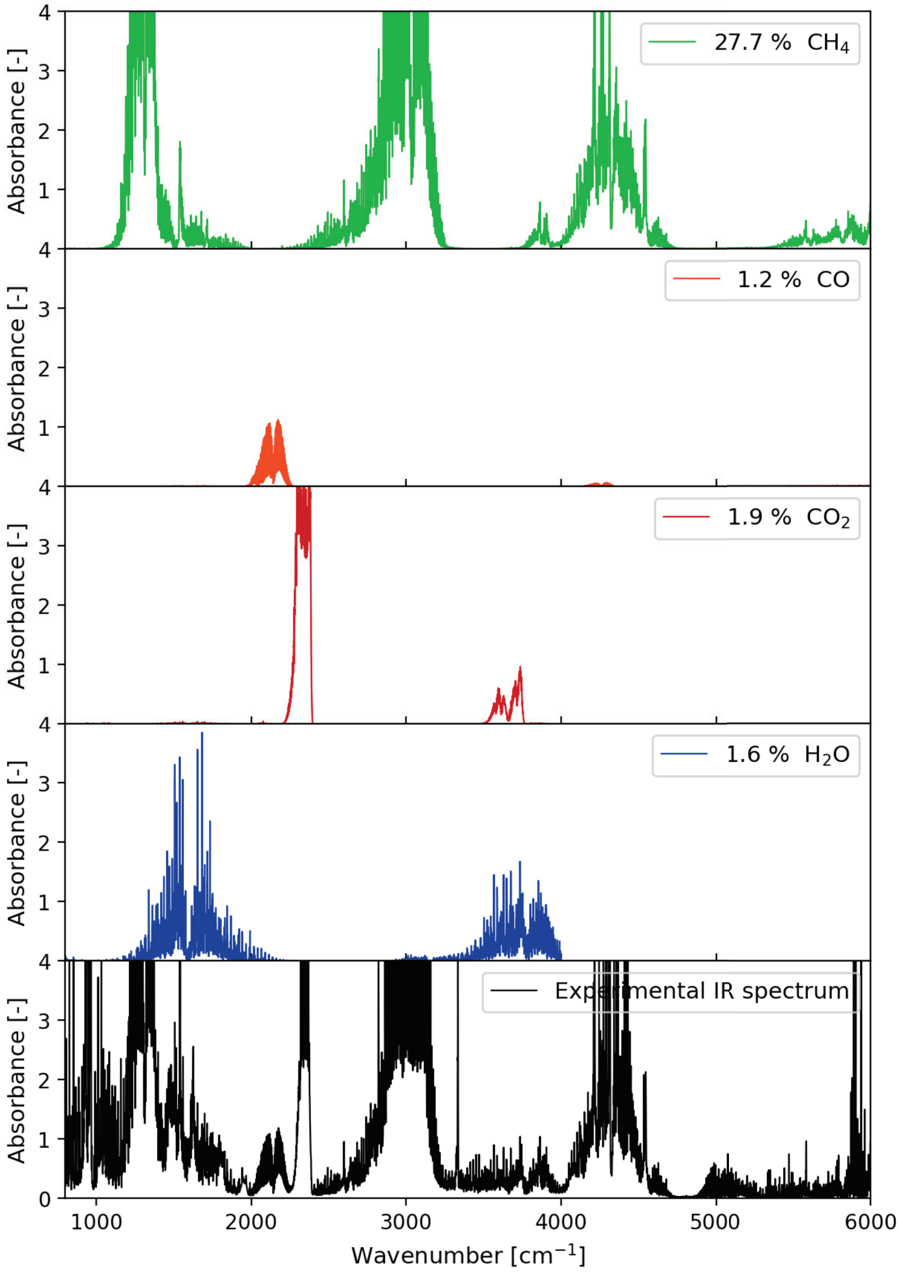

Figure 5.3: FTIR spectra from series 1 at approximately 700 °C during heating, compared to calibration spectra for CH_4, CO, CO_2 and H_2O in appropriate concentrations.

shown for a broader temperature range in Figure 5.4a. A peak in CH_4 concentration is observed between 400 °C and 850 °C, and upon further temperature increase, the concentration diminishes. The maximum value in CH_4 concentration varies from one series to another, as shown in Figure 5.4 and Table 5.1. CH_4 is only present during the first part of the baking cycle when the furnace is heating up, and not during the cooling period in the end.

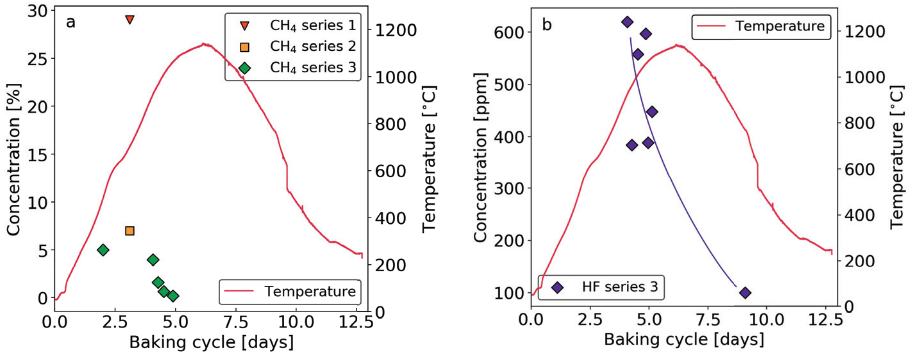

Figure 5.4: Concentration of CH_4 for all three series and HF for series 3. There is a peak in CH_4 between 400 °C and 850 °C, where the peak height varies from series to series. The concentration in HF is at its maximum around 1150 °C, ranging from 400 ppm to 620 ppm. A line is added as a guide for the eye, and is not an exact trend line.

During the series 3, considerable levels of HF were measured at the maximum temperature, as presented in Figure 5.4b. The IR spectra from series 3 at 1050 °C is shown in Figure 5.5. In this figure, the IR spectral data is compared to calibration data for CH_4, CO, and H_2O in appropriate concentrations. Compared to the data in Figure 5.3, the level of CH_4, CO_2 and H_2O are reduced, while the concentration of CO increased. This coincides with the overall trends presented in Figure 5.2 and Table 5.1. There are two gas species shown in Figure 5.5 which is not present in Figure 5.3. The spikes shown between 3500 cm^{-1} and 4300 cm^{-1} demonstrate the presence of HF, while the peak at 1000 cm^{-1} is due to the presence of SiF_4. SiF_4 is only detected together with HF. At the maximum temperature, around 1150 °C, the measured HF concentration varied from 400 ppm to 620 ppm. HF was only measured in short periods due to its reactive nature and the corrosive effect on the FTIR silica based optics. The correlation between measured HF and SiF_4 suggest that SiF_4 is formed by

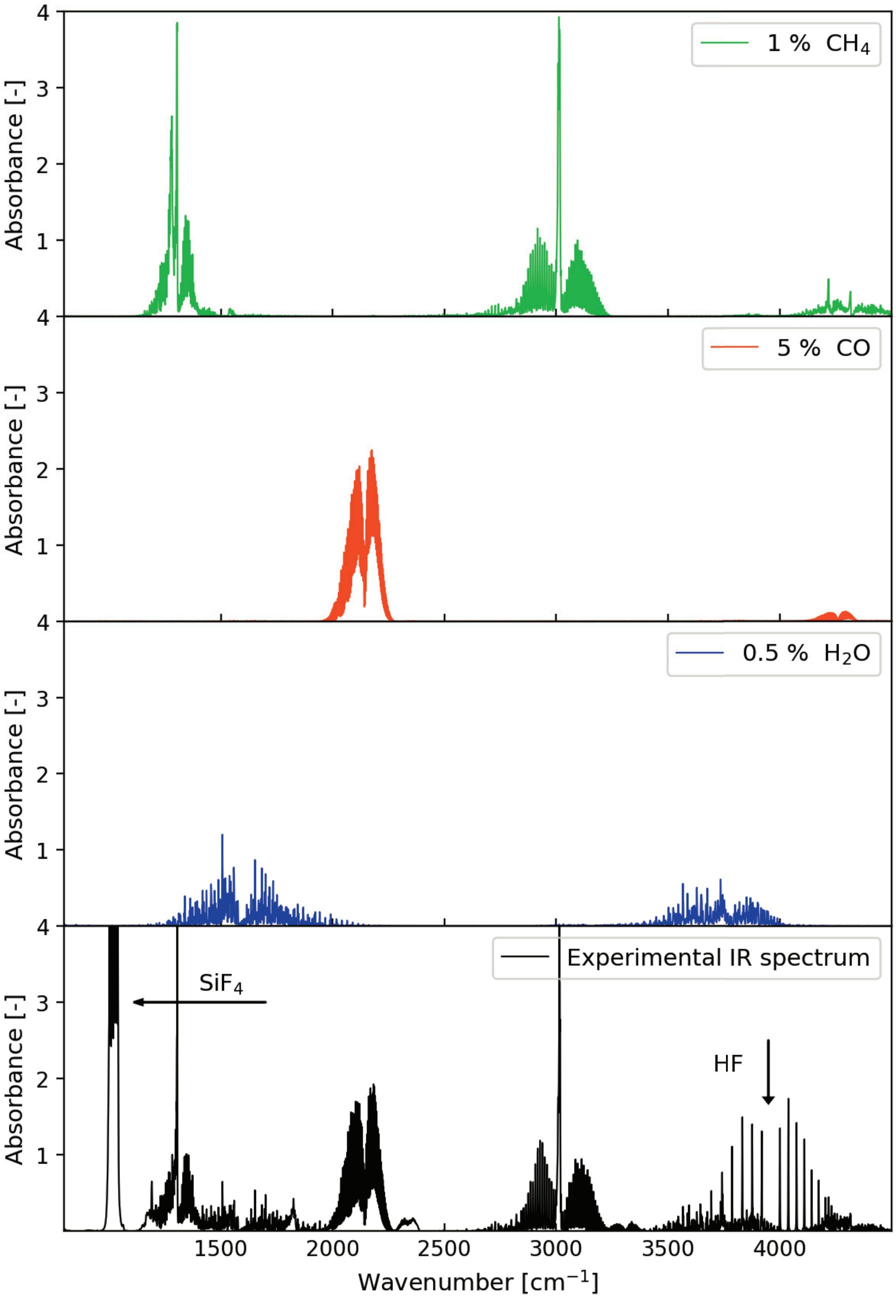

Figure 5.5: FTIR spectra from series 3 at 1050 °C, compared to calibration spectra for CH_4, CO, and H_2O in appropriate concentrations. Spectral features of SiF_4 and HF are marked.

the reaction between HF and the mirrors in the instrument.

The FITR analysis has revealed the presence of several other compounds in the pit gas during these experiments. As shown in Table 5.1, NH_3 was measured between 0.1 % and 1 % during the heating period of series 1 and 2. In series 3, HCN was measured to 200 ppm in the same period. In addition to the presented levels of methane, both ethane and propane were detected in the same temperature range, but in lower concentrations compared to methane. In series 2, 300 ppm of HF was detected at 400 °C in the cooling period of the cycle. The detection of HF in both series 2 and series 3 emphasizes the importance of that specific compound. Two sulfur compounds were also detected towards the end of series 3. A distinct shift from COS to SO_2 was detected at 625 °C during cooling. The FTIR signal was outside the calibration range (maximum 200 ppm), and extrapolation of library data indicated 700 ppm of COS being present in the pit. Below 625 °C, the maximum level of SO_2 was measured to 2500 ppm.

Measurements by gas chromatograph

To complement the FTIR measurements with data on H_2, N_2 and O_2, a gas chromatograph was used during series 3. These results are presented in Table 5.2, including CO_2 which also was measured by the GC. During the first part of the baking cycle, at 930 °C during heating, the hydrogen level was roughly estimated to >50 %, while the respective level of N_2 and O_2 were estimated to 16 % and 3 %. The H_2 calibration range for the gas chromatograph was between zero and 20 %, and to estimate the H_2 concentration outside this range, a linear extrapolation was used. The extrapolation introduces an unknown degree

Table 5.2: Estimated pit gas composition from gas chromatography measurements. The H_2 estimate is outside the calibration range and linear extrapolation was used to obtain the presented value.

Temperature	H_2	N_2	O_2	CO_2
930 °C (heating)	>50 %	16 %	3 %	0
890 °C (cooling)	0.75 %	78 %	3.1 %	7.5 %
850 °C (cooling)	0.58 %	80 %	3.1 %	9.5 %

of uncertainty and the hydrogen level is therefore only an approximate estimate. The estimated concentration demonstrate however that the H_2 level was significantly higher than 20 %. During the cooling period of series 3, a longer sampling period was carried out with the gas chromatograph. In the temperature range of 890 °C to 850 °C, the measured concentration of H_2 was reduced from 0.75 % to 0.58 %, while the CO_2 concentration increased from 7.5 % to 9.5 %, N_2 increased from 78 % to 80 %, and O_2 was stable at 3.1 %.

Condensation of water and pitch residues

The second series covered large parts of the baking cycle, including continuous measurements during the heating period of the cycle. Water was drained from the condensation vessel during the first 24 hours of the baking cycle, with an average condensation rate of $0.19\,\mathrm{kg\,h^{-1}}$. The gas flow through the setup is controlled by the pressure difference over a nozzle in the FTIR instrument, and during the period of water condensation, the flow was estimated to range from $0.5\,\mathrm{L\,min^{-1}}$ to $1.0\,\mathrm{L\,min^{-1}}$. Based on the measured condensation rate and the estimated gas flow, the average water content of the analyzed pit gas was ranging from $3.25\,\mathrm{g\,L^{-1}}$ to $6.5\,\mathrm{g\,L^{-1}}$ gas. During the period of water condensation, the temperature increased from 75 °C to 330 °C, and the condensation rate was fairly constant.

The condensation vessel proved valuable as the temperature increased from 400 °C and up to 800 °C, when accumulation of pitch residues was observed in the vessel. In the bottom, a brown/yellow, sticky condensate was observed as shown in Figure 5.6, demonstrating good control of pitch condensation. Without the condensation vessel, the pitch components could accumulate in the narrow parts of the setup, potentially causing problems for the experiment due to reduced gas flow through the setup. The discolored filter material shown in Figure 5.6 is due to lighter volatiles escaping the vessel and becoming trapped in the filter. There were periods where the white filter material was covered with a black layer, probably consisting of carbon powder and pitch residue. The level of condensation of pitch components was strongly reduced as the temperature increased beyond 800 °C.

Figure 5.6: Images of pitch condensate in the condensation vessel (left), and discoloring of the white filter material in the filter (right).

5.2 Discussion

5.2.1 The chemical environment in the pit

The main conclusion based on the three series is that the pit atmosphere changes dramatically during a baking cycle. In addition, the concentration of some species varies significantly from one anode pit to another. There are several reasons for these variations, where the change in temperature during the cycle, and the reactions occurring inside the anodes during heating are especially important. In Table 5.1, the gas composition at maximum temperature (1150 °C) and at 700 °C during both heating and cooling is presented. The concentration of CH_4 is high during heating, while CO_2 is dominating during cooling. The significant different pit atmospheres during the two periods, demonstrate that the chemical conditions are not the same. As the temperature increases during heating, the coal tar pitch becomes thermally unstable causing the formation of volatile hydrocarbons, with CH_4 as the main hydrocarbon detected. The low thermal stability of CH_4 upon further temperature increase results in a strong decrease in concentration above 1000 °C [173]. The pitch decomposition process is also ending in this temperature region, and the evaporation and cracking of pitch components stop. In the high temperature region, after the reduction in CH_4 concentration, CO becomes the dominating carbon specie until the temperature reaches approximately 900 °C to 700 °C during cooling where CO_2 becomes the main carbon compound in the pit atmosphere. The shift between CO and CO_2 is very distinct and clearly visible in Figure 5.2. The observed shift between CO and CO_2 are as expected based on thermodynamic considerations. The lower pressure inside the anode pit causes the surrounding air to enter the pit through the packing coke. When the temperature becomes high enough, oxygen reacts with the packing coke to form CO and/or CO_2. With solid carbon present, it is proposed that the Boudouard reaction (Equation 5.1) governs the overall thermodynamic equilibrium between CO and CO_2.

$$\mathrm{C\,(s)} + \mathrm{CO_2(g)} = 2\,\mathrm{CO\,(g)} \tag{5.1}$$

Above 700 °C, the reaction shifts to the right and CO becomes the dominating carbon compound in the pit atmosphere. From the chemical equilibrium, it is evident that the ratio $p^2_{\mathrm{CO}}/p_{\mathrm{CO_2}}$ describes the equilibrium conditions of the reaction. The ratio between p^2_{CO} and $p_{\mathrm{CO_2}}$ is plotted for the experimental data from series 1, 2 and 3 in Figure 5.7, together with equilibrium data. All the data are shown as a function of temperature for the last part for the baking cycle, i.e. from 1200 °C to the end of the cycle. The general trend from Figure 5.7 is that the pit gas atmosphere is in fairly good agreement with the equilibrium data. This is especially evident for series 1, but also the case for the data from series 2 and 3. The data for series 2 and series 3 are both below the theoretical ratio, demonstrating a higher partial pressure of CO_2 compared to the equilibrium calculations. The higher CO_2 partial pressure could originate from non-optimal kinetics in the pit, caused by thermal variations in the packing coke, or due to the inflow of air from the top of the pit during cooling. The reactivity of carbon towards oxygen and CO_2 has however not been investigated in this work, making if difficult to conclude in this regard. Introduction of air through a leak along the setup is also a potential source of elevated CO_2 partial pressure in pit gas, and a more thorough discussion of leakage is carried out below. To summarize, it can be concluded that, based on the data in Figure 5.7, the Boudouard reaction is a reasonably good model for the pit atmosphere in the last part of the baking cycle.

Comparisons of the three experimental series show that the main components have the same trends with respect to temperature. The quantitative levels are however not equal from one series to the next. These discrepancies can both be due to experimental challenges occurring during measurements, but also actual differences between the series. This is clearly observed in Figure 5.4a, where the maximum level of CH_4 is ranging from 7 % to 29 %. Due to the variations from series to series, it is difficult to conclude on the exact concentrations for the various compounds based on this work. The trends in concentration and the relative levels of the various compounds as a function of baking temperature are however established with certainty.

The probe and the thermocouple are positioned in the gap between the anodes

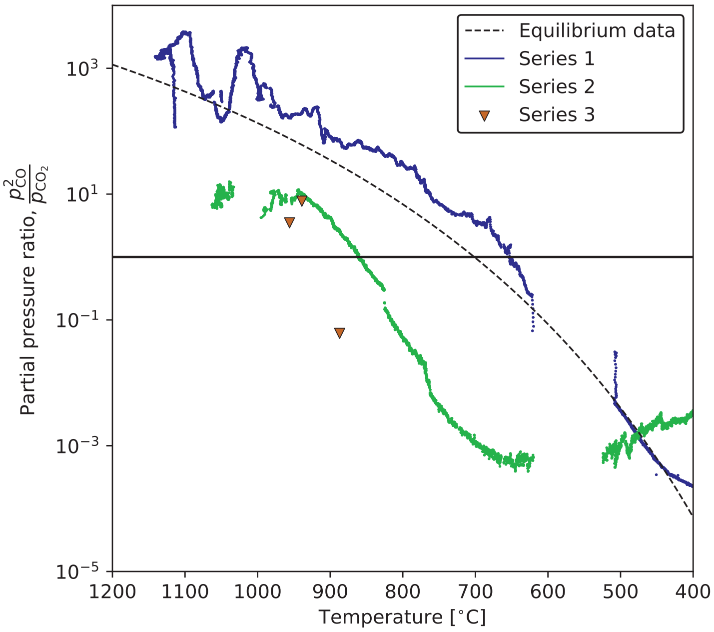

Figure 5.7: Ratio between p_{CO}^2 and p_{CO_2} plotted for series 1, 2 and 3, and compared to the thermodynamic equilibrium data.

and the flue wall, surrounded by the packing coke. The heating rate during the first part of the cycle is assumed to create a thermal gradient from the anode's center towards its surface. By this arrangement, the temperature measured by the thermocouple is not necessarily the same as the actual temperature inside the anodes. A modeling work describing the flow of flue gas in a baking furnace, reports on thermal gradients across the face of the flue wall of 50 °C to 100 °C [152]. A non-uniform temperature distribution can thus be assumed, both from the center of the anode towards the flue wall, but also across the face of the flue wall itself. The chemical and physical reactions taking place inside the anodes are thus not occurring at the exact temperature that is measured at the probe. The delay in heat transport towards the center of the anode would always result in a lower temperature inside the anode during heating, while being the other way around during cooling. As a result of non-uniform heat distribution, the processes inside the anodes (evaporation, decomposition and cracking of pitch) are occurring at a lower temperature compared to the temperature at the measured probe.

The measurements carried out with the gas chromatograph during series 3 complement the overall FTIR measurements. Continuous measurements were difficult to carry out during series 3 due to the high concentration of HF, and thus only partly coverage was obtained. Both the FTIR and the GC instruments are vulnerable to the corrosive nature of HF, and only shorter periods of measurements were carried out with the GC connected. The accuracy of the linear extrapolation yielding the >50 % estimate is uncertain, and should not be used as a quantitative measure. Nevertheless, the H_2 estimate demonstrates that the concentration of H_2 is very high in this part of the baking cycle. The high concentrations of CH_4 and H_2 are explained by the decomposition and cracking of pitch. In Figure 5.4a, a peak in the concentration of CH_4 is measured at approximately 700 °C, and at 930 °C during heating, the concentration of H_2 is estimated to be high. As the anodes are heated up, the pitch starts to decompose and lighter pitch components evaporate from the anode, including CH_4. This evaporation process carries on until all lighter pitch components are removed from the anodes. Hydrogen is then formed by the cracking of the pitch, breaking bonds between hydrogen and carbon in the anode binder. The gas development is found to be considerable, diluting the overall pit gas composition as seen by the low nitrogen content in Table 5.2. As the temperature increases, the thermodynamic stability of CH_4 decreases dramatically. The equilibrium pressures calculated in FactSage, for equimolar quantities of CH_4 and CO_2 as input values, are shown in Figure 5.8. There is a clear shift from CH_4 to H_2 as the temperature increases, and H_2 becomes the dominating gas specie for the temperature range approximately from 600 °C to 800 °C.

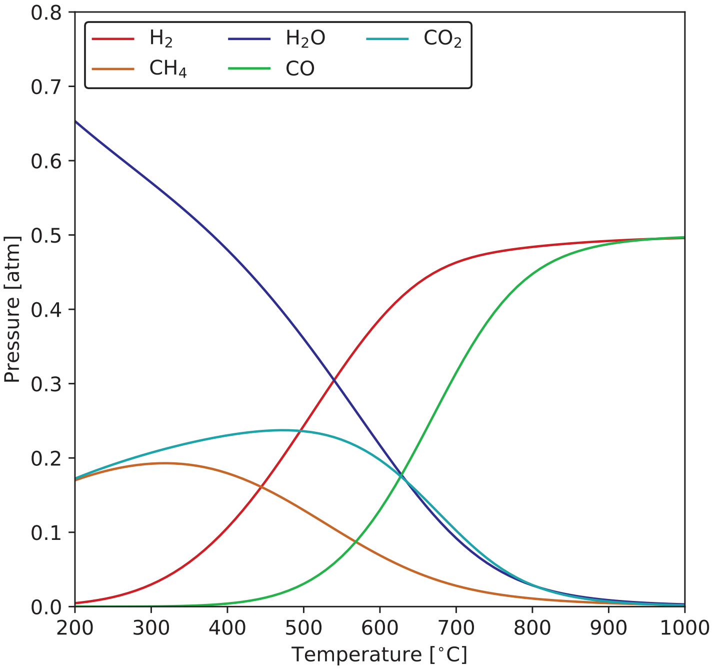

Figure 5.8: Equilibrium data for a gas mixture with equimolar quantities with CH_4 and CO_2 as input values. The figure shows a clear shift from CH_4 and CO_2 to H_2 for increasing temperature.

The thermal decomposition of coal tar pitch is causing the formation of hydrogen and hydrocarbons of various lengths, and the hydrocarbons are expected to crack into shorter chains as the temperature increases. CH_4 is measured in high concentrations, and the thermal instability of CH_4 is causing the decomposition into solid carbon and hydrogen gas as shown in Figure 5.8. Hydrogen could also be originating from of the heavier pitch components not evaporating from the anode, but cracking directly at sufficiently high temperature. The results from the autopsies, presented in Figures 4.14 and 4.15 in Chapter 4, demonstrate a significant deposition of solid carbon at the flue wall and inside open porosity. This deposition is clearly linked to the cracking and decomposition of pitch from the anodes.

The chemical reactions occurring in the pit atmosphere during heating are controlled by kinetics, and the equilibrium pressures in Figure 5.8 are thus not necessarily obtained. There are several competing reactions occurring in the pitch, yielding hydrogen and hydrocarbons of various lengths, and determination of the dominating reaction during heating is difficult. The main result is however formation of CH_4 and hydrogen, causing a reducing atmosphere in the pit. The general activity in the pit atmosphere (i.e. formation of pitch volatiles etc.) is reduced as the temperature reaches its maximum, and the flow of incoming air will become more and more dominant for the overall pit gas composition. This becomes clear by the GC measurements at 890 °C during cooling, where nitrogen is the overall dominating gas specie. The high temperature and the reduced gas activity enable thermodynamic equilibrium in the pit atmosphere to be reached, as demonstrated in Figure 5.7. The chemical conditions in the baking furnace are thus kinetically controlled during heating, while being more thermodynamically controlled during cooling.

The estimated concentration of nitrogen and oxygen (16 % and 3 %, respectively) during heating demonstrate a significant dilution of the incoming air by the pitch decomposition products. The nitrogen to oxygen ratio in the pit gas atmosphere at 930 °C during heating is 5.3. Compared to the ratio of air (∼4), the results show that the relative oxygen level is lower in the pit. The presence of 3.1 % oxygen measured at 930 °C is however not in accordance with the expected oxygen concentration, which was assumed to be much lower. The high oxygen level could be explained in two ways. First, the oxygen reactivity towards carbon could be lower than first expected, reducing the oxygen consumption rate in the pit. The combination of slow reaction kinetics and a relative high flow of air through the pit, would leave unreacted oxygen in the pit atmosphere showing up on the GC measurements. Second, there could be a leakage in the system causing air to enter the gas stream and thus influencing the measurements. A leakage would lead to the introduction of oxygen somewhere between the anode pit and the gas chromatograph. Investigations of air burn of carbon anodes demonstrate that the oxygen reactivity towards carbon is high at elevated temperatures [174, 175]. The estimated hydrogen concentration is also considerably higher than the oxygen estimate. The reaction between hydrogen and oxygen forming water (Equation 5.2) has a value of ΔG of $-118\,\mathrm{kJ\,mol^{-1}}$ at 930 °C, i.e. being highly shifted to the right.

$$2\,\mathrm{H_2(g)} + \mathrm{O_2(g)} = 2\,\mathrm{H_2O\,(g)} \tag{5.2}$$

It is therefore expected that incoming oxygen would react with the packing coke and hydrogen in the pit atmosphere resulting in a low content of oxygen in the pit. The measured oxygen in the pit atmosphere is therefore more likely originating from a leakage somewhere along the sampling line. By assuming that the oxygen originates from a leak, the actual pit gas at 930 °C during heating would consequently contain nitrogen, but no oxygen. The air from the leakage would mix with the pit gas (which already contains nitrogen), yielding a higher nitrogen to oxygen ratio compared to air. This corresponds with the measured concentration levels presented in Table 5.2. In the last part of the cycle, between 890 °C to 850 °C, the pit gas concentration is very different from the heating period. The concentration of oxygen is measured to 3.1 %, while nitrogen is measured to be approximately the same as in air. The formation of CH_4 and H_2 from the pitch is now terminated and with a continuous inflow of air through the packing coke, the level of nitrogen in the pit gas is naturally high. A leakage along the line would thus mainly increase the concentration of oxygen, and not affect the concentration of nitrogen to the same extent. The pipes along the line from the probe to the FTIR instrument were thoroughly inspected for leakage prior to measurement startup. However, the system was opened at several occasions during filter change and when emptying the condensation vessel. A leakage could also have occurred in the tubes between the FITR instrument and the gas chromatograph, but the exact location is difficult to determine.

To summarize the overall trends in pit gas composition, the main gas components are shown in the schematic illustration of the baking cycle in Figure 5.9. Here, the trends in concentration of various gas compounds are shown together with the temperature profile. The approximate concentration levels are also indicated based on the experimental measurements. The figure show that the pit gas is dominated by CO_2 and CH_4 in addition to water during the heating period. At further temperature increase, there is a shift from CH_4 and CO_2 towards H_2 and CO. During the cooling period, thermodynamic equilibrium is reached and the Boudouard reaction (Equation 5.1) shifts back towards CO_2 which becomes the dominating carbon compound. In addition to the compounds shown in Figure 5.9, the remaining atmosphere is mostly made up by N_2.

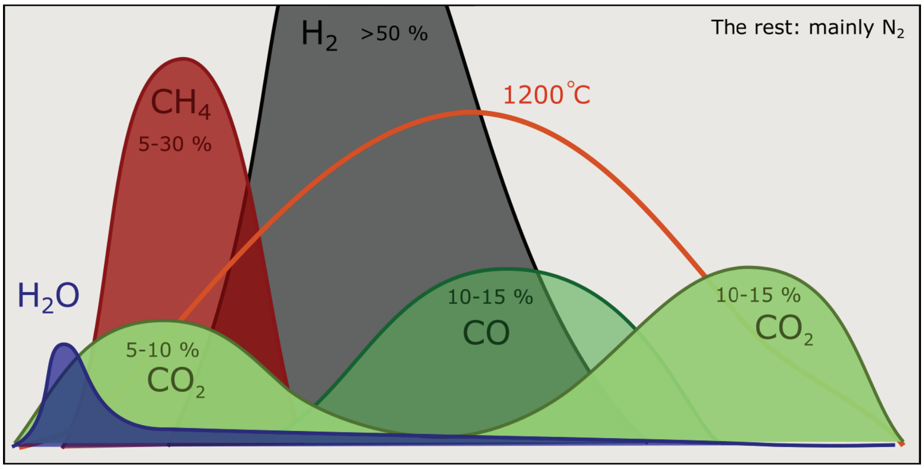

Figure 5.9: A schematic illustration of the pit gas composition during anode baking. This figure gives an overview of changes in concentration for the main components with respect to time and temperature in the baking cycle. The approximate concentrations are indicated. The remaining atmosphere is mostly made up by N_2.

5.2.2 The effects of HF formation on refractory degradation

The implementation of the condensation vessel in series 2 and 3 enabled the collection of water during the first days of the baking cycle. The condensation of water was most pronounced during the first 24 h in series 2, with an average condensation rate of $0.19\,\mathrm{kg\,h^{-1}}$. Based on the assumed flow rate, this corresponds to a humidity of $3.25\,\mathrm{g\,L^{-1}}$ to $6.5\,\mathrm{g\,L^{-1}}$. The high level of humidity has a dramatic effect on the chemical environment, especially when focusing on the volatility of fluorides as discussed in Section 4.3.2. The previous assessment focused on a dry gas atmosphere. The presence of water will change the volatility of fluorides, which can be estimated by thermodynamic calculations. The volatility of various fluorides from a cryolite sample in humid atmosphere is shown in the lower part of Figure 5.10. When comparing the activity of HF with $NaAlF_4$, it becomes clear that the onset of HF volatility is at a lower temperature than $NaAlF_4$, in addition to yielding a higher activity altogether. The same is observed for the upper part of Figure 5.10, where the corresponding vapor pressure above an industrial electrolyte in humid atmosphere is presented. The humid atmosphere causes the formation of HF at lower temperatures and with a higher activity, compared to the dry system. There are now two dominating chemical equilibria active in the system, where the first governs the formation of $NaAlF_4$ and NaF (Equation 5.3) and the second governs the formation of HF (Equation 5.4).

$$\mathrm{Na_3AlF_6(s) = NaAlF_4(g) + 2\,NaF\,(l)} \tag{5.3}$$

$$\mathrm{9\,Na_3AlF_6(s) + 14\,H_2O\,(g) = 28\,HF\,(g) + 26\,NaF\,(l) + NaAl_9O_{14}(s)} \tag{5.4}$$

There are two aspects of importance to learn from these calculations. First, the addition of AlF_3 to the electrolyte increasing the acidity of the bath will increase the volatility of fluorides in general. This is the same observation made when assessing the effects of sodium in Section 4.3.2. Second, the introduction of water changes the dominating volatile fluoride from $NaAlF_4$ to HF. With water present in the furnace, the stability of the lining is now potentially depending on both the sodium containing fluorides and HF. This changes the overall chemical environment and give rise to a new set of chemical equilibria involving the lining. The dominating phase in the refractory lining is mullite, and the thermodynamic stability of mullite towards HF is thus of great interest. As the temperature in the furnace increases, mullite and HF react in accordance with Equation 5.5 forming a condensed oxyfluoride phase ($SiAl_2F_2O_4$). This reaction

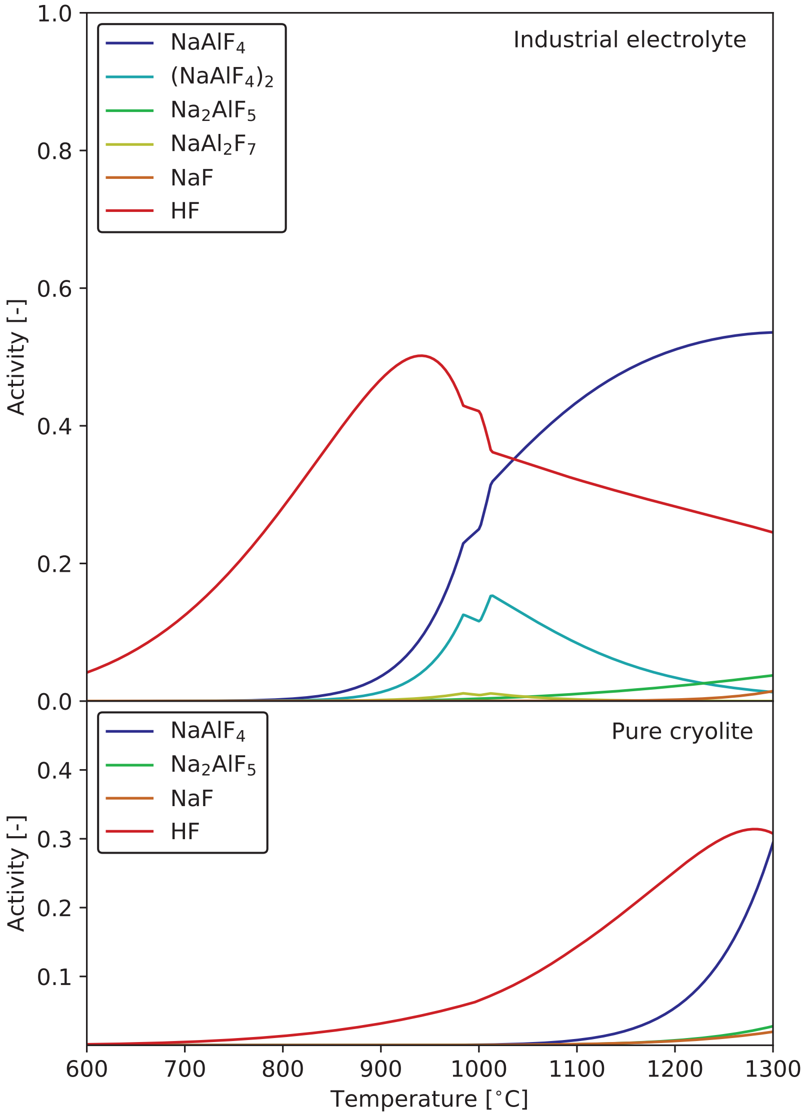

Figure 5.10: Comparison of fluoride volatility in pure cryolite and industrial electrolyte with 1 % water present. The industrial cryolite contains 80 wt% cryolite, 11.5 wt% AlF_3, 5 wt% CaF_2 and 3.5 wt% Al_2O_3. The volatility of fluorides is significantly shifted towards lower temperatures for the industrial electrolyte compared to pure cryolite.

is thermodynamically favorable at moderate temperatures, up to approximately 1000 °C.

$$Al_6Si_2O_{13}(s) + 4\,HF(g) = 2\,SiAl_2F_2O_4(s) + Al_2O_3(s) + 2\,H_2O(g) \tag{5.5}$$

Once $SiAl_2F_2O_4$ is formed, its stability is described by Equation 5.6. This reaction is spontaneous at temperatures above 1100 °C, shifting the fluoride volatility towards SiF_4.

$$4\,SiAl_2F_2O_4(s) = 2\,SiF_4(g) + Al_2O_3(s) + Al_6Si_2O_{13}(s) \tag{5.6}$$

If SiF_4 comes in contact with humid pit atmosphere, the reaction shown in Equation 5.7 is theoretically possible.

$$SiF_4(g) + 2\,H_2O(g) = SiO_2(s) + 4\,HF(g) \tag{5.7}$$

This reaction is spontaneous above approximately 850 °C and would result in deposition of solid SiO_2. During series 3, HF was measured in significant concentrations, as presented in Figure 5.4b. The measurements show a concentration of HF in the range of 400 ppm to 600 ppm for temperatures between 900 °C and 1100 °C. The IR spectra was too complex for a precise manual interpretation, even though an effort was made to compare the experimental IR spectra to calibration data. The data in Figure 5.4b are therefore as given by the built-in model in the instrument. A manual comparison of the overall experimental signal and the calibration data indicated however that the output form the instrument model is most likely underestimating the HF concentration. Based on the assignment of the vibrational modes in the spectra, the actual HF concentration is suggested in the range of 1500 ppm to 2000 ppm.

The important point here is however not the exact HF concentration, but the fact that a significant level of HF is measured in the furnace. This observation gives validity to the reaction path described by Equations 5.4 to 5.7, where HF acts as an alternative source for destabilization of the refractory lining. If the path terminates with Equation 5.6, fluorine ends up as gaseous SiF_4 with the possibility to leave the furnace through the off-gas. Consequently, it would not be expected to find any fluorides in the spent refractory lining. By having humidity present in the furnace, the electrolyte in the green anodes will react and form HF before decomposing into $NaAlF_4$ and NaF. The anodes are thus «cleaned» for traces of electrolyte before the decomposition temperature is reached, reducing the probability of forming sodium containing fluorides. The results from the autopsies presented in Chapter 4 demonstrate that the level of sodium in the spent lining is very low, with no traces of fluorides at all. The previous conclusion has been that the reason for the low sodium level is a corresponding low content of electrolyte in the green anodes. With the current observations of both water and HF in the anode pit, an additional cause for the low sodium content is possible. Since HF is measured in the pit gas, some electrolyte must be present in the green anodes, as it is probably the dominating source of fluorine in the furnace. Another consequence of the HF reaction path is the formation of SiF_4, a gaseous silicon compound. The reaction between HF and the lining is thus removing silicon from the lining, while the re-oxidation of silicon through the reaction between SiF_4 and water results in a deposition of solid silica. The observation of reaction layers depleted of silicon is presented in Chapter 4, are also reported in the literature [52, 53, 163]. The observation of HF in the anode pit in combination of the HF reaction path gives an alternative mechanism for silicon depletion and deposition in the flue wall.

A prerequisite for formation of HF is the presence of a humid pit atmosphere, which could be obtained in two ways. Water is coming into the pit through the green anodes and hence evaporating during heating of the furnace, and also through the inflow of humid air from the surroundings through the packing coke. The water introduced by the anodes would dominate in the beginning, but it is difficult to determine when the anodes become completely dry. The inflow of air is occurring during the whole baking cycle and would have a more steady contribution of humidity to the pit atmosphere.

In the production process of carbon anodes in the open furnace investigated in this work, the green anodes are cooled by immersion in a water basin for ~2 hours. This is done after the forming and pressing process which often occurs 50 °C above the pitch' softening point [24, 28–39]. To regain structural stability and avoid deformation of the anodes when stacked in the pit, cooling below the softening point is necessary. Water is thus following the anodes from the cooling basin to the pit where it evaporates during heating. The fraction of energy used on evaporation of water from the anodes is found in Appendix C. It would thus be beneficial to reduce the amount of water introduced to the furnace, both from a economical and chemical point of view. Heating and evaporation water is obviously energy demanding, and a reduction in water content would entail reduced operational costs. One approach could be to establish the relation between the water content in the green anodes and soaking time in the water basin. A reduction in soaking time should increase the residual heat in the anodes, which would increase the evaporation of water during storage of the green anodes.

5.2.3 Evaluation of the experimental method

Measuring the pit gas atmosphere during anode baking has proved to be a challenging but rewarding exercise. Prior to the startup of this project, detailed knowledge of the processes going on in the anode pit was limited, and knowing what requirements to impose on the experimental equipment was not straight forward. This led to the continuous development of the setup, where the experience from series 1 was used to improve the setup before carrying out series 2, and further to series 3.

The variation in the gas flow through the measurement system was the most difficult challenge during the measurement campaigns. The pressure at two positions along the setup for series 2 is presented in Figure 5.11. Here, the probe pressure and pump pressure are shown, in addition to the pressure difference between the two. Between the pump and the probe, there is a nozzle in the FTIR instrument constricting the flow to a maximum of $2\,\mathrm{L\,min^{-1}}$, corresponding to a pressure difference of approximately 600 mbar. During normal and open conditions, the probe pressure is measured to 960 mbar to 1000 mbar, depending on the baking process and the reduced pressure in the pit. The pump pressure is ranging from 360 mbar to 400 mbar, giving the pressure difference of approximately 600 mbar. In the beginning of series 2 (Figure 5.11), the system is open and the flow through the equipment is high. After 1-2 days the probe pressure starts to decrease, causing a reduction in gas flow. The pump is trying to compensate by creating an even higher under pressure, but the probe pressure continue to decrease, until the probe and pump pressures are equal, and the flow is basically zero. After a couple of days with no flow, the system is opened again and the pressure difference (and hence the gas flow) is gradually increasing.

The varying gas flow through the system had several causes during the three series in this project. The main difficulty has been the condensation of pitch components in the relatively cool pipes, after leaving the pit through the probe. In the first series, the experiment was initiated when the pit temperature was above 1000 °C, to be sure that most pitch components had been removed from the pit atmosphere. By waiting until the temperature was above 1000 °C, any water from the green anodes would also be evaporated and removed from the pit atmosphere. By increasing the pipe dimensions and introducing a condensation vessel, the second experiment was better equipped to run during the heating period and consequently last the whole baking cycle. As presented in

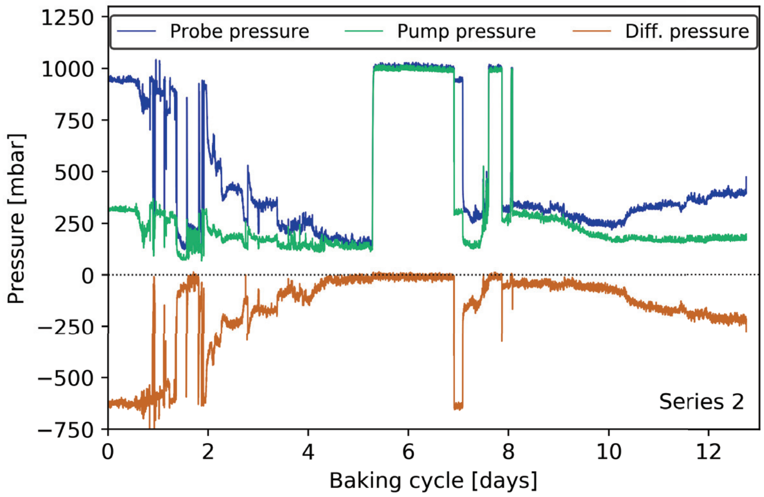

Figure 5.11: The pressure measured in the probe and at the pump during series 2. The figure also shows the difference between the two pressures, indicating the driving force for gas flow through the system.

Figure 5.11, there were still some difficulties with keeping the system open through the whole of series 2. The condensation vessel worked as planned, and most of the heavier pitch components that evaporated from the anodes, were gathered in the vessel. Considerable amounts of water was also collected in the condensation vessel during the first day of the experiment. After the vessel was emptied for water, there was however still a lot of humidity left in the system and in the gas. Series 2 was carried out during winter, with an outside temperature below $-20\,°C$. The gas exiting the pump contained a lot of humidity, the the full system blockage observed almost halfway through the cycle was due to the pump outlet freezing shut.

The choice of filter material had an important effect on the experiments. In series 1, the filter unit was filled with glass wool with the main goal to remove solid particles and corrosive gas species that could harm the FTIR instrument. This approach resulted in some periods where the FTIR measured high concentrations of SiF_4. The formation of SiF_4 is an important indicator for the degradation processes occurring in the pit, and thus very interesting with respect to the degradation of refractory material. Having an artificially high SiF_4 signal from the glass wool would therefore cover up potential SiF_4 signal from the pit. As a part of the modifications carried out prior to series 2, the filter unit was changed to the one shown in Figure 3.5. The new filter unit comprised an inner cylinder containing the filter material, making it easy to change filter material during the experiments. The filter material was changed from glass wool to a polymer-based material (styrene-divinylbenzene (XAD2)) in order to avoid untimely formation of SiF_4. The new filter material was a fine grained adsorbent powder, normally used for quantitative experiments. The pressure drop over the filter unit (and through the filter material) was not high as long as the filter material was dry. However, as soon as humid gas from the condensation vessel started to wet the filter material, the pressure drop started to increase. In addition, some lighter pitch components reached the filter unit and condensed the top of the filter material, causing a significant increasing pressure drop over the filter. Consequently, the filter material had to be replaced every 1-2 days during the first part of the baking cycle, in order to keep the system open.

Chapter 6

Finite element modeling of creep in refractory lining

6.1 Recap of the model

Finite element modeling was used to investigate creep as a potential mechanism for the observed deformation of the refractory lining in the open furnace. The geometry of the model with the top boundary condition is shown in Figure 6.1. The geometry is divided into three regions, aiming to simulate the three regions

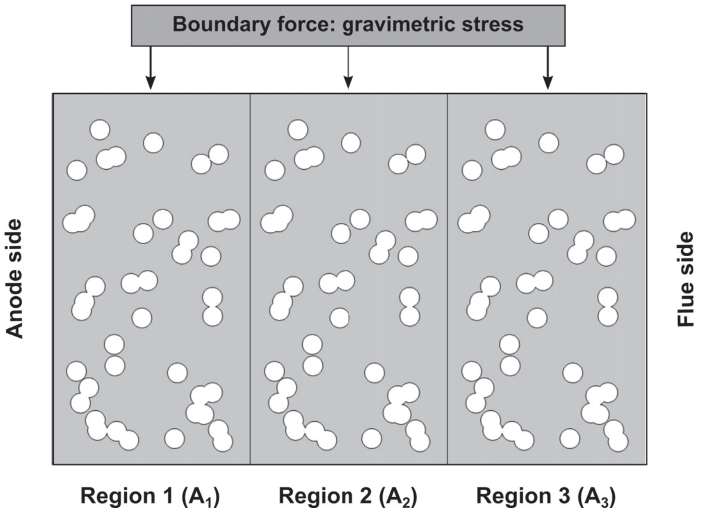

Figure 6.1: Illustration of the model, showing the three regions, the anode and flue side, and the boundary force from the gravimetric stress.

of the cross section separating the anode side from the flue side. The same geometry is used when modeling the three sections. The modeling was divided into two cases, where two sets of boundary conditions were imposed on the geometry. In Case 1, the vertical boundaries were free to move vertically, but not horizontally. In Case 2, the two outermost vertical boundaries were still only allowed to move vertically, while the two internal vertical boundaries were free to move in all directions. The horizontal boundary in the bottom was fixed for both cases. The gravimetric stress was set as the boundary condition on the top horizontal boundary, and was varying during the simulations. The force on the top boundary was set to 0.025 MPa, 0.0625 MPa and 0.1 MPa representing the top, middle and bottom sections, respectively, as illustrated by Figure 3.6.

6.2 Results

6.2.1 Deformation and stress distribution

The deformed geometry for Case 1 and Case 2 with the stress distribution in the three sections are presented in Figures 6.2 and 6.3. The figures show the geometry with 2 mm pore radius after simulation. The color gradients show how the build-up of stress is distributed, ranging from high (red) to low (blue). The stress distributions for Case 1 and Case 2 are similar and the same observations can be done from the two figures. The stress build-up is in general increasing going from the top towards the bottom, correlating with the gravimetric stress increasing downwards in the pit wall. The overall degree of deformation is also increasing as the gravimetric stress is increasing, i.e. the bottom section is more deformed than the top section. By focusing on a single section (i.e. fixing the gravimetric stress level), it is clear that region 1 has less stress build-up compared to region 2 and 3. This is the case for all heights, but most pronounced in the bottom section. Again, there is a correlation between the stress distribution and the observed deformation. In the regions having deformed the most, the stress build-up is lower compared to the less deformed regions. The material is under compressive stress and responds with a varying degree of deformation, causing the material to relax. The more the material is deformed, the more the stress build-up is reduced by material relaxation.

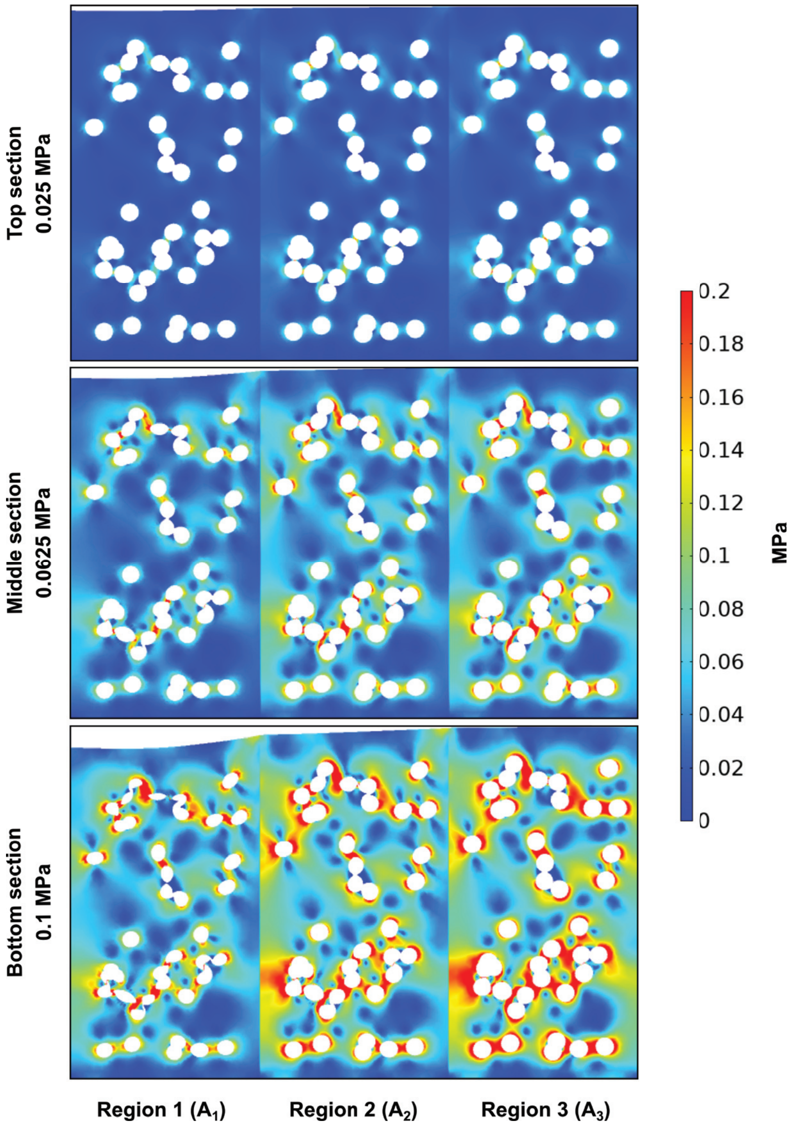

Figure 6.2: Stress distribution for Case 1 with 2 mm pore radius.

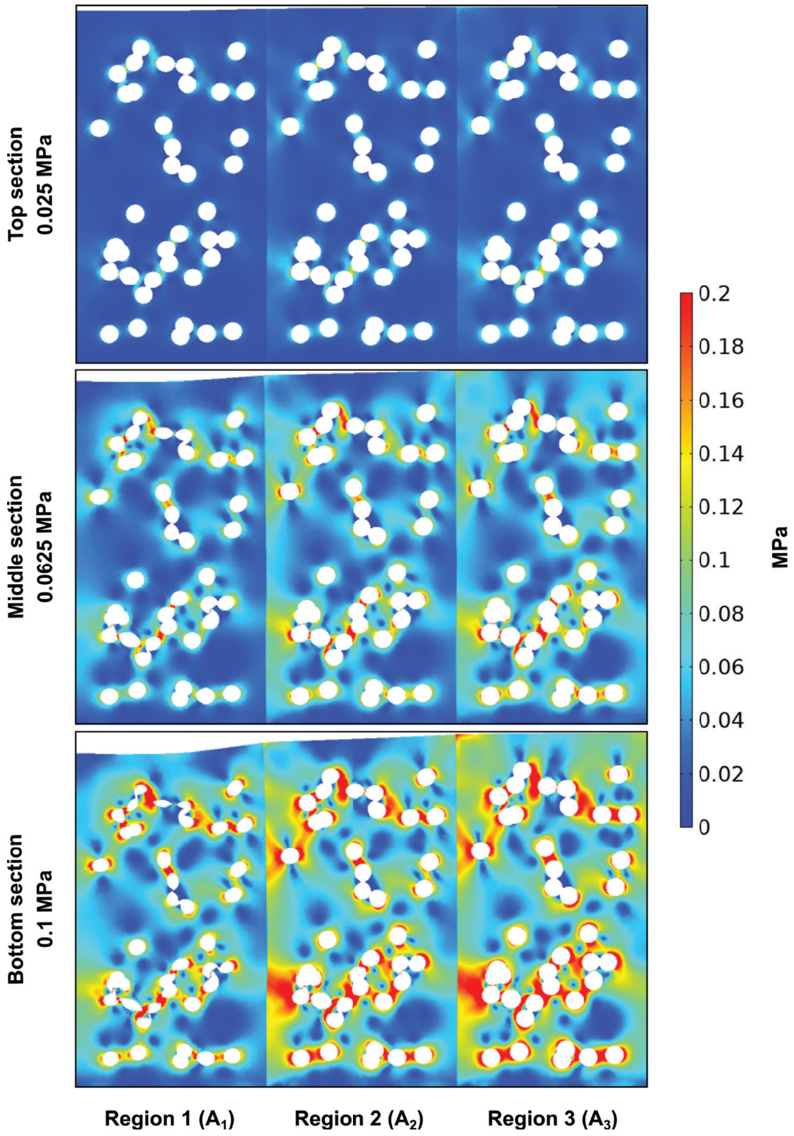

Figure 6.3: Stress distribution for Case 2 with 2 mm pore radius.

6.2.2 Reduction in porosity

The degree of deformation was calculated based on the deformed geometries, and expressed in terms of reduction in porosity. The calculated porosity from Case 1 is presented and compared with experimental data from the autopsies in Figure 6.4a. The reduction in porosity in Case 1 correlates well with the experimental data. Data for pore radius 0.5 mm, 1 mm and 2 mm is included in the figure. The reduction in porosity is more or less independent of the pore sizes used in the simulations. The calculated porosity for Case 2 is presented and compared with experimental data in Figure 6.4b. Here, the results show the same trend, with slightly different change in porosity compared to Case 1. The overall picture is however the same, where the reduction in porosity is significant and comparable to the experimental data. The autopsy results from the bottom section were used to fit the creep parameters as described in Section 3.5.5, yielding a set of parameters comparable with literature data. As the gravimetric stress is varied, the densification level is corresponding well with the reduction in porosity observed in the top and middle section

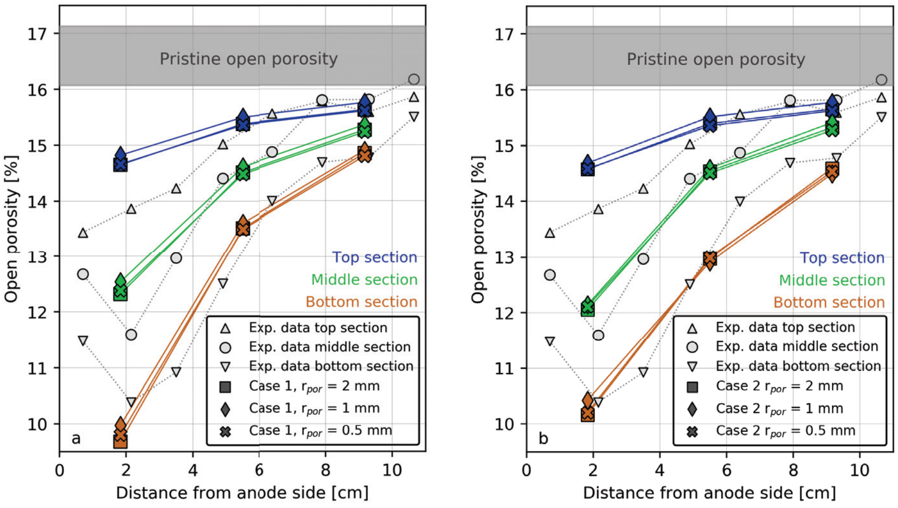

Figure 6.4: Reduction in porosity for a) Case 1 and b) Case 2. Data for three pore sizes are included (0.5 mm, 1 mm and 2 mm). The dotted line show the experimental data from the open furnace before laboratory heat treatment.

6.3 Discussion

6.3.1 Creep as densification mechanism

There are two important observations to be made from this modeling work. First, the calculated gravimetric stress is in general large enough to give a significant change in porosity at reasonable time spans, temperature levels and creep parameters. This means that the lining is exposed to a stress level during anode baking that is high enough to induce significant creep in the lining. Second, when focusing on one region (fixed A parameter), the variation in creep for increasing gravimetric stress correlates well with the experimental data. The uneven reduction of open porosity can also clearly be seen in the CT images in Figures 4.11 and 4.12. The gradual increase in the stress due to gravity is sufficient to induce a gradient in the porosity downwards in the lining.

The pre-exponential factor used in the simulations is varying with a factor 10, from $3 \cdot 10^{10}$ to $3 \cdot 10^{11}$, between the flue side and the anode side. This corresponds to a reduction in Q from 485 kJ mol^{-1} to 459 kJ mol^{-1}. The reducing atmosphere at the anode side is thus significantly influencing the thermomechanical properties of the lining. For isothermal conditions, the product between the pre-exponential factor and the exponential expression ($A \cdot \exp(\frac{-Q}{RT})$ is constant. The choice of A over Q as the the tunable parameter was arbitrary, and going through the same optimization procedure with Q as the variable would yield the same result. The same holds for the choice of temperature, which was fixed to 1100 °C for all simulations in this work, a simplification of the actual temperature regime in the furnace. A higher temperature could have been chosen, but in order to maintain the creep corresponding to the experimental data from the autopsy, a reduction in the pre-exponential factor, A, or an increase in the thermal activation barrier, Q, is necessary. Hence, the actual values of the temperature, the pre-exponential factor and the thermal activation barrier used in this modeling work must be seen in context of each other.

It is proposed that the partial pressure of oxygen have a considerable destabilizing effect on the refractory lining. A broad grain size distribution, where the largest grains are several millimeter in size, is very important for the thermomechanical stability of traditional refractory materials. The largest grains give structural stability, while the smaller grains and the binder fill the pores and bind the grains together. The reduction in porosity discussed in this thesis is shown to occur in the bonding phase, where the smallest grains and pores are located, see Figures 4.11 and 4.12. During anode baking, as the lining material is creeping, the smaller grains and pores in the bonding phase are reoriented and compacted, while the larger grains and pores are not significantly affected. Investigations of how the partial pressure of oxygen and grain size distribution affects the creep rate of refractory lining should be carried out. More knowledge on these relations could make it possible to reduce to creep by tailoring the microstructure of the lining material.

6.3.2 The effect of carbon deposition on densification

From the experimental work presented in Figure 4.8 it is clear that the open porosity is reduced when going from the flue side towards the anode side. This trend is fairly linear for most of the data and is explained by an increased creep rate at the anode side, proposedly caused by a different chemical environment on the anode side compared to the flue side. Closest to the anode side, however, there is an increase in open porosity for the middle and bottom sections compared to the overall trend, i.e. the degree of deformation for this region is reduced. Deposition of carbon was observed in the region closest to the anode side. The deposition takes place at the refractory surface and in the open porosity, filling the pores with carbon and hence affecting the mechanical properties of the lining in this region. The pristine lining can roughly be regarded as a composite material consisting of two materials or phases; the refractory material and the pores. An estimate of the average elastic modulus of such mixed materials can be determined by the law of mixtures [61]:

$$E_{\mathrm{tot}} = E_{\mathrm{ref}} V_{\mathrm{ref}} + E_{\mathrm{por}} V_{\mathrm{por}} \tag{6.1}$$

where E is the elastic modulus and V the volume fraction of the refractory material and the pores. The pores have no elastic modulus ($E_{\mathrm{por}} = 0$), and the effect of porosity on the total elastic modulus can thus be expressed by the reduction of the refractory volume fraction (V_{ref}) in the following manner:

$$V_{\text{ref}} = V_{\text{tot}} - V_{\text{por}}, \tag{6.2}$$

which can be inserted into Equation 6.1 to yield:

$$E_{\text{tot}} = E_{\text{ref}}(V_{\text{tot}} - V_{\text{por}}) \tag{6.3}$$

The stiffness of the material is hence reduced as the volume fraction of pores is increasing. A linear relation between the elastic modulus and the porosity is clearly shown for alumina in Figure 2.6. As the pores closest to the anode side are filled with deposited carbon, a third constituent is entering the composite material and Equation 6.3 is expanded to comprise carbon, as shown in Equation 6.4.

$$E_{\text{tot}} = E_{\text{ref}}(V_{\text{tot}} - V_{\text{por}} - V_{\text{C}}) + E_{\text{C}}V_{\text{C}} \tag{6.4}$$

As the pores are filled with deposited carbon, the lining becomes stiffer (higher elastic modulus) and more resistant towards the gravimetric stress exposed by the overlaying bricks. As a result, the creep rate in this region is reduced resulting in less deformation of the lining and hence less reduction of open porosity. The deposition of carbon in the open porosity could thus explain the deviation from the overall trend in the open porosity shown in Figure 4.8, for the samples closest to the anode side.

The overall variation in density observed across the brick is however not largely affected by the deposition of carbon. Only the region closest to the anode is affected by the deposition, and there is still a significant difference in density between the anode side and the flue side. The thermomechanical challenges arising from the non-uniform density across the lining are thus not significantly reduced by the deposition of carbon in the open porosity close to the anode side.

Chapter 7

Discussion

In this study, the degradation of the aluminosilicate refractory lining in two anode baking furnaces were investigated by combining experimental investigations of spent lining, measurements of pit gas atmosphere and finite element simulations of the lining. Pronounced wear patterns were observed in both the open and closed furnace, but the trends were more distinct in the open furnace. This is especially evident for the variations in density and open porosity, but also with the depletion and deposition of silica. The impurity oxide particles with high iron content are however only observed in the closed furnace. Both the vertical and horizontal position in the lining were important parameters when analyzing and discussing the observed phenomena from the open furnace.

A significant densification were observed in the lining after years in service, being highly uneven in nature. In the open furnace, the densification was dependent on the sampling position, showing a considerable increase going downwards into the pit. The dominating mechanism for densification is proposed to be creep by viscous flow. Finite element modeling demonstrates that the observed rates of densification from the autopsy samples could be reproduced using the equation for steady state creep at reasonable time and temperatures. The CT imaging shows that the reduction in porosity is mostly occurring in the bonding phase, in vicinity to the smaller grains surrounded by smaller pores. The larger grains and pores are largely unaffected by the creep process. Measurements of the pit gas composition demonstrated the highly reducing atmosphere at the anode side, while the conditions at the flue side are more oxidizing. Based on the variation in densification across the flue wall, and the considerable difference in gas atmosphere at the anode side and the flue side, it is proposed that the reducing atmosphere at the anode side is increasing the creep rate. Sodium was not found in any considerable amounts in either furnace, and any role in the densification of the investigated flue walls was disregarded. The densification at the flue side is observed to be negligible, demonstrating that the combination of baking temperature and oxidizing atmosphere is not sufficient to induce the creep process. The temperature is not varying much across the flue wall, and the major difference between the flue side and the anode side is the gas atmosphere, supporting the suggestion of the reducing pit atmosphere having an effect on the creep rate. The largest difference in densification between the anode side and the flue side is observed in the open furnace. There are two reasons for this. First, the flow pattern in the open furnace allows for a more stagnant pit gas, potentially enhancing the reducing atmosphere. Second, the thickness of the lining separating the anode side and the flue side is larger for the open furnace compared to the closed furnace, being 11 cm and 4 cm respectively. The distance over which the atmosphere gradient is formed is thus longer in the open furnace. When comparing the density variation in the four outermost centimeters in the open furnace with the density data from the closed furnace, the difference is however less striking. Whether it is the flow pattern of the flue gas, the difference in service time or the difference in material thickness that have the largest impact on the observed wear patterns, is however not easy to determine. It is probably a combination of all factors that contribute to the observations found in the open and closed furnace.

The density is generally observed to increase from the flue side towards the anode side. For the middle and bottom sections however, increase in density for the outermost parts of the lining is deviating from the expected trend. The density of the lining closest to the anode side is lower than expected based on the overall densification, as seen in Figure 4.7. This behavior is linked to the deposition of carbon at the refractory flue wall. Carbon is observed in the outer layers of the flue wall, filling open porosity in the lining. The filling of the porosity will increase the stiffness of the lining, making it less susceptible to creep by viscous flow. Even though these regions are closest to the reducing atmosphere, which should yield a higher creep rate, the overall creep rate is lower compared to what is measured further into the lining.

The uneven densification in the refractory flue wall is a clear disadvantage for the operation of the furnace. The bricks in the open furnace are observed to bend towards the anode side, as shown in Figure 4.24, and thereby introducing an instability in the flue wall. During temperature cycling, thermal expansion and contraction of the lining material is constantly repeated for every cycle. The furnace is designed to handle this cycling, with joints and gaps in the lining giving room for expansion of the flue wall. As the voids and gaps are filled with packing coke and deposited carbon, the flue wall becomes less and less capable to handle the thermal variations of the baking cycle. The variation in density across the lining between the anode side and the flue side is introducing additional stresses, which ultimately results in the bending of the flue wall. As the stress builds up over years in service, the flue wall becomes increasingly vulnerable for mechanical stresses from the operation. The filling of packing coke in the pits after the anodes have been put in place, could affect the flue wall stability, as one side of a given flue wall is filled before the other side, imposing a horizontal force on the wall potentially leading to the bending of the wall.

Depletion and deposition of silica is found in both the open and closed furnace. Thermodynamic calculations showed that sufficient partial pressures of SiO is formed at a proper combination of high temperature and reducing atmosphere. This would result in the volatilization of silica and give rise to a transport mechanism for silica in the furnace. The impurity oxide particles found in the closed furnace have a high iron content. Determination of the iron source has been outside the scope of this PhD work and has thus not been carried out. From an operational point of view, the transport of silica and deposition of impurity oxide particles are not as important as the non-uniform densification discussed above. These observations are found on a limited length scale (sub-millimeter) and should not have a considerable impact on the thermomechanical stability of the flue walls.

The gas measurements have given insight in the development of pit gas composition during the baking process, focusing on trends in the chemical composition. The first part of the baking cycle is dominated by the decomposition of pitch and the subsequent formation of CH_4 and H_2. As the temperature increases towards the maximum baking temperature, CO and subsequently CO_2

becomes the dominating species (in addition to N_2) where the partial pressures follow the equilibrium conditions of the Boudouard reaction well. This work has shown that water and humidity in the pit are of importance to the formation of HF and the following reactions with the lining. The thermodynamic assessment shows that HF and mullite react to form $AlSi_2F_2O_4$ at moderate temperatures, which, during further temperature cycling, decomposes into alumina, mullite and SiF_4. By leaving the furnace with the off-gas, SiF_4 acts as a carrier of silicon, transporting it from the lining and out of the furnace. At certain conditions, SiF_4 could also react with the humidity in the pit, causing deposition of silica to occur in accordance with Equation 5.7. The presence of humidity is therefore giving rise to an alternative mechanism for depletion and deposition of silicon. Water cooling of green anodes after mixing and forming is necessary, but should be performed in a controlled manner to reduce excess water. By establishing the relationship between soaking time and water content in the anodes, the overall input of water in the furnace could be controlled and possibly reduced. This would be beneficial in a chemical, thermomechanical and economical perspective.

The level of sodium in the investigated samples was found to be very low, and its role in the degradation processes was therefore not important for the two furnaces investigated in this work. A higher sodium content would result in the formation of low melting sodium aluminosilicate phases. The gravimetric stress would still be the dominating factor in the creep process, and the presence of phases with a lower melting point would cause the creep rate to increase. The low sodium content in the investigated samples is mainly credited to good cleaning routines of the anode butts. Having proper routines for cleaning of the recycled anode butts is thus a very important measure for maintaining the high life time of the refractory lining.

Changes in quality of the raw materials used in anode production could change the chemical environment in the pit. The processing of heavy, sour crude oils have been increasing in the recent years, and the petroleum coke is become increasingly more sour with a higher level of impurities [12, 26, 27]. The chemical environment would thus become more acidic as the sulfur content in the green anodes increases. The *in situ* gas monitoring method can further be modified to measure the level of sulfur in the pit gas. The aluminosilicate lining is however not that sensitive to reactions with acidic compounds, as it is more vulnerable to basic species containing e.g. sodium. This change in anode precursor quality is therefore not expected to have a large impact on the life time of the refractory wall. The environmental consequences could however be more severe, potentially increasing the need for cleaning of the off-gas before release to the local environment.

Further development of the method for pit gas measurements has its potential. The industry is increasingly more focused on emissions from the furnaces, where e.g. polyaromatic hydrocarbons (PAHs) are important. This work has also detected significant concentrations of HF which should be captured and not released to the environment surrounding the furnace. To be able to quantitatively determine the release of hazardous gases, the precision of the method must be improved. First, a flow meter should be installed so that the flow of flue gas can be linked to the gas concentration through the cycle. Second, the gas should be diluted to reduce the signal detected by the FTIR. During the three experimental series in this work, the signal has been very strong, causing partial saturation of the IR detector. The estimate precision of pit gas concentration would increase by diluting the gas and thus reducing the signal. Third, by installing a more active filter, HF can be captured and stopped before reaching the FTIR. Without having to worry about HF corroding the instrument's optics, measurements of other compounds can be carried out more continuously.

The variations in density observed across the cross section of the flue wall is suggested to be caused by a difference in reducing atmosphere. To verify this suggestion, creep experiments of refractory materials at various atmospheres should be carried out. Most of the reduction in porosity is observed in the bonding phase of the lining, where the smallest grains and pores are found. The grain size distribution in the raw materials and the microstructure of the final refractory product are hence of importance for the creep process. The refractoriness of the lining material is also an important factor for the thermomechanical stability of the lining. By increasing the alumina content in the material, a subsequent increase in refractoriness is expected. Investigations on how the grain size distribution, microstructure and the chemical composition of the lining affect the creep rate, especially in combination with a varying degree of reducing atmosphere, would give valuable information on how to reduce or avoid creep in the flue walls during anode baking.

Chapter 8

Conclusions

The aim of this PhD work was to investigate degradation processes of refractory linings in anode baking furnaces. The combination of industrial autopsies and material characterization, *in situ* monitoring of pit gas atmosphere, and FEM modeling of creep in refractory materials were used to identify the various processes going on in the pit and in the lining. Large variations in density and open porosity were observed in the open furnace, were the densification was most pronounced at the anode side. High operational temperature in combination with the gravimetric stress from the wall itself was proposed to cause creep by viscous flow in the material. Finite element modeling supported this hypothesis by showing that corresponding creep rates could be reproduced by FEM simulations. The pit gas measurements gave details on the development of the chemical environment in the pit during baking, where a reducing atmosphere was generally detected. During the heating period, CH_4 and H_2 from the pitch decomposition dominated, before CO and CO_2 became the dominating carbon compounds through the maximum temperature and cooling period. HF was detected in significant concentrations at the maximum temperature. Regions in the lining with depletion and deposition of silica were observed in both furnaces. The reducing atmosphere in combination with high temperature and the presence of HF in the pit gas gave rise to potential mechanisms for transport of silica. The depletion of silica is occurring at a sub-millimeter range, and is thus not the dominating factor for the reduction in thermomechanical properties of the refractory lining. Large variations in density and open porosity is on the other hand proposed to be the largest factor influencing the life time of the refractory lining in the anode baking furnace.

Bibliography

[1] Primary Aluminum Production Statistics. `http://www.world-aluminium.org/statistics`. [Last accessed: 2019-08-05].

[2] G. Koch, J. Varney, N. Thompson, O. Moghissi, M. Gould, and J. Payer. International Measures of Prevention, Application, and Economics of Corrosion Technologies Study (IMPACT). Technical report, NACE International, 2016.

[3] S. Das and W. Yin. Trends in the Global Aluminum Fabrication Industry. *JOM*, 59 (2):83–87, 2007.

[4] European Parliament and Council of the European Union. Regulation (EU) No. 333/2014. *Off. J. EU*, (333):15–21, 2014.

[5] Ducker Worldwide. Aluminium Content in North American Light Vehicles 2016 to 2028, 2017. `http://www.drivealuminum.org/wp-content/uploads/2017/10/Ducker-Public_FINAL.pdf`. [Last accessed: 2019-03-26].

[6] A. Kelkar, R. Roth, and J. Clark. Automobile Bodies: Can Aluminum Be an Economical Alternative to Steel? *JOM*, 53(8):28–32, 2001.

[7] Energy Consumption in Norway. `https://www.worlddata.info/europe/norway/energy-consumption.php`. [Last accessed: 2018-09-12].

[8] A. Solheim. Aluminuim Electrolysis - Main Principles and Technology. Technical report, SINTEF, 2009.

[9] P. Prigent and M. L. Bouchetou. Gaseous Corrosion of Aluminosilicate Refractories in Anode Baking Furnaces Used for Aluminium Produciton - Part 1. *Interceram*, 58(2-3):121–126, 2009.

[10] J. Thonstad, P. Fellner, G. M. Haarberg, J. Hives, H. Kvande, and Å. Sterten. Industrial Aspects of Aluminium Production. In *Aluminium Electrolysis - Fundamentals of the Hall-Heroult Process*, pages 1–8. Aluminium-Verlag Marketing and Kommunikation GmbH, 3rd edition, 2001. ISBN 3-87017-270-3.

[11] K. Grotjheim and H. Kvande. *Understanding the Hall-Heroult Process for Production of aluminium*. Aluminium-Verlag, 1986. ISBN 3-37017-181-2.

[12] K. L. Hulse. The Role and Behaviour of Anodes in the Cell. In *Anode Manufacture*, pages 1–20. R&D Carbon Ltd., 1st edition, 2000. ISBN 3-9521028-5-7.

[13] K. Grotjheim and H. Kvande. *Introduction to Aluminium Electrolysis - Understanding the Hall-Heroult Process*. Aluminium-Verlag, 2nd edition, 1993.

[14] W. T. Choate and J. A. Green. U.S. Energy Requirements for Aluminum Production Historical Perspective, Theoretical Limits and Current Practices, 2007. `https://www1.eere.energy.gov/manufacturing/resources/aluminum/pdfs/al_theoretical.pdf`. [Last accessed: 2018-09-12].

[15] E. H. M. Moors. Technology Strategies for Sustainable Metals Production Systems: a Case Study of Primary Aluminium Production in The Netherlands and Norway. *J. Clean. Prod.*, 14:1121–1138, 2006.

[16] H. G. Schwarz, S. Briem, and P. Zapp. Future Carbon Cioxide Emissions in the Global Material Flow of Primary Aluminium. *Energy*, 26(8):775–795, 2001.

[17] A. Taberaux. Prebake cell technology: A global review. *JOM*, 52(2):23–29, 2000.

[18] M. Sørlie and H. A. Øye. Cathode Failures. In *Cathodes in Aluminium Electrolysis*, chapter 11, pages 409–585. Aluminium-Verlag Marketing and Kommunikation GmbH, 3rd edition, 2010. ISBN 978-3-87017-294-7.

[19] O. S. Kjos, T. A. Aarhaug, B. Wittgens, and A. Brunsvik. At-line Analysis of Polycyclic Aromatic Hydrocarbons in Aluminium Primary Production. *Light Metals*, pages 541–546, 2014.

[20] T. A. Aarhaug, A. Ferber, O. S. Kjos, and H. Gaertner. Online Monitoring of Aluminium Primary Production Gas Composition by Use of Fourier Transform Infrared Spectroscopy. *Light Metals*, pages 647–652, 2014.

[21] T. A. Aarhaug, O. S. Kjos, H. Gudbrandsen, A. Ferber, and A. P. Ratvik. Evaluation of Gas Composition from Laboratory Scale Electrolysis Experiments with Anodes of Different Sulphur Content. *Light Metals*, pages 533–536, 2016.

[22] A. Radjenović. Properties of Carbon Anode Components for Aluminium Production. *Nafta*, 63(3-4):111–114, 2012.

[23] W. K. Fischer and R. C. Perruchoud. Interdependence Between Properties of Anode Butts and Quality of Prebaked Anodes. *Light Metals*, pages 721–724, 1991.

[24] F. Keller and P. O. Sulger. Preconditions for the Production of High Quality Anodes. In *Anode Baking*, pages 17–60. R&D Carbon Ltd., 2008. ISBN 978-2-940348-19-0.

[25] K. L. Hulse. Impact of Raw Materials and Formulation. In *Anode Manufacture*, pages 77–158. R&D Carbon Ltd., 1st edition, 2000. ISBN 3-9521028-5-7.

[26] L. Edwards, N. Backhouse, H. Darmstadt, and M. J. Dion. Evolution of Anode Grade Coke Quality. *Light Metals*, pages 1207–1212, 2012.

[27] L. Edwards. The History and Future Challenges of Calcined Petroleum Coke Production and Use in Aluminum Smelting. *JOM*, 67(2):308–321, 2015.

[28] K. Azari, H. Alamdari, G. Aryanpour, D. Ziegler, D. Picard, and M. Fafard. Compaction Properties of Carbon Materials Used for Prebaked Anodes in Aluminum Production Plants. *Powder Technol.*, 246:650–657, 2013.

[29] K. Azari, H. Alamdari, G. Aryanpour, D. Picard, M. Fafard, and A. Adams. Mixing Variables for Prebaked Anodes Used in Aluminum Production. *Powder Technol.*, 235:341–348, 2013.

[30] C. Sommerseth, R. J. Thorne, A. P. Ratvik, E. Sandnes, H. Linga, L. P. Lossius, and A. Svensson. The Effect of Varying Mixing Temperatures and Baking Level on the Quality of Pilot Scale Anodes - a Factorial Design Analysis. *Metals*, 7(3):74–85, 2017.

[31] Z. Kuang, J. Thonstad, S. Rolsett, and M. Sorlie. Effect of Baking Temperature and Anode Current Density on Anode Carbon Consumption. *Metall. Mater. Trans. B*, 27B:177–183, 1996.

[32] A. Sarkar, D. Kocaefe, Y. Kocaefe, D. Sarkar, D. Bhattacharyay, B. Morais, and J. Chabot. Coke-pitch Interactions During Anode Preparation. *Fuel*, 117:598–607, 2014.

[33] B. Majidi, P. Rolfe, M. Fafard, D. P. Ziegler, and H. Alamdari. Numerical Modeling of Compaction and Flow of Coke/pitch Mixtures Using Discrete Element Method. *Constr. Build. Mater.*, 169:315–324, 2018.

[34] A. Hussein, M. Fafard, D. Ziegler, and H. Alamdari. Effects of Charcoal Addition on the Properties of Carbon Anodes. *Metals*, 7(3):98–106, 2017.

[35] G. Aryanpour, H. Alamdari, K. Azari, D. Ziegler, D. Picard, and M. Fafard. Analysis on the Die Compaction of Anode Paste Material Used in Aluminum Production Plants. *Powder Technol.*, 254:228–234, 2014.

[36] F. Chevarin, L. Lemieux, D. Ziegler, M. Fafard, and H. Alamadari. Air and CO_2 Reactivity of Carbon Anode and Its Constituents: an Attempt To Understand Dusting Phenomenon. *Light Metals*, pages 1147–1152, 2015.

[37] K. Azari, H. Alamdari, H. Ammar, M. Fafard, A. Adams, and D. Ziegler. Influence of Mixing Parameters on the Density and Compaction Behavior of Carbon Anodes Used in Aluminum Production. *Adv. Mater. Res.*, 409:17–22, 2012.

[38] D. Kocaefe, A. Sarkari, S. Das, S. Amrani, D. Bhattacharyayl, D. Sarkari, Y. Kocaefe, B. Morais, and M. Gagnon. Review of Different Techniques to Study the Interactions Between Coke and Pitch in Anode Manufacturing. *Light Metals*, pages 1045–1050, 2013.

[39] K. L. Hulse. The Paste Plant. In *Anode Manufacture*, pages 21–72. R&D Carbon Ltd., 1st edition, 2000. ISBN 3-9521028-5-7.

[40] F. Keller, P. O. Sulger, M. W. Meier, D. S. Severo, and V. Gusberti. Specific Energy Consumption in Anode Bake Furnaces. *Light Metals*, pages 408–413, 2010.

[41] W. K. Fischer, M. W. Meier, and M. W. Lustenberger. Cooling of Green Anodes after Forming. *Light Metals*, pages 351–357, 1999.

[42] F. H. Becker and F. Goede. Ring pit Furnaces for Baking of High Quality Anodes - an Overview. *Aluminium International*, (9):1–15, 2006.

[43] Riedhammer Gmbh. Carbon Baking Technology: Open Top Anode Baking Furnace, . `http://www.riedhammer.de/System/00/00/95/9565/ed_deDE/Internetversion.pdf`. [Last accessed: 2018-12-11].

[44] Riedhammer Gmbh. Carbon Baking Technology: Closed Type Baking Furnace, . `http://www.riedhammer.de/System/00/00/95/9566/ed_enUS/Internetversion.pdf`. [Last accessed: 2018-12-11].

[45] F. Keller and P. O. Sulger. Basics of Anode Baking. In *Anode baking*, pages 61–105. R & D Carbon Ltd., 2008. ISBN 978-2-940348-19-0.

[46] Riedhammer GmbH. Baking Furnaces for Anodes of Highest Quality. *Aluminium*, 88(7-8):32–35, 2012.

[47] T. Brandvik, Z. Wang, A. P. Ratvik, and T. Grande. Autopsy of Refractory Lining in Anode Kilns with Open and Closed Design. *Int. J. Appl. Ceram. Technol.*, 16(2): 602–613, 2019.

[48] A. Seltveit. Hovedkvaliteter. In *Ildfaste Materialer*, pages 165–337. Tapir forlag, 2nd edition, 1992. ISBN 82-519-0971-6.

[49] H. Barthel, G. Routschka, and C. Majcenovic. Introduction. In *Refractory Materials: Pocket Manual - Design, Properties, Testing*, pages 1–16. Vulkan Verlag, 3rd edition, 2008.

[50] C. Sadik, I. El Amrani, and A. Albizane. Recent Advances in Silica-Alumina Refractory: A review. *J. Asian Ceram. Soc.*, 2(2):83–96, 2014.

[51] O.-J. Siljan, C. Schoning, and T. Grande. State-of-the-art Alumino-silicate Refractories for al Electrolysis Cells. *JOM*, 54(5):46–55, 2002.

[52] N. Oumarou, D. Kocaefe, and Y. Kocaefe. Investigation of the Refractory Bricks Used for the Flue Wall of the Horizontal Anode Baking Ring Furnace. *Ceram. Int.*, 42(16):18436–18442, 2016.

[53] F. Brunk. Corrosion and Behavior of Fireclay Bricks Used in the Flues of Open Anode Baking Furnaces. *Light Metals*, pages 641–646, 1995.

[54] D. A. Jarvis. Refractories in the Industrial Production of Aluminium and its Alloys. *Interceramic Refractories*, pages 68–71, 2010.

[55] C. Schøning, T. Grande, and O.-J. Siljan. Cathode Refractory Materials for Aluminium Reduction Cells. *Light Metals*, pages 231–238, 1999.

[56] D. Frulli. Production and Properties of Refractory Raw Materials Based on Andalusite and Mullite - Influence of Impurities in the Refractory Behaviour. *Refractories Worldforum*, 8(3):1–4, 2016.

[57] G. Routschka, K. Santowski, and E. Goerenz. Dense shaped refractory products. In *Refractory materials: Pocket manual - Design, properties, testing*, pages 61–85. Vulkan Verlag, 3rd edition, 2008.

[58] A. Seltveit. Materialegenskaper. In *Ildfaste Materialer*, chapter 5, pages 105–160. Tapir forlag, 2nd edition, 1992. ISBN 82-519-0971-6.

[59] B. Amrane, E. Ouedraogo, B. Mamen, S. Djaknoun, and N. Mesrati. Experimental Study of the Thermo-mechanical Behaviour of Alumina-silicate Refractory Materials Based on a Mixture of Algerian Kaolinitic Clays. *Ceram. Int.*, 37:3217–3227, 2011.

[60] C. N. Djangang, A. Elimbi, U. C. Melo, G. L. Lecomte, C. Nkoumbou, J. Soro, J. Yvon, P. Blanchart, and D. Njopwouo. Refractory Ceramics From Clays of Mayouom and Mvan in Cameroon. *Appl. Clay Sci.*, 39:10–18, 2008.

[61] D. W. Richerson. Mechanical Behavior and Measurement. In *Modern Ceramic Engineering*, pages 211–242. Taylor & Francis group CRC Press, 2006. ISBN 1-57444-693-2.

[62] R. M. Spriggs. Expression for Effect of Porosity on Elastic Modulus of Polycrystalline Refractory Materials, Particularly Aluminum Oxide. *Sci. Sinter.*, 18(1): 68–70, 1986.

[63] F. P. Knudsen. Effect of Porosity on Young's Modulus of Alumina. *J. Am. Ceram. Soc.*, 45(2):94–95, 1962.

[64] S. M. Lang. Properties of High-temperature Ceramics and Cermets-elastisity and Density at Room Temperature. *Natl. Bur. Standards Monograph*, 6, 1960.

[65] D. H. Chung. Elastic and Anelastic Properties of Fine-grained Polycrystalline Alumina at Elevated Temperatures. *Bull. Ceram. Res*, 26(297), 1961.

[66] W. H. Duckworth, J. K. Johnston, L. R. Jackson, and H. Z. Schofield. Mechanical Properties of Ceramic Bodies. Technical report, Battelle memorial institute report to Office of naval research, 1950.

[67] R. M. Spriggs and T. Vasilos. Effect of Grain Size and Porosity on Transverse Bend Strength and Elastic Modulus of Hot-pressed Alumina and Magnesia. *Am. Ceram. Soc. Bull.*, 40(4):187, 1961.

[68] B. L. Majumder. Young's Modulus of Elasticity of Ceramic Materials by Flexture. *Trans. Ind. Ceram. Soc.*, 11(3):168–181, 1952.

[69] H. Z. Schofield, J. F. Lynch, and W. H. Duckworth. Fundamental Studies of Ceramic Materials. Technical report, Battelle memorial institute report to Office of naval research, 1949.

[70] R. L. Coble and W. D. Kingery. Effect of Porosity on Physical Properties of Sintered Alumina. *J. Am. Ceram. Soc.*, 39(11):377–385, 1956.

[71] J. Li, T. Mattila, and V. Vuorinen. MEMS Reliability. In *Handbook of Silicon Based MEMS Materials and Technologies*, pages 744–763. 2015. doi: http://dx.doi.org/10.1016/B978-0-323-29965-7.00041-5.

[72] D. W. Richerson. Time, Temperature, and Environmetal Effects on Properties. In *Modern Ceramic Engineering*, pages 243–283. Taylor & Francis group CRC Press, 2006. ISBN 1-57444-693-2.

[73] T. G. Langdon. Identifying Creep Mechanisms in Plastic Flow. *Z. Metallkd.*, 96 (5):522–531, 2005.

[74] L. B. Borovkova, E. S. Lukin, and D. N. Poluboyarinov. Creep of Aluminosilicate Refractories. *Ogneupory*, (7):39–43, 1969.

[75] L. V. Sokolova and V. S. Bakunov. Creep in Aluminosilicate Materials. *Keramika*, (5):18–20, 1983.

[76] P. A. Lessing, R. S. Gordon, and K. S. Mazdiyasni. Creep of Polycrystalline Mullite. *J. Am. Ceram. Soc.*, 58(3-4):149, 1975.

[77] A. P. Hynes and R. H. Doremus. High-Temperature Compressive Creep of Polycrystalline Mullite. *J. Am. Ceram. Soc.*, 74(10):2469–2475, 1991.

[78] H. Rahnim, C. Olagnon, G. Fantozzi, and R. Torrecillas. Experimental Characterisation of High Temperature Creep Resistance of Mullite. *Ceram. Int.*, 23:497–507, 1997.

[79] H. Ohira, H. Shiga, M. G. M. U. Ismail, Z. Nakai, T. Akiba, E. Yas, and U. Da. Compressive Creep of Mullite Ceramics. *J. Mater. Sci. Lett.*, 10:847–849, 1991.

[80] H.-T. Lin and P. F. Becher. Creep Behavior of a SiC-Whisker-Reinforced Alumina. *J. Am. Ceram. Soc.*, 73(5):1378–1381, 1990.

[81] E. Tkalcec, R. Nass, T. Krajewski, R. Rein, and H. Schmidt. Microstructure and Mechanical Properties of Slip Cast Sol-Gel Derived Mullite Ceramics. *J. Eur. Ceram. Soc.*, 18:1089–099, 1998.

[82] D. S. Wilkinson. Creep Mechanisms in Multiphase Ceramic Materials. *J. Am. Ceram. Soc.*, 81(2):275–299, 1998.

[83] C. O. Hulse and J. A. Pask. Analysis of Deformation of a Fireclay Refractory. *J. Am. Ceram. Soc.*, 49(6):312–318, 1966.

[84] O.-J. Siljan, T. Grande, and C. Schøning. Refractories for Aluminium Electrolysis Cells Part 4 - Comparison of Laboratory Investigations and Autopsies of Pot Linings. *Aluminium*, (77):809–814, 2001.

[85] C. Schøning and T. Grande. The Stability of Refractory Oxides in Sodium-Rich Environments. *JOM*, 58(2):58–61, 2006.

[86] K. Tschope, C. Schøning, J. Rutlin, and T. Grande. Chemical Degradation of Cathode Linings in Hall-Heroult Cells - An autopsy Study of Three Spent Pot Linings. *Metall. Mater. Trans. B*, 43B:290–301, 2012.

[87] A. Solheim, C. Schøning, and E. Skybakmoen. Reactions in the Bottom Lining of Aluminum Reduction Cells. *Light Metals*, pages 877–882, 2010.

[88] G. Routschka and H. Wuthnow. Appendices. In *Refractory materials: Pocket manual - Design, properties, testing*, pages 425–591. Vulkan Verlag, 3rd edition, 2008.

[89] P. Prigent and M. L. Bouchetou. Gaseous Corrosion of Aluminosilicate Refractories in Anode Baking Furnaces Used for Aluminium Produciton - Part 2. *Interceram*, 58(4):202–209, 2009.

[90] B. Mishra, B. B. Sahu, and B. K. Panda. Failure Mechanism of Alumino Silicate Refractories in Anode Baking Furnace. *Trans. Ind. Ceram. Soc.*, 67(3):147–150, 2008.

[91] K. Tschope. *Degradation of Cathode Lining in Hall-Heroult Cells*. PhD thesis, Norwegian University of Science and Technology (NTNU), Trondheim, 2010.

[92] K. Tschöpe, J. Rutlin, and T. Grande. Chemical Degradation Map for Sodium Attack in Refractory Linings. *Light Metals*, pages 871–876, 2010.

[93] R. Pelletier, C. Allaire, O. Siljan, and A. Tabereaux. The Corrosion of Potlining Refractories: A Unified Approach. *JOM*, (8):18–22, 2001.

[94] O.-J. Siljan, T. Grande, and C. Schøning. Refractories for Aluminium Electrolysis Cells Part 2 - Physical Properties of Penerating Melt, Reduction by Metals and Volatile Fluorides. *Aluminium*, (77):385–390, 2001.

[95] O.-J. Siljan, T. Grande, and C. Schøning. Refractories for Aluminium Electrolysis Cells Part 3 - Laboratory Test for Cryolite Resistance. *Aluminium*, (77):610–615, 2001.

[96] Z. Wang, J. Rutlin, and T. Grande. Sodium Diffusion in Cathode Lining in Aluminium Electrolysis Cells. *Light Metals*, pages 841–847, 2010.

[97] F. Brunk. Corrosion and Behaviour of Fireclay Bricks of Varying Chemical Composition Used in Bottom Lining of Reduction Cells. *Light Metals*, pages 477–482, 1994.

[98] O.-J. Siljan. *Sodium Aluminium Fluoride Attack on Alumino Silicate Refractories*. Phd, Norges Teknisk Naturvitenskapelige Universitet (NTNU), 1990.

[99] R. Pelletier and C. Allaire. Corrosion in Potlining Refractories: Effect of Cathode Material Interpreted Using a Unified Approach. *JOM*, 55(11):58–62, 2003.

[100] A. V. Proshkin and D. A. Simakov. State of the Art and Trends in the Development of Base Plate Materials for Aluminum Electrolysis Cells. *Refract. Ind. Ceram.*, 46 (2):104–109, 2005.

[101] A. V. Proshkin, A. M. Pogodaev, P. V. Polyakov, V. V. Pingin, and I. A. Yarosh. Properties of Refractory Materials for Primary Aluminium Production Electrolyzers. *Refract. Ind. Ceram.*, 49(2):84–89, 2008.

[102] M. Sørlie and H. A. Øye. Laboratory Testing of Carbon Cathode Materials at Operational Temperatures. *Light Metals*, pages 625–631, 1989.

[103] A. M. Pogodaev, A. V. Proshkin, P. V. Polyakov, A. F. Shimansky, I. S. Yakimov, and I. A. Yarosh. Processes in Refractory Materials of the Cathode Assembly of Electrolysis Cells for Aluminum Production. *Russ. J. Non-Ferr. Met.*, 51(4):279–284, 2010.

[104] O.-J. Siljan, T. Grande, and C. Schøning. Refractories for aluminium electrolysis cells. Part I : Deterioration mechanisms based on phase equilibria. *Aluminium*, 77 (4):294–300, 2001.

[105] J. Butter and A. Bongers. Alterations of Anode Baking Furnace Bricks During Operation. *Light Metals*, pages 633–639, 1995.

[106] P. R. T. Tiba, B. H. Teider, F. Figueirdo, J. B. Gallo, and V. C. Pandolfelli. Systematic Analysis of Flue Wall bricks Used on Anode Baking Furnaces. *Light Metals*, pages 1015–1019, 2010.

[107] M. C. Franken, S. J. Everstein, P. S. van Berkel, and R. M. Feldmann. LP bricks; a New Generation of Refractories That Meet Higher Demands in Anode Baking Furnaces. *Light Metals*, pages 709–713, 2005.

[108] T. Tonnesen and R. Telle. Anode Baking Furnaces – Wear of Applied Refractories. *Refractories Worldforum*, 1(2):84–89, 2009.

[109] J. Butter. Recycling of Anode Baking Furnace Refractory Bricks. *Light Metals*, pages 633–640, 1994.

[110] M. Zaidani, R. K. A. Al-Rub, A. R. Tajik, Z. A. Qureshi, and T. Shamim. The Influence of Flue Wall Deformation on Anode Baking Homogeneity for the Aluminum Production. *Travaux 46, Proceedings of 35th International ICSOBA Conference*, pages 685–698, 2017.

[111] F. Keller and P. O. Sulger. Anode Bake Furnace Operation. In *Anode Baking*, pages 163–239. R&D Carbon Ltd., 2008. ISBN 978-2-940348-19-0.

[112] Powder Diffraction File database - International Center for Diffraction Data. `http://www.icdd.com/index.php/pdf-4/`. [Last accessed: 2019-08-09].

[113] T. Ban. Structure Refinement of Mullite by the Rietveld Method and a New Method for Estimation of Chemical composition. *J. Am. Ceram. Soc.*, 75(1):227–230, 1992.

[114] R. T. Downs and D. C. Palmer. The Pressure Behavior of Alpha Cristobalite. *Am. Mineral.*, 79(1-2):9–14, 1994.

[115] T. F. W Barth. The Cristobalite structres: I. High-Cristobalite. *Am. J. Sci.*, 23:350, 1932.

[116] A. Benhammou, Y. El Hafiane, A. Abourriche, Y. Abouliatim, L. Nibou, A. Yaacoubi, N. Tessier-Doyen, A. Smith, and B. Tanouti. Influence of Sintering Temperature on the Microstructural and Mechanical Properties of Cordierite Synthesized From Andalusite and Talc. *Mater. Lett.*, 172:198–201, 2016.

[117] W. A. Dollase and W. H. Baur. The Superstructure of Meteoritic Low Tridymite Solved by Computer Simulation. *Am. Mineral.*, 61:971–978, 1976.

[118] International Standard. ISO 5017:2013 Dense shaped refractory products - Determination of bulk density, apparent porosity and true porosity. `https://www.iso.org/standard/56179.html`. [Last accessed: 2019-08-23].

[119] ImageJ website. `https://imagej.nih.gov/ij/`. [Last accessed: 2019-08-17].

[120] Kanthal APM datasheet, Sandvik Group, Sweden. `https://www.kanthal.com/en/products/material-datasheets/tube/kanthal-apm/`. [Last accessed: 2019-07-01].

[121] T. Brandvik, H. Gaertner, A. P. Ratvik, T. Grande, and T. A. Aarhaug. In Situ Monitoring of Pit Gas Composition During Baking of Anodes for Aluminum Electrolysis. *Metall. Mater. Trans. B*, 50(2):950–957, 2019.

[122] C. W. Bale, E. Bélisle, P. Chartrand, S. A. Decterov, G. Eriksson, A. E. Gheribi, K. Hack, I.-H. Jung, Y.-B. Kang, J. Melançon, A. D. Pelton, S. Petersen, C. Robelin, J. Sangster, P. Spencer, and M.-A. Van Ende. FactSage Thermochemical Software and Databases - Recent Developments. *Calphad*, 54:35–53, 2009.

[123] FactSage database documentation. `http://www.crct.polymtl.ca/fact/documentation/FSData.htm#FACT53`. [Last accessed: 2019-08-09].

[124] N. Ottosen and H. Petersson. Introduction. In *Introduction to the Finite Element Method*, chapter 1, pages 1–10. Pearson Education Limited, 1992.

[125] R. Crahmaliuc. 75 Years of the Finite Element Method (FEM), 2019. `https://www.simscale.com/blog/2015/11/75-years-of-the-finite-element-method-fem/`. [Last accessed: 2019-05-14].

[126] A. Hrennikoff. Solution of Problems of Elasticity by the Framework Method. *J. Appl. Mech.*, 8(4):169–175, 1941.

[127] R. Courant. Variational Methods for the Solution of Problems of Equilibrium and Vibrations. *Bull. Am. Math. Soc.*, 49:1–23, 1943.

[128] G. Strang and G. Fix. *An Analysis of the Finite Element Method*. Wellesley-Cambridge Press, 2nd edition, 2008. ISBN 0980232708.

[129] J. Fish and T. Belytschko. Introduction. In *A First Course in Finite Elements*, pages 1–9. Wiley & Sons, 2007.

[130] COMSOL Multiphysics 5.4, www.comsol.com, COMSOL AB, Stockholm, Sweden.

[131] X. Wu, Z. Zhang, G. Piao, X. He, Y. Chen, N. Kobayashi, S. Mori, and Y. Itaya. Behavior of Mineral Matters in Chinese Coal Ash Melting during char-CO_2/H_2O Gasification Reaction. *Energy & Fuels*, 23:2420–2428, 2009.

[132] X. Cao, L. Kong, J. Bai, Z. Ge, C. He, H. Li, Z. Bai, and W. Li. Effect of Water Vapor on Coal Ash Slag Viscosity Under Gasification Condition. *Fuel*, 237:18–27, 2019.

[133] T. Nakamura, G. Petzow, and L. J. Gauckler. Stability of the Perovskite Phase $LaBO_3$ (B = V, Cr, Mn, Fe, Co, Ni) in Reducing Atmosphere I. Experimental Results. *Mater. Res. Bull.*, 14(5):649–659, 1979.

[134] G. Pecchi, C. Campos, and O. Peña. Thermal Stability Against Reduction of $LaMn_{1-y}Co_yO_3$ Perovskites. *Mater. Res. Bull.*, 44:846–853, 2009.

[135] F. Iguchi, Y. Endo, T. Ishida, T. Yokobori, H. Yugami, T. Otake, T. Kawada, and J. Mizusaki. Oxygen Partial Pressure Dependence of Creep on Yttria-Doped Ceria Ceramics. *Solid State Ion.*, (176):641–644, 2005.

[136] M. I. Osende, C. Baudin, M. I. Osendi, and C. Baudin. Mechanical Properties of Mullite Materials. *J. Eur. Ceram. Soc.*, 16(16):217–224, 1996.

[137] L. E. Mong. Elastic Behavior and Creep of Refractory Bricks Under Tensile and Compressive Loads. *J. Res. Nat. Bur. Stand.*, 38(2):229, 1947.

[138] V. M. Panferov, E. Z. Korol', N. V. Pitak, L. N. Turchinova, and T. A. Ansimova. Thermomechanical Properties of Mullite-Corrundum Refractories. *Ogneupory*, 7: 20–24, 1983.

[139] F. J. Klug, S. Prochazka, and R. H. Doremus. Alumina-Silica Phase Diagram in the Mullite Region. *J. Am. Ceram. Soc.*, 70(10):750–759, 1987.

[140] D. E. Damby, E. W. Llewellin, C. J. Horwell, B. J. Williamson, J. Najorka, G. Cressey, and M. Carpenter. The Alpha-Beta Phase Transition in Volcanic Cristobalite. *J. Appl. Crystallogr.*, (47):1205–1215, 2014.

[141] A. J. Perrotta, D. K. Grubbs, E. S. Martin, and N. R. Dando. Chemical Stabilization of β-cristobalite. *J. Am. Ceram. Soc.*, 72(3):441–447, 1989.

[142] M. D. Alcala, C. Real, and J. M. Criado. A New "Incipient-wetness" Method for the Synthesis of Chemically Stabililzed Beta-cristobalite. *J. Am. Ceram. Soc.*, 79(6): 1681–1684, 1996.

[143] O. San and C. Özgür. Investigation of a High Stable Beta-cristobalite Ceramic Powder From CaO-Al_2O_3-SiO_2 System. *J. Eur. Ceram. Soc.*, 29:2945–2949, 2009.

[144] T. Brandvik, Z. Wang, A. P. Ratvik, and T. Grande. Investigations of Spent Refractory Lining in an Anode Baking Furnace. *Light Metals*, pages 1281–1288, 2017.

[145] D. W. Richerson. Densification. In *Modern Ceramic Engineering*, pages 477–527. Taylor & Francis group CRC Press, 2006. ISBN 1-57444-693-2.

[146] I. I. Vishnevskii, L. D. Smirnove, A. V. Kushchenko, and V. S. Shapovalov. Structure and Creep of Mullite-corundum Refractories. *Ogneupory*, (11):9–13, 1985.

[147] R. Torrecillas, G. Fantozzi, S. de Aza, and J. S. Moya. Thermomecanical Behaviour of Mullite. *Acta Mater.*, 45(3):897–906, 1997.

[148] R. Torrecillas, J. M. Calderon, J. S. Moya, M. J. Reece, C. K. L. Davies, C. Olagnon, and G. Fantozzi. Suitability of Mullite for High Temperature Applications. *J. Eur. Ceram. Soc.*, (19):2519–2527, 1999.

[149] H. Ohira, M. G. M. U. Ismail, Y. Yamamoto, T. Akiba, and S. Somiya. Mechanical Properties of High Purity Mullite at Elevated Temperatures. *J. Eur. Ceram. Soc.*, 16:225–229, 1996.

[150] P. Prigent, M. L. Bouchetou, J. Poirier, and P. Hubert. The Effect of the Addition of Fine Andalusite Particles in Refractory Bricks on Gaseous Corrosion. *JOM*, 60 (5):58–63, 2008.

[151] J. R. Uhrig. A unique Refractory Solution for Anode Baking Furnace Flues. *Light Metals*, pages 553–557, 2004.

[152] F. Grégoire and L. Gosselin. Comparison of Three Combustion Models for Simulating Anode Baking Furnaces. *Int. J. Therm. Sci.*, 129:532–544, 2018.

[153] J. Alcaniz-Monge, D. Cazorla-Amoros, and A. Linares-Solano. Characterisation of Coal Tar Pitches by Thermal Analysis, Infrared Spectroscopy and Solvent Fractionation. *Fuel*, 80:41–48, 2001.

[154] O. S. Efimova, G. P. Khokhlova, and Y. F. Patrakov. Thermal Conversion of Coal-Tar Pitch in the Presence of Silicon Compounds. *Solid Fuel Chem.*, 44(1):5–11, 2010.

[155] R. W. Wallouch, H. N. Murty, and E. A. Heintz. Pyrolysis of Coal Tar Pitch Binders. *Carbon*, 10:729–735, 1972.

[156] J. Zieliñski, B. Pacewska, T. Brzozowska, and J. Machnikowski. Studies on Thermal Decomposition of Pitch-Polymer Compositions. *J. Therm. Anal. Calorim.*, 60: 293–297, 2000.

[157] G. C. Reyniers, G. F. Froment, F.-D. Kopinke, and G. Zimmermann. Coke Formation in the Thermal Cracking of Hydrocarbons. 4. Modeling of Coke Formation in Naphtha Cracking. *Ind. Eng. Chem. Res.*, 33:2584–2590, 1994.

[158] M.-F. S. G. Reyniers and G. F. Froment. Influence of Metal Surface and Sulfur Addition on Coke Deposition in the Thermal Cracking of Hydrocarbons. *Ind. Eng. Chem. Res.*, 34:773–785, 1995.

[159] S. M. Sadrameli. Thermal/Catalytic Cracking of Hydrocarbons for the Production of Olefins: A State-of-the-art Review I: Thermal Cracking Review. *Fuel*, 140:102–115, 2015.

[160] W. G. Appleby, J. W. Gibson, and G Good. Advances in Catalysis. *Ind. Eng. Chem. Process. Des. Dev.*, 1(2):102–110, 1948.

[161] P. E. Eberly, C. N. Kimberlin, W. H. Miller, and H. V. Drushel. Coke formation on Silica-Alumina Cracking Catalysts. *Ind. Eng. Chem. Process. Des. Dev.*, 5(2): 193–198, 1966.

[162] Y. Ozawa and K. B. Bischoff. Coke Formation Kinetics on Silica-Alumina Catalyst. *Ind. Eng. Chem. Process. Des. Dev.*, 7(1):67–71, 1968.

[163] Z. Wang, S. Rørvik, A. P. Ratvik, and T. Grande. Formation of Carbon Build-up on the Flue Wall of Anode Baking Furnace. *Light Metals*, pages 1265–1274, 2017.

[164] T. Brandvik, A.P. Ratvik, and T. Grande. Thermodynamic Assessment of the Chemical Durability of Refractory Lining in Anode Baking Furnaces. *Travaux 45, Proceedings of the 34th International ICSOBA Conference*, 2016.

[165] P. R. Zafred, S. W. Sofie, and P. S. Gentile. Progress in Understanding Silica Transport Process and Effects in Solid Oxide Fuel Cell Performance. In *Proceedings of the ASME Eighth International Fuel Cell Science, Engineering and Technology Conference*, pages 421–426, 2010.

[166] S. R. Muller, W. Simon, H. M. Widmer, K. Grolimund, G. Schomburg, and P. Kolla. Reaction of Fused Silica With Hydrogen Gas. *J. Am. Ceram. Soc.*, 65(9):457–460, 1982.

[167] D. I. Butt, R. E. Tressler, and K. I. Spear. Corrosion of SiC Materials in N_2-H_2-CO Gaseous Environments: 1, Thermodynamics and Kinetics of Reactions. *J. Am. Ceram. Soc.*, 75(12):3257–3267, 1992.

[168] N. S. Jacobson. Corrosion of Silicon-Based Ceramics in Combustion Environments. *J. Am. Ceram. Soc.*, 76(1):3–28, 1993.

[169] R. R. Sickafoose Jr. Active Gaseous Corrosion of Porous Silicon Carbide. *J. Am. Ceram. Soc.*, 76(2):316–324, 1993.

[170] E. A. Gulbransen and S. A. Jansson. The High-Temperature Oxidation, Reduction, and Volatilization Reactions of Silicon and Silicon Carbide. *Oxid. Met.*, 4(3):181–201, 1972.

[171] G. R. Belton and F. D. Richardson. A volatile Iron Hydroxide. *Trans. Faraday Soc.*, 58(1):1562–1572, 1962.

[172] P. L. Surman and J. E. Castle. Gas Phase Transport in the Oxidation of Fe and Steel. *Corros. Sci.*, 9(10):771–777, 1969.

[173] D. Trommer, D. Hirsch, and A. Steinfeld. Kinetic Investigation of the Thermal Decomposition of CH_4 by Direct Irradiation of a Vortex-flow Laden with Carbon Particles. *Int. J. Hydrogen Energy*, 29:627–633, 2004.

[174] R. J. Tyler. Intrinsic Reactivity of Petroleum Coke to Oxygen. *Fuel*, 65(2):235–240, 1986.

[175] B. R. Stanmore. Use of the Differential Thermal Gravimetric Analyser for Carbon/Oxygen Reactivity Measurement. *Fuel*, 70(12):1485–1487, 1991.

[176] Prebaked Anodes for Aluminium Electrolysis - Technical report. `https://www.rd-carbon.com/data/documents/publications/general/Prebaked_Anodes_Aluminium_Electrolysis_2014.pdf`. [Last accessed: 2019-08-06].

Appendix A

X-ray diffraction patterns

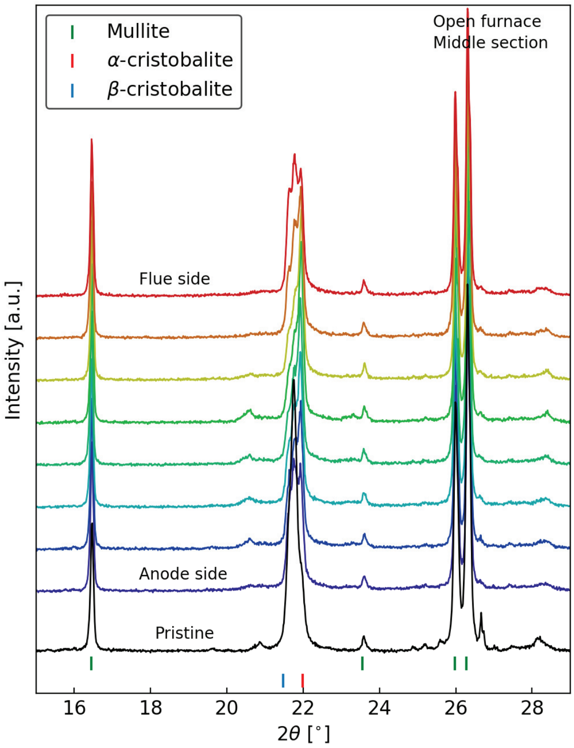

Figure A.1: X-ray diffraction patterns of samples from the middle section of the open top baking furnace compared to the pristine material. The samples are collected at various distance from the anode (in accordance with the sectioning in Figure 3.3), here shown with an offset in intensity to highlight the variations in the cristobalite reflection at ~21.9°.

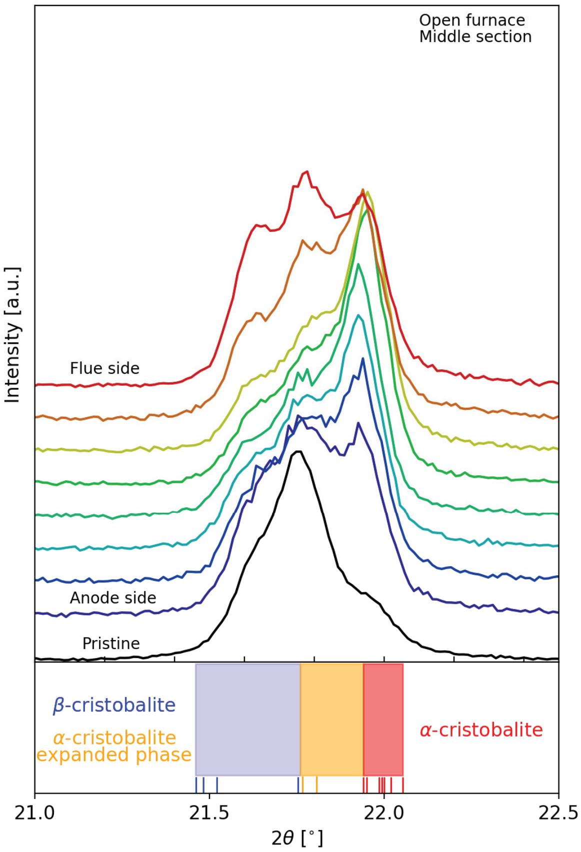

Figure A.2: X-ray diffraction patterns of samples from the middle section of the open top baking furnace compared to the pristine material. The shift between α- and β- cristobalite as a function of distance from the anode is emphasized. The lower part of the figure is adapted from Damby *et al.* [140].

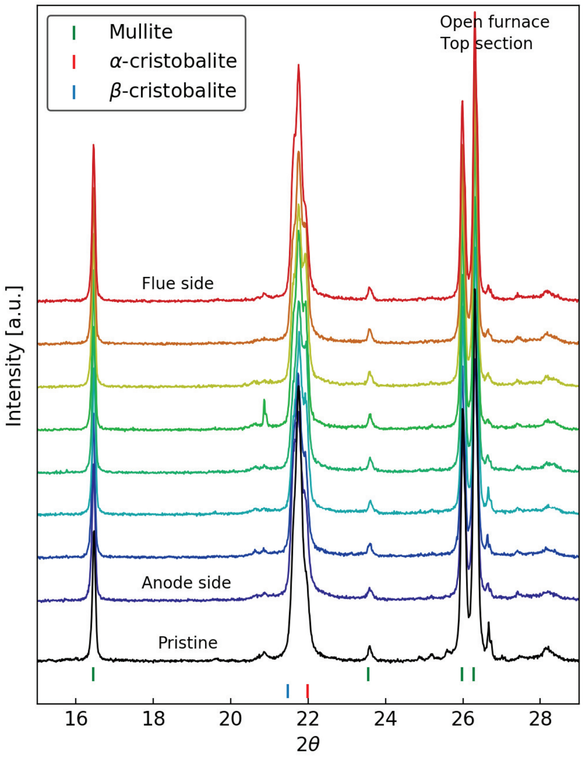

Figure A.3: X-ray diffraction patterns of samples from the top section of the open top baking furnace compared to the pristine material. The samples are collected at various distance from the anode (in accordance with the sectioning in Figure 3.3), here shown with an offset in intensity to highlight the variations in the cristobalite reflection at ∼21.9°.

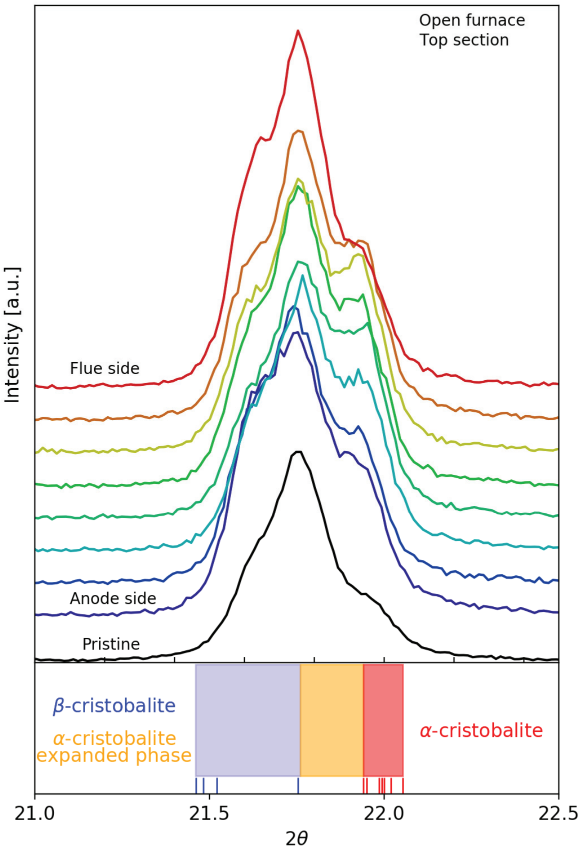

Figure A.4: X-ray diffraction patterns of samples from the top section of the open top baking furnace compared to the pristine material. The shift between α- and β- cristobalite as a function of distance from the anode is emphasized. The lower part of the figure is adapted from Damby *et al.* [140].

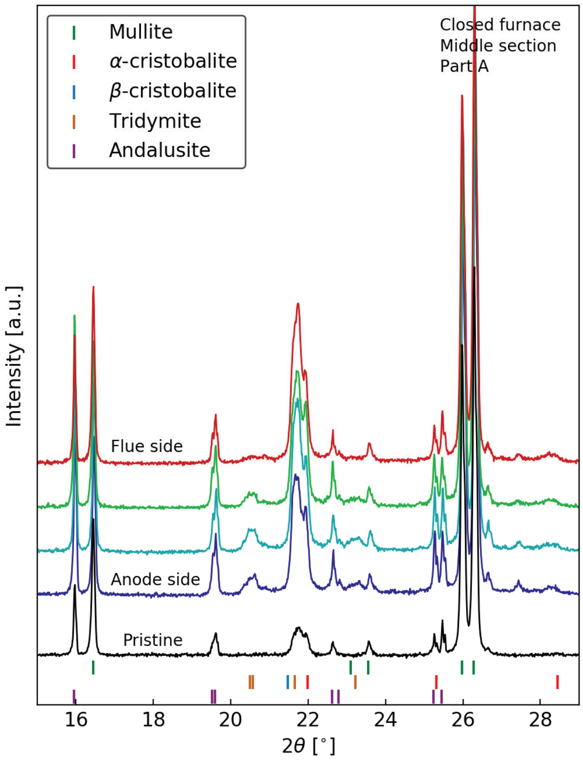

Figure A.5: X-ray diffraction patterns of samples from the middle section of Part A in the closed top baking furnace compared to the pristine material. The samples are collected at various distance from the anode (in accordance with the sectioning in Figure 3.3), here shown with an offset in intensity to highlight the variations in the cristobalite reflection at ∼21.9°.

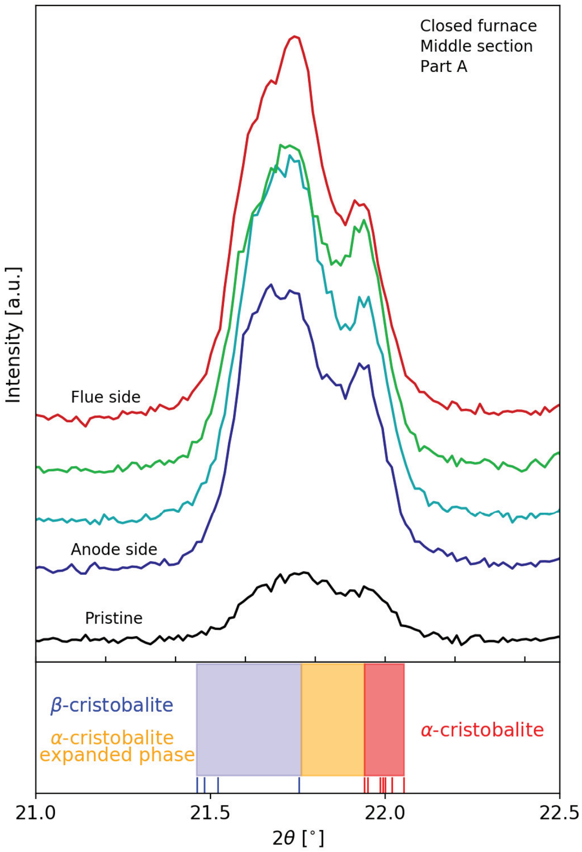

Figure A.6: X-ray diffraction patterns of samples from the middle section of Part A in the closed top baking furnace compared to the pristine material. The shift between α- and β- cristobalite as a function of distance from the anode is emphasized. The lower part of the figure is adapted from Damby *et al.* [140].

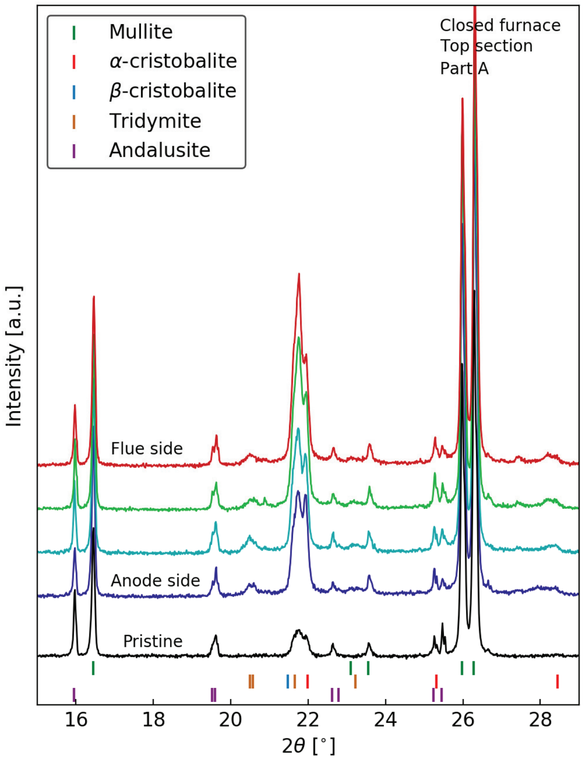

Figure A.7: X-ray diffraction patterns of samples from the top section of Part A in the closed top baking furnace compared to the pristine material. The samples are collected at various distance from the anode (in accordance with the sectioning in Figure 3.3), here shown with an offset in intensity to highlight the variations in the cristobalite reflection at ∼21.9°.

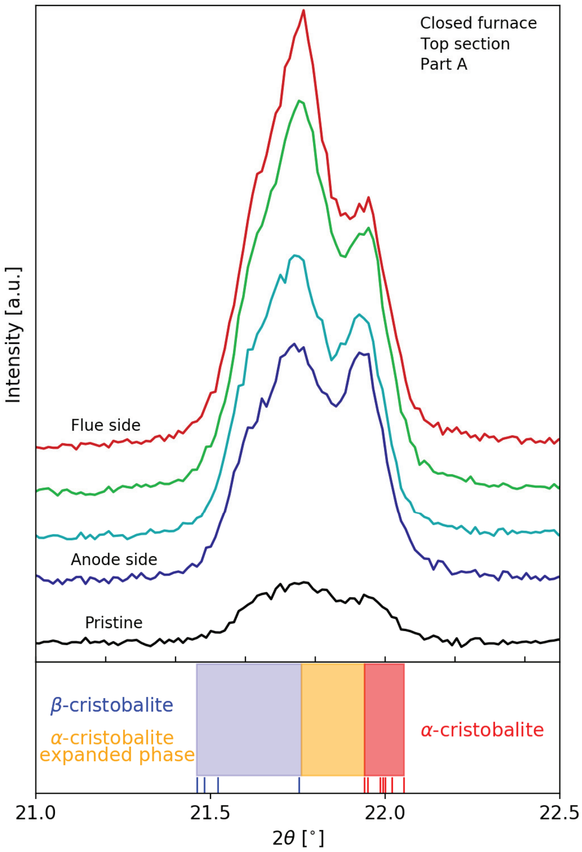

Figure A.8: X-ray diffraction patterns of samples from the top section of Part A in the closed top baking furnace compared to the pristine material. The shift between α- and β- cristobalite as a function of distance from the anode is emphasized. The lower part of the figure is adapted from Damby *et al.* [140].

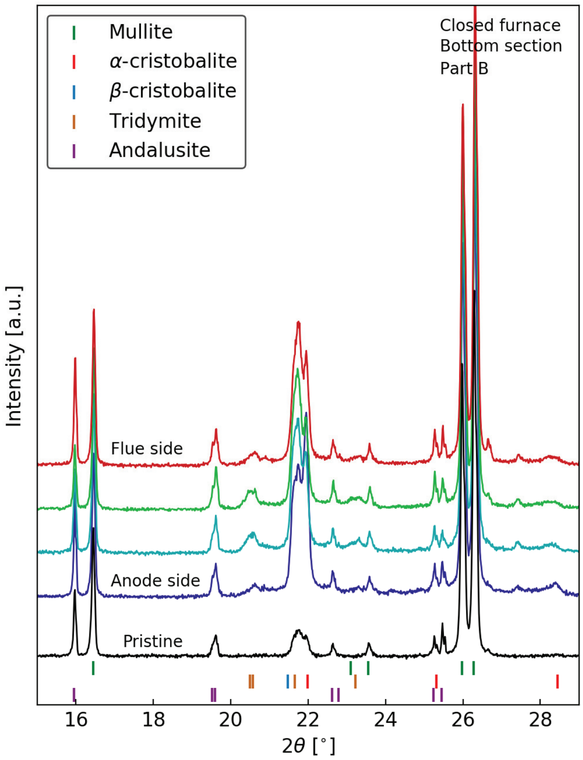

Figure A.9: X-ray diffraction patterns of samples from the bottom section of Part B in the closed top baking furnace compared to the pristine material. The samples are collected at various distance from the anode (in accordance with the sectioning in Figure 3.3), here shown with an offset in intensity to highlight the variations in the cristobalite reflection at ∼21.9°.

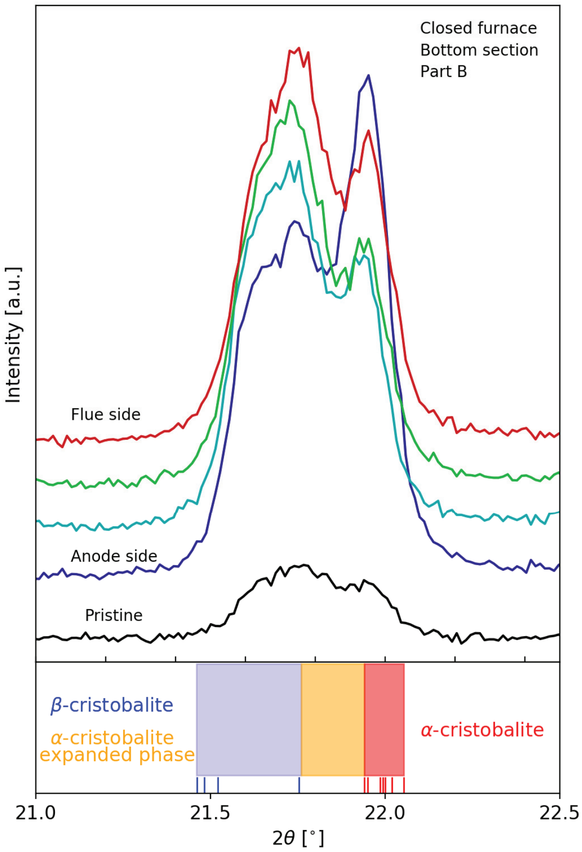

Figure A.10: X-ray diffraction patterns of samples from the bottom section of Part B in the closed top baking furnace compared to the pristine material. The shift between α- and β- cristobalite as a function of distance from the anode is emphasized. The lower part of the figure is adapted from Damby *et al.* [140].

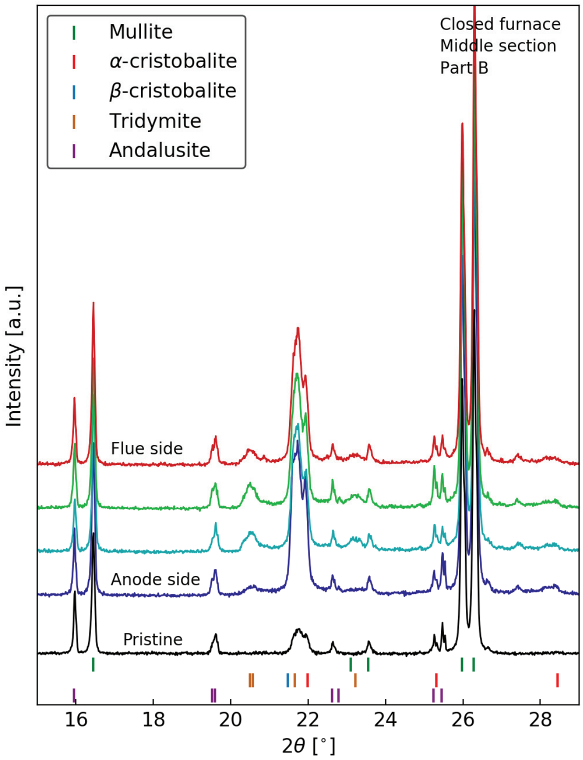

Figure A.11: X-ray diffraction patterns of samples from the middle section of Part B in the closed top baking furnace compared to the pristine material. The samples are collected at various distance from the anode (in accordance with the sectioning in Figure 3.3), here shown with an offset in intensity to highlight the variations in the cristobalite reflection at ~21.9°.

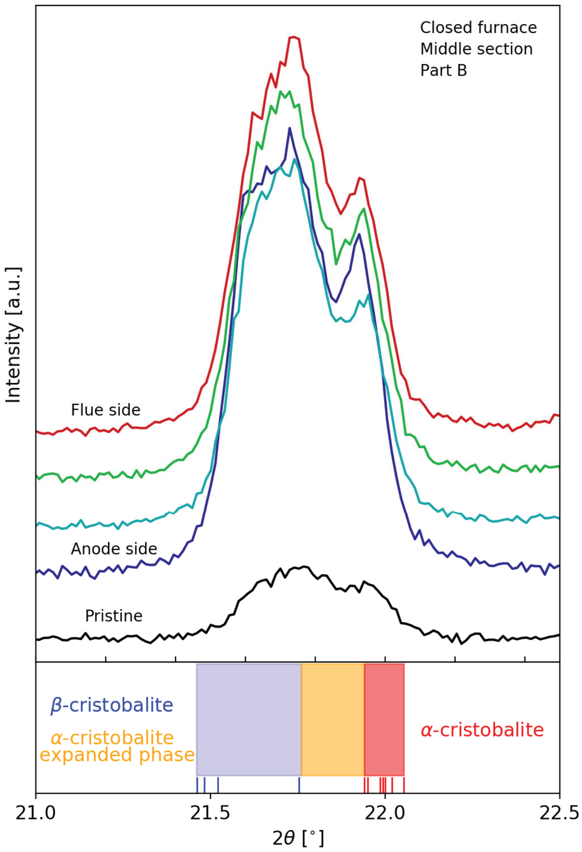

Figure A.12: X-ray diffraction patterns of samples from the middle section of Part B in the closed top baking furnace compared to the pristine material. The shift between α- and β- cristobalite as a function of distance from the anode is emphasized. The lower part of the figure is adapted from Damby *et al.* [140].

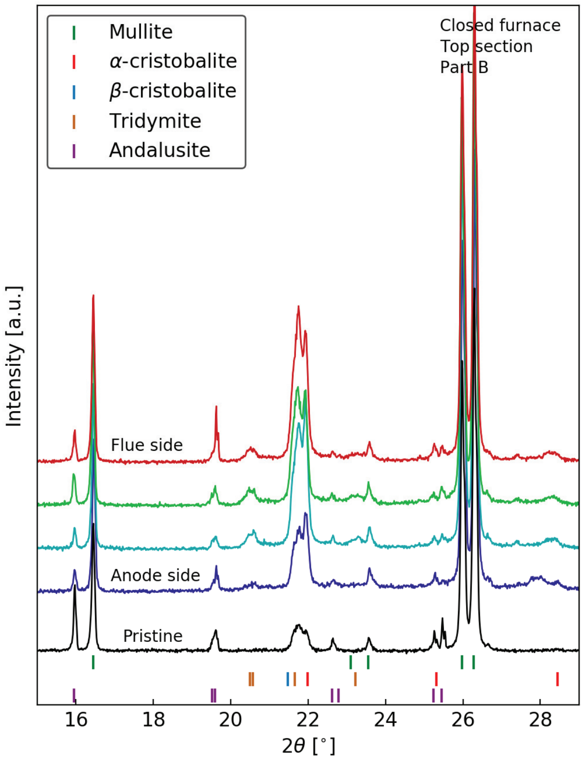

Figure A.13: X-ray diffraction patterns of samples from the top section of Part B in the closed top baking furnace compared to the pristine material. The samples are collected at various distance from the anode (in accordance with the sectioning in Figure 3.3), here shown with an offset in intensity to highlight the variations in the cristobalite reflection at ∼21.9°.

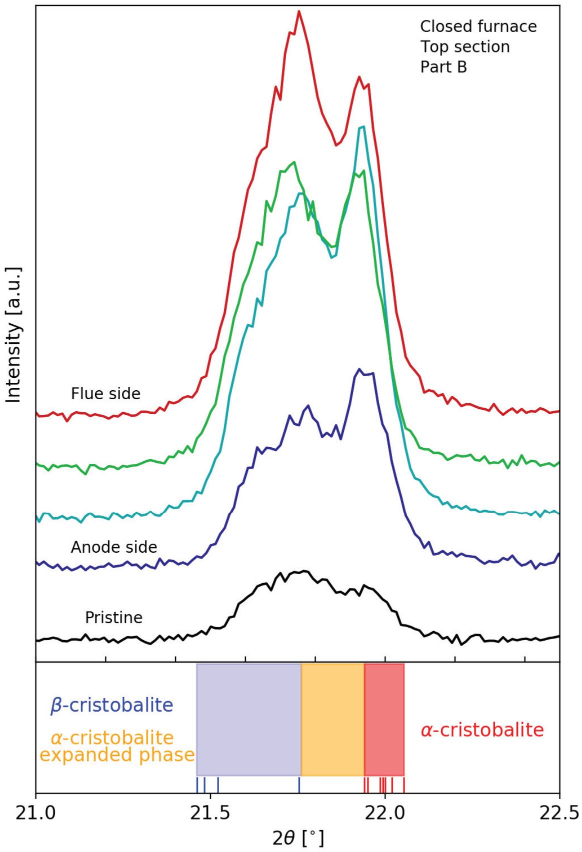

Figure A.14: X-ray diffraction patterns of samples from the top section of Part B in the closed top baking furnace compared to the pristine material. The shift between α- and β- cristobalite as a function of distance from the anode is emphasized. The lower part of the figure is adapted from Damby *et al.* [140].

Appendix B

Scanning electron imaging

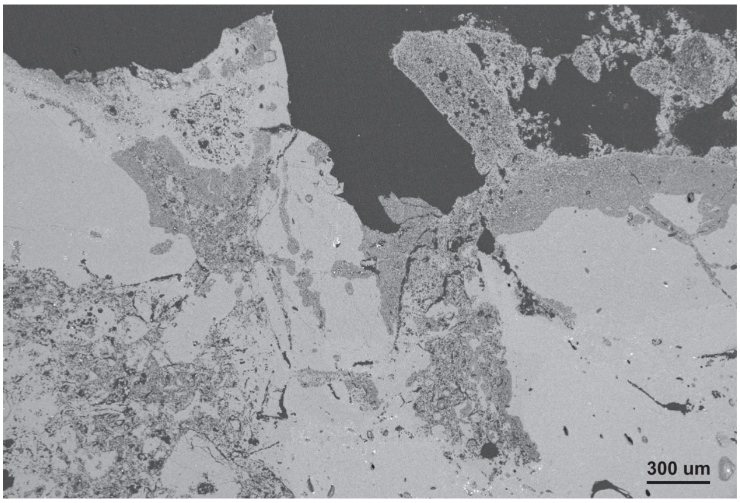

Figure B.1: SEM image of the bottom section of the open furnace with the pit facing surface pointing upwards in the figure. The reacted regions depleted of silicon is clearly visible.

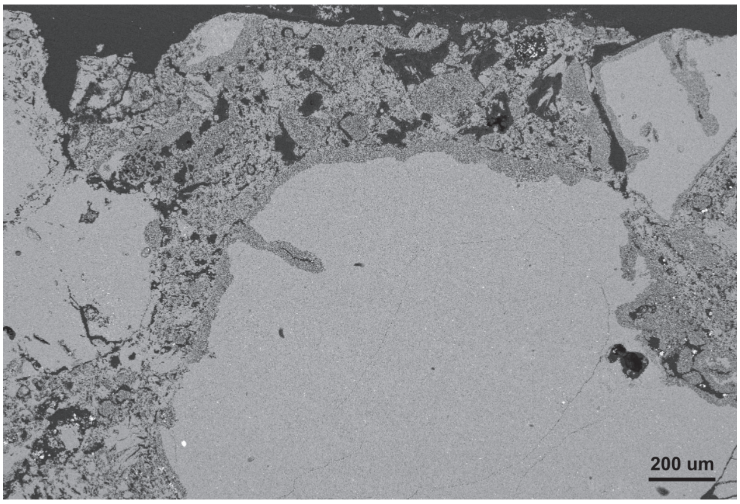

Figure B.2: SEM image of the bottom section of the open furnace with the pit facing surface pointing upwards in the figure. The reacted regions depleted of silicon is clearly visible.

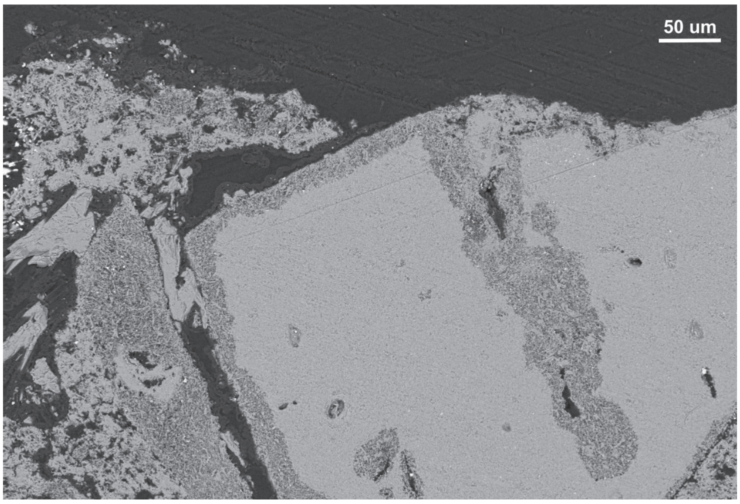

Figure B.3: SEM image of the bottom section of the open furnace with the pit facing surface pointing upwards in the figure. This figure is a smaller section of the top right corner of the image in Figure B.2.

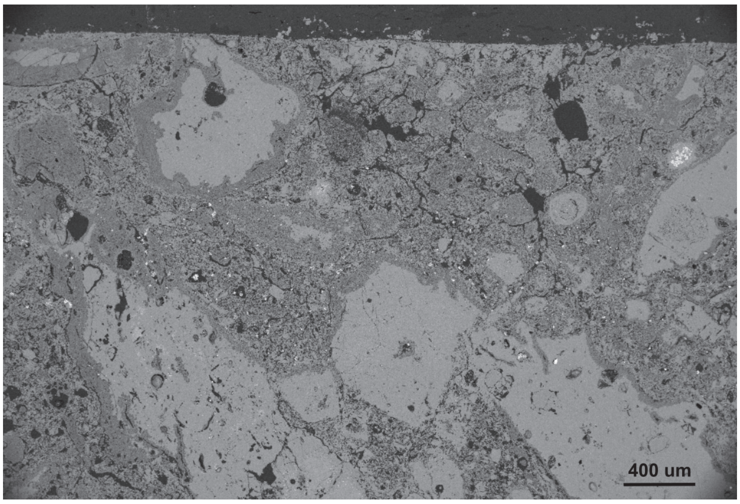

Figure B.4: SEM image of the middle section of the open furnace with the pit facing surface pointing upwards in the figure. The reacted regions depleted of silicon is clearly visible.

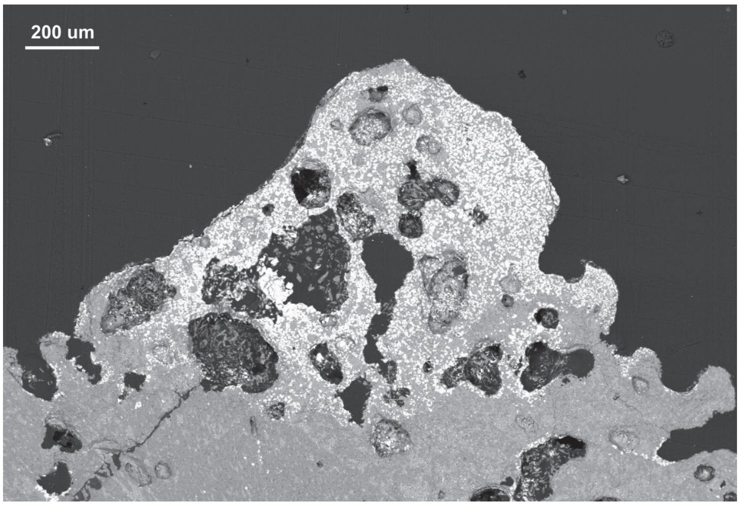

Figure B.5: SEM image of the top section of the closed furnace with the pit facing surface pointing upwards in the figure. The figure shows the distribution of particles with high content of impurity elements as shown by region 4 in Table 4.3.

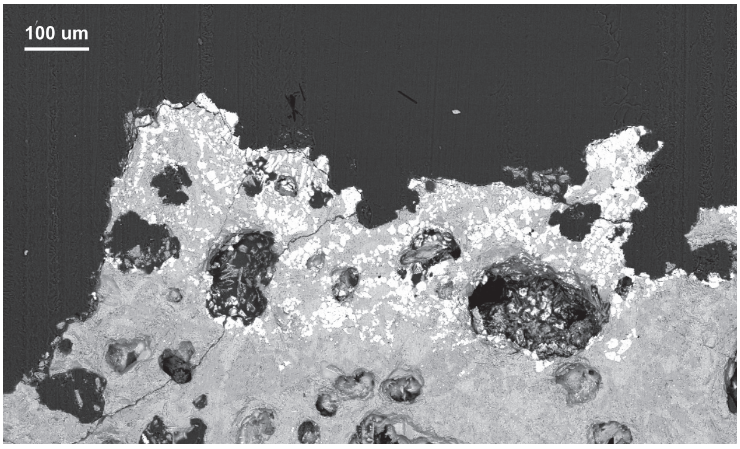

Figure B.6: SEM image of the top section of the closed furnace with the pit facing surface pointing upwards in the figure. The figure shows the distribution of particles with high content of impurity elements as shown by region 4 in Table 4.3.

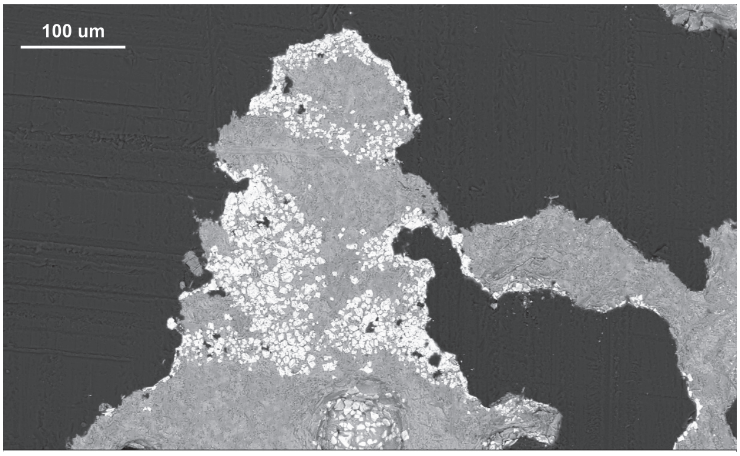

Figure B.7: SEM image of the top section of the closed furnace with the pit facing surface pointing upwards in the figure. The figure shows the distribution of particles with high content of impurity elements as shown by region 4 in Table 4.3.

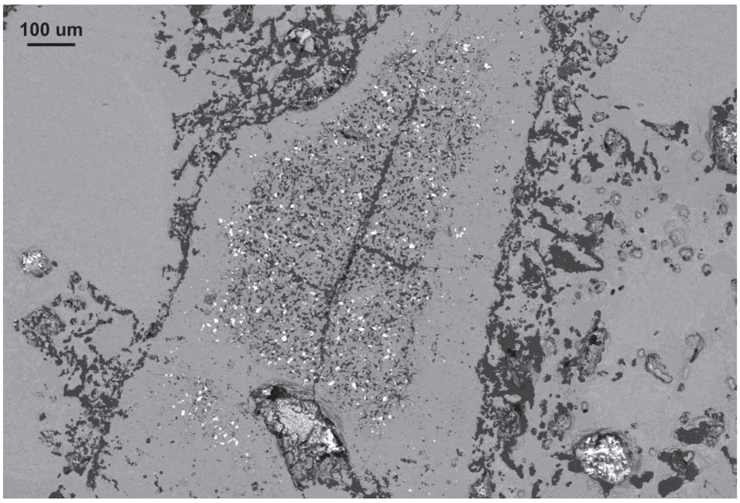

Figure B.8: SEM image of the top section of the closed furnace showing deposition of particles in the open porosity of the lining.

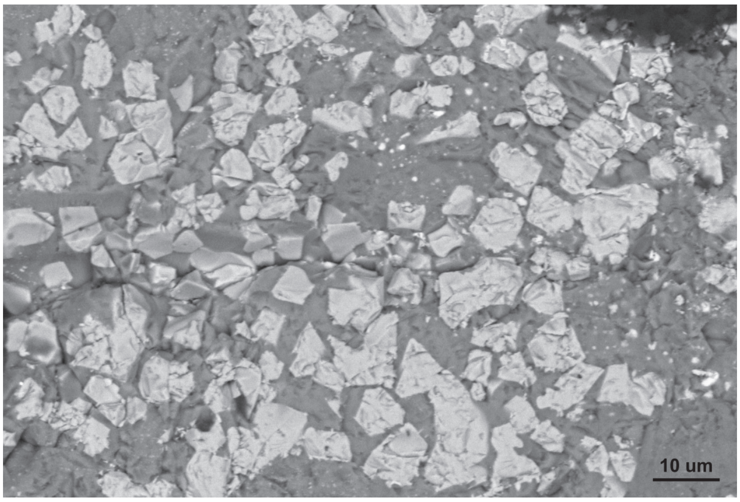

Figure B.9: SEM image of the top section of the closed furnace. The figure shows the distribution of particles with high content of impurity elements as shown by region 4 in Table 4.3.

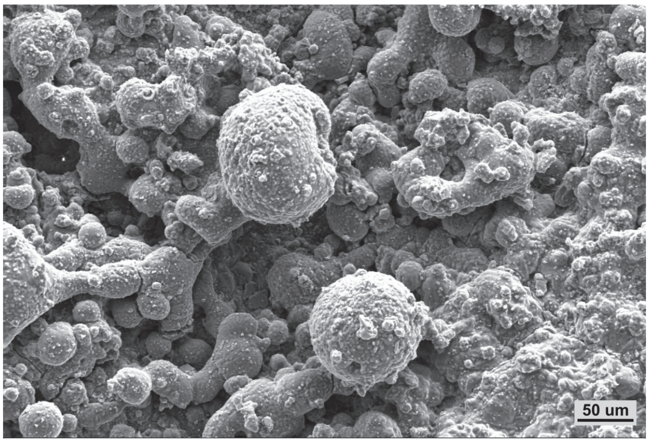

Figure B.10: Detailed SEM image with secondary electron contrast of the particles on the fracture surface in the bottom section of the closed furnace. Both the particles with high silica content and the smaller particles with high content of impurity elements are visible.

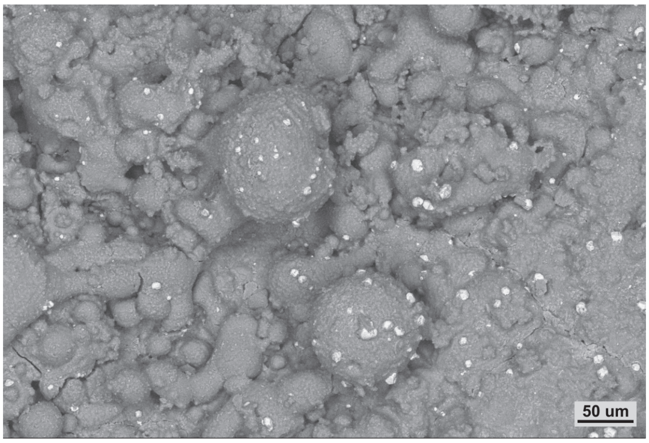

Figure B.11: Detailed SEM image with back scatter electron contrast of the particles on the fracture surface in the bottom section of the closed furnace. Both the particles with high silica content and the particles with high content of impurity elements are visible. The atomic contrast makes it easier to see the particles with high content of impurity elements (white).

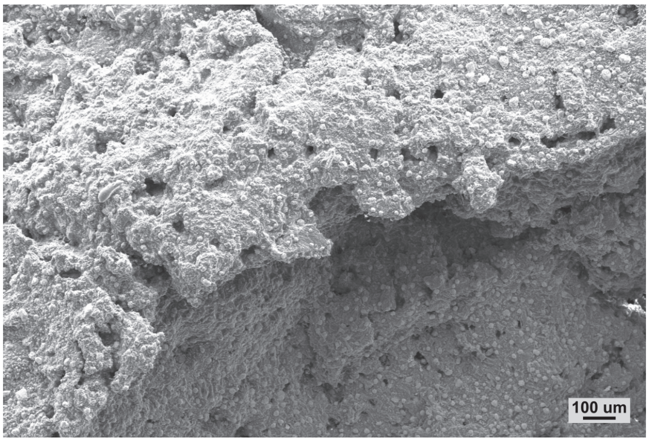

Figure B.12: SEM image of the distribution of particles with high content of impurity elements at the fracture surface in the bottom section of the closed furnace, by secondary electron imaging.

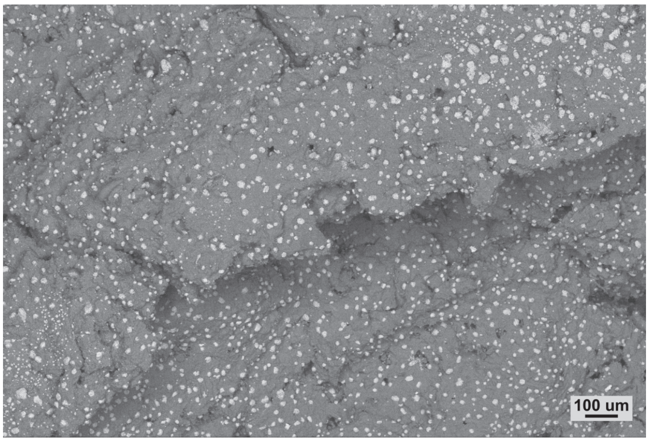

Figure B.13: SEM image of the distribution of particles with high content of impurity elements at the fracture surface in the bottom section of the closed furnace, by back scatter imaging. The atomic contrast makes it easier to see the particles with high content of impurity elements (white).

Appendix C

Energy considerations

Typical fuel cost of anode baking is around 2 GJ/tonnes baked anode [40, 176], in addition to the energy supplied by the burning of the decomposition products from the pitch. By assuming an anode with 10 % porosity and a varying degree of water filling that porosity, the energy related to heating and evaporating the water can be calculated. The anode volume is calculated from average weight (1020 kg) and average density ($1.6\,\mathrm{g\,cm^{-3}}$). The anodes are heated from 25 °C to 150 °C in these calculations, and the energy spent on heating and evaporating water is the related to a fixed total energy consumption. The fraction of energy consumed by the water is presented as a function of water content in the anode in Figure C.1.

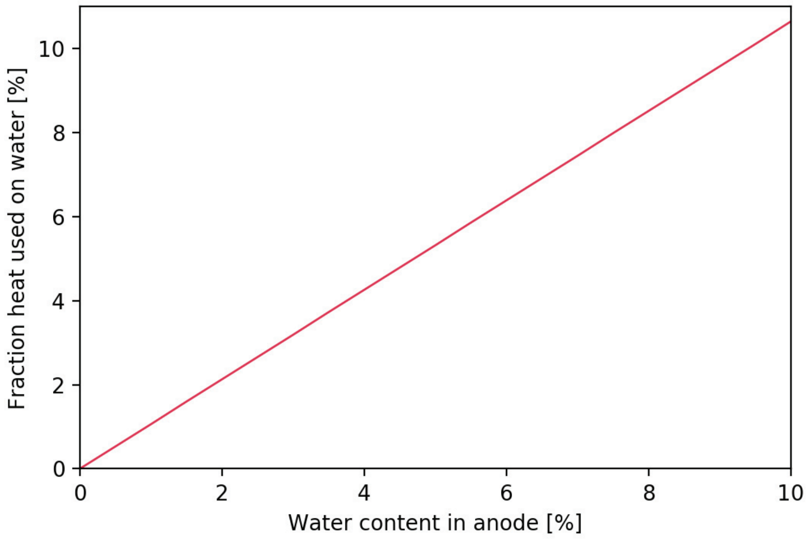

Figure C.1: Fraction of total energy spent on heating and evaporation of water.

Appendix D

Publications

D.1 Conference proceeding 1

T. Brandvik, A. P. Ratvik and T. Grande. Thermodynamic Assessment of the Chemical Durability of Refractory Lining in Anode Baking Furnaces, *Travaux 45, Proceedings of the 34^{th} International ICSOBA Conference*, 2016.

Thermodynamic Assessment of the Chemical Durability of Refractory Lining in Anode Baking Furnaces

Trond Brandvik[1], Arne Petter Ratvik[2], and Tor Grande[3]
1. PhD Candidate
3. Professor
Department of Materials Science and Engineering, Norwegian University of Science and Technology (NTNU), Trondheim, Norway
2. Senior Research Scientist, SINTEF Materials and Chemistry, Trondheim, Norway
Corresponding author: trond.brandvik@ntnu.no

Abstract

The aluminosilicate refractory lining in anode baking furnaces undergoes thermal cycling and are exposed to harsh chemical environments. Consequently, the thermal stability and chemical durability of the refractory material is important for the lifetime of the lining. Here, we present a thermodynamic assessment of the stability of the aluminosilicate materials resembling the chemical environment of the anode baking furnace. Volatile species (NaF, $NaAlF_4$, SiO, CO, etc.) from anodes were identified based on typical chemical composition of green anodes. The most likely chemical reactions of the volatile species and the oxide components in the lining are evaluated. The variation in the volatility of substances due to the thermal cycling and reducing conditions during anode baking was examined in particular. Changes in the mineralogical composition in the lining were predicted based on the thermodynamic calculations and these are summarized in form of isothermal predominance phase diagrams. Formation of sodium aluminosilicate phases and volatile SiF_4 are proposed to be the main consequence of the chemical degradation of the lining due to traces of the cryolite in the green anodes.

Keywords: Anode baking furnace; refractory lining; degradation.

1. Introduction

Carbon anodes constitute an important part in the process of aluminum electrolysis [1,2]. Today, mostly pre-baked carbon anodes are used in modern electrolysis plants due to their higher current efficiency, lower cell voltage and lower energy consumption, compared to the Søderberg anodes [3,4]. The production of pre-baked anodes takes place in anode baking furnaces, separated from the electrolysis process. The principle of pre-baked anode production is quite similar from plant to plant, with some variations with respect to the furnace design [5], i.e. open or closed furnace. Green anodes, made out of coke, recycled anode butts and pitch, are stacked within the furnace and exposed to thermal treatment. As the green anodes are heated up, the structural integrity is reduced when reaching the softening point of the pitch [5]. To prevent any deformation, the green anodes are placed in a confined space (the pit) with no room for movement. To avoid carbon oxidation during baking, the anodes are covered with packing material, usually fine-grained carbon materials such as petroleum coke or metallurgical coke [5]. The recycled anodes used as a precursor in green anode production originates from the electrolysis cell, where the anodes are taken out of operation when they reach approximately 20-25 % of their original size. Besides the anode cover materials, the anodes are exposed to the cryolite bath during operation, and some of the bath and anode cover materials are transferred with the anodes. Impurities, like sodium and fluorine, originating from frozen bath and anode cover materials, are therefore found in increased amounts in the green anodes compared to the expected amounts based on the impurity level of the petroleum coke [1,6].

In the anode baking furnace, the anodes are separated from the hot flue gas by aluminosilicate refractory walls. The operational temperature in the furnace cycles from ambient conditions to 1200-1300 °C in cycles of 20-30 days. During the heat cycle, the cryolite contamination in the green anodes will evaporate as gas species such as NaF and $NaAlF_4$. The presence of such gaseous species will, together with the temperature cycling under reducing conditions, create harsh operational environments for the refractory walls. In time, the refractory wall will degrade causing its operational performance to decrease, and ultimately lead to the need of replacement of the lining [7,8].

Mineralogical changes in refractory materials due to exposure to sodium and fluorine containing compounds have been thoroughly investigated during the last couple of decades [1,2,7–18]. The focus has primarily been on cathode refractory lining in aluminum electrolysis cells. When aluminosilicate refractories are exposed to sodium fluoride, a series of reactions occur, depending on the silica/alumina ratio in the bricks and the amount of fluoride. The main reaction products are the sodium aluminosilicate phases nepheline ($NaAlSiO_4$) and albite ($NaAlSi_3O_8$), together with cryolite (Na_3AlF_6) and β-alumina ($NaAl_9O_{14}$ or $NaAl_{11}O_{17}$) [9,10]. In addition, both SiF_4 and $NaAlF_4$ have been detected during melt intrusion, constituting the dominating gas specie for high and low silica content respectively [11]. The phase stability of aluminosilicate refractories during NaF exposure has been summarized in a degradation map, primarily based on mass balances [9]. Later, Tschöpe et al. [17] investigated the phase stability in aluminosilicate refractories during exposure to Na(g). The result was summarized in a similar degradation map. Autopsy of a lining from anode baking furnaces have revealed the presence of mullite ($Al_6Si_2O_{13}$), corundum and cristobalite, in addition to an amorphous phase [1,2,7]. The amorphous phase was most abundant close to the anode side of the refractory, corresponding with elevated sodium content in the samples. No sign of fluorides was found in the spent lining [1,2,7].

In this work, a thermodynamic assessment of the chemical stability of the aluminosilicate refractories during anode baking is reported. First, possible reactions between the refractory material and volatile fluorides originating from the recycled anode butts are evaluated. These findings are summarized in form of degradation maps, and compared to similar findings for the degradation of refractory materials in aluminum electrolysis cells. Finally, the effect of other trace impurities in the green anodes and the effect of reducing conditions during the baking process are evaluated.

3. Method

In order to investigate phase stability in aluminosilicate refractories during exposure of volatile sodium fluorides, a thermodynamic assessment was carried out. The thermochemical software FactSage (version 7.0) was used to carry out equilibrium calculations through minimization of Gibb's energy. FactSage is a thermochemical software containing various modules and databases, enabling the user to do a variety of equilibrium calculations [19]. In this work, the *Equilibrium* module has been used in combination with the *FactPS* database to analyze the phase composition during various amounts of NaF and $NaAlF_4$. The objective of this assessment has been to predict chemical stability for aluminosilicate materials as a function of NaF or $NaAlF_4$ exposure. The compositional range from pure silica to pure alumina was thus investigated. From a refractory corrosion perspective, a "worst case" scenario has been investigated, with increasing amount of volatile sodium fluorides at a temperature in the upper region of the operational conditions (1300 °C).

3. Results

3.1. Reaction with Volatile Fluorides

The major gas species in equilibrium with liquid cryolite at 1300 °C are $NaAlF_4$ and NaF described by the chemical equilibrium

$$Na_3AlF_6(liq) = 2\ NaF(g) + NaAlF_4(g) \qquad (1)$$

The partial pressure of the volatile fluorides is in the range of 10^{-2} ($NaAlF_4$) and 10^{-1} bar (NaF) at 1300 °C. The chemical reaction of these two volatile fluorides with each of the two main components in the refractory material (SiO_2 or Al_2O_3) was investigated in order to determine the oxide stability for each combination. $NaAlF_4$ is found to be coexistent with Al_2O_3, while NaF reacts with Al_2O_3 according to Equation 2. SiO_2, on the other hand, is not coexistent with neither NaF nor $NaAlF_4$, and reacts according to Equations 3 and 4. Reaction 2 and 3 are strongly shifted to the right, while reaction 4 is far more sensitive to the partial pressure of the two gases.

$$4NaF(g) + 14Al_2O_3(s) = 3NaAl_9O_{14} + NaAlF_4(g) \qquad (2)$$

$$NaAlF_4(g) + 4SiO_2(s) = SiF_4(g) + NaAlSi_3O_8 \qquad (3)$$

$$4NaF(g) + 5SiO_2(s) = 2Na_2Si_2O_5 + SiF_4(g) \qquad (4)$$

This simple analysis illustrates that the presence of either SiO_2 or Al_2O_3 will result in formation of sodium aluminosilicates, sodium disilicate, β-alumina and volatile $SiF_4(g)$, where the latter will be transported out of the anode baking furnace.

3.2. $NaAlF_4$ Exposure

The degradation map for aluminosilicate refractories due to reaction with $NaAlF_4$ is shown in Figure 1. The map is constructed based on a combination of the thermodynamic assessment and the mass balances of the dominating reactions found by thermodynamic calculations. This is not a true phase diagram, but rather a diagram presenting the thermodynamically stable condensed phases for a given material composition and amount of $NaAlF_4$. Six regions with the corresponding stable condensed phases for each region are displayed in the diagram. With increasing amount of $NaAlF_4$ for a given composition of aluminosilicate material, a series of chemical reactions occur. The red arrow in Figure 1 indicates the reaction path for a refractory lining with 70 mol% SiO_2 and 30 mol% Al_2O_3 when exposed to an increasing amount of $NaAlF_4$.

The main reactions in region 1, 2 and 3 along the reaction path are summarized in Table 1. In Figure 2, the concentrations of each specie during the same reaction path are given as a function of the amount of $NaAlF_4$. In between region 1, 2 and 3, there are regions with no change in phase composition except the increasing activity of $NaAlF_4$. These are the regions that only have two stable condensed phases. The constant amount of phases in these regions is explained by Figure 3, where the chemical potential for the main gaseous species, $NaAlF_4$ and SiF_4, is plotted along the reaction path. In region 1, 2 and 3 the chemical potential for $NaAlF_4$ is constant, while it increases in the intermediate regions. At some point, the chemical potential reaches the threshold for the next reaction, indicated by the boundaries in Figure 1. There are some discrepancies between the boundaries in the degradation map in Figure 1 and the region borders in Figures 2 and 3.

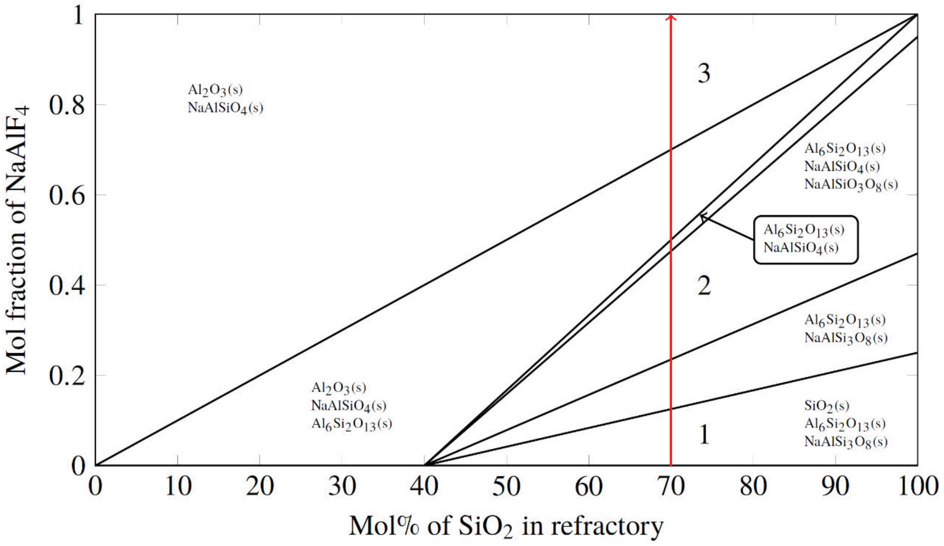

Figure 1. Phase stability for aluminosilicate refractory materials during exposure of $NaAlF_4$. The phase composition is given by the mole percentage of SiO_2 in the refractory, ranging from pure Al_2O_3 to pure SiO_2, while the exposure of $NaAlF_4$ is given as mole fraction relative to the content of aluminosilicate refractory in the system.

The degradation map is constructed based on a combination of thermodynamic calculations and mass balance considerations, while the plotted data in Figures 2 and 3 are exported directly from the equilibrium calculations. These mass balance considerations impose some simplifications to the degradation map, and consequently minor discrepancies between Figure 1 and Figures 2 and 3.

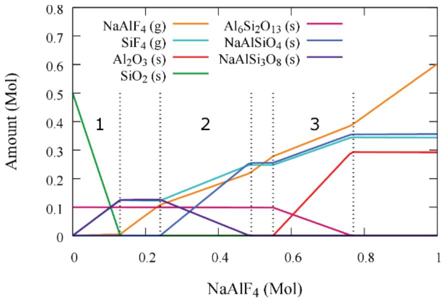

Figure 2. Phase composition of a refractory material with 70 mol% SiO_2 during $NaAlF_4$ exposure. The regions 1, 2 and 3 are related to the chemical reactions presented in Table 1.

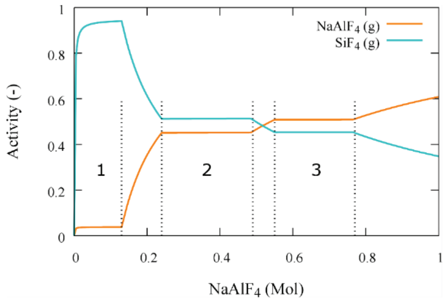

Figure 3. Chemical activity of the main gaseous species during $NaAlF_4$ exposure to a refractory with 70 mol% SiO_2. The regions 1, 2 and 3 are related to the chemical reactions presented in Table 1.

Table 1. Chemical reactions for lining with 70 mol% SiO_2 for increasing amount of $NaAlF_4$. The region numbering is related to the indicated regions in Figure 1.

Region	Chemical reaction
1	$NaAlF_4 + 4SiO_2 = SiF_4 + NaAlSi_3O_8$
2	$NaAlSi_3O_8 + NaAlF_4 = SiF_4 + 2NaAlSiO_4$
3	$Al_6Si_2O_{13} + NaAlF_4 = SiF_4 + 3Al_2O_3 + NaAlSiO_4$

The main conclusion from the consideration of exposure of aluminosilicate refractories to $NaAlF_4$ are that phases in the pristine material (SiO_2 and $Al_6Si_2O_{13}$) are consumed in the reaction with $NaAlF_4$, while $NaAlSiO_4$ and SiF_4, with $NaAlSi_3O_8$ as an intermediate compound, are formed.

3.3. NaF Exposure

A corresponding degradation map for the aluminosilicate refractory lining under NaF exposure is constructed in the same manner, and is presented in Figure 4. The map has some similarities with the diagram reported by Schøning et al. in 1999 [9], which was constructed by considering only the mass balances of the dominating reactions proposed by the authors. The use of thermochemical software, in addition to mass balance considerations, has enabled the identification of several other stability regions resulting in a more complex diagram. This is the same approach as Tschöpe et al. [17] used to construct the degradation map for cathode lining under Na(g) exposure. The diagram can be divided in two main compositional regions, delimited by the mullite composition at 40 mol% SiO_2. The main chemical reactions occurring for increasing NaF exposure to lining with 0 to 40 mol% SiO_2 are given in Table 2. At higher silica content, the reaction paths are less straightforward, due to the complexity of the stability regions. A reaction path for lining with 70 mol% SiO_2 during increasing NaF exposure is presented in Table 3.

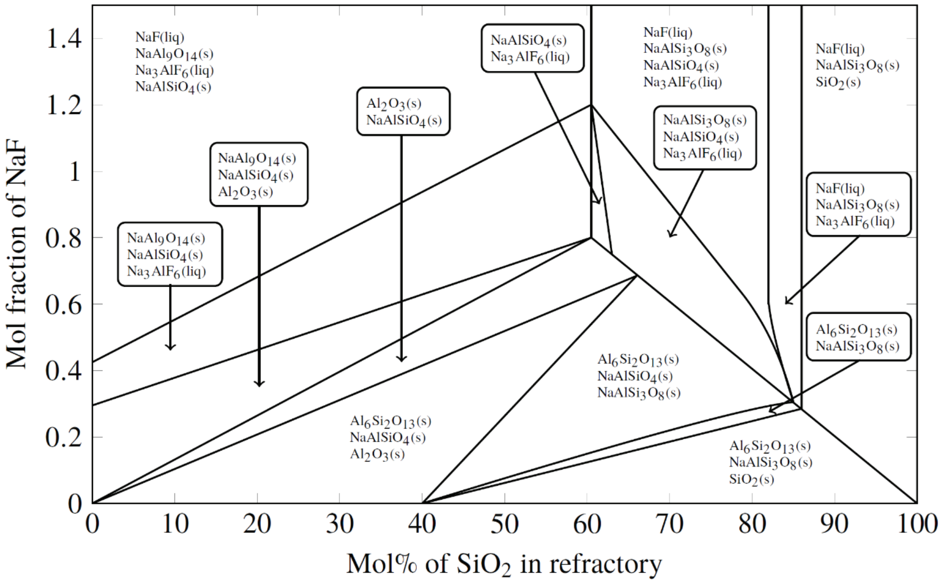

Figure 4. Phase stability for aluminosilicate refractory materials during exposure of NaF. The phase composition is given by the mole percentage of SiO_2 in the refractory, ranging from pure Al_2O_3 to pure SiO_2, while the exposure of NaF is given as mole fraction relative to the content of aluminosilicate refractory in the system.

Table 2. Main chemical reactions for increasing NaF exposure to lining with 0 to 40 mol% SiO_2.

Region	Chemical reaction
1	$3Al_6Si_2O_{13}(s) + 8NaF(g) = 5Al_2O_3(s) + 6NaAlSiO_4(s) + 2NaAlF_4(g)$
2	$4Al_2O_3(s) + 8NaF(g) + 3SiF_4(g) = 3NaAlSiO_4(s) + 5NaAlF_4(g)$
3	$14Al_2O_3(s) + 4NaF(g) = 3NaAl_9O_{14}(s) + NaAlF_4(g)$
4	$2NaF(g) + NaAlF_4(g) = Na_3AlF_6(liq)$

Table 3. Main chemical reactions for increasing NaF exposure to lining with 70 mol% SiO_2.

Region	Chemical reaction
1	$2Al_6Si_2O_{13}(s) + 35SiO_2(s) + 12NaF(g) = 12NaAlSi_3O_8(s) + 3SiF_4(g)$
2	$8Al_6Si_2O_{13}(s) + 48NaF(g) + 23SiF_4(g) = 13NaAlSi_3O_8(s) + 35NaAlF_4(g)$
3	$4Al_6Si_2O_{13}(s) + 24NaF(g) + 5SiF_4(g) = 11NaAlF_4(g) + 13NaAlSiO_4(s)$ $8NaAlSi_3O_8(s) + 8NaAlF_4(g) = 16NaAlSiO_4(s) + 8SiF_4(g)$
4	$2NaF(g) + NaAlF_4(g) = Na_3AlF_6(liq)$ $2NaAlSiO_4(s) + SiF_4(g) = NaAlSi_3O_8(s) + NaAlF_4(g)$

NaF exposure to aluminosilicate refractories causes consumption of the virgin phases (SiO_2, Al_2O_3 and $Al_6Si_2O_{13}$), while nepheline and β-alumina, or albite and nepheline are the main reaction products, in addition to SiF_4 and $NaAlF_4$, depending on the refractory composition.

3.4. Summary of Fluoride Exposure

The predominance diagrams shown in Figures 1 and 4 represent a "worst case" scenario. The partial pressure of NaF and $NaAlF_4$ at 1300 °C is in the range of 10^{-2} to 10^{-1} bar, and combined with the flow of flue gas through the furnaces, the real partial pressure of these volatile fluoride gasses is most likely considerably lower. From an industrial point of view, the interesting parts of the degradation maps are thus the regions in the diagrams with low content of fluorides. When only addressing the lower parts of the diagrams, the number of relevant phases become considerably lower, including only oxide phases. Post-mortem analysis of refractory lining with 60 mol% silica reported that only silica, alumina, mullite and an amorphous phase were present [1,2,7]. This is in accordance with the degradation maps developed in this work. The presented degradation maps should therefore be helpful for post-mortem analysis of spent refractory lining in anode baking furnaces where aluminosilicate materials are used.

3.5 Reducing Atmosphere

At elevated temperatures, volatile hydrocarbons and CO will evaporate from the green anodes leading to a reducing atmosphere in the furnace. The equilibrium partial pressure for CO (p_{CO}) is governed by the Boudouard reaction and is presented in Equation 5.

$$2CO(g) = CO_2(g) + C(s) \qquad (5)$$

As the temperature varies during a heat cycle, p_{CO} changes accordingly. Equilibrium data for Equation 5 is presented in Figure 5, showing a rightwards shift in the chemical equilibrium as the temperature decreases. In the upper left part of the diagram, the gas mixture is stable and the partial pressure of CO_2 (p_{CO_2}) can be found for a given partial pressure of CO. In the lower right part of the diagram, the gas mixture is unstable, resulting in carbon deposition. A decrease in the temperature causes the deposition range to increase, as showed in Figure 5. The ratio of p_{CO} and p_{CO_2} is also governing the partial pressure of O_2 (p_{O_2}), via Equation 6.

$$CO_2(g) = CO(g) + \tfrac{1}{2}O_2(g) \qquad (6)$$

By fixing the temperature and p_{CO_2}, p_{O_2} can be calculated as a function of p_{CO}. Figure 6 shows how the partial pressure of oxygen varies with temperature, p_{CO_2} and p_{CO}. p_{O_2} varies with several orders of magnitude as a response to changes in temperature or the p_{CO_2}/p_{CO} ratio.

Separate calculations were carried out to investigate the influence of reducing conditions on the phase equilibria between fluorides and the aluminosilicates. These calculations demonstrate that the phase stability presented in Figures 1 and 4 is not significantly affected by the reducing atmosphere due Equation 5.

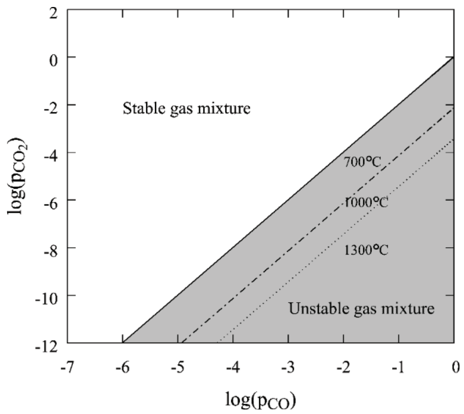

Figure 5. Equilibrium data for the Boudouard reaction (Equation 5), presented for 1300 °C, 1000 °C and 700 °C. The grey area indicates unstable gas mixture resulting in carbon deposition.

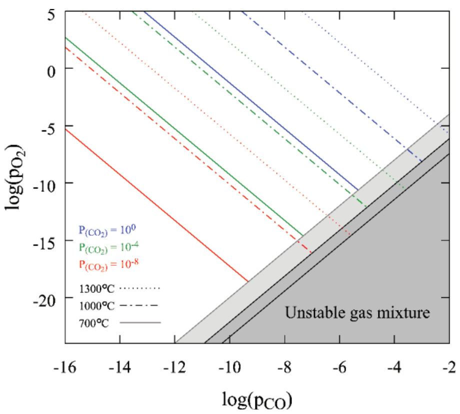

Figure 6. Equilibrium data for Equations 5 and 6 for 1300 °C, 1000 °C and 700 °C. The grey area indicates unstable gas mixture resulting in carbon deposition. The colored lines are plotted for fixed p_{CO_2}, and the line types indicate various isothermal conditions.

3.6. Carbon deposition

As the temperature varies during a heat cycle, there will be periods where the temperature is sufficiently low to cause carbon deposition. Autopsies of spent linings report blackening of the refractories close to the anode side, which is confirmed to be caused by carbon deposition [7]. The refractory wall is built up with flexible gaps allowing the wall to expand and contract with the temperature variations. The carbon deposited in these gaps reduce the wall's flexibility and will eventually cause internal stresses to build up during the heat cycle.

As shown in Figure 5, carbon deposition is also possible during anode cooling in the baking process since the region of the CO-CO_2 gas mixture becomes reducing as the temperature is going down.

4. Conclusion

Exposure of aluminosilicate refractories to gaseous sodium fluorides cause the transformation of the phases (corundum, cristobalite and mullite) in the pristine materials into β-alumina, nepheline and albite, in addition to gaseous SiF_4 and $NaAlF_4$. The phase stability of the pristine material due to NaF and $NaAlF_4$ exposure was summarized in isothermal predominance diagrams. From an industrial point of view, only the parts of the diagrams associated with low fluoride exposure is of interest, due to the expected partial pressures of gaseous sodium fluorides in the furnace. The diagrams correspond with reported data from spent refractory lining, showing that such diagrams are helpful when analyzing post-mortem samples. The presence of CO in the furnace shifts the atmosphere towards a more reducing nature. The prediction of phase stability in the isothermal predominance diagrams is however not influenced significantly by the presence of CO.

5. Acknowledgement

Financial support from the Norwegian Research Council and the partners Hydro, Alcoa, Elkem Carbon and Skamol through the project ”Reactivity of Carbon and Refractory Materials used in metal production technology” (CARMA) is acknowledged.

6. References

1. P. Prigent, M.L. Bouchetou, Gaseous corrosion of alumino-silicate refractories in anode baking furnaces used for aluminium produciton part 1, *Interceram*, 58 (2009) 121–126.
2. P. Prigent, M.L. Bouchetou, Gaseous corrosion of alumino-silicate refractories in anode baking furnaces used for aluminium produciton part 2, *Interceram*, 58 (2009) 202–209.
3. E.H.M. Moors, Technology strategies for sustainable metals production systems: a case study of primary aluminium production in The Netherlands and Norway, *J. Clean. Prod*., 14 (2006) 1121–1138.
4. H.-G. Schwarz, S. Briem, P. Zapp, Future carbon dioxide emissions in the global material flow of primary aluminium, *Energy*, 26 (2001) 775–795.
5. F.H. Becker, F. Goede, Ring pit furnaces for baking of high quality anodes - an overview, *Alum. 82*, 9 (2006).
6. A. Radjenović, Properties of carbon anode components for aluminium production, *Nafta*, 63 (2012) 111–114.
7. P. Prigent et al., The effect of the addition of fine andalusite particles in refractory bricks on gaseous corrosion, *JOM*, 60 (2008) 58–63.
8. F. Brunk, Corrosion and behavior of firecal bricks usen in the flues of open anode baking furnaces, *Light Met.*, (1995) 641–646.
9. C. Schøning, T. Grande, O.-J. Siljan, Cathode refractory materials for aluminium reduction cells, *Light Met.*, (1999) 231–238.
10. O.-J. Siljan, T. Grande, C. Schøning, Refractories for aluminium electrolysis cells part 1 - Deterioration mechanisms based on phase equilibria, *Alum. 77 Jahrgang*, (2001) 294–300.
11. O.-J. Siljan, T. Grande, C. Schøning, Refractories for aluminium electrolysis cells part 2 - Physical properties of penerating melt, reduction by metals and volatile fluorides, *Alum. 77 Jahrgang*, (2001) 385–390.
12. O.-J. Siljan, T. Grande, C. Schøning, Refractories for aluminium electrolysis cells part 3 - Laboratory test for cryolite resistance, *Alum. 77 Jahrgang*, (2001) 610–615.
13. O.-J. Siljan, T. Grande, C. Schøning, Refractories for aluminium electrolysis cells part 4 - Comparison of laboratory investigations and autopsies of pot linings, *Alum. 77 Jahrgang*, (2001) 809–814.
14. O.-J. Siljan, C. Schoning, T. Grande, State-of-the-art alumino-silicate refractories for al electrolysis cells, J. Miner. Met. Mater. Soc., 54 (2002) 46–55.
15. C. Schøning, T. Grande, The stability of refractory oxides in sodium-rich environments,

JOM, 58 (2006) 58–61.

16. K. Tschope et al., Chemical degradation of cathode linings in hall-heroult cells - an autopsy study of three spent pot linings, *Metall. Mater. Transcations B*, 43B (2012) 290–301.
17. K. Tschöpe, J. Rutlin, T. Grande, Chemical degradation map for sodium attack in refractory linings, *Essent. Readings Light Met. Electrode Technol. Alum. Prod*., 4 (2013) 978–983.
18. J. Butter, A. Bongers, Alterations of anode baking furnace bricks during operation, *Light Met*., (1995) 633–639.
19. C.W. Bale et al., FactSage thermochemical software and databases — recent developments, *Calphad*, 33 (2009) 295–311.

D.2 Conference proceeding 2

T. Brandvik, Z. Wang, A. P. Ratvik and T. Grande. Investigations of Spent Refractory Lining in Anode Baking Furnaces, *Light Metals*, pages 1281-1288, 2017.

D.3 Conference proceeding 3

T. Brandvik, A. P. Ratvik and T. Grande. Effects of Water Cooling of Green Anodes on Anode Furnace Operation, *Travaux 47, Proceedings of the 36th International ICSOBA Conference*, pages 555-562, 2018.

Effects of Water Cooling of Green Anodes on Anode Furnace Operation

Trond Brandvik[1], Arne Petter Ratvik[2], and Tor Grande[3]
1. PhD Candidate
3. Professor
Department of Materials Science and Engineering, NTNU Norwegian University of Science and Technology, Trondheim, Norway
2. Senior Research Scientist
SINTEF Industry, Trondheim, Norway
Corresponding author: trond.brandvik@ntnu.no

Abstract

Water can be present in significant amounts in green anodes due to cooling with water after the forming process. The chemical environment in the pit can potentially be affected by the presence of water and may cause degradation mechanisms of the refractory lining so far not considered. A thermodynamic assessment of the role of water on formation of HF(g) due to traces of cryolite bath in the green anodes is presented. It is shown that water results in the formation of HF, and subsequently, it is predicted that HF will react with the refractory materials forming a solid oxyfluoride phase at moderate temperatures. The oxyfluoride is however not thermally stable during the whole baking cycle and SiF_4 will evaporate upon further heating. Finally, the effect of water on carbon gasification and CO and H_2 production during anode baking is also addressed. The findings are discussed in relation to previous studies of the degradation of refractory linings in anode baking furnace.

Keywords: Water cooling, volatile HF, anode baking furnace, refractory lining.

1. Introduction

The importance of sodium fluorides in relation to degradation processes of refractory material in anode baking furnaces has been investigated in several works [1–4]. Studies of spent lining from anode baking furnaces have revealed large amounts of sodium in spent linings. These observations demonstrate the occurrence of reactions between volatile sodium fluorides and aluminosilicate refractory lining. Thermodynamic calculations have illustrated how cryolite, when present in green anodes, can be a source of significant levels of sodium fluorides vapor in the pit during baking [5]. At elevated temperatures, the refractory lining will react with both volatile NaF and $NaAlF_4$ forming various sodium aluminosilicates and SiF_4(g), in accordance to stability diagrams reported earlier [5]. In contrast to the abovementioned studies, recent investigations of both open and closed anode baking furnaces have shown little or no traces of sodium in the spent lining [6]. Consequently, the proposed reactions between volatile fluorides and the refractory lining are not as dominating as reported earlier, demonstrating that other mechanisms is the main cause for degradation of the refractory linings in the furnaces. The reducing atmosphere in the bottom of the pit has been given some attention in that respect, but it has been difficult to conclude on a single mechanism [6,7]. Recent *in situ* experiments of gas composition in the anode baking furnace during baking have given some valuable insight regarding the chemical conditions which the refractories are being exposed to [8]. Transient concentration of e.g. CO and CO_2 were recorded, in addition to large concentration CH_4 in the first part of the firing cycle. Moreover, the study did show significant levels of water vapor in the furnace during the first part of the baking cycle, expected to origin from the extensive use of water cooling of green anodes. The presence of water in the anodes prior to heat treatment introduces new chemical aspects not considered before. Here, the previous calculations of reactions in a dry gas atmosphere is expanded to comprise the effects of water vapor. The aim of this work was to address the effect of water on the refractory stability at elevated temperatures. The cost of heating and evaporating water was discussed and related to the total energy cost of the anode baking process. The effect of water on carbon gasification was finally also discussed.

2. Thermodynamic assessment

A thermodynamic assessment was carried out with the thermochemical software FactSage 7.2. In the first part of the assessment, phase stability was investigated in a system consisting of cryolite, carbon and water at various temperatures, through equilibrium calculations by minimization of Gibb's energy. Subsequently, the result from the first part was used to determine the stability of aluminosilicate refractories in similar environments. This work was based on the *Equilibrium* module in combination with the *FactPS* database as described earlier [5].

3. Results & Discussion

3.1. Volatile Fluorides

The major effect caused by the entry of water in the anode pit is the formation of gaseous HF. The volatility of $NaAlF_4$ and NaF is not affected and the vapor pressure remains as reported earlier as long as solid cryolite is present [5]. This is summarized in Figure 1a, where the vapor pressure of $NaAlF_4$, NaF, HF and water are shown as a function of temperature with 5 mol% water present in the pit atmosphere. A significant volatility of fluorides caused by the formation of HF is evident at lower temperatures. The partial pressure of HF is as high as 0.01 bar at 850 °C, meaning that the refractory lining in the pit is exposed to fluoride containing gas at considerably lower temperatures than previously anticipated. As the amount of water in the system increases, the partial pressure of HF increases accordingly as shown in Figure 1b. The presence of water together with cryolite during anode baking could thus be source of volatile HF at temperatures significantly below that of the volatile fluorides $NaAlF_4$ and NaF.

The two dominating chemical equilibria discussed are Reaction (1) and (2). Reaction (1) shows the formation of liquid NaF and gaseous $NaAlF_4$. There is also a considerable vapor pressure of NaF, even though it remains stable as a liquid.

$$Na_3AlF_6\,(s) = 2NaF\,(liq) + NaAlF_4\,(g) \qquad (1)$$

The addition of water to the system enables the second equilibrium presented in Reaction (2).

$$9Na_3AlF_6\,(s) + 14H_2O\,(g) = 28HF\,(g) + 26NaF\,(liq) + NaAl_9O_{14}\,(s) \qquad (2)$$

Here, cryolite reacts with water and forms gaseous HF, in addition to liquid NaF and β-alumina. Reaction (2) is the main cause of the enhanced volatility of the fluorides due to the presence of water in the pit.

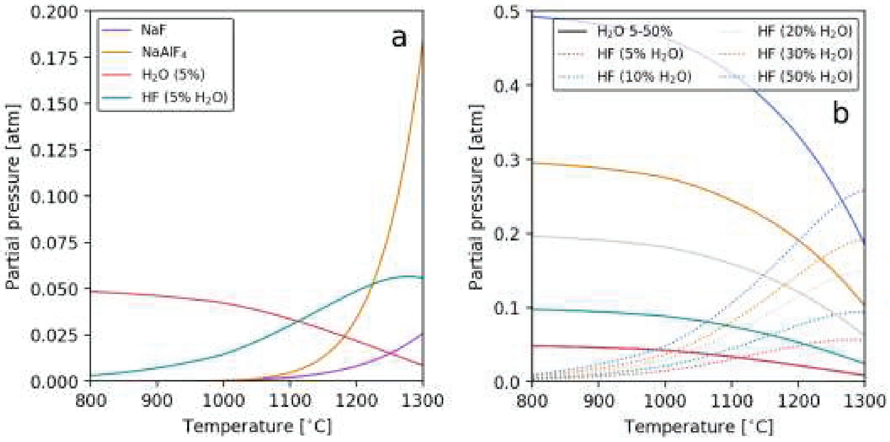

Figure 1. Partial pressures of fluorides for varying temperature (a) and both varying H_2O content and temperature (b).

3.2. Refractory stability in HF-rich environments

With HF present in the anode pit, the thermodynamic stability of the aluminosilicate refractories are potentially no longer only dependent on the presence of sodium fluorides in the furnace. Aluminosilicate refractory materials used in anode baking furnaces normally contains 40-60 wt% alumina with the remaining mostly being silica and some minor minerals [1,3,6]. For this compositional range, the dominating phase in the material is mullite ($Al_6Si_2O_{13}$). The stability of mullite in HF rich atmospheres is hence of great interest. As the temperature rises, mullite and HF react to form $SiAl_2F_2O_4$, alumina and water, in accordance with Reaction (3). This reaction describes the formation of a condensed oxyfluoride phase. The reaction is spontaneous at moderate temperatures.

$$Al_6Si_2O_{13}\,(s) + 4HF\,(g) = 2SiAl_2F_2O_4\,(s) + Al_2O_3\,(s) + 2H_2O\,(g) \qquad (3)$$

$SiAl_2F_2O_4$ is not thermally stable, and the stability of $SiAl_2F_2O_4$ is described by Reaction (4).

$$4SiAl_2F_2O_4\,(s) = 2SiF_4\,(g) + Al_2O_3\,(s) + Al_6Si_2O_{13}\,(s) \qquad (4)$$

Upon temperature increase above ~1100 °C, the reaction shifts to the right and SiF_4 becomes the dominating fluoride phase. As the temperature cycles during the baking cycle, Reaction (3) is favored at low temperature, while Reaction (4) is favored at high temperatures. Fluorine originating from the spent anode butts could thus be found both as a solid ($SiAl_2F_2O_4$) and in the vapor phase (SiF_4) indicating a potential dynamic fluorine reaction pattern.

3.3. Implications of HF

Previous investigations of spent refractory lining have shown regions with SiO_2 depletion [1,6,7,9,10]. These observations are most pronounced close to the surface facing the pit atmosphere, demonstrating that the pit atmosphere is crucial for the depletion process. Formation of volatile SiO(g) under reducing atmosphere and high temperatures have been suggested as a possible mechanism for SiO_2 depletion [1,6,7]. The presence of HF in the pit opens up for an alternative mechanism for SiO_2 depletion. In the first part of the baking cycle, where the HF pressure is potentially highest and the temperature moderate, the condensed fluoride phase ($SiAl_2F_2O_4$) is formed. Once formed, the solid fluoride is not stable during the whole baking cycle. Above ~1100 °C, $SiAl_2F_2O_4$ decomposes to SiF_4(g), alumina and mullite. The dominating fluoride compound is thus shifting from $SiAl_2F_2O_4$ to SiF_4 during the baking process, enabling both Si and F to leave the furnace as SiF_4.

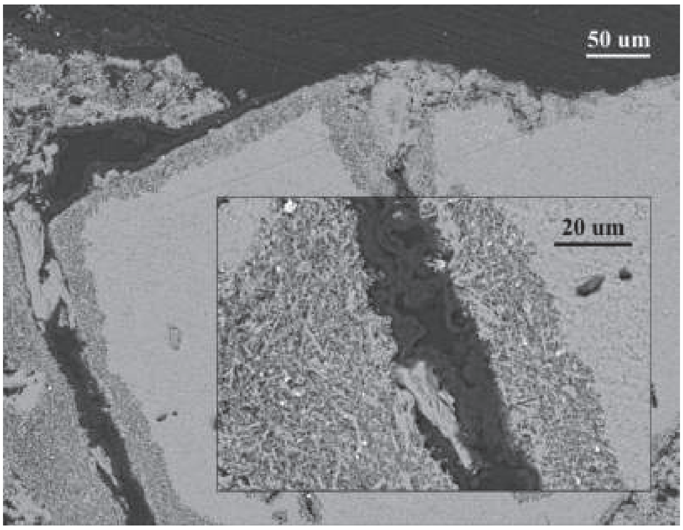

Figure 2. Spent lining from an open anode baking furnaces after 160 baking cycles. Regions facing the refractory surface and open porosity are clearly affected. The reaction layer is depleted of SiO_2, with only mullite and Al_2O_3 left in the structure [7].

SiO_2 depletion is often found as a reaction layer facing the outer parts of the refractory (Figure 2), or close to open porosity further into the lining [7]. The observed thickness of the reaction layer is up to ~200 μm, depending on the distance from the anode pit. The sample presented in Figure 2 is from an open top anode baking furnace collected after 160 baking cycles. Due to the thermal cycling during the carbon anode production, contributions from each baking cycle are most likely minor. By distributing the accumulated reaction layer observed in Figure 2 over 160 cycles, the increase in thickness per baking cycle is approximately 200-300 nm. The thickness of the reaction layer is observed to decrease from the refractory surface on the anode pit side and into the lining [7]. The chemical activity of the reactive gas species is largest in the anode pit, and decrease into the porosity of the lining. Based on the observation of the spent refractory lining the composition of the gas atmosphere, in combination with the baking temperature cycle, are of importance when considering possible mechanisms for SiO_2 depletion in the lining. SiO_2 depletion through the formation of HF and $SiAl_2F_2O_4$ corresponds well with the lack of observed fluorine in the spent lining. The mechanism enables both Si and F to exit the furnace as SiF_4, leaving mullite and alumina in the reaction layer. The overall degradation is however difficult to associate to the depletion of SiO_2 alone. A ~200 µm thick layer of SiO_2 depletion should not be the dominating factor for the macroscopic degradation of the lining observed after many cycles.

To summarize, the observed SiO_2 depletion can be caused by formation of HF formation due to the presence of water in the green anodes. The presence of water may also have and important additional energy cost, which is further treated below.

3.4. Energy consumption due to water in green anodes

During the production of prebaked anodes, the anodes are mixed and formed at temperatures above the softening point of the pitch (typically around 150-190 °C) [11,12]. To regain structural integrity, the anodes need to be cooled down below the softening temperature of the pitch prior to storage and baking. This process is often carried out through water cooling, resulting in absorption of water into open porosity of the green anodes. If proper measures is not taken, water remains in the pores of the green anodes and follows the green anodes into the baking furnace, and is thus heated up together with the anodes. The energy consumption related to anode baking would thus include the cost of heating water. The extra energy consumption due to water is interesting form an economical perspective.

The fuel cost related to the baking of carbon anodes is typically around of 2 GJ/ton baked anode [13,14], in addition to the heat supplied through burning of volatiles form the pitch. The energy consumption related to heating of water can be estimated by assuming a carbon anode porosity of 20 % and that a fraction of this porosity is filled with water. The volume of the anodes are calculated from the average weight (1020 kg) and density (1.6 g/cm^3) and related to the operation of an open top anode baking furnace. When considering the heating and vaporization of water, the liquid is heated from 25 °C and the gas up to 150 °C. By varying the amount of water in the open porosity, and relating the additional heat to a fixed total energy consumption, the fraction of energy spent on evaporation of water can be calculated as presented in Figure 3.

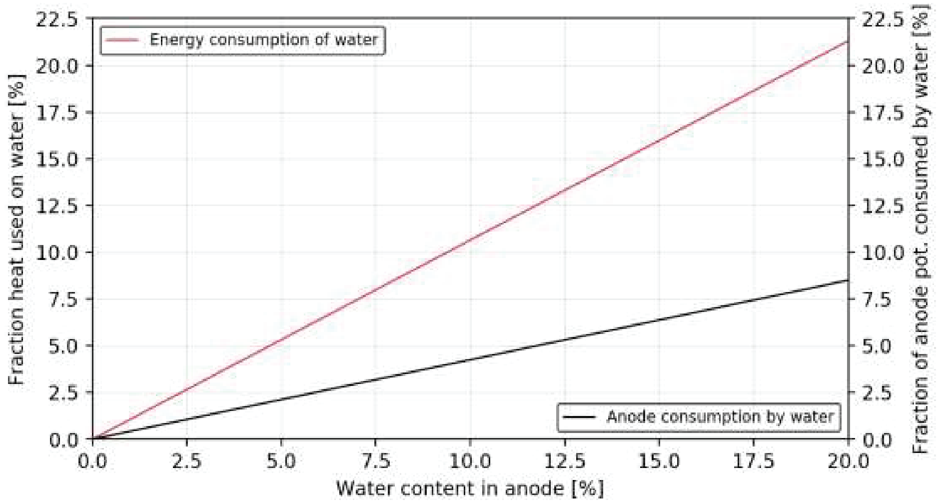

Figure 3. Fraction of total energy consumption spent on heating and vaporization of water (red). Fraction of anode that can potentially react with water, if all water reacts in accordance to Reaction 5.

The energy consumption related to heating and vaporization of water constitutes a significant part of the total energy consumption. If 10 % of the open porosity is filled with water, approximately 10 % of the overall energy cost of baking anodes is related to evaporation of water. The baking step is the most expensive in the production of carbon anodes for aluminum electrolysis. Taking into account the volume of carbon anodes produced, and the total cost of baking such anodes, it is a great potential for cost reduction by controlling the water content in the green anodes.

Due to the way green anodes are produced, they need to be cooled below the softening point of the pitch in order to maintain structural integrity. If water cooling is the most effective way of cooling, then it would be beneficial to address the effect of soaking time on the final water content. If the anodes could be removed from the cooling bath at an earlier stage in the process, then the residual heat would help dry the anodes. This would probably prolong the cooling process, and thus require larger storage facilities for the anodes while being cooled (and dried) in air, but could have a significant positive effect on the overall cost of the anode baking.

3.5. Gasification of carbon by water

Another aspect with water being present in the anodes are the reactions occurring between carbon and water as presented in Figure 4. At elevated temperatures, carbon and water reacts to form CO and H_2 in accordance to Reaction 5. This reaction is dominating above 700 °C, converting all available water vapor into H_2 and CO gas. Below 700 °C, the thermodynamic equilibrium concentrations are controlled by a variety of chemical reactions. Upon temperature decrease, the kinetic barrier for achieving thermodynamic equilibrium is increasing, hence the reactions are kinetically controlled in disfavor of e.g. CH_4.

$$C\ (s) + H_2O = CO\ (g) + H_2\ (g) \qquad (5)$$

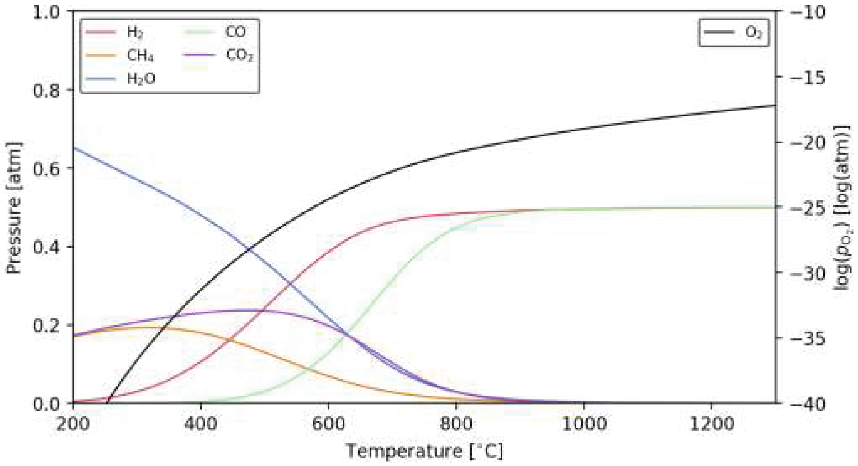

Figure 4. Thermodynamic equilibrium concentrations for carbon and water at increasing temperatures. The dominating reaction converts all available carbon and water vapor into CO(g) and H_2(g) above 700 °C.

The presence of water does however not affect the chemical activity of oxygen, which is mostly controlled by temperature (as shown in Figure 4). The reducibility of the pit atmosphere should therefore not vary significantly with the water content in the anodes. Previous works have linked the depletion of SiO_2 to the formation of volatile SiO(g) in reducing atmosphere and elevated temperatures [1,6,7]. Since water does not affect the oxygen activity and hence not the degree of SiO formation, water vapor would not influence the process of SiO_2 depletion.

Reaction (5) demonstrates that carbon and water vapor reacts and forms CO and H_2 above 700 °C and thereby potentially reduce the carbon output from the anode baking furnace. The amount of carbon reacted with water according to Reaction (5) is shown in Figure 3. With 10 % water content in the anode, approximately 4 % of the anode could potentially react with the water.

6. Conclusions

Due to water cooling of green anodes, water may remain in the porosity in the green anodes. The presence of water in the green anodes could influence the anode baking furnace and the baking process. Here, it was shown by thermodynamic calculations that water and cryolite from spent anode butts will react to form HF(g). HF in the pit atmosphere will further react with the refractory lining, and the reaction with HF can potentially explain the previously observed depletion of SiO_2 at the surface of the refractory lining. Presence of water in the anodes would also increase the total energy consumption of the baking process. Anode baking is a costly step in the anode production process, and reductions in cost can be made by minimizing the water content in the green anodes. Finally, water vapor will react with the anodes and form CO and H_2, consequently reducing the carbon content in the baked anodes. Altogether, the present analysis point out the importance to reduce the water content in the anodes.

7. Acknowledgement

Financial support from the Norwegian Research Council and the partners Hydro, Alcoa, Elkem Carbon and Skamol through the project ”Reactivity of Carbon and Refractory Materials used in metal production technology” (CaRMa) is acknowledged.

8. References

[1] F. Brunk, Corrosion and Behavior of Firecal Bricks used in the Flues of Open Anode Baking Furnaces, Light Met., (1995) 641–646.

[2] P. Prigent, M.L. Bouchetou, Gaseous Corrosion of Alumino-Silicate Refractories in Anode Baking Furnaces used for Aluminium Produciton Part 2, Interceram, 58 (2009) 202–209.

[3] P. Prigent, M.L. Bouchetou, Gaseous Corrosion of Alumino-Silicate Refractories in Anode Baking Furnaces used for Aluminium Produciton Part 1, Interceram, 58 (2009) 121–126.

[4] P.R.T. Tiba, B.H. Teider, F. Figueirdo, J.B. Gallo, V.C. Pandolfelli, Systematic analysis of flue wall bricks used on anode baking furnaces, Light Met., (2010) 1015–1019.

[5] T. Brandvik, A.P. Ratvik, T. Grande, Thermodynamic Assessment of the Chemical Durability of Refractory Lining in Anode Baking Furnaces, ICSOBA 2016, (2016).

[6] T. Brandvik, A.P. Ratvik, Z. Wang, T. Grande, Investigations of Spent Refractory Lining in an Anode Baking Furnace, Light Met., 4 (2017) 1281–1288.

[7] T. Brandvik, Z. Wang, A.P. Ratvik, T. Grande, Autopsy of Refractory Lining in Anode Kilns with Open and Closed Design, Int. J. Appl. Ceram. Tech., DOI: 10.1111/ijac.13108, (2018).

[8] T.A. Aarhaug, T. Brandvik, O.S. Kjos, H. Gaertner, A.P. Ratvik, A study of anode baking gas composition, in: Light Met., 2018: pp. 1379–1385.

[9] Z. Wang, S. Rørvik, A.P. Ratvik, T. Grande, Formation of Carbon Build-Up on the Flue Wall of Anode Baking Furnace, Light Met., (2017) 1265–1274.

[10] N. Oumarou, D. Kocaefe, Y. Kocaefe, Investigation of the refractory bricks used for the

flue wall of the horizontal anode baking ring furnace, Ceram. Int., 42 (2016) 18436–18442.
[11] C. Sommerseth, R. Thorne, A. Ratvik, E. Sandnes, H. Linga, L. Lossius, A. Svensson, The effect of varying mixing temperatures and baking level on the quality of pilot scale anodes—a factorial design analysis, Metals (Basel)., 7 (2017) 74.
[12] K. Azari, H. Alamdari, G. Aryanpour, D. Picard, M. Fafard, A. Adams, Mixing variables for prebaked anodes used in aluminum production, Powder Technol., (2013).
[13] F. Keller, P.O. Sulger, M.W. Meier, D.S. Severo, V. Gusberti, Specific Energy Consumption in Anode Bake Furnaces, Essent. Readings Light Met. Electrode Technol. Alum. Prod., 4 (2013) 408–413.
[14] International Aluminium Institute, Prebaked Anodes for Aluminium Electrolysis, (n.d.) 1–20.

D.4 Scientific paper 1

T. Brandvik, Z. Wang, A. P. Ratvik and T. Grande. Autopsy of Refractory Lining in Anode Kilns with Open and Closed Design, *J. App. Ceram. Tech.*, 16(2):602-613, 2019.

Received: 7 August 2018 | Revised: 7 August 2018 | Accepted: 31 August 2018

DOI: 10.1111/ijac.13108

International Journal of Applied Ceramic TECHNOLOGY

ORIGINAL ARTICLE

Autopsy of refractory lining in anode kilns with open and closed design

Trond Brandvik[1] | **Zhaohui Wang**[1,2] | **Arne Petter Ratvik**[2] | **Tor Grande**[1]

[1]Department of Material Science and Engineering, NTNU Norwegian University of Science and Technology, Trondheim, Norway

[2]SINTEF Industry, Trondheim, Norway

Correspondence
Tor Grande, Department of Material Science and Engineering, NTNU Norwegian University of Science and Technology, Trondheim, Norway.
Email: grande@ntnu.no

Funding information
Norwegian Research Council

Abstract

Aluminosilicate refractory lining constitutes a major part of anode baking kilns, and during anode baking the lining is exposed to harsh conditions which limits the lifetime. Here, autopsies of refractory linings from both an open and closed top furnace are reported aiming to determine the microstructural and mineralogical changes in the lining during operation. Significant variations in density and porosity were observed, both across the brick cross sections, but also for the vertical position in the lining. The chemical and mineralogical composition of the bricks were investigated by electron microscopy and X-ray diffraction. Only minor changes in the mineralogical composition of the materials were observed, and sodium originating from green anodes was only observed to a minor degree. Evidence of silicon oxide transport from the lower to the upper part of the linings was observed, reflecting the changes in reducing-oxidizing conditions during an anode baking cycle. The main degradation mechanisms in these linings were due to densification of the material over time, particularly the uneven densification across a lining wall. The present findings are discussed and related to the main differences in the two furnace designs.

KEYWORDS
aluminosilicates, chemical durability, refractories

1 | INTRODUCTION

The production of primary aluminum is carried out through electrolytic reduction of dissolved alumina in a fluoride electrolyte with carbon oxidation as the complementary anode reaction.[1,2] The dominating anode technology today is prebaked carbon anodes due to the superior properties compared to Søderberg anodes.[3,4] The green anodes are made of a mixture of petroleum coke, recycled anode butts and coal tar pitch, which are subjected to heat treatment (baking) in anode baking furnaces.[2] The fabrication of prebaked carbon anodes is fairly similar from plant to plant, however with the furnace design having two major configurations; ie, open and closed top.[1,5,6] The main construction element in the anode baking furnace is the refractory flue wall, which separates the anodes from the flue gas during operation. The flue walls consist mostly of alumina and silica, with some variations in alumina to silica ratio. Due to the harsh operational conditions in the furnace during baking, the refractory flue walls degrade over time.[1,5-7] One contributor to this degradation is the thermal cycling, ranging from room temperature to 1200°C in each baking cycle lasting ~14-17 days, giving rise to thermal induced stress. In addition, the gaseous environment surrounding the refractories at the anode side may also contribute. Green anodes are made of 20%-25% recycled anode butts, which contains traces of the electrolyte and impurities like Na and F. The presence of cryolite will cause volatile species like NaF and $NaAlF_4$ to form during baking, which may react with the refractory materials resulting in degradation of the wall.[1,7-10] Typically, CO, CH_4, H_2, as well as other hydrocarbons, are formed during baking, either from the coke itself or the coal tar pitch. These reducing gaseous species may cause reduction of the aluminosilicate lining.[1,7,8] To be able to absorb thermal expansion during heating, the flue wall is made with mortar-filled gaps between the bricks allowing some flexibility as the temperature cycles. Volatile hydrocarbons are likely to crack at the hot flue wall resulting in carbon deposition filling the gaps and thus reducing the walls' flexibility. This will result in a reduction in the walls' ability to absorb thermal expansion and hence an increase in the development of thermal stress during baking.

The aim of this work was to investigate the degradation of the refractory lining in anode baking furnaces. In order to address the differences between the open and closed furnace design, two autopsies were carried out with focus on changes in the mineralogy, microstructure and density in both flue walls. Preliminary data from the first autopsy have been reported earlier,[11] and the study is in this report continued to include an additional autopsy and extended microstructure and mineralogical characterization. Finally, a thorough discussion with respect to possible degradation mechanisms and differences between open and closed top furnace is presented.

2 | THE ANODE BAKING FURNACE

The baking furnaces are in general designed as a ring pit furnace, where the individual sections are connected in series. Each section is divided into several pits, where the pits are separated from each other by the refractory flue walls. A typical pit is 5 m deep, 5 m long, and 1 m wide. The flue gas is flowing inside hollow flue walls allowing for heating of the furnaces by combustion. The green anodes are placed in the pits and covered with packing coke to prevent anode oxidation during baking.[12] Heating is performed by burners fueled with typically natural gas, LPG or oil, which are moved around the furnace in fire trains (the part of the furnace where the heating occurs). A typical fire train covers eight sections, where three are assigned to preheating, three to maximum temperature baking, and the two at the end are assigned to cooling. As the train moves one section every 22-28 hours, the anodes in a given section will first be preheated for three periods, then baked at maximum temperature, before cooled down to room temperature. There are usually two to three fire trains moving around the furnace, leaving several unoccupied sections between each train available for anode replacement and furnace maintenance. During the first part of the baking cycle, volatile hydrocarbons evaporate from the green anodes and are combusted in the flue gas as the temperature increases, contributing to the overall heat input to the furnace. The main structural difference between the open and closed furnace design is the section covers used in the closed design. The flow of hot flue gas through the furnace is affected by the use of section covers, thus the flue gas flow pattern is varying between the two furnace designs and subsequently affecting the operational environment in the furnace during baking.

2.1 | Open top furnace design

The open top baking furnace does not have section covers. The anodes are thus not separated from the surrounding atmosphere, emphasizing the need for packing coke to avoid anode oxidation during baking. Without a section cover, the flue wall itself must be sealed in order to keep the hot gas within the flue. The flue walls in the open top furnace are thus constructed as hollow two-layered refractory walls, where the flue gas is inside each wall. A section from an open top furnace is illustrated in Figure 1A. The cross section of the flue wall shows the flow direction of the flue gas as illustrated by arrows. Within the flue wall there are baffles and tie bricks controlling the flow pattern of the flue gas, in addition to giving the wall mechanical stability.[12] The open arrangement of the pits dictates that the vapors released from the anodes must be sucked through the flue walls to avoid harmful release to the working environment. This is achieved by reducing the pressure within the flue walls. The two-layered flue wall lining has a width of 10-12 cm, which differs significantly from the closed top design.

2.2 | Closed furnace design

The closed top furnace design utilizes section covers to close off the sections that are being subjected to heat treatment. The sections are thus more or less sealed toward the working environment during baking resulting in better control of the atmosphere within the section. The flue walls used in this design are made by a single-layered, hollow refractory wall, where the flue gas flows within channels in the wall. A section of a closed baking furnace is illustrated in Figure 1B. The cross section shows the two parts of the flue wall, defined by how each part leads the flue gas. In part A the flue gas enters the wall at the bottom and is transported upwards through the channels in the wall. At the top of the flue wall, the flue gas is released underneath the section cover, before being transported down by the reduced pressure in part B. The flue gas outlet is in the bottom right corner of part B where the gas is transported into part A of the next section. The flue wall arrangement is varying to some extent between different closed furnaces, but the overall design concept is the same. The lining separating the anode from the flue is in this design 4 cm thick, significantly thinner compared to the open top furnace design.

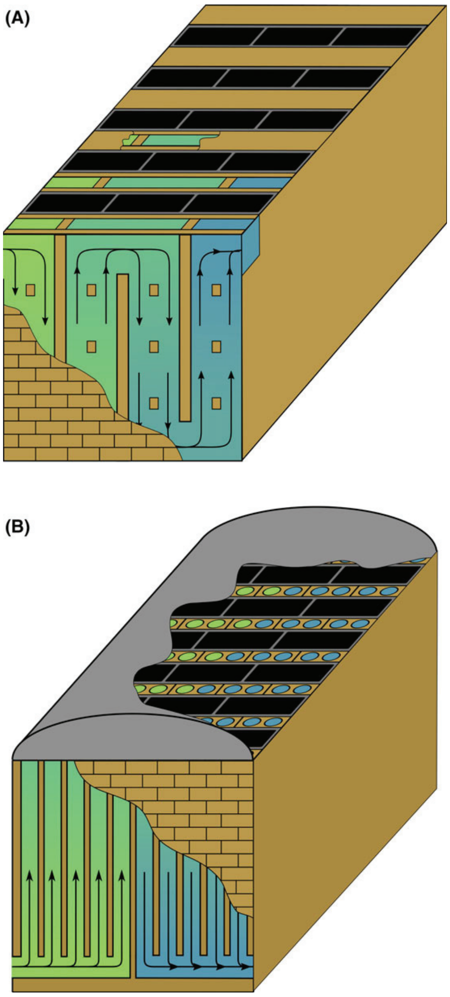

FIGURE 1 Flue wall cross sections, distribution of flue walls and anode pits are displayed for both (A) open and (B) closed top baking furnace. The closed furnace flue wall is divided into two parts where part A carries the flue gas upwards (green), while part B transports the flue gas downwards (blue) and into the next section. The gray cover section is illustrated for the closed furnace [Color figure can be viewed at wileyonlinelibrary.com]

3 | EXPERIMENTAL

3.1 | Autopsy

Samples from spent refractory lining from anode baking furnaces with both open and closed top design were collected, after approximately 160 and 63 cycles in operation, respectively. From the furnace with open top design, sampling was performed at three heights: top, middle, and bottom, where the top layer was collected ~1 m below the top of the flue wall. The closed top furnace design has two sections of the refractory wall (part A and B), where each part were sampled at three heights, similarly as for the open top furnace. Figure 2 shows the cross section of the refractory bricks used in the closed (A) and the open (B) top designs, illustrating the differences in width. In order to investigate structural and mineralogical changes as a function of distance from the anode side, all samples were cut into smaller sections with the size of 1-2 cm^3. Due to the difference in width of the refractory lining in the two furnaces, the division into the smallest sections varied as shown in Figure 2. Samples from the open top design were divided into eight smaller sections, while samples from the closed top design were divided into four or five sections. All samples were polished down to 1 μm prior to further characterization by microscopy. If otherwise is not explicitly stated, the results are referring to the polished samples. Some investigations were also conducted on fracture surfaces. X-ray diffraction were performed using powders obtained by grinding with a Herzog HSM pulverizing mill in a WC vessel, before subsequent sieving to <63 μm.

3.2 | Material characterization

The as-cut samples were analyzed with respect to apparent density and open porosity by the Archimedes' method as described in ISO5017 using water as immersion liquid. The weight difference after heat treatment at 1150°C for 48 hours in air were determined gravimetrically in order to quantify the amount of deposited carbon in the open porosity. The qualitative phase composition of the samples was investigated by powder X-ray diffraction using a Bruker D8 DaVinci diffractometer with a LynxEye SuperSpeed detector and CuKα radiation. Microstructural and chemical analysis was carried out with a Zeiss Supra 55 VP field emission scanning electron microscopy (SEM), with the associated energy dispersive X-ray spectroscopy (EDS). X-ray fluorescence (XRF) analysis was done by a Bruker S8 Tiger 4 kW X-ray diffractometer.

4 | RESULTS

4.1 | Pristine composition and microstructure of the refractory bricks

The refractory materials in both furnaces are similar in microstructure prior to service. In Figure 3, the microstructure of the pristine refractory material from the open baking furnace is presented. The microstructure is in general heterogeneous with a broad particle size distribution and a significant level of open porosity. The chemical compositions of the two materials determined by XRF is presented in Table 1, demonstrating the similarities of the two

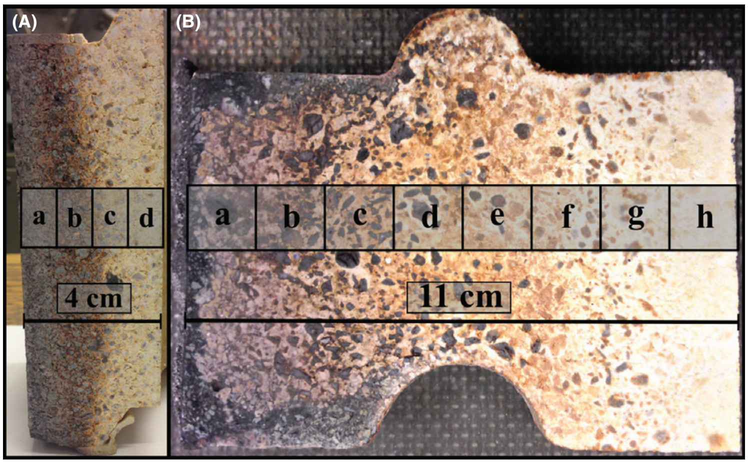

FIGURE 2 Cross sections of spent lining from both (A) closed and (B) open furnaces. The left side on both samples have been facing the anode side as indicated by the discoloring [Color figure can be viewed at wileyonlinelibrary.com]

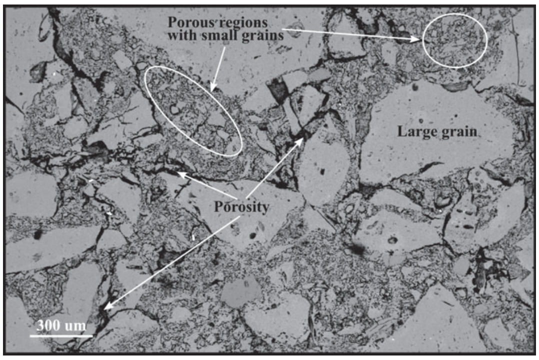

FIGURE 3 Microstructure of pristine refractory material, illustrating the heterogeneity of the material used in both the open and closed baking furnace. Large grains (bright), porous regions with small grains and pores (dark) are labeled

materials with respect to chemical composition. The sodium content of both materials is below the XRF detection limit of 0.02 wt% Na_2O (Table 1).

A typical phase composition of the pristine materials from both furnace designs is presented in Figure 4C. The main phases present in the materials from the open furnace lining are mullite ($Al_6Si_2O_{13}$) and cristobalite (SiO_2). The brick from the closed furnace consists of comparable levels of mullite, significantly lower cristobalite content and minor amount of andalusite (Al_2SiO_5), which remains from the raw materials used.

4.2 | Phase composition of spent lining

X-ray diffraction patterns of the anode facing samples from both furnaces are presented in Figure 4A and B. In general, there are no major variations with respect to phase composition in the materials of either of the two linings. The open top furnace samples (Figure 4A) consist of mullite and cristobalite, with a relatively constant mineralogical composition. The largest variation is observed with respect to cristobalite, being especially evident for the reflections at ~21.9°. The phase transition between α-cristobalite, the stable polymorph at ambient conditions, and β-cristobalite is reported between 170°C and 270°C, dependent on defects or strains.[13-15] The X-ray diffractograms demonstrate the presence of both α- and β-cristobalite in various amounts. Suppression of the β- to α-cristobalite transition has been investigated and it can be effected by solid solution of other oxides in the crystal structure.[14-16] The ratio of α- to β-cristobalite in the samples is varying, but there is no clear trend with respect to vertical position or distance from the anode side. X-ray diffractograms for the closed furnace show the similar observations regarding the content of α- and β-cristobalite (Figure 4B). Andalusite is observed in addition as in the pristine material, and the content of this phase is varying, having a higher intensity in the top section, compared to the middle and bottom sections. Finally, it is worth pointing out that there is no evidence for the presence of significant amounts of an amorphous phase in either of the linings based on the XRD data.

4.3 | Visual investigations of spent lining

Optical images of the cross section of the flue wall from both the closed and open anode baking furnace are shown in Figure 2. The as-cut cross sections of the refractory material show clear indications of exposure to harsh environments during operation. Both linings have been exposed to the anodes at the left side, evident from the discoloring. Carbon deposition or reactions in the lining was suspected as one possible mechanism for the darkening of the region

TABLE 1 Chemical composition of the pristine refractory material used in the open and closed baking furnace as measured by XRF. All values are given in wt%

Furnace	Al_2O_3	SiO_2	Fe_2O_3	TiO_2	CaO	K_2O	MgO	Density [g/cm^3]	Open porosity [%]
Open	50.8	46.3	1.1	1.6	0.2	0.2	0.1	2.38	16.3
Closed	55.0	42.7	1.0	0.8	0.0	0.4	0.2	2.43	14.2

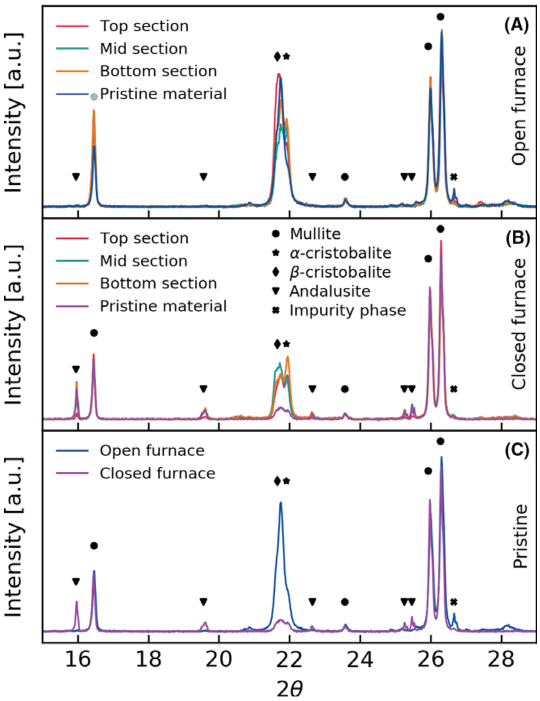

FIGURE 4 Phase composition of (A) samples from the open furnace, (B) samples from the closed furnace and (C) the two pristine materials. A and B include the samples facing the anode pit for all three heights in addition to the pristine materials in C [Color figure can be viewed at wileyonlinelibrary.com]

facing toward the anode. Heat treatment of samples at 1150°C for 48 hours demonstrated significant weight loss close to the anode side, corresponding to combustion of deposited carbon as reported earlier.[11] The color of the samples (not shown) did also change due to the thermal treatment in air, giving additional evidence that the discoloring is due to carbon deposition and partly reduction of the lining toward the anode side.

4.4 | Density and microstructure of refractory lining in open top design

Apparent density and open porosity measured for the three sampling heights in the open top furnace are summarized in Figure 5, showing a distinct increase in density. The gray region corresponds to the distribution of the measured density of the unreacted pristine materials. The densification is more pronounced closer to the anode side, in addition to being significantly higher in the bottom of the furnace compared to the middle and top section. Close to the flue side, the density is converging toward the pristine material for all three sampling heights. Density were measured both before and after heat treatment, corresponding to the filled and open markers in Figure 5, respectively. The density is significantly reduced after heat treatment caused by removal of deposited carbon within the open porosity. The open porosity presented in Figure 5 confirms the variation in the density, showing that the increase in the density is accompanied by a corresponding reduction in the open porosity.

The autopsy samples were thoroughly examined by electron microscopy, showing microstructural changes at the regions closest to the anode side. This change in microstructure is mainly found in grains facing the anode pit directly, or in the vicinity of open pores. Figure 6A shows the characteristic needle-like microstructure observed in the degraded layer in the bottom section. The layer is varying in width, up to ~200 µm. EDS analysis demonstrated that the degraded area has a low silica content, ie, there has been a depletion of silica from the refractory during operation. The remaining needle-like grains are composed of an aluminosilicate phase, close to mullite in composition. This chemical wear is primarily observed in the middle and bottom section of the flue wall, whereas the top section shows far less chemical wear of this kind. In the top section, the microstructural changes are quite different compared to the middle and bottom sections. While there are few signs of chemical wear, grains with very high silica content are present. In Figure 6B, an EDS image of the top section shows that the level of silica (yellow) and alumina (purple) varies significantly in this section. The chemical composition of the regions labeled 1, 2, and 3 in Figure 6B are presented in Table 2. Region 1 has a high silica content, while Region 2 and 3 show varying chemical composition. The probing volume of the EDS is larger than each individual crystal of each phase, and the EDS represent average compositions and not the composition of the mineral phases present in the material. The regions with high silica content are found all over the outer surface of

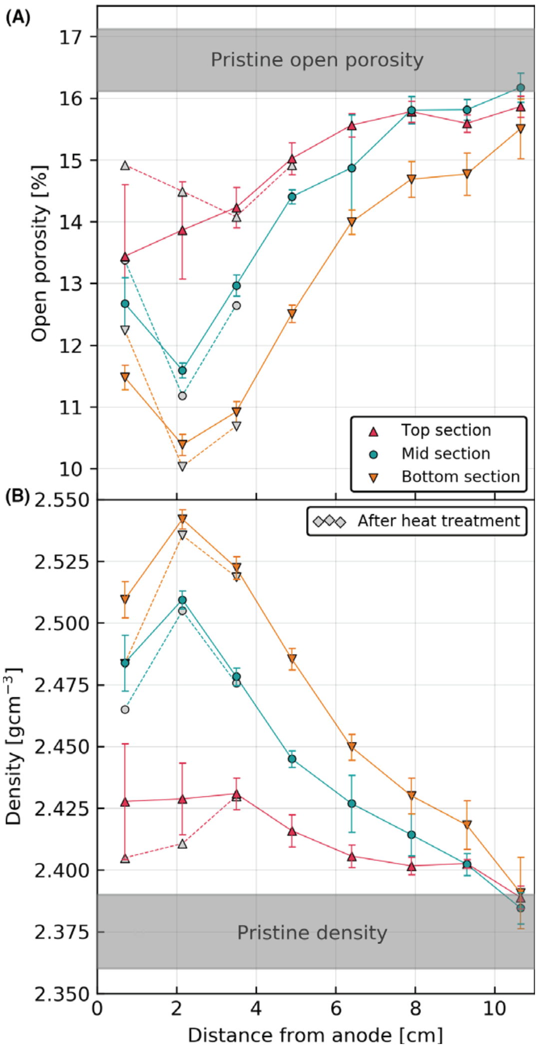

FIGURE 5 (A), Density and (B) open porosity of spent lining from the open top baking furnace. Filled and open markers are the density measured before and after heat treatment, respectively [Color figure can be viewed at wileyonlinelibrary.com]

the top section toward the anodes, both in the regions where the refractory wall is facing the anodes directly, and the regions close to open porosity.

The microstructure of the outer regions of a spent brick is shown In Figure 6C, showing variation in atomic contrast close to the surface. The average chemical composition of region 4 and 5 is found in Table 2, demonstrating significantly higher alkali content in the lighter region closer to the surface. No evidence of fluorine anions were observed by EDS in any of the samples. Even though there is a significant higher sodium content in point 4 compared

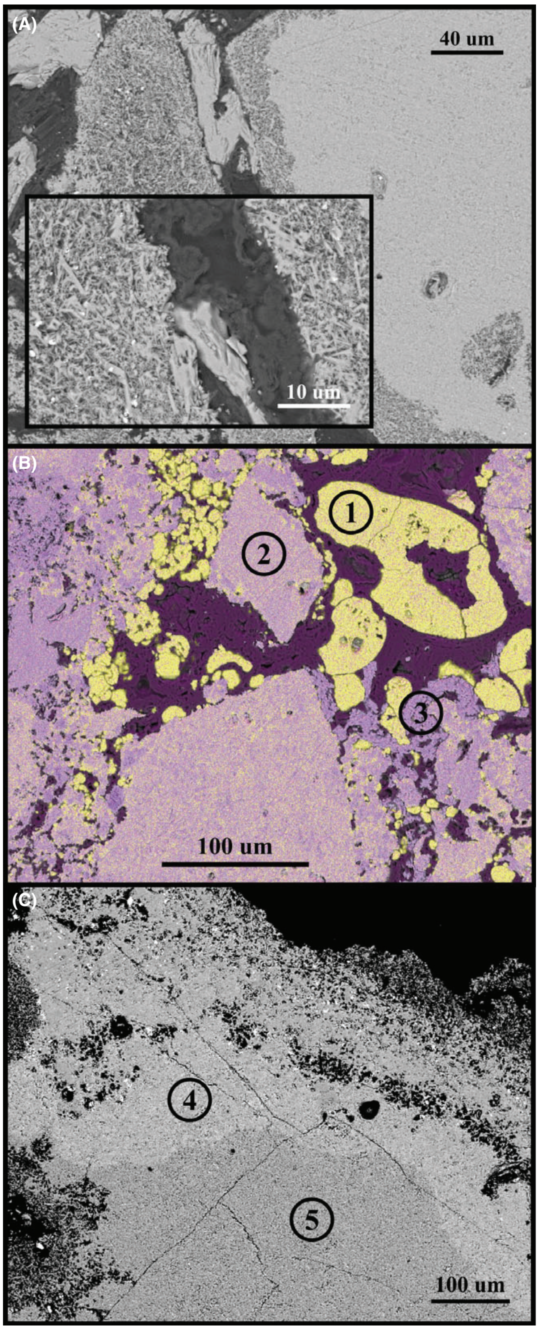

FIGURE 6 SEM micrographs from the anode facing surface in an open baking furnace. (A), Backscatter image of the microstructure of the bottom section, (B) EDS image from the top section and (C) regions with high and low content of alkali metals from the bottom section. Chemical composition measured at point 1-5 are found in Table 2 [Color figure can be viewed at wileyonlinelibrary.com]

TABLE 2 Average chemical composition of regions marked in Figure 6. All values are given in mol%

Region	Al	Si	O	Na	K	Ca	Mg	Ti
1	6.1	30	63	0.5				
2	22	17	61					
3	33	8	59					
4	20	17	61	0.8	0.5	0.2	0.4	0.7
5	20	17	62	0.2	0.1	0.6	0.3	0.5

to point 5, the overall sodium content is low. The absence of an amorphous phase from the X-ray diffraction investigations corresponds well with the relatively low levels of sodium. Previous investigations of similar furnaces often showed a glassy layer with a high sodium content in the outer parts of the sample.[7] This is not observed in any of samples from the spent lining.

4.5 | Density and microstructure of refractory lining in closed top design

Spent lining density from the closed top furnace are presented in Figure 7. The density is also in this case higher compared to the pristine density, but there is no major difference between part A and part B. Some variation in densification is found within each part, where the top section are less affected by densification and has a lower density compared to the middle and bottom sections, which are relatively similar. It is important to note the difference in the width of bricks in the two furnace designs, 11 cm vs 4 cm, and the minor variations in the density of the closed furnace could be due to the relative narrow cross section. Within the 4 cm outer region in the open design shown in Figure 4, the variation in the density is comparable to the one shown in Figure 7. No significant reduction in density after heat treatment was observed.

The microstructural changes observed in the open top furnace are also found in the closed top furnace. Both depletion and deposition of silica are observed at various positions in the furnace. The chemically etched regions with the needle-like microstructure and low silica content are also present in the closed furnace, but not as continuous layers and mainly close to open porosity or the anode-facing surface. The deposition of near-spherical silica particles were observed similarly in the closed furnace as for the open furnace design. The systematic variations with respect to sampling height are however not found in the same manner. Both the chemical wear, silicon depletion and deposition were observed in the top and bottom section, and cannot be related to the vertical position in the wall as clearly as for the open furnace. The degree of chemical degradation is also less in the closed furnace compared to the open furnace, possibly reflecting the difference in the number of exposed baking cycles.

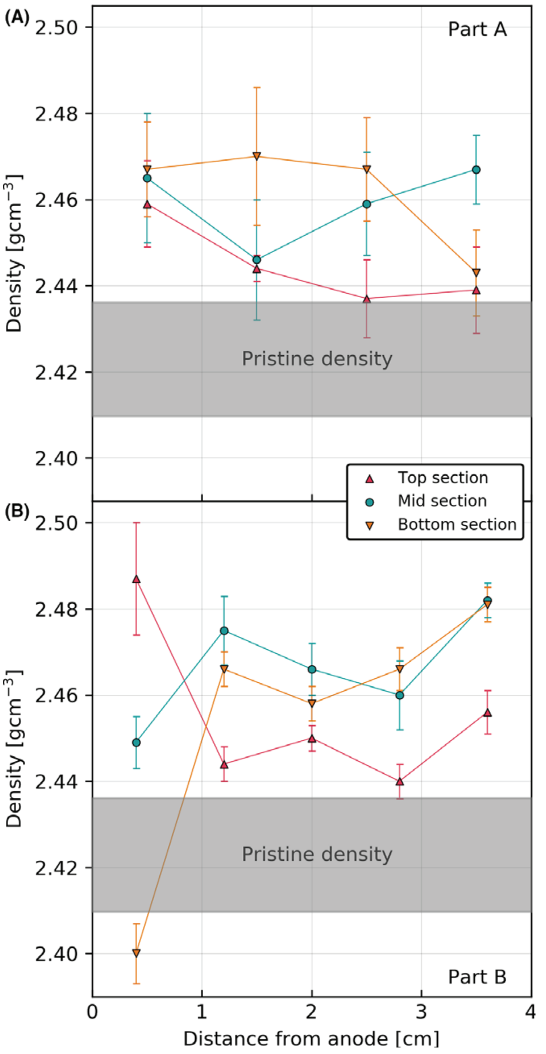

FIGURE 7 Density of spent samples from (A) part A and (B) part B of the closed baking furnace [Color figure can be viewed at wileyonlinelibrary.com]

X-ray diffraction analysis demonstrate that there is a low content of amorphous phase in the closed furnace, similar as observed for the open furnace design. This corresponds with the overall low level of sodium found in the spent lining, and the absence of a glassy layer close to the anode. A phase with high amounts of Al, Ni, and Fe was found in the top section of the closed furnace as shown in Figure 8. The phase was found in various amounts in the top section of both part A and part B. The average chemical composition of this phase is summarized in Table 3, marked as region 6.

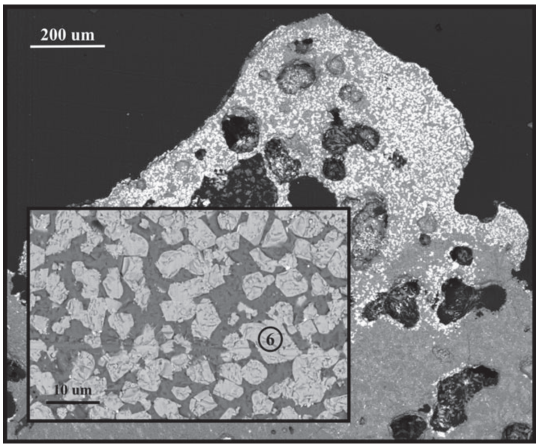

FIGURE 8 Top section of the closed baking furnace

TABLE 3 Average chemical composition for the regions indicated in Figures 8 and 9. All values are shown in mol%

Region	Al	Si	O	Na	Mg	Fe	Ni	Zn
6	19	0.2	54	1.6	3.4	14	6.6	0
7	1.9	0.6	57	0.8	0.2	36	0.1	2.0
8a	0.8	34	64	0.2		0.1	0.1	0.3
8b	27	9.0	63	0.5	0.3	0.7	0.1	0.4
9	0.8	34	64	0.2				0.3
10	1.9	1.4	64	0.7		31		1.2

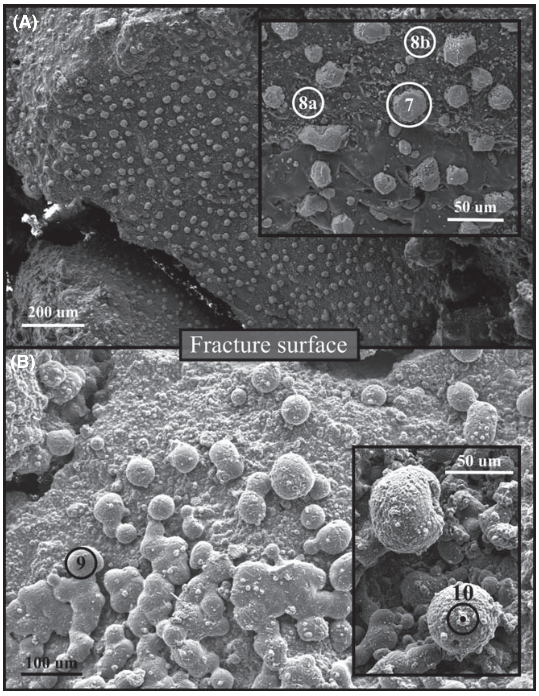

FIGURE 9 Fracture surface of the bottom section from the closed baking furnace. (A), An overview of the surface with the precipitated particles, and (B) particles with very high silica content observed in the same region

Investigations of a fracture surface from the bottom lining of the closed furnace revealed precipitation of iron rich particles all over the surface, see Figure 9. The fracture, going from the anode side toward the flue side, was present prior to sampling startup and can thus have occurred during operation of the furnace. The composition of the lighter particles (region 7) and the background phases (region 8a and 8b) in Figure 9 is summarized in Table 3. The particles have a high and stable content of Fe, while variation is observed for the material below the Fe-rich particles. In most cases the refractory is rich in silica although an aluminosilicate phase is also observed below the particles. At the same fracture surface, particles of almost pure silica were observed, while on top of these silica rich particles, a lighter phase was observed. Both phases are marked as region 9 and 10 in Figure 9, with the corresponding chemical composition given in Table 3.

5 | DISCUSSION

5.1 | Densification mechanism

The observed changes in density and open porosity demonstrate significant changes in the microstructure of the refractory lining. The observed densification results in reduction of the porosity and dimensional changes of the bricks in the regions with densification. Refractory materials are designed to operate at high temperature conditions, with the ability to withstand high temperature sintering or densification. This is achieved by the wide particle size distribution in the raw materials, where the largest particles give dimensional stability with smaller particles filling the voids. In order for densification to occur the center of particles must move closer toward each other, which is achieved by mass transport away from particle contact points. Due to the heterogeneous nature of the microstructure, a relative high amount of mass needs to be transported away from the contact points before significant densification can be accomplished, resulting in slow sintering kinetics. Hence, it is not likely that high temperature alone should account for the degree of refractory densification as presented in Figure 5. Addition of glass modifiers (eg, Na, K, or Ca) to the aluminosilicate refractory will, however, have a large impact on the thermal stability of the flue wall, increasing sintering kinetics significantly by enabling plastic deformation. The variations in densification presented in Figure 5 demonstrate that the conditions for densification are varying across the flue brick, being more in favor closer to the anode side.

There is a general agreement in the literature that sodium and/or fluorine containing gas species are important factors in the degradation of refractory lining in anode baking furnaces.[1,2,5,7,17,18] Green anodes usually consist of 20%-25% recycled anode butts, which, due to the exposure to cryolite during electrolysis, pose a potential source of sodium and fluorine in the furnace. At elevated temperatures, cryolite present in the green anodes can evaporate forming gaseous fluorides and possibly reduce the phase stability of the refractory lining.[10] Common for most reactions between gaseous fluorides and aluminosilicates is the formation of a sodium aluminosilicate phase (albite or nepheline) in addition to gaseous SiF_4.[10] If any reaction between volatile fluorides and the lining have occurred, sodium aluminosilicates would be present in the lining. Figure 6c and Table 2 show lining with significant variation in sodium content, where the highest sodium concentration is found closest to the surface. These regions with elevated sodium content are found close to open porosity or the refractory surface facing the anodes. If the elevated sodium content is to be linked directly to the density variations presented in Figure 5, clear variations in sodium content with respect to vertical sampling position are expected. This is however not observed, making it difficult to correlate variations in densification to the distribution of regions with increased sodium content.

The sodium levels presented in Table 2 are quite low compared to earlier reports.[1,7] Furthermore, the chemical composition in these regions are not corresponding to the expected sodium aluminosilicate phases. The formation of nepheline ($NaAlSiO_4$) and albite ($NaAlSi_3O_8$) is regarded as irreversible reactions, and once formed, the reaction products are not likely to disappear. In addition, the amount of amorphous phase in both linings is low. High levels of gaseous NaF or $NaAlF_4$ close to the anode side of the lining would have resulted in significant increase in sodium level and presence of sodium containing phases. The lack of sodium aluminosilicates in the spent lining is therefore disregarding the importance of degradation due to volatile fluorides.[10] The present data demonstrate clearly the minor effect of volatile fluorides in the pit atmosphere in the two furnaces investigated. Consequently, the cryolite level in the anode butts must have been low, indicating good cleaning routines and operational of the baking furnaces.

A reduction in densification is observed by postheat treatment, as presented in Figure 5. Parts of the overall densification observed for spent lining can thus be related to carbon deposition in the open porosity. Coal tar pitch from the green anodes evaporates during heating, resulting in an atmosphere with high level of various hydrocarbons. At higher flue wall temperatures, parts of the hydrocarbons are likely to crack at the refractory surface, especially in areas with low suction, leaving solid carbon at the surface and in the open porosity, and consequently increased density. The reduction in density after heat treatment in air confirmed oxidation of carbon, hence supporting the proposed carbon cracking reaction.[1,2,9] The preliminary study confirmed the presence of carbon in the outer layers facing the anode pit, with a significant reduction in carbon level farther into the lining.[11] This corresponds to investigations on similar samples showing carbon build-up on the flue wall.[9] The overall stability of the flue wall during thermal cycling is maintained by the use of mortar-filled gaps in the wall. These gaps enable the refractories to expand as the temperature increases, without causing compressional stress in the lining. However, over the course of years in operation, the gaps are filled with fines from the packing coke and deposited carbon, resulting in reduced overall flexibility. As the wall stiffens, the wall's ability to absorb thermal expansion is reduced, causing increased thermal stress to build up within the wall.

5.2 | Transport of SiO_2

Most reports agree on two reaction schemes being the main cause of the changes in the silicon oxide content, ie, either a reaction with gaseous fluorides, or a reaction caused by reducing atmosphere.[1,2,5,7,10,11,17,18] The lack of sodium aluminosilicate in the spent lining investigated here supports the minor influence of fluorides in the present two cases, disregarding the first alternative as the main mechanism. Low partial pressures of oxygen in combination with high temperature and compounds like CO, CH_4 or H_2, is proposed to have a destabilizing effect on the refractory oxide lining. In the bottom of the open furnace, reaction layers depleted of silica was observed. In order for SiO_2 to be removed from the lining, conditions favoring sufficiently high partial pressures of SiO must be present. As carbon is present at the flue wall through deposition and cracking of hydrocarbons from the anode, the material system describing the conditions at the lining is thus consisting of solid carbon and silica, in addition to gaseous CO, CO_2, and SiO. The partial pressures of these compounds are all linked together and highly dependent on the temperature in the furnace. Equations 1-3 describe the equilibriums reactions between these gas species and solid carbon and silica.

$$\mathrm{C\ (s)} + \mathrm{CO_2(g)} = \mathrm{2CO\ (g)} \tag{1}$$

$$\mathrm{CO_2(g)} = \mathrm{CO\ (g)} + 1/2\,\mathrm{O_2(g)} \tag{2}$$

$$\mathrm{SiO_2(s)} = \mathrm{SiO\ (g)} + 1/2\,\mathrm{O_2(g)} \tag{3}$$

At isothermal conditions, the Gibbs phase rule show that the system only has one degree of freedom. Hence, by fixing one of the partial pressures, the remaining partial

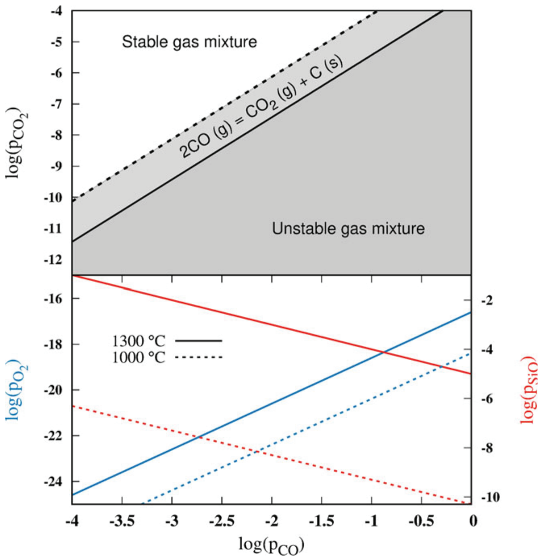

FIGURE 10 Partial pressures of CO_2, O_2, and SiO plotted as functions of p_{CO}. Pressures for 1300°C and 1000°C are presented with solid and dotted lines, respectively. The top section of the figure shows the stability region for the Boudouard reaction, with the equilibrium line separating the two regions [Color figure can be viewed at wileyonlinelibrary.com]

pressures can be calculated. The Boudouard reaction in Equation 1 describes the equilibrium between solid carbon, CO and CO_2, which is shown in the top part of Figure 10. As long as carbon is present (and the system is in equilibrium), the ratio between $p_{CO}{}^2$ and p_{CO2} is fixed as shown by the line in the upper section of Figure 10. By increasing this ratio and moving into the grey area, the gas mixture becomes unstable and solid carbon is precipitated. Based on Equations 2 and 3, partial pressures of O_2 and SiO at equilibrium are plotted as a function of the partial pressure of CO in the lower part of Figure 10, where the solid and dotted lines correspond to 1300°C and 1000°C, respectively.

At low p_{O2}, the partial pressure of SiO becomes high enough to result in SiO_2 volatility at 1300°C. The oxygen partial pressure is expected to be low in the bottom of the open furnace, and thus favor such conditions, explaining the observed silica depletion in the reaction layers. In the top section of the same furnace, particles of precipitated silica were observed at the surface of the lining facing the anodes. This suggests a transport of SiO(g) from the bottom or middle section upwards to the top section of the furnace, before re-oxidation into SiO_2. In the open baking furnace, the anodes are covered with a layer of packing coke in order to avoid oxygen intrusion in the top section. The air burn of packing coke is however not completely avoiding oxygen intrusion because of the lower temperature in the packing coke toward the top. Consequently, the partial pressure of oxygen is significantly higher in the top section compared to the bottom. An increase in oxygen pressure is accompanied by oxidation of SiO(g), resulting in precipitation of SiO_2 particles in the top section. The thermodynamics show that a transport of silica from the bottom section to the top section in the open furnace is possible considering local equilibrium in the lower and upper part. Investigations of similar samples have shown that both silica depletion and deposition could occur in the same region, given that the local conditions favor both reactions.[9] In the closed furnace, on the other hand, oxygen intrusion is reduced by the use of section covers, resulting in a significantly lower oxygen partial pressure in the flue gas below the section covers, compared to the surrounding air. A similar gradient in oxygen partial pressure in the pit is therefore not expected, corresponding with the lack of systematic depletion and deposition of silica with respect to vertical position. Silica reduction and re-oxidation were both observed in the top and bottom section indicating favorable conditions more locally and transport of silica occurring over shorter distances.

5.3 | Metal oxide precipitates

The chemical composition of the particles presented in Figure 8 are fundamentally different compared to the surrounding aluminosilicate material. The high content of iron and nickel cannot be rationalized by the nominal composition of the refractory material. It is therefore unlikely that the high concentration of metal cations is due to a redistribution of the trace elements in the pristine aluminosilicate refractory material. Furthermore, no significant reduction in metal content of green and baked anodes during baking is found, suggesting the anodes not being the source of Ni and Fe. The packing coke could be a potential source of both Fe and Ni, but no additional study was done to verify this suggestion. In Figure 9, the fracture surface is covered in particles with very high iron content. The density of precipitated particles decreases when moving into the refractory from the anode side, supporting the suggestion of precipitation from gaseous compounds in the pit atmosphere. Iron hydroxide could be a potential iron carrier compound in these conditions,[19] but to identify the specific mechanism resulting in transport of these elements requires further studies and are beyond the scope of this investigation.

5.4 | Importance of furnace design and flow pattern

In the open baking furnace, densification, silica depletion, and deposition were observed systematically with respect to both vertical position and distance from the anode.

Chemical wear was observed as uniform layers in the middle and bottom section of the lining, while silica deposition was found in the top section. The densification was more pronounced in the bottom section and decreasing upwards in the furnace, in addition to being most pronounced closer to the anode side for the whole lining. In the closed furnace, observations were less systematic and not following the same trends. Chemical wear was observed in specific areas, and not as the uniform degraded layer found in the open furnace. The areas where silica depletion was observed were found both in the top and bottom section without any apparent global trend. With respect to gaseous attack, the main difference between the two furnace designs is the flow pattern of the flue gas. As illustrated in Figure 1, the flue gas in the open furnace flows within the flue wall, and is never in direct contact with the anode side of the flue wall. In the closed furnace, the flue gas is released under the section covers after it escapes part A of the flue walls and is subsequently transported into part B. The main driving force for gas transport inside the furnace is the pressure difference across the flue walls (both furnaces) and between the anode pit and the area below the section covers (only closed furnace). The reduced pressure inside the flue walls results in a mainly sideways gas transport from the anode pit and into the walls. In the open furnace, this is the main method for gas transportation out of the anode pits. For the closed furnace, the section covers results in a reduced pressure above the packing coke, leading to a transport of anode pit gas upwards, in addition sideways into the flue walls. This variation in gas transport from the anode pit to the flue should have an impact on the degradation pattern. The absence of clear degradation trends with respect to the vertical position in the closed furnace could relate to the upwards transport of pit gas, reducing vertical variations in pit atmosphere. Both the degradation and silica deposition occurs in the top and bottom sections, possibly due to local conditions at the flue wall, rather than global trends over the whole flue wall. In the open furnace, the reduced pressure in the flue wall cause a horizontal transport of pit gas, and any variations in pit atmosphere could to a larger extent be maintained. However, the clear trend in silica depletion and deposition in the open furnace indicate some transport of gaseous SiO from the bottom or middle section to the top section. It is difficult of estimate how much of the reduced silica that actually is transported upwards, since some could have gone into the flue walls and deposited elsewhere. In addition, the temperature cycling influences the gas transport, and silica depletion and deposition, making the description of the mechanisms more complex.

Depletion and deposition of SiO_2 was observed to a much larger degree in the open furnace compared to the closed furnace. This is not unexpected, considering the difference in the number of baking cycles each flue wall has been exposed to. The samples from the open furnace have been 160 cycles in operation, while the samples from the closed furnace have been 63 cycles in operation. Nevertheless, both flue walls were taken out of operation due to reduced performance, ie, reduced structural and mechanical integrity, indicating that the silica transport is not the governing mechanism for the overall reduction in thermomechanical properties of the flue walls. It is more likely that the density variations have a larger implication on the overall thermomechanical stability of the flue walls, and thus is the main reason for the reduction in overall performance of the flue walls.

The variation in density (Figures 5 and 7) have some important differences when comparing the open and closed furnace. The clear trends observed for the open furnace, both with respect to distance from the anode and the vertical position in the lining, are not found equally distinct in the closed furnace. There could be several reasons for this observation, where the different flow pattern for the flue gas being one of them. Another important difference between the two sets of samples is the cross sectional width separating the anode side from the flue side, which is about 1/3 for the closed furnace compared to the open furnace. The density variations observed for the first 4 cm in the open furnace are comparable to the variation in the density variations found in the closed furnace, indicating that the mechanism governing the densification could be the same for both furnaces. A final major difference is the position of the burners used to control flue gas temperature. In the open furnace, the burners are positioned inside the flue walls, never being in direct contact with the atmosphere surrounding the anode side of the flue walls. Any residues from the combustion of fuel will not mix with the pit atmosphere, and therefore not affect any chemical processes going on at the refractory surface facing the anode side. In the closed furnace, on the other hand, the burners are located underneath the section covers and inside the fire shafts, being directly in contact with the pit atmosphere.

6 | CONCLUSIONS

Autopsies of spent refractory linings in an open and a closed baking furnace were carried out with focus on mineralogical and microstructural changes. The study has illustrated differences and similarities with respect to degradation patterns of the two furnace designs. In the open baking furnace, significant densification was observed, in addition to transport of silicon oxide from the bottom to the top section. Both phenomena show clear dependencies of vertical position in the lining and horizontal distance from the anode into the flue wall. Similar observations have been reported for the closed baking furnace, but the variations were not systematic with respect to the position. Thermodynamic considerations support formation of SiO(g) due to reducing atmosphere as the main mechanism for SiO_2 transport. The difference in flue wall design is suggested to be the main reason for the observed variations between the two furnaces. Anode gas is transported out of the pit both horizontally and vertically, due to a reduced pressure in the flue wall and below the section covers, respectively. The former is found in the open furnace while both is the case in the closed furnace, linking to the variations in observed degradation trends. The observed densification demonstrate a significant change in brick dimensions during operation, most likely being the main cause of the reduction in thermomechanical stability of the flue wall. Finally, no significant levels of sodium or fluorine were observed in either of the furnace linings, demonstrating that chemical attach due to traces of electrolyte in the green anodes were not taking place in these two cases.

ACKNOWLEDGMENTS

The authors acknowledge the financial support from the Norwegian Research Council and the industrial partners Hydro Aluminium, Alcoa, Elkem Carbon and Skamol A/S through the project “Reactivity of Carbon and Refractory Materials used in metal production technology” (CaRMa).

ORCID

Tor Grande http://orcid.org/0000-0002-2709-1219

REFERENCES

1. Prigent P, Bouchetou ML. Gaseous corrosion of aluminosilicate efractories in anode baking furnaces used for aluminium produciton part 1. Interceram. 2009;58(2–3):121–6.
2. Prigent P, Bouchetou ML, Poirier J, Hubert P. The effect of the addition of fine andalusite particles in refractory bricks on gaseous corrosion. JOM. 2008;60(5):58–63.
3. Moors EHM. Technology strategies for sustainable metals production systems: a case study of primary aluminium production in The Netherlands and Norway. J Clean Prod. 2006;14:1121–38.
4. Schwarz H-G, Briem S, Zapp P. Future carbon dioxide emissions in the global material flow of primary aluminium. Energy. 2001;26(8):775–95.
5. Prigent P, Bouchetou ML. Gaseous corrosion of aluminosilicate refractories in anode baking furnaces used for aluminium produciton part 2. Interceram. 2009;58(4):202–9.
6. Prigent P, Bouchetou ML, Poirier J. Andalusite: an amazing refractory raw material with excellent corrosion resistance to sodium vapours. Ceram Int. 2011;37(7):2287–96.
7. Brunk F. Corrosion and behavior of firecal bricks used in the flues of open anode baking furnaces. Light Metals. 1995;641–6.
8. Oumarou N, Kocaefe D, Kocaefe Y. Investigation of the refractory bricks used for the flue wall of the horizontal anode baking ring furnace. Ceram Int. 2016;42(16):18436–42.
9. Wang Z, Rørvik S, Ratvik AP, Grande T. Formation of carbon cuild-up on the flue wall of anode baking furnace. Light Metals. 2017;1265–74.
10. Brandvik T, Ratvik AP, Grande T. Thermodynamic assessment of the chemical durability of refractory lining in anode baking furnaces. Proceedings 34th Conference and Exhibition ICSOBA Qubec City, Cananda, October 2016.
11. Brandvik T, Ratvik AP, Wang Z, Grande T. Investigations of spent refractory lining in an anode baking furnace. Light Metals. 2017;4:1281–8.
12. Becker FH, Goede F. Ring pit furnaces for baking of high quality anodes – an overview. Aluminium. 2006;82:9.
13. Damby DE, Llewellin EW, Horwell CJ, Williamson BJ, Najorka J, Cressey G, et al. The alpha-beta phase transition in volcanic cristobalite. J Appl Crystallogr. 2014;47:1205–15.
14. Perrotta AJ, Grubbs DK, Martin ES, Dando NR. Chemical stabilization of p-cristobalite. J Am Ceram Soc. 1989;72(3):441–7.
15. Alcala MD, Real C, Criado JM. A new “incipient-wetness” method for the synthesis of chemically stabililzed beta-cristobalite. J Am Ceram Soc. 1996;79(6):1681–4.
16. San O, Özgür C. Investigation of a high stable beta-cristobalite ceramic powder from $CaO\text{-}Al_2O_3\text{-}SiO_2$ system. J Eur Ceram Soc. 2009;29:2945–9.
17. Butter J, Bongers A. Alterations of anode baking furnace bricks during operation. Light Metal. 1995;633–9.
18. Uhrig JR. A unique refractory solution for anode baking furnace flues. Light Metal. 2004;553–7.
19. Belton GR, Richardson FD. A volatile iron hydroxide. Trans Faraday Soc. 1962;58(1):1562.

How to cite this article: Brandvik T, Wang Z, Ratvik AP, Grande T. Autopsy of refractory lining in anode kilns with open and closed design. *Int J Appl Ceram Technol*. 2019;16:602–613. https://doi.org/10.1111/ijac.13108

D.5 Scientific paper 2

T. Brandvik, H. Gaertner, A. P. Ratvik, T. Grande and T. A. Aarhaug. *In situ* Monitoring of Pit Gas Composition During Baking of Anodes for Aluminium Electrolysis, *Metall. Mater. Trans. B.*, 50(2):950-957, 2019.